IOP Publishing
Reports on Progress in Physics
Rep. Prog. Phys. **85** (2022) 036101 (95pp)
https://doi.org/10.1088/1361-6633/ac2aaf

Review

Active optical metasurfaces: comprehensive review on physics, mechanisms, and prospective applications

Jingyi Yang[1,2], **Sudip Gurung**[1,2], **Subhajit Bej**[2], **Peinan Ni**[2]
and Ho Wai Howard Lee[1,2,*]

[1] Department of Physics & Astronomy, University of California, Irvine, CA 92697, United States of America
[2] Department of Physics, Baylor University, Waco, TX 76798, United States of America

E-mail: Howardhw.lee@uci.edu

Received 30 December 2020, revised 7 June 2021
Accepted for publication 28 September 2021
Published 3 March 2022

Abstract
Optical metasurfaces with subwavelength thickness hold considerable promise for future advances in fundamental optics and novel optical applications due to their unprecedented ability to control the phase, amplitude, and polarization of transmitted, reflected, and diffracted light. Introducing active functionalities to optical metasurfaces is an essential step to the development of next-generation flat optical components and devices. During the last few years, many attempts have been made to develop tunable optical metasurfaces with dynamic control of optical properties (e.g., amplitude, phase, polarization, spatial/spectral/temporal responses) and early-stage device functions (e.g., beam steering, tunable focusing, tunable color filters/absorber, dynamic hologram, etc) based on a variety of novel active materials and tunable mechanisms. These recently-developed active metasurfaces show significant promise for practical applications, but significant challenges still remain. In this review, a comprehensive overview of recently-reported tunable metasurfaces is provided which focuses on the ten major tunable metasurface mechanisms. For each type of mechanism, the performance metrics on the reported tunable metasurface are outlined, and the capabilities/limitations of each mechanism and its potential for various photonic applications are compared and summarized. This review concludes with discussion of several prospective applications, emerging technologies, and research directions based on the use of tunable optical metasurfaces. We anticipate significant new advances when the tunable mechanisms are further developed in the coming years.

Keywords: active metasurfaces, nanophotonics, photonics devices, nonlinear metasurfaces, metasurfaces

(Some figures may appear in colour only in the online journal)

---

[*] Author to whom any correspondence should be addressed.
Corresponding editor: Dr Masud Mansuripur.

Contents

1. Introduction

Photonic metamaterials, artificially-constructed materials composed of subwavelength scale nano-antennas that could tailor the electromagnetic response of the incoming light, have been a topic of significant interest in the last two decades. These nanostructured materials can exhibit unique optical properties that cannot be achieved with conventional materials. Some of these properties include negative refraction, tailored nonlinear optical properties, sub-diffraction-limited imaging, strong confinement of electromagnetic fields, giant optical activity, and strong magneto-optical property [1–5]. Although metamaterials show significant promise for novel optical applications, practical challenges such as high optical losses, complications in fabrication using the conventional nanolithography techniques, and strong wavelength-dependence due to the resonant structures/multilayer stacks limit the use of current bulk metamaterials for practical applications. In contrast, newly-developed optical metasurfaces (two-dimensional versions of bulk metamaterials) show promise for overcoming these challenges.

Metasurfaces are arrays of subwavelength anisotropic light scatters (optical antennas) with customized unit cells. Each unit cell is deterministically configured to control the amplitude, phase, and polarization of the transmitted, reflected, and diffracted light [6–8]. These metasurfaces can be employed for various applications such as beam steering, focusing, and optical switching, and for complex scattering formation such as holograms [9]. Due to the flat nature of metasurfaces (typical thickness <100 nm), they could enable ultrathin optical components such as flat lenses [10, 11], wave plates [12], holographic surfaces [13–17], and compact orbital angular momentum manipulation and detection devices [18–21] over a broad range of the electromagnetic spectrum.

When the experimental demonstration of metallic metasurfaces was accomplished in 2008, researchers realized that these nanostructured surfaces have significant promise for constructing future ultrathin optical devices. However, the low optical efficiency and lack of post-fabrication tunability in metallic metasurfaces remained key issues limiting their utilization in real-world applications. As a result, over the last few years, researchers have put significant efforts in the development of metasurfaces using low loss dielectric materials and semiconductors, for instance, silicon [22–38], conducting oxide [39–42], titanium oxide (TiO_2) [43–47], and silicon nitride (SiN) [48, 49]. The research into alternative materials is further advancing metasurfaces toward use in ultrathin optical components with high efficiency [50]. For instance, with the advancement of the dielectric metasurfaces, achromatic and broadband metasurface lenses (also called metalens) with a transmission efficiency of $>50\%$ have been achieved in the visible regime of the electromagnetic spectrum [47, 51–53]. Applications based on efficient metasurfaces that have been successfully demonstrated in the last few years include a compact spectrometer [54], phase gradient/advanced microscopy device [33, 55, 56], on-chip laser/emission device [57], full-color holographic devices [13–15, 17, 58, 59], metasurface-based bio-sensors [60], compact full-Stokes polarization camera [61], and laser pulse shaping instrument [62]. Recent developments in optical metasurfaces have been reviewed in several papers and book chapters [7, 8, 63–81]. This review article will focus on the advancements in tunable metasurfaces.

As noted above, metasurfaces hold considerable promise for future advances in fundamental optics and novel optical applications due to their unprecedented ability to control the amplitude, phase, and polarization of the transmitted, reflected, and diffracted light with interaction distance in the subwavelength dimensions [82]. However, the electromagnetic responses of conventional metasurfaces are fixed after fabrication due to the static electron density of the noble metals/semiconductors, the optical constants of the dielectric materials, and the fixed structural shapes/geometries. These limit the practical and more advanced applications of the metasurfaces such as dynamic manipulation of the wavefront of the incident electromagnetic wave.

Therefore, there is a significant need to develop tunable metasurface components for post-fabrication tunability and novel functionalities. A variety of research teams are investigating active versions of metasurfaces. Figure 1 shows the number of published journal articles related to metasurfaces and tunable metasurfaces (all topics related to dynamic properties) over the last decade (2010–2020). Note that the number of articles on tunable metasurfaces is increasing significantly (close to one-third of the metasurface articles in the last three years) due to the need for incorporating advanced active functionalities in ultrathin optical metasurfaces.

An active optical metasurface provides dynamic control of the transmitted/reflected/diffracted wavefronts, including individual or simultaneous control of the optical phase, amplitude, polarization state, and spectral/temporal/spatial responses (figure 2(a)). With full control of the flow of light using active metasurfaces, novel optical functions can be realized. Conceptual visualizations of functional tunable metasurfaces are shown in figure 2(b), where each individual resonant element (or a sub-group of elements) is controlled by external stimuli separately (e.g., electrical, thermal, optical, or mechanical control). Ideally, each individual element can be controlled (or 'pixelized') separately, allowing dynamic optical features from each element. However, to date, there is no experimental demonstration of active nanoscale metasurfaces with control of each individual element due to the practical technical challenges, and instead only a limited group of elements can currently be modulated.

With a proper choice of the material and a judicious design of the unit cell, metasurfaces can enable post fabrication tunability of the phase and amplitude. These will allow optical functions such as dynamic beam steering and tunable focusing (figures 2(c) and (d)). For example, in an electrically-tunable metasurface, resonant elements could be connected separately in unique gating addresses to ensure a fine control of the phase and creating a tunable phase front for light steering (figure 2(c)). Depending on the number of discrete voltage inputs, a different series of voltages could be applied to tune the wavefront and to steer light with different angles. Similarly, it would help in the realization of a metalens with tunable focus (figure 2(d)). A functional metasurface should exhibit great potential for large phase and amplitude modulation of transmitted/reflected light, high operational speed and efficiency, and low energy consumption. It would also be ultrathin and lightweight and consist of subwavelength scale unit elements to ensure future device scalability. Such a metasurface could be the basis for a whole new class of flat photonic devices and applications (figure 2).

Significant attempts have been made in the last few years to realize metasurfaces with controllable amplitude and phase modulation, using both alternative materials and novel designs. Alternative materials being investigated include conducting oxide materials, liquid crystals (LCs), two-dimensional materials, phase change materials, etc. Novel tuning mechanisms being investigated include flexible/stretchable mechanisms, phase change mechanisms, electrical tuning, nano-mechanical tuning, and nonlinear optical tuning. Most of these studies in the field of metasurfaces are in the stage of proof-of-principle demonstrations, and since each mechanism has its advantages and disadvantages in terms of optical performance characterizations, comparing tunable mechanisms for a case-specific optical application is challenging.

The goal of this review article is to provide a comprehensive overview of the physics, mechanisms, and prospective applications of the recently-developed tunable metasurfaces. During the time of preparing this review article, several other good review papers on tunable metasurfaces were also reported [83–96]. In this review article, we focus on presenting the fundamental principles in some detail for each tunable mechanism, assessing the key pros and cons for each mechanism by analyzing a large number of references related to active metasurfaces, and outlining several prospective applications that could be enabled by that mechanism. In addition, since each different tunable mechanism has its own performance characteristics, including the (I) ability of phase and amplitude control, (II) operation speed, (III) efficiency, (IV) power consumption, (V) operation wavelength range, (VI) fabrication technique/type of unit cell element, and (VII) device or tunable feature dimension, we attempt to outline all the performance metrics on most of the reported tunable metasurfaces and summarize the capabilities of each

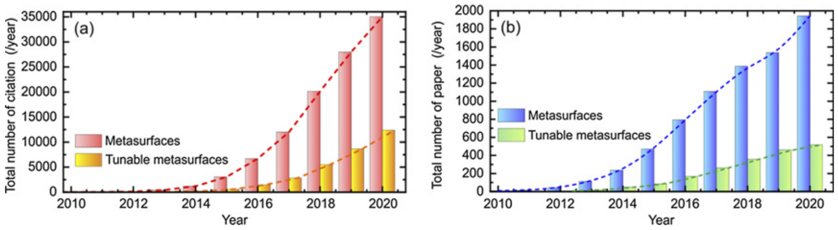

Figure 1. The number of (a) published articles and (b) citations on 'metasurfaces' and 'tunable metasurfaces' in 2010–2020 from Web of Science. The 'tunable metasurfaces' numbers include the research related to the keyword of tunable, active, dynamic, nonlinear, and reconfigurable metasurfaces.

tunable mechanism and its potential for various photonic applications. We focus on experimental demonstration related to operation wavelength in the visible or near-infrared regime that can lead to nanoscale photonic devices. This review provides a detailed overview of functional metasurfaces and their potential to develop novel optical imaging, sensing, spectroscopy, energy harvesting, and communication applications (figure 3).

To provide a broad overview of the performance characteristics of different mechanisms, table 1 (top) gives a brief comparison of ten different tunable metasurfaces and their performance characteristics. Note that only the best performances are listed in the table. Each mechanism has its own advantages and disadvantages, and those will be discussed through the following sections (see table 1 bottom for details on performance metrics on all the listed tuning mechanisms).

2. Electrically-tunable metasurfaces

Electrical modulation is one of the physical mechanisms for the modulation of the complex refractive index of semiconductors or active electro-optic materials. Typically, the electronic modulation requires contact layers such as a metal or semiconductor; thus, they can be easily integrated with metallic- or semiconductor-based metasurfaces operating in transmission or reflection. Several electrically-active materials have been utilized to control the metasurface properties, including transparent conducting oxide (TCO) materials, two-dimensional semiconductors, LCs and III–V semiconductors as discussed below.

2.1. *Gate-tunable conducting oxide metasurfaces*

TCOs are semiconductors with high transmittance at visible and near-infrared wavelengths. They can be heavily n-type doped with typical free charge carrier concentrations, N of 10^{19} to 10^{21} cm^{-3}, thus exhibiting metallic characteristics (e.g., negative permittivity) in the visible/near infrared (figure 4) [50, 97, 98]. While the conducting oxides exhibit metallic properties, their material loss is significantly lower than noble metals (gold and silver) due to the carrier concentration of the materials, making them attractive as alternative plasmonic metasurface materials. Several research groups have studied the plasmonic properties of the conducting oxides in different plasmonic or metamaterial structures, showing opportunities for visible/near infrared plasmonic applications with lower loss [97–113].

The complex permittivity (ε) of a conducting oxide is strongly related to its intrinsic carrier concentration (N). Hence, the complex refractive index can be derived by using the conventional free-electron Drude model, which is usually used to describe metals. The dispersive permittivity of a conducting oxide can be expressed as

$$\varepsilon\left(\omega\right)=\varepsilon_{\infty}-\frac{q^2N}{\varepsilon_0 m_{\mathrm{e}}^{*}}\left(\frac{1}{\omega^2+\mathrm{i}\omega\gamma}\right),$$

where ω is the angular frequency of the incident wave, $m_{\mathrm{e}}{}^{*}$ is the effective electron mass in TCO films, N is the carrier concentration of TCO, and γ is the collision frequency of TCO [114]. Based on the above equation, the complex permittivity of TCO can be evaluated according to the carrier concentration. Figure 4(a) shows the calculated complex permittivity of indium tin oxide (ITO), one of the most common TCO materials [114]. Note that the material dispersion shifts significantly to a shorter wavelength with a higher carrier concentration. The plasma frequencies shift all the way from near-infrared ($N \sim 10^{19}$ cm^{-3}) to ultraviolet range ($N \sim 10^{21}$ cm^{-3}) with different carrier concentrations of the material. For an operation wavelength such as $\lambda_0 = 1550$ nm, the real part of the permittivity can be tuned from positive (dielectric property) to negative value (metallic property) by changing the carrier concentration, hence exhibiting the potential of TCO for active metasurfaces. Note that the carrier concentration of TCO can be varied by different fabrication methods, e.g., atomic layer deposition (ALD), chemical vapor deposition, magnetron sputtering, and pulsed laser deposition (sputtered ITO and ALD-fabricated aluminum-doped zinc oxide (AZO) in figure 4(b)), by post-processing techniques (e.g., annealing), and by deposition conditions [97, 98, 105, 113, 114]. In addition, the standard free electron Drude model (red dashed curves in figure 4(c)) describes the permittivity accurately in the visible and near-infrared regime.

Notably, a metal-oxide-semiconductor-field effect structure combining the TCO film, a dielectric insulator, and the metal layers can be formed to gate the TCO film. By applying external bias, the Fermi level of TCO and band alignment can be modulated accordingly (figure 5(a)). Thus, the carrier distribution and the permittivity of the material can be modulated accordingly. Figure 5(b) shows the accumulation layer revealed by the field-effect electrostatic calculations. The carrier concentration of the ITO film at the Al_2O_3/ITO interface

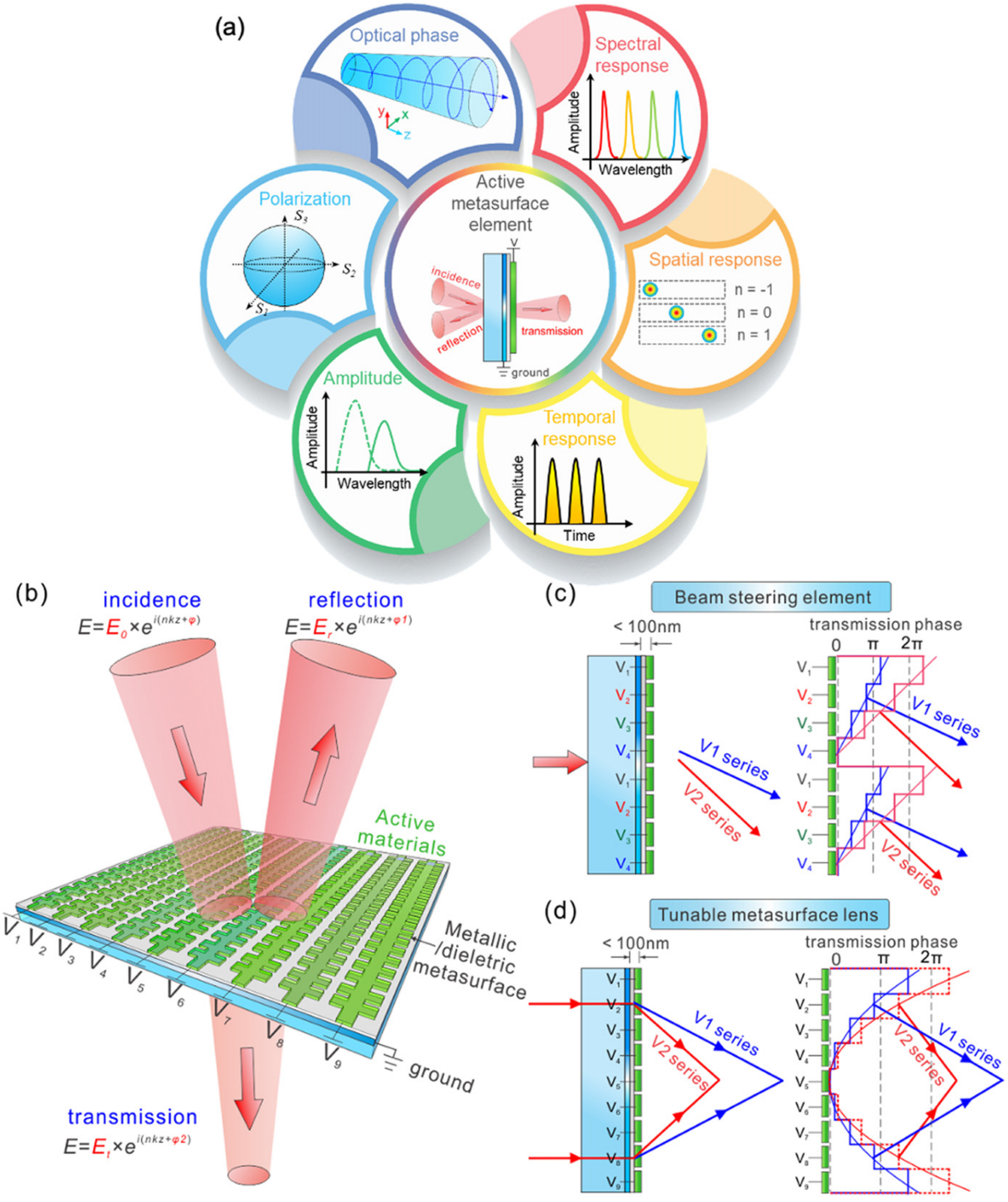

Figure 2. Fundamental light properties controlled by active metasurfaces. (a) Ideal active metasurface that exhibits the ability for efficient control of the optical phase, amplitude, polarization state, and the spatial/spectral/temporal responses of the transmitted/reflected/diffracted light. Schematic of (b) an example of an electrically-tunable metasurface. (c) Dynamic beam steering with four-level input voltages, and (d) tunable metalens with controllable focus.

Table 1. Overview of the performance characteristics of ten mechanisms, the key pros/cons, and the demonstrated applications of tunable mechanisms.[a]

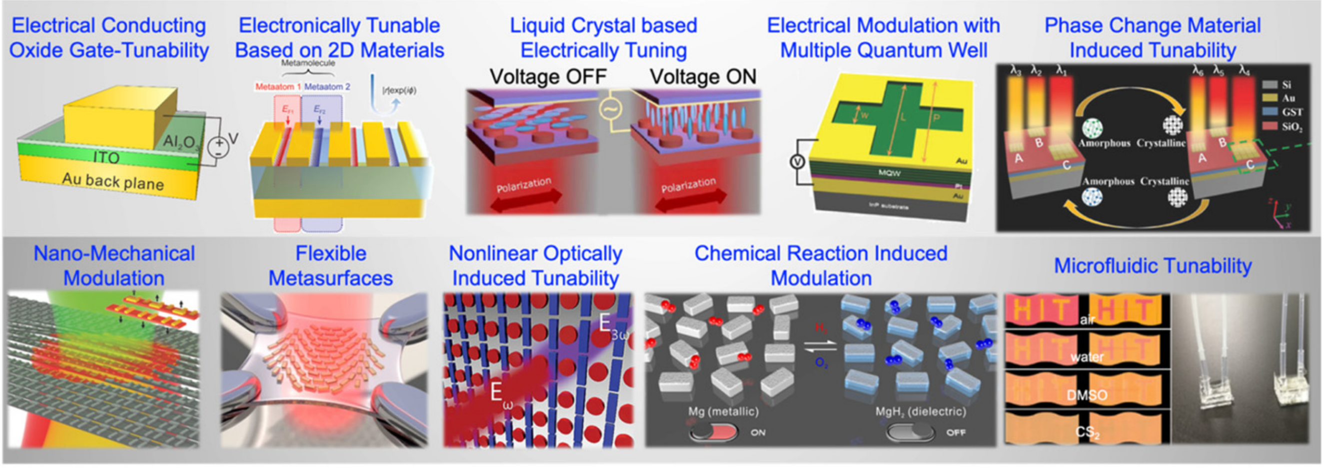

Mechanism	Phase shift	Amplitude modulation	Operation speed	Power consumption	Efficiency	Unit dimension	Operation wavelength	Advantages	Key Limitations	Demonstrated Applications/ functions
Conducting oxide field-effect tunability	👍 Δφ = 303°	👍 ΔR/R = 89%	👍 10 MHz; >1 GHz (Est.)	👍 2-10 V; 2.5 fJ (Est.)	👎 <30%	👍 p = 400 nm	NIR to Mid IR	• Potentially high-speed operation • Low power operation • Compatible to MOS devices	• Low efficiency • Mainly in reflection • Challenge on large area due to breakdown	• Beam steering • Tunable absorber • Tunable lens
Electrical tuning based on 2D materials	👍 Δφ =237°	👍 ΔR/R = 95.8%	👍 ~20 GHz	👍 0-3 V	👎 <50%	👍 single layer p ~1000 nm	Mid IR to Far IR	• High operation speed • Low power consumption • Ultrathin device	• Limited wavelength range • Limited modulation • Challenge on large area integration	• Tunable absorber/ modulators • Tunable lens
Liquid crystal based electrical tuning	👍 Δφ = 360°	👍 ΔT/T = 500%	👎 <1 kHz	👍 0-4 V	👍 97%	👌 LC = 4-6 μm p = 240 nm	Visible to NIR	• High efficiency • Larger tuning of refractive index	• Slow switching speed • Large liquid crystal size	• Beam steering • Color filter • Spatial light modulator
Electrical modulation with multiple quantum well	👎 Δφ ~70°	👍 ΔR/R = 270%	👍 100 MHz	👍 0-4 V 1 mW/cm²	👍 90%	👎 p = 910 nm	NIR to Mid IR	• Low power consumption • Fast modulation speed	• Limited to long wavelength range • Large element size • Small change of refractive index	• Beam steering • Absorption modulator • Reflection modulation
Phase change material induced tunability	👍 Δφ = 300°	👍 ΔR = 100%	👎 <1 kHz	👌 <15 V; 21 nJ	👎 5-75%	👍 p = 300 nm	Visible to Mid IR	• Large tunable refractive index range • Numerous material candidates	• Slow switching speed • Irreversible in some cases • Less compatible for devices	• Switching • Beam steering • Tunable holography • Bifocal lens
Reconfigurable nanomechanical tunability	👍 Δφ = 360°	👍 ΔR = 95%	👌 1 MHz	👍 1 V; 2.5 μW	👍 90%	👍 p = 300nm	Visible to THz	• Large modulation for both phase and amplitude • Low power consumption	• Challenge on individually pixelized for each element • Relatively large element dimension	• Beam steering • Tunable filters • Tunable lens
Flexible metasurfaces	👍 Δφ = 360°	👍 ΔR/R = 160%	👎 Not demo.	👎 Not demo.	👍 ~90%	👍 p = 380 nm	Visible to NIR	• Good flexibility for large phase and amplitude modulation	• Slow modulation speed • Sensitive to environment • Hard to pixelized	• Tunable lens • Tunable color filters
Nonlinear optically induced tunability	👍 Δφ = 90°	👍 ΔR/R = 90%	👍 ~15 THz	👎 1.2-12 kW/cm² for phase shift/SHG	👎 η_{SHG}~0.8%	👍 p ~300 nm	NIR to Far IR	• Large refractive index change • Possible for new frequency generation • High switching speed	• Low conversion efficiency • High-power pump laser required • Unable individually pixelized	• Ultrafast all optical switch • Dynamic holography • Frequency conversion
Hydride-loading transition metal tunability	👍 Δφ = 180°	👍 ΔR = 50%	👎 <0.1 Hz	H_2 and O_2	👍 <75%	👍 P = 280 nm	Visible to NIR	• Large tunability from metal to dielectric	• Slow tunable speed • Unable individually pixelized • Special tunable condition	• Dynamic color display and holography • Beam steering
Microfluid-based tunability	Not demo.	👍 ΔR = 40%	👎 <60 Hz	refractive index liquid	👍 55-95%	👍 P = 300 nm	Visible to NIR	• Compatible with microfluidic chip • Decent device efficiency	• Slow switching speed • Unable individually pixelized • Additional microfluidic channel	• Tunable color display

[a] Note that only the best performances are listed in the table. The listed parameters are exacted from the various references in tables 2–14. NIR: near infrared; SHG: second harmonic generation.

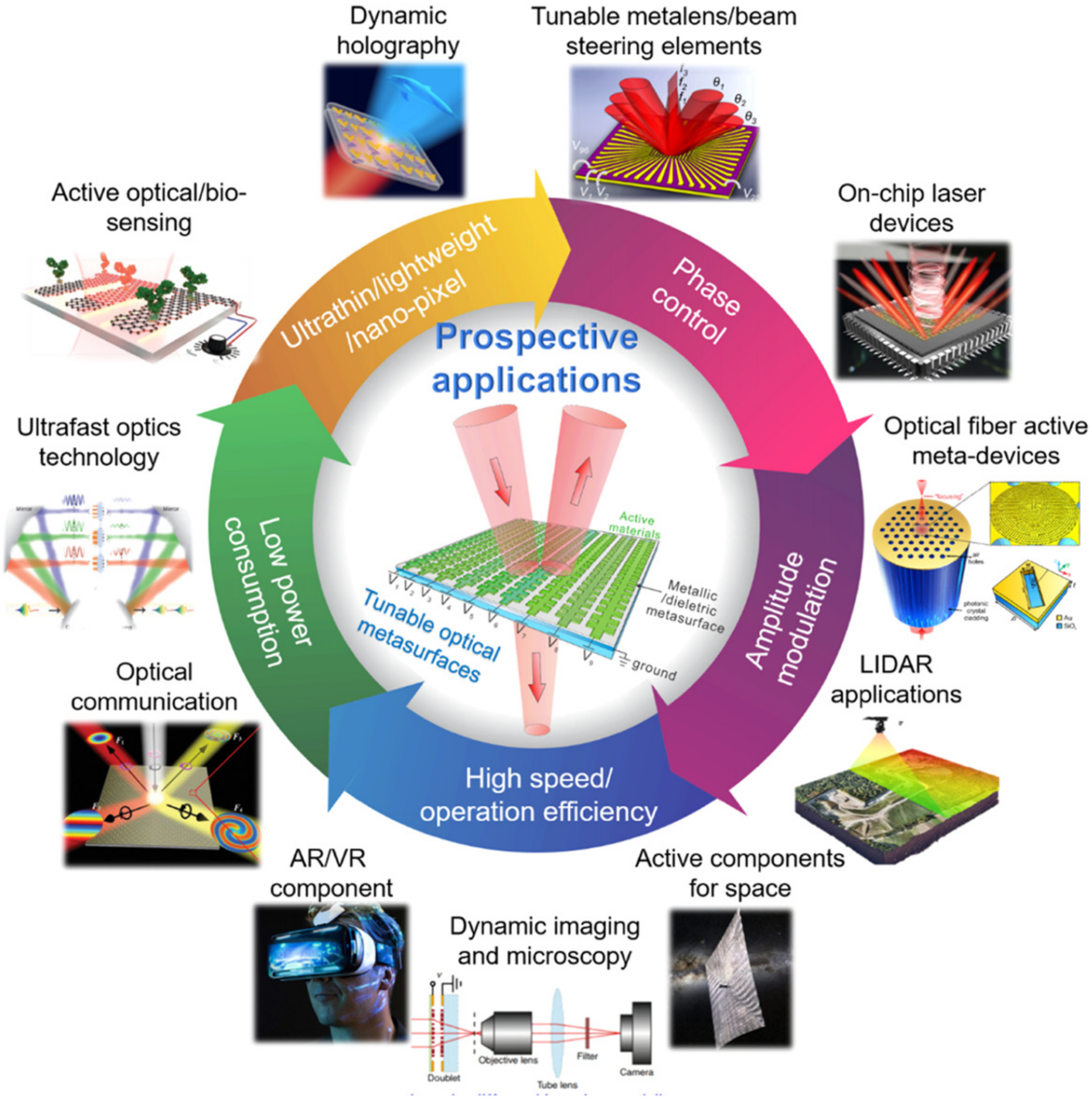

Figure 3. Overview of tunable metasurfaces based on different advanced tunable mechanisms. Efficient active metasurfaces will exhibit large optical phase and amplitude modulation, high operation speed and efficiency, low power consumption during the operation, and be ultrathin and lightweight in device architecture. Reconfigurable metasurfaces show significant promise for advanced nanophotonic applications for imaging, display, sensing, communication, energy, and space technologies.

increases three times as compared to the bulk value when applying an electric bias of 4 V (figure 5(c), top), leading to the change of permittivity (ε_r) for different applied biases at an operation wavelength of 1550 nm [116].

Additionally, the permittivity of the ITO can reach to the epsilon-near-zero (ENZ) region ($-1 < \varepsilon_r < 1$) at an applied bias of 2–4 V (highlighted by the gray area in the inset of figure 5(c), bottom). When satisfying the ENZ condition, a considerable enhancement of the electric field can be realized in the accumulation layer of the ITO; this field enhancement provides promising opportunities for light manipulation in advanced devices [117–121]. Since the drift velocity of electrons that form the accumulation layer can exceed THz, with the small footprint and low capacitance of nano-devices, the modulation frequency could potentially exceed tens of GHz (up to THz depending on the resistor–capacitor circuit). For instance, GHz modulation was demonstrated in a TCO/Si photonic modulator [114, 122], which can be applied to electrical TCO meta-devices. Note that the field-effect dynamics also depend strongly on the material properties such as the Fermi level, effective electron mass, electron mobility, material bandgap, and the work function of the materials. Designing the structure with the proper metal/dielectric/semiconductor combination can increase the carrier concentration modulation and depletion/accumulation layer (also called Debye length).

Recent work on TCO-based metasurfaces exhibits promising results. Huang *et al* reported a gate-tunable metasurface working in the near-infrared wavelengths [116]. The proposed metasurface consists of a gold grating on top of an Al_2O_3 layer, an ITO film, and a gold reflector (figures 6(a) and (b)). The dynamic control of amplitude and phase of the reflected wavefront has been achieved. The gold stripes can be connected to different electrodes for applying different electrical bias, which allows them to impose different

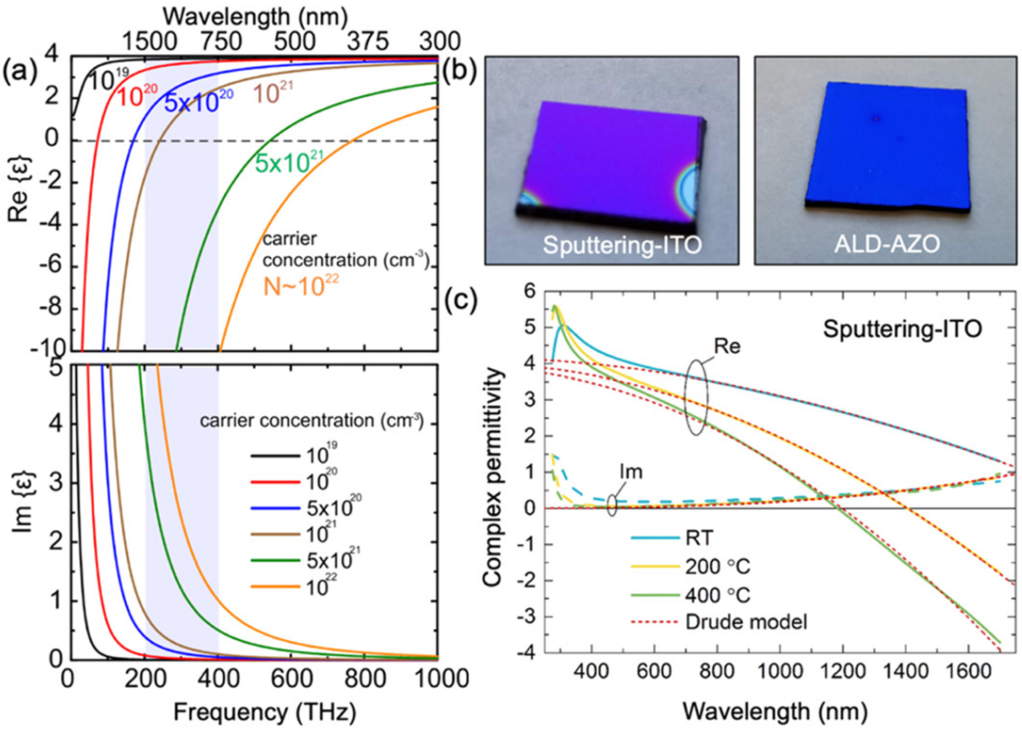

Figure 4. (a) Complex permittivity of ITO with different carrier concentrations N, calculated by the Drude–Lorentz model. Reprinted with permission from [114]. Copyright (2014) American Chemical Society. (b) TCO can be fabricated by various fabrication techniques. The examples shown here are ITO films fabricated by magnetron sputtering and AZO films fabricated by ALD. Reproduced from [115]. © IOP Publishing Ltd. All rights reserved. (c) The measured permittivity of ITO thin films fabricated in different sputtering temperatures. Carrier concentration and thus ENZ wavelengths can be tuned routinely. The Drude model precisely described the permittivity in the wavelength range of most interest.

phase shifts. Using the field-effect dynamics and the tunable coupling to the ENZ resonance, $\sim\pi$-phase shift can be realized at a wavelength of $\sim$1550 nm under the applied bias of 2.5 V (figure 6(c)). In addition, a modulation frequency of $>$10 MHz is achieved, showing relatively fast modulation based on the TCO field-effect dynamics. Since there is no actual current passing through the field-effect structure, the TCO tunable metasurface is expected to operate with low power consumption. The switching energy is estimated as low as 0.7 pJ bit^{-1}. By properly designing the structure and the RF probe, they estimated that switching energy of 2.5 fJ bit^{-1} and modulation speed of up to 3 THz can be achieved. Furthermore, the TCO-based metasurfaces can perform electrical switching between ±1 order diffracted wavefronts by having control over the subgroups of metasurface elements, hence demonstrating an electrically tunable beam-steering application based on the phased array metasurface (figure 6(d)).

It is noteworthy that devices based on the electrical tuning of TCOs usually have a Debye length with a thickness of $\sim$1–2 nm depending on the screening effect of high carrier concentration TCO film (figures 5(b) and (c)). Therefore, the impact of the electrical modulation effect is restricted by the thin Debye length. This limitation can be potentially relieved through dual or even multiple gates with multiple depletion/accumulation layers within the resonant element for achieving larger phase modulations. Shirmanesh *et al* demonstrated an active metasurface based on a dual-gated reflectarray conducting oxide metasurface architecture (figure 7(a)) [123]. Based on the top and the bottom electron accumulation layers and improved gate dielectric material with high breakdown field and DC permittivity (Al_2O_3/HfO_2 nanolaminates ‘HAOL’, DC permittivity $k_{\text{HAOL}} = 22$, breakdown field $= 7.2$ MV cm^{-1}), phase modulation as large as 300° and a relative modulation in reflectance of 89% were achieved at a wavelength of $\sim$1550 nm with an applied bias of 6.5 V. Applying a similar concept for tunability, Shirmanesh *et al* from the same group further demonstrated a reconfigurable metasurface with multifunctionalities of beam-steering and tunable light focusing on a single device (figure 7(b), top) [124]. The device consists of 96 individual metasurface elements connected to a printed circuit board (PCB). Each element allows a maximum phase modulation of $>$270° at a wavelength of 1522 nm by applying voltages. Since the PCB can provide 100 individual voltages that can be independently controlled via a number of programmable micro-controllers, beam-steering with an angle of 23.5° from a four-level phase grating and a tunable metalens with a controllable focal length of 1.5–3 μm were demonstrated (figure 7(b), bottom), showing the first electrically-tunable metasurface device with multifunctionalities.

Park *et al* demonstrated a similar conducting oxide tunable metasurface in the mid-infrared regime (figure 8(a)) [125]. In their case, a π-phase change, and a relative modulation

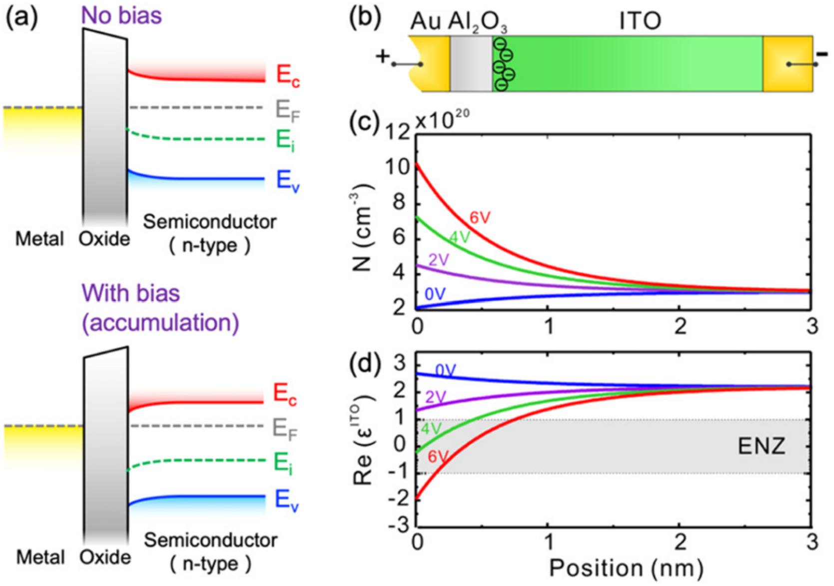

Figure 5. Conducting oxide field-effect dynamic for the manipulation of optical properties. (a) Schematic of the field-effect structure and (b) their corresponding band diagram under bias. (c) Spatial distribution of the carrier concentration N under different applied voltages. (d) The corresponding real part of ITO permittivity at a wavelength of 1550 nm. Reprinted with permission from [116]. Copyright (2016) American Chemical Society.

of 35% in reflectance were observed. The applied voltage of ±40 V for the π-phase change is relatively high due to the 115 nm-thick Al_2O_3 gate dielectric layer, and the reflectance is ∼2%–3%. Park *et al* from the same group further exploited similar electrically-tunable ITO metafilms to demonstrate a tunable absorber (figure 8(b)) [126]. The tunable reflectance of ∼15% was realized with the ITO operating in the ENZ regime via a dynamic change resulting from the formation of accumulation or depletion active layers (positive/negative biases). A modulation speed of up to 125 kHz was demonstrated in this work. Later, Zhao *et al* utilized indium silicon oxide (ISO) to replace the ITO in a similar patch antenna for realizing a reflective metasurface and demonstrated a reflectance change of 57% at an operation wavelength of 2.73 μm and a maximum resonant wavelength shift of 620 nm under an applied bias of −8 V [127]. Thyagarajan *et al* reported an amplitude-tunable metasurface that can operate in the visible. The tunability is based on the ionic conductance of a silver layer. In this work, inverse dolmen structures are milled onto the Ag/Al_2O_3/ITO heterostructures (figure 8(c)) [128]. A relative amplitude change of 30% in reflectance can be achieved with a relatively low applied voltage of 5 mV. However, the modulation frequency is <600 Hz because of the long migration time of the silver ions in this configuration. Although the modulation mechanism of this device is not precise due to field-effect dynamics, the structure is similar and worth noticing. Electrical tuning of plasmonic mid infrared absorbers has also been demonstrated experimentally by Yi *et al* (figure 8(d)) [129]. In their case, an active ITO layer strongly coupled to the optical near field of the plasmonic absorber allows for tunability. However, the amplitude modulation depth is relatively low since the field in the ITO layer is not strongly overlapped with the resonant mode.

Another critical factor that limits the performance of these active conducting oxide metasurfaces is the parasitic loss in metal or relatively weak light–matter interactions. Instead of using the metal-oxide-conducting oxide field-effect structures, several attempts have been made to replace the lossy metal layer with a low-loss semiconductor. George *et al* have demonstrated continuous electrical tuning of the diffraction efficiency from AZO gratings with subwavelength periodicity in the visible range (at a wavelength of 532 nm) via the field-effect tuning (figure 9(a)) [130]. In this work, the AZO film is under negative bias voltages between −1 V and −3.5 V and induces a change of diffraction efficiency (∼0.5%) with a fixed period of the grating. By integrating the ITO material with the silicon dielectric structure, Howes *et al* demonstrated transmission modulation based on all-dielectric Huygens metasurfaces (figure 9(b)) [131]. The structure consists of a silicon Huygens metasurface with an ITO film on top and a fused silica substrate. Taking advantage of the coupling of the Huygens mode in the silicon antenna and the ENZ mode in the electrically-tunable ITO layer, they electrically tuned the ENZ point and altered the local field enhancement within the ITO, thus leading to dynamic control of absorption/transmission. Electrically-tunable beam steering properties were also demonstrated with the proposed device by introducing a two-level grating electrically.

Note that several interesting, advanced device designs and functionalities based on the active conducting oxide metasurfaces have been proposed and numerically reported [132–141]; however, this article focuses more on the experimental demonstrations.

The conducting oxide field-effect mechanism is one of the most promising tuning mechanisms for active metasurfaces because it combines the advantages of (i) the complex field-effect tunable permittivity of conducting oxide materials, (ii)

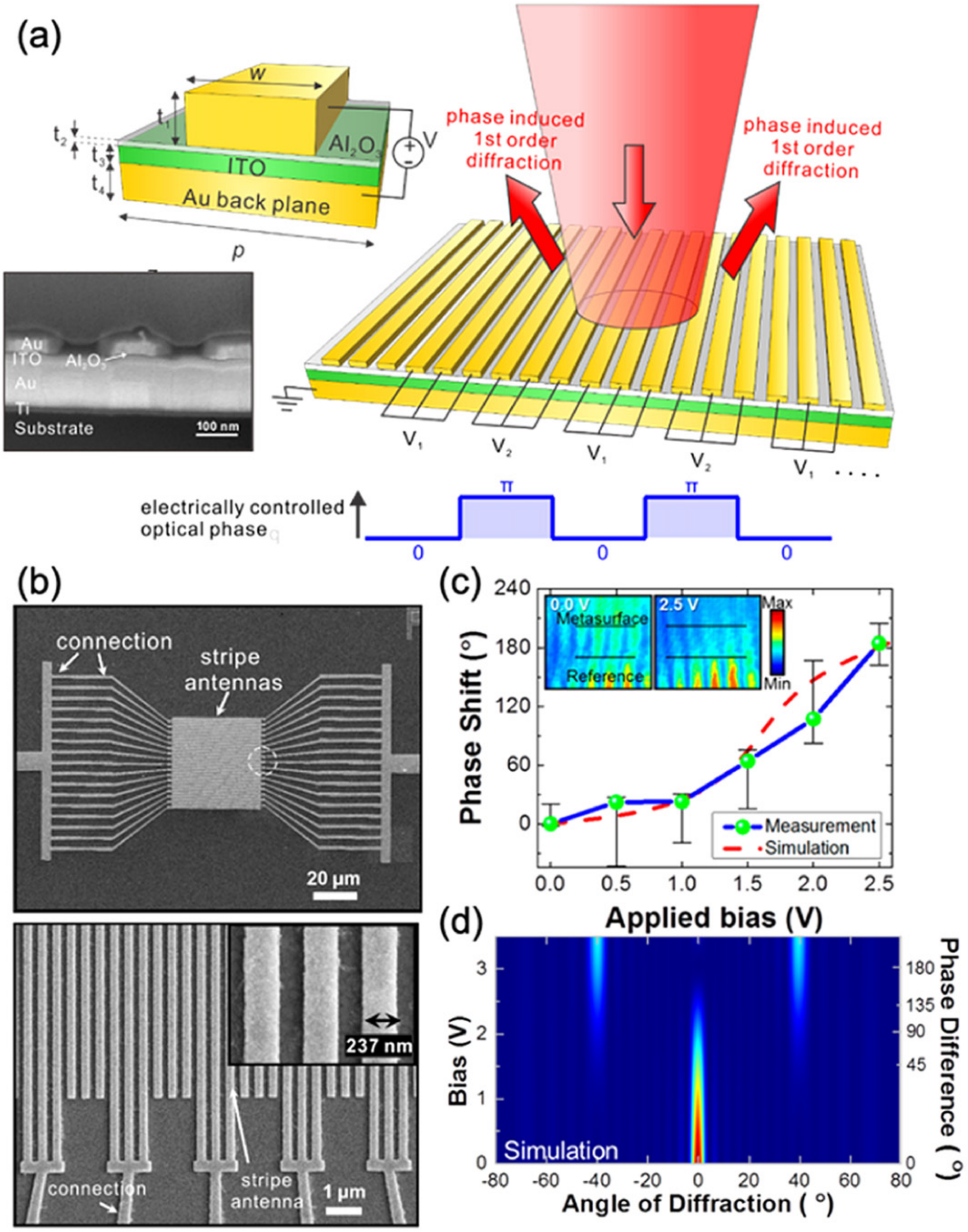

Figure 6. Tunable TCO metasurface with π-phase shift modulation and beam steering functionality at a wavelength of 1550 nm. (a) and (b) Schematic and SEM images of tunable metasurfaces. (c) Measured phase shift versus applied bias voltages. (d) Demonstrated beam steering functionality. Reprinted with permission from [116]. Copyright (2016) American Chemical Society

the control over phase and amplitude of metasurfaces, and (iii) the access of the ENZ mode of conducting oxide films for enhanced confinement, which could lead to efficient optical modulation. In addition, meta-devices based on conducting oxides could potentially achieve an operation speed of >10 GHz (although only up to 10 MHz has been demonstrated on active metasurfaces) and with low power consumption (similar to the electronic transistor in a computer). The current limitations of this approach are generally low efficiency and narrow bandwidth when operating at the maximum phase modulation due to the resonant mode (e.g., the dip of reflectance) and lossy metallic resonator customarily employed. Because the Debye length of the TCO accumulation layer in the field-effect structure is relatively short (∼1–2 nm in the interface of TCO and insulator), it is desirable to combine the field-effect structure with resonant mode with a highly confined field in the metal/insulator/TCO interface for efficient modulation. This causes difficulties in integrating the tunable effects of the dielectric metasurfaces based on Mie-type resonance. Also, the lower carrier concentration of the TCO materials (compared with metallic nitride materials or metals) leads to difficulties in coupling the ENZ mode for efficient modulation in the visible, where the metallic structures suffer from a relatively high loss. Finally, most of the reported tunable TCO

(a) Dual-gated tunable metasurface at 1550 nm with >300° phase modulation

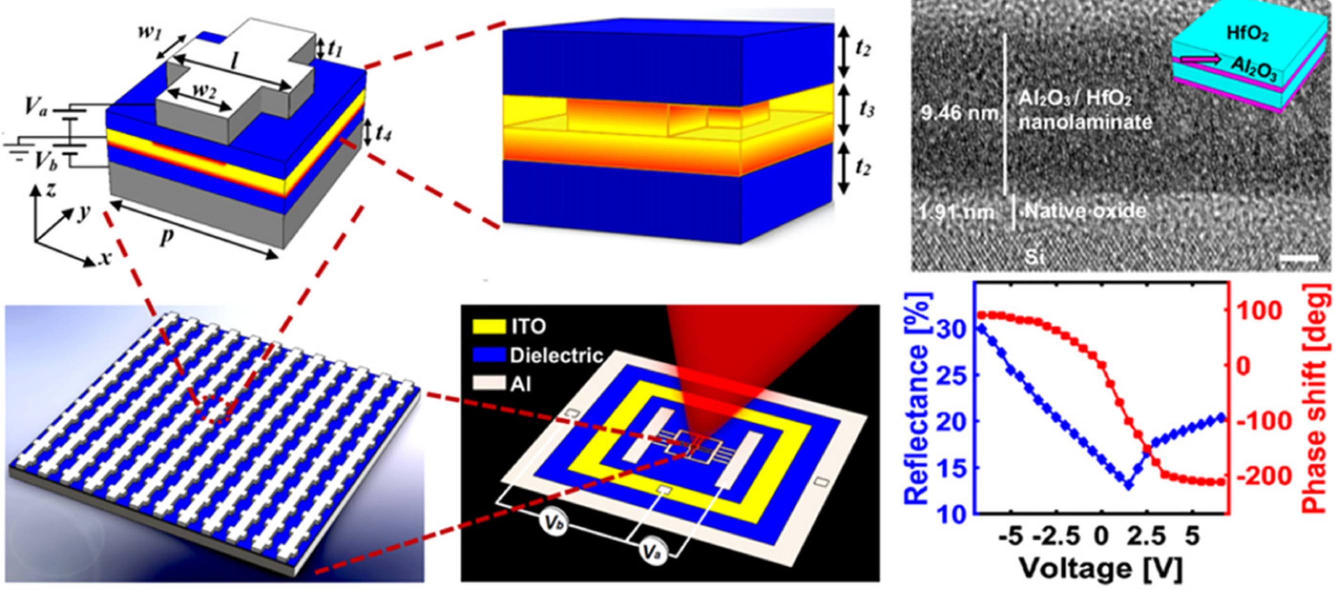

(b) Tunable metasurfaces capable of both dynamic beam steering and reconfigurable light focusing

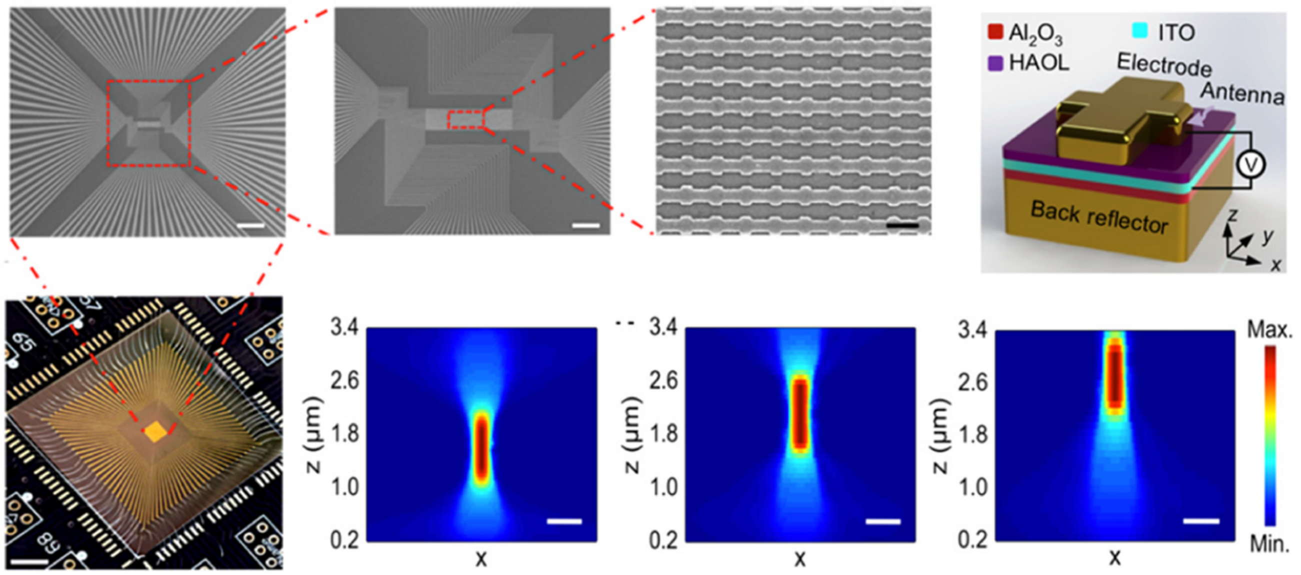

Figure 7. Electro-optically tunable multifunctional metasurfaces. (a) Schematic and SEM images of the dual-gated metasurface. Phase modulation of >300° is achieved at a wavelength of 1550 nm. Reprinted with permission from [123]. Copyright (2018) American Chemical Society. (b) SEM, schematic and photographic images of the multifunctional metasurface with 96 independently-addressable elements that can realize dynamic beam steering and tunable light focusing on a single device. The functionality of a tunable metalens with a controllable focal length between 1.5–3 μm is thus demonstrated. Reprinted with permission from [124]. Copyright (2020) American Chemical Society.

metasurface structures have a relatively small active region (in the order of tens of micrometers) to avoid large leakage of current from the thin insulating layer. To develop large-area active metasurface devices based on the TCO-tuning mechanism, a large area and high-quality insulating layer is required, posing certain nanofabrication challenges when combining this layer with the metasurface elements. Nevertheless, this TCO electrically-tunable mechanism provides significant potential for developing novel tunable metasurface devices (section 9).

2.2. Two-dimensional materials enabled active metasurfaces

2.2.1. Graphene-based tunable metasurfaces. Graphene consists of flat single-layered carbon atoms in a honeycomb lattice arrangement (figure 10) [142]. Compared to the TCO materials, graphene has relatively high electron mobility (10^3–10^5 cm^2 V^{-1} s^{-1}) and optical transparency, as well as flexibility, robustness, and environmental stability [143, 144]. Graphene displays voltage-dependent electrical conductivity

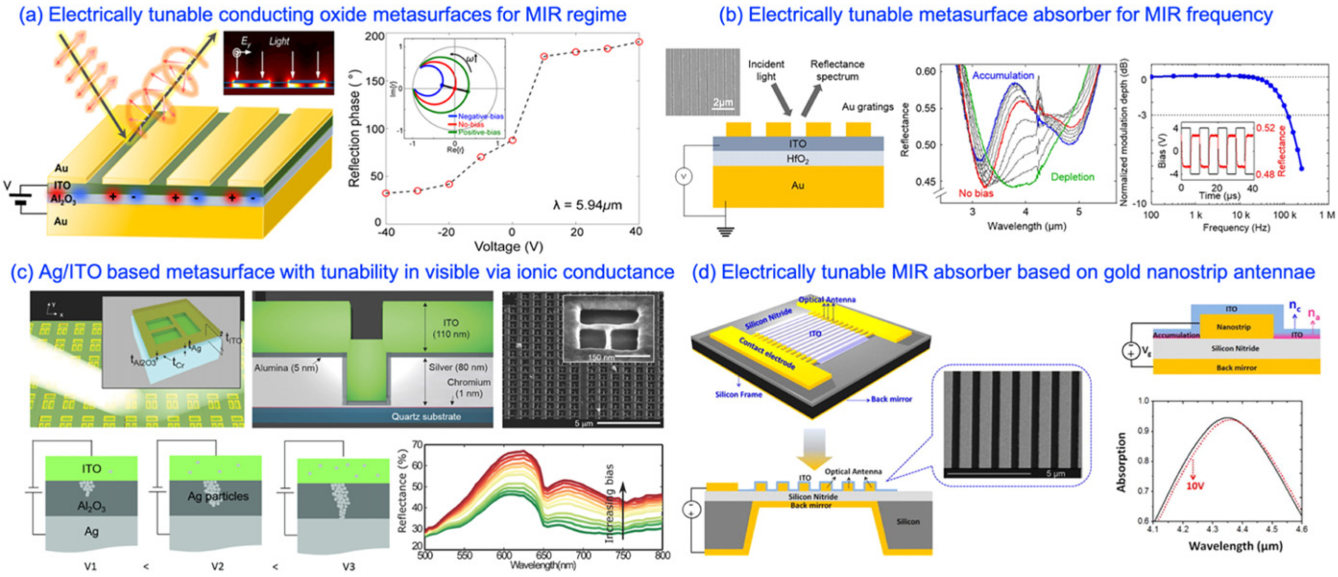

Figure 8. Examples of electrically-tunable metasurfaces based on TCO. (a) (Left) Sketch of an electrically-tunable metasurface consisting of plasmonic gap resonators and (right) the phase modulation and trajectory of the complex reflection coefficient with increasing frequency for three different scenarios (right). Reprinted with permission from [125]. Copyright (2017) American Chemical Society. (b) Schematic of an electrically-tunable ITO film clamped between a HfO_2-coated Au substrate and an array of Au strips. By applying positive (negative) electric biases, the carrier concentration of the ITO can be decreased (depleted) or increased (accumulated). Reprinted by permission from Springer Nature Customer Service Centre GmbH: Springer. Scientific Reports. [126] © 2015. (c) Ag/ITO based dolmen metasurface structure with tunability in the visible regime via ionic conductance [128] John Wiley & Sons. © 2017 WILEY-VCH Verlag GmbH & Co. KGaA, Weinheim. (d) Schematic of an electrically-tunable mid infrared metasurface absorber based on gold nanostrip antennae. Reprinted from [129], with the permission of AIP Publishing.

(1/resistivity) and can be employed as an electrically-tunable plasmonic/metasurface material in the mid-infrared to far-infrared [145].

Figure 10 shows an illustration of the electrically-tunable property in a single-layer graphene-based field effect transistor. The optical property of graphene is governed by the surface conductivity and related to its chemical potential (Fermi level, E_F) [146]. The Fermi level of graphene can be controlled via applying electrical bias in a wide frequency range. The intraband transition governs the surface conductivity of graphene in the mid-infrared to terahertz frequency range ($\hbar\omega \ll 2|E_F|$), and the surface conductivities at the near-infrared and visible frequencies are governed by the inter-band transition ($\hbar\omega > 2|E_F|$), respectively [146].

To demonstrate the dynamic surface conductivity of graphene in the terahertz to visible frequency range, the conductivity of graphene with two different Fermi energy levels ($E_F = 0.2$ eV and 0.4 eV) is shown in figure 11(a) [147]. At the terahertz and near-infrared frequencies, graphene shows a lossy behavior ($|\mathrm{Im}(\sigma)/\mathrm{Re}(\sigma)| < 1$), whereas it shows plasmonic behavior ($\mathrm{Im}(\sigma)/\mathrm{Re}(\sigma) > 1$) in the mid-infrared. Hence, in the mid-infrared (figure 11(b)), graphene can support transverse magnetic surface plasmon polaritons with an extremely low loss. Moreover, at the terahertz and mid-infrared frequencies, the conductivity of graphene has a large tunability.

The Drude model can describe the optical property of graphene. The in-plane effective permittivity can be written as

$$\varepsilon_{\mathrm{eff,in}} = 1 + \frac{i\sigma_s(\omega)}{\varepsilon_0 \omega t_g},$$

where $\sigma_s(\omega)$ is the surface conductivity of the graphene, ε_0 is the vacuum permittivity, and t_g is the thickness of the graphene. Typically, the mobility of graphene is 1000 $cm^2\ V^{-1}\ s^{-1}$. The carrier density and Fermi level of graphene can be manipulated by changing the electrostatic doping, $N = E_F^2/(\pi\hbar^2 v_f^2)$ under different electrical biases, where E_F is Fermi level (typically -1.0 to 1.0 eV), $\hbar$ is the reduced Planck's constant, and v_f is the Fermi velocity. Also, due to the low carrier concentration N of the sheet of $\sim 10^{11}$ cm^{-2}, the gate-tunable property of graphene is much larger than traditional bulk materials [148], since any modification of carrier concentration can cause a significant change in the Fermi energy. This change of Fermi energy, in turn, can substantially change the optical property of the graphene.

The first demonstration of tuning graphene plasmons by applying an electrical bias was done by Ju *et al* [149]. Their metasurface based on graphene nanoribbons, operates in the far infrared. It showed a blue shift of plasmon resonance and modulation of transmittance as the voltage was varied, which happened because of the strong electric field confinement of the localized surface plasmons to the surface of the sub-wavelength graphene nanoribbon. The relation between the plasmon resonance frequency ω_p, ribbon width w, and carrier concentration can be written as $\omega_p \propto (\sqrt{w}/\sqrt[4]{n} \propto (\sqrt{w}/\sqrt{E_F})$. The resonance frequency can be varied from 1 to 10 THz by engineering the width of the nanoribbon. When applying gate-voltage, the resonance blue shifted and gained oscillator strength due to the increased carrier concentration. As a result, the resonance frequency blue shifted (~1 THz), and the relative transmission increased from 7% to 13%

(a) Electrical tuning of diffraction efficiency from AZO gratings

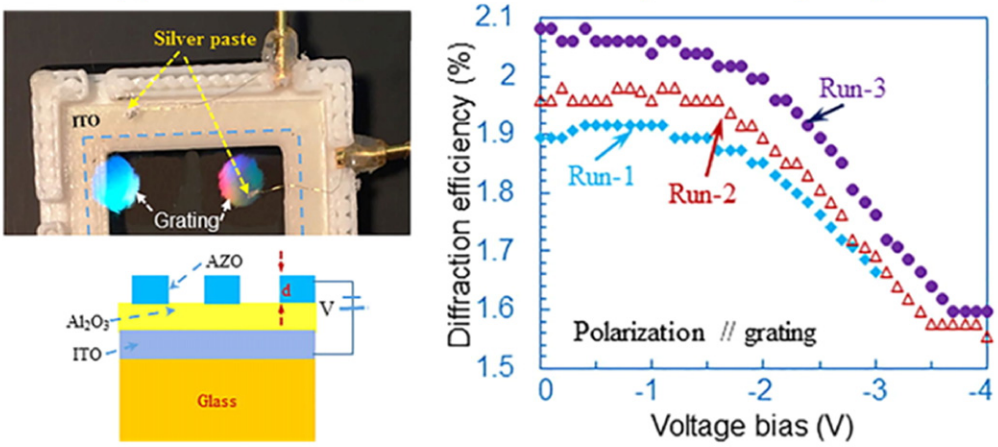

(b) Tunable Mie resonances of dielectric metasurface by using the ENZ point of thin conductive oxides.

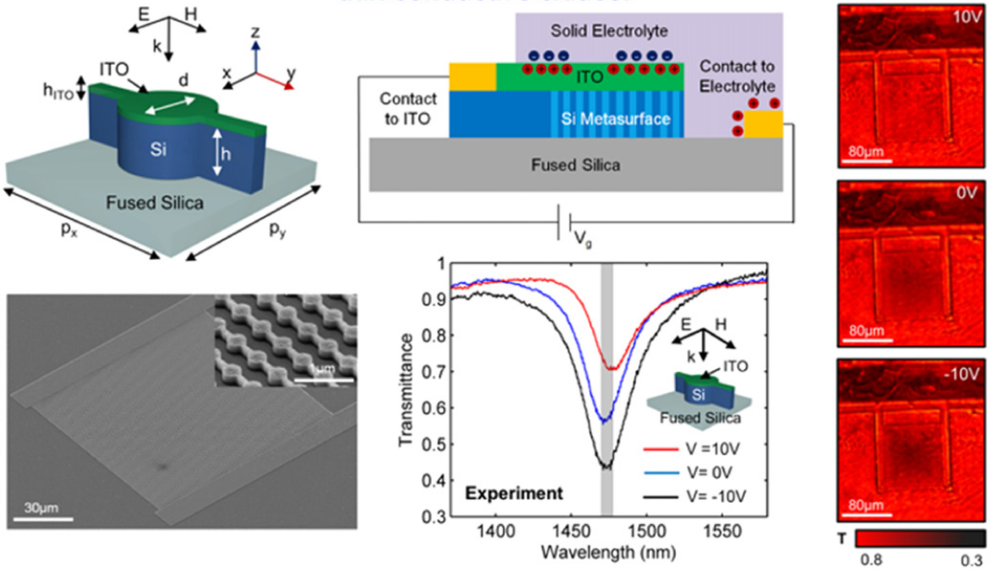

Figure 9. Examples of electrically-tunable metasurfaces based on TCO. (a) An AZO grating device where voltage is applied across the AZO grating and ITO. Reprinted from [130], with the permission of AIP Publishing. The device shows modulation of diffraction efficiencies at a wavelength of 532 nm upon applying an electrical bias. (b) Dynamic transmission control by all-dielectric Huygens metasurfaces. Reproduced with permission from [131]. © The Optical Society. By coupling the Mie resonance with the ENZ mode in ITO, the transmission could be modulated by the applied bias ranging between −10 V to 10 V.

(figure 12(a)). Liu *et al* investigated the electrical tunability of terahertz plasmonic crystals consisting of a graphene nano-holes array arranged in a square lattice [150]. Multiple electrically-tunable resonances in extinction spectra were experimentally investigated.

In an alternative approach, single/few-layers graphene has also been integrated with plasmonic metasurfaces where graphene forms the active layer, and device tunability has been achieved via free-carrier tuning effects in the mid-infrared regime. Lee *et al* integrated a graphene layer with a periodic hexagonal metallic array (figure 12(b)) [151]. By applying the gate voltage, the complex permittivity of graphene was dynamically controlled, which translated to the change in transmission. Both the amplitude and phase of the transmitted wave could be modulated at room temperature. Changes in transmission as large as 47% and changes in phase of 32.2° with a single-layer graphene have been reported. Moreover, the transmission of the gate voltage-controlled metamaterials exhibits hysteretic behavior, which can be useful for photonic memory devices. However, the device operates under a relatively large bias voltage of several hundred volts. Additional efforts have been made for efficient modulation of the amplitude of the transmitted/reflected wave [152, 153]. Gao *et al* reported periodic arrays of metallic ring apertures with a single layer graphene that show transmission modulation of 50% with modulation speed in hundreds of MHz [154].

Zeng *et al* demonstrated a hybrid graphene metasurface spatial light modulator (SLM) in the mid-infrared wavelength of ∼8 μm, consisting of 6 × 6 pixels [142]. The resonant absorption of the structure can be tuned by controlling the conductivity of the graphene under a gate voltage of a few volts,

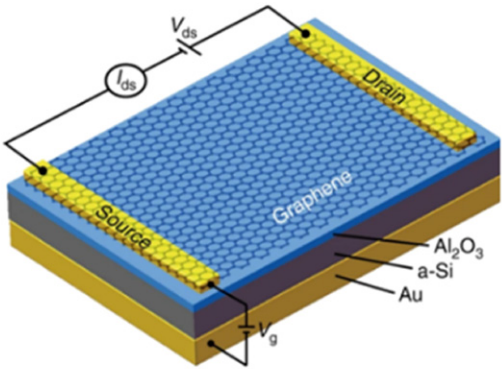

Figure 10. (a) Schematic of a graphene-based FET. Reprinted by permission from Springer Nature Customer Service Centre GmbH: Springer. Light: Science & Applications. [142] © 2018.

which results in high modulation depths of up to 90%. Moreover, the modulation speed can be as fast as 1 GHz, which is ideal for high speed, free-space mid-infrared modulation. Kim *et al* demonstrated electrically-tunable perfect absorption with a graphene plasmonic ribbon integrated with subwavelength noble metal plasmonic antennas [155]. The radiating mode and plasmonic mode of graphene critically couple to satisfy the perfect absorption condition. High absorption of 96.9% at a wavenumber of 1389 cm^{-1} (corresponding to wavelength of 7.2 μm) in the graphene plasmonic nanostructure, with modulation efficiency of 95.9% in reflection, was observed. Also, a tunable perfect absorber with a graphene–gold metasurface hybrid geometry that operates from near-infrared to THz regime has been demonstrated by Yao *et al* [156]. The graphene-integrated metasurface consists of gold unit elements incorporated into a subwavelength-thick optical cavity (figure 12(c)). The critical coupling condition can be satisfied by application of gate voltage across the graphene layer, achieving a modulation depth of up to 95%. The proposed absorber can operate in the wavelength range of 5–7 μm with a modulation speed of 20 GHz.

Besides amplitude modulation, phase modulation plays an integral part in dynamic wavefront modulation. Sherrott *et al* have experimentally demonstrated a phase modulation of 237° using a gate-tunable graphene–Au metasurface at a wavelength of 8.5 μm (figure 13) [157]. The device can also be employed for beam steering with an average efficiency of 23% and steering angles up to 30° for reflected light. But the reflectance (1.5%–12%) is generally low. Although experimental demonstration has not been realized yet, the graphene-integrated metasurfaces have the potential of complete phase modulation. Kim *et al* proposed in simulation an electronically-reconfigurable reflecting metasurface with a full 2π phase and independent amplitude modulation [158]. This configuration provides tuning of the graphene Fermi level in the individual meta-molecule level through changing the gate voltage.

Graphene-incorporated plasmonic metasurfaces have shown promising properties such as absorption and phase modulation. In addition, owing to the high mobility of graphene, the speed of modulation is relatively high ($\sim$50 GHz) compared to other electrically-tunable metasurfaces. Tunable single-layer graphene-loaded plasmonic metasurfaces are preferred in the THz and mid infrared regime. However, the quality factor is limited due to the high non-radiative losses of the plasmonic unit cells in the mid-infrared to far infrared, which restricts the modulation depth. Also, the tunable range of the graphene-integrated plasmonic metasurface is limited to mid-infrared to terahertz frequencies. In addition, because of the single atomic layer dimension, fabrication of high-quality structured graphene with fine control of shape and size is challenging. However, with the advent of new fabrication techniques, two-dimensional graphene-integrated metasurfaces are promising with respect to tunability and speed.

2.2.2. Transition metal dichalcogenides based tunable metasurfaces.

Transition metal dichalcogenides (TMDCs) are two-dimensional direct band gap semiconductors. The chemical composition of TMDCs can be expressed as MX_2, where M is a transition metal (Mo, W, etc), and X is a chalcogen (S, Se, or Te). One property of a TMDC monolayer can be observed in doping (injection of excess electrons). When injected with excess electrons, neutral excitons can generate negatively-charged trions and can significantly change the optical property of TMDCs. Doping can be implemented via photochemical or electrical gating. Hence, the excitonic resonance of atomically-thin TMDCs on a metasurface can be manipulated to achieve active control over the optical properties.

Zhang *et al* demonstrated photo-chemical and electrical tuning of the dielectric Fano resonance of a photonic crystal (PhC) using MoS_2 in a field-effect transistor (FET) geometry (figure 14(a)) [159]. When illuminated at a wavelength of 532 nm, O_2 and H_2O adsorbed by MoS_2 releases trapped electrons and dope the MoS_2 monolayer. These excess electrons suppress A excitons and increases A^- trions. Similarly, by applying a positive gate voltage gate, excess electrons can be electrically injected into the MoS_2 monolayer. Lee *et al* demonstrated the coupling between excitons and surface lattice resonance (SLR) or lattice localized surface plasmons (lattice-LSPs) can be electrically controlled in a MoS_2-integrated plasmonic metasurface (figure 14(b)) [160]. By applying gate voltage from 0–80 V, the coupling between excitons and lattice-LSPs of Ag nano-disc arrays changed progressively from strong neutral exciton (A^0)–plasmon coupling to strong negatively trion (A^-)–plasmon coupling. Similar work has been demonstrated with few layers of WS_2 integrated onto a square-shaped silver nano antenna by Liu *et al* [161].

Ni *et al* reported a gate-tunable light-emitting metasurface by coupling the excitonic resonance of a monolayer MoS_2 with a gap plasmon metasurface [162]. In their device, applying a positive gate bias created an electron accumulation layer at the interface between the MoS_2 layer and the gate dielectric layer. Those accumulated electrons bonded to the neutral excitons, giving rise to negatively-charged excitons (trions). On the other hand, the excess electrons can be repelled from the MoS_2 layer into the metallic electrode under the negative bias,

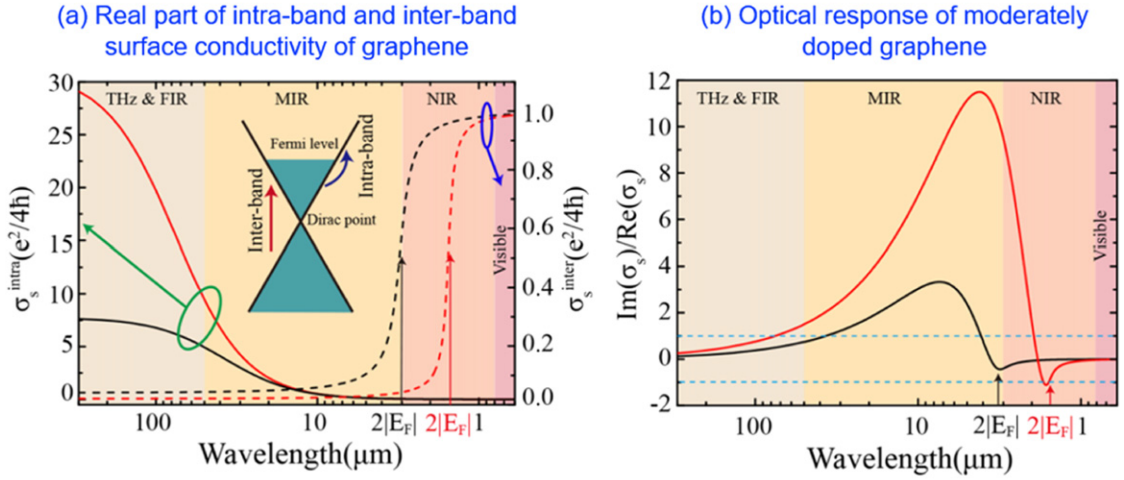

Figure 11. Conductivity and optical property dependence on the Fermi level. (a) Surface conductivities of graphene with $E_F = 0.2$ eV (black) and $E_F = 0.4$ eV (red). Inset: the band structure of graphene. (b) Large tunability in conductivity is achieved at near infrared, THz and far infrared frequencies. Reproduced with permission from [147]. Copyright © The Korean Ceramic Society.

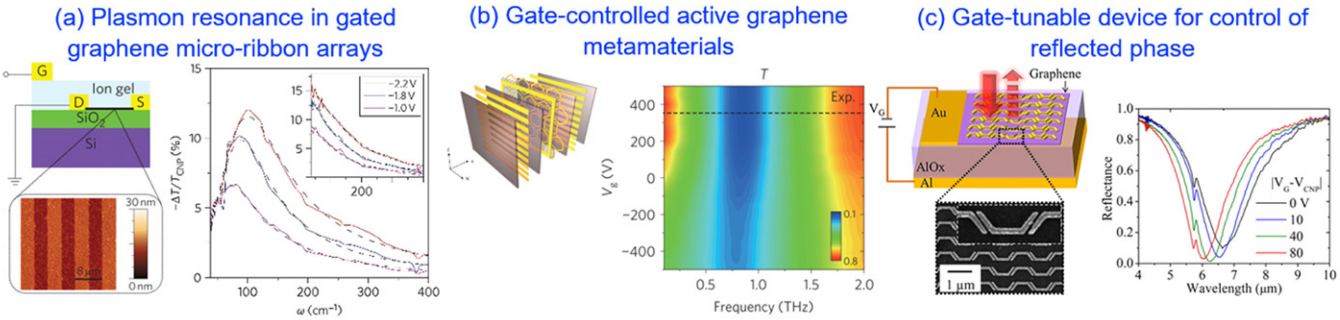

Figure 12. Tunability via free-carrier effects in patterned-graphene structures and graphene–metal hybrid metasurface structures. (a) Electrical tuning of terahertz resonance of plasmon using graphene micro-ribbon array. Inset: relative transmission versus wavenumber with applied voltage. Reprinted by permission from Springer Nature Customer Service Centre GmbH: Nature. Nature Nanotechnology. [149] © 2011. (b) Illustration and optical transmission of a gate-controlled extraordinary active graphene metasurface. Reprinted by permission from Springer Nature Customer Service Centre GmbH: Nature. Nature Materials. [151] © 2012. (c) Schematic, SEM and reflection spectra of the graphene-integrated tunable metasurface. Reprinted with permission from [156]. Copyright (2014) American Chemical Society.

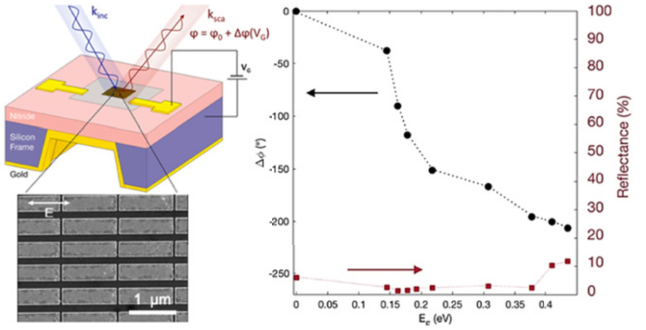

Figure 13. Gate-tunable graphene plasmonic device to control the reflected phase and amplitude. Reprinted with permission from [157]. Copyright (2017) American Chemical Society.

dissociating the trions into neutral excitons. As a result, the photoluminescence property of the metasurface structure can be modulated by tuning the gate voltage. van de Groep *et al* experimentally demonstrated a tunable, atomically-thin WS_2 zone plate lens with a focal intensity modulation of 33% at a wavelength of 625 nm (figure 15(a)) [163]. Contrary to the previous approach where the size and shape of the meta-atom governed the resonant wavelength and provided the necessary field intensity, the design of metasurfaces incorporating 2D excitonic materials relies on the material's resonance itself. For instance, WS_2 displays a strong excitonic resonance in the visible spectral range with A and B excitons located at wavelengths of 625 nm and 520 nm, respectively. By applying a bias of 3 V, the excitonic reflection peak of the A exciton was suppressed completely and a small, redshifted peak at a wavelength of 655 nm was observed (figure 15(b)). This is because of the screening of electron–hole interaction due to the increased electron density. In addition, there is also an interconversion to negatively charged exciton states (A^- trions). This complete, yet fully reversible, removal of the excitonic resonances produces significant changes in the susceptibility (χ). Since the scattered field due to the WS_2 ring is highly dependent on the susceptibility, the amplitude of the focused beam due to the WS_2 zone plate can be tuned by applying voltage (figure 15(c)). Because of the use of ionic liquid for voltage biasing, the modulation speed is limited to ∼40 ms. Metasurfaces made from 2D excitonic materials rely on the

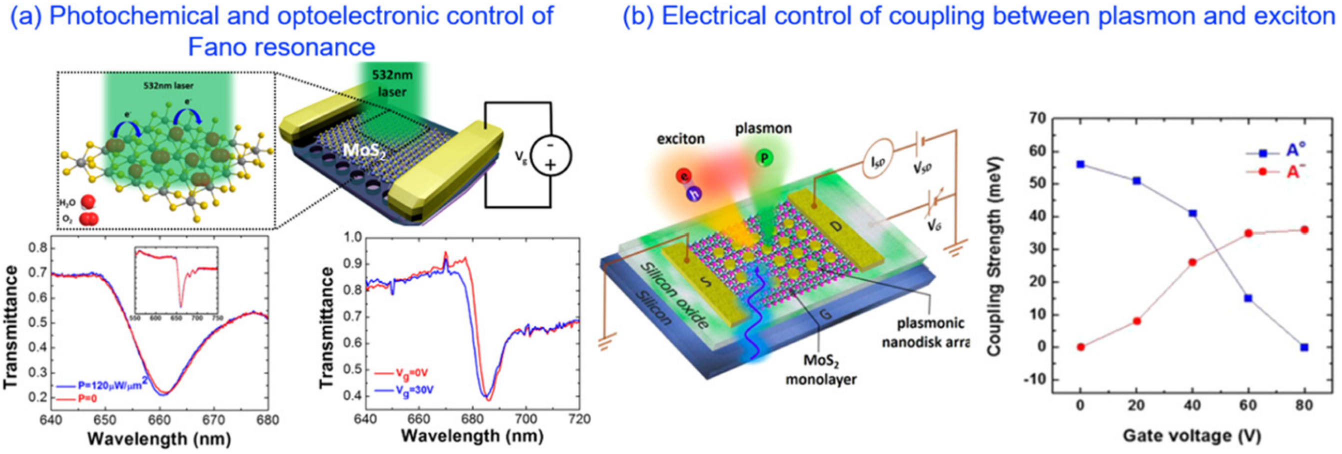

Figure 14. (a) Schematic of MoS_2-integrated dielectric PhC for control of photonic Fano resonance via photochemical and optoelectronic excitation. Reprinted with permission from [159]. Copyright (2018) American Chemical Society. (b) Schematic of a gate-tunable device for control of coupling between plasmon and exciton. Reprinted with permission from [160]. Copyright (2017) American Chemical Society.

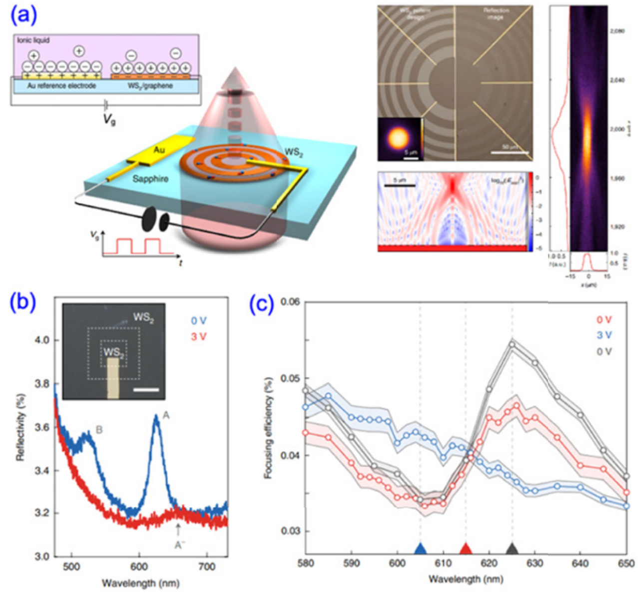

Figure 15. Exciton resonance tuning of an atomically thin lens. (a) Schematic of the electrically-tunable WS_2 zone plate lens. (b) Reflectivity spectra of WS_2 with (red) and without (blue) gate bias. (c) Focusing efficiency spectra of the zone plate lens in pristine (red, $V_g = 0$ V), (blue, $V_g = 3$ V), and restored state (gray, $V_g = 0$ V). Reprinted by permission from Springer Nature Customer Service Centre GmbH: Nature. Nature Photonics. [163] © 2020.

resonance of materials, and the controllable light–matter interaction is naturally obtained from the materials. Thus, this novel approach opens entirely new design strategies for tunable flat optics [164].

2.3. Liquid crystal-based reconfigurable metasurfaces

LC is one of the most widely utilized active materials for optics due to the broad tuning range of refractive index, high transmission efficiency, low power consumption, and high integrability. Depending on their symmetry properties and arrangements, LC can be broadly classified into four mesophases; nematic, cholesteric, smectic, and columnar. The nematic phase refers to the situation when molecular arrangements are correlated while their positions are not correlated. In this case, the individual LC molecule can move along the long axis direction (figure 16). As a result, the nematic phase is the most flexible LC with large fluidity, small viscosity, and large dielectric anisotropy ($\Delta\varepsilon$), allowing for dynamic control of the molecular orientation by applying an external electric field. Therefore, the nematic phase LC has been widely employed in tunable optical components for various applications. In the cholesteric phase, the LC molecules are oriented one-dimensionally while their orientations are helically twisted between different layers. For the smectic phase, LC molecules receive more positional limitations than the nematic phase; they are consequently constrained in a two-dimensional layered structure, which makes the smectic phase less movable than the nematic phase due to the relatively narrow travel range of LCs. The columnar mesophase consists of a one-dimensional stacked columnar structure containing disk-shaped LC molecules [165].

Electro-optical tuning of nematic phase LCs has been widely employed to realize tunable optical devices [166]. Figure 16 illustrates the basic principle of the phase change properties of nematic LCs under electrical bias. The director of the LC molecule orientation is denoted as n, and the angle between director n and the electric field of the incident light as θ (figure 16, bottom). Without any external bias, LC molecules with a nematic phase tend to align parallel to the rubbing direction of the polyimide layer, driven by the anchoring force generated by the rubbing process. For the incident light of which the electric field is parallel to the orientation direction of the LC molecule ($\theta = 0°$), the accumulated phase obtained by the transmitted incident light at 0 V, denoted by $\varphi(0)$, is determined by

$$\varphi(0) = \frac{2\pi l}{\lambda}\sqrt{\varepsilon(0)},$$

where λ is the wavelength of the incident light, l is the length of the LC cell, and $\varepsilon(0)$ represents the dielectric constant of

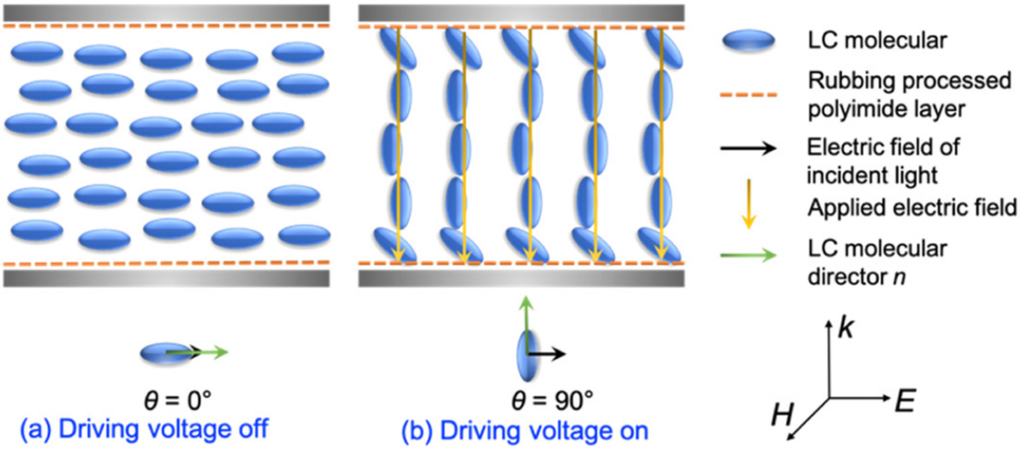

Figure 16. Schematic depicts the phase change principle of a nematic LC with applied bias.

the LC at 0 V. Once a voltage (V) is applied between the top and the bottom electrodes of the LC cell, the LC molecules change to the perpendicular direction as a result of the driving of the applied electric field (figure 16(b)). Therefore, the accumulated phase of the transmitted light changes to $\varphi(V)$, where $\varphi(V) = 2\pi l\sqrt{\varepsilon(V)}/\lambda$ and $\varepsilon(V)$ is the dielectric constant of the LC under bias voltage. The phase change of the transmitted light, $\Delta\varphi$ between driving bias on and off states can be obtained by the following equation

$$\Delta\varphi = \varphi(V) - \varphi(0) = \frac{2\pi l}{\lambda}[\sqrt{\varepsilon(V)} - \sqrt{\varepsilon(0)}].$$

The LC molecules will return to their initial orientation state at 0 V again once the bias voltage is removed under the driving of the anchoring force, which comes from polyimide layers. The tunability of the LC molecules' orientations under an applied electrical field can be readily implemented to modulate the optical response of a plasmonic metasurface infiltrated with LC, due to strong modulation of the effective dielectric constant of the ambient environment.

For the early demonstrations of electrically tunable LC-based metasurfaces, metallic plasmonic nanostructures with different geometries, such as nanodot arrays, split-rings resonators, zig-zag wires, grating, etc, with different functionalities have been obtained. Figure 17(a) shows a plasmonic metasurface composed of a lateral hexagonal array of gold nanodots embedded in an LC layer. In the field-off state without applied voltage, the LC molecules align vertically to the surface of the LC cell, and its far-field absorption spectra exhibit two peaks, corresponding to the normal and the lateral plasmon modes, respectively [167]. Under an external bias, the orientation of the LC molecules changes into the direction parallel to the surface of the cell (figure 17(a), left). Such realignment of the LC molecules orientation under different applied biases significantly changes the effective refractive index of the external environment of the nanodot arrays. It thus shifts the positions of the peaks appearing in the absorption spectra which are attributed to the two plasmon modes. As a result, a stronger shift of the lateral mode (~12 nm) is observed under an applied electric field of 2 V μm^{-1}. Moreover, the modulation speed of the LC embedded plasmonic metasurface has also been evaluated by other works. For example, millisecond timescale switching between electric and magnetic resonances has been observed from a U-shaped split-ring resonator (SRR) based metasurface due to the change of the LCs molecules' orientation under the electric field (figure 17(b)), which shows the possibility using this approach for active control of light reflection with fast speed [168]. In this work, the on-switching process has a faster speed within 1 millisecond than the off-switching process (~1 s). The off-switching process is limited by the inherent relaxation process of the LC molecules. However, faster switching can be expected by proper optimization of the structure and the electrode design. For example, an array of connected V-shaped plasmonic resonators, i.e., a continuous zigzag-wire patterned metasurface, can be hybridized with an LC cell. Since such a metallic metasurface configuration can simultaneously serve as the polarizer and a transparent electrode. Importantly, this hybridization offers the advantage of the simplicity of the overall structure. Large and hysteresis-free modulation of the metasurface transmission (~50% in absolute value) in near-infrared regime (~1550 nm) has been achieved by applying voltage of only 7 V [171]. Another design strategy based on a zigzag-wire array metasurface has been adopted (figure 17(c)). This design can help to minimize the surface anchoring of LC molecules by reducing the contribution of the substrate to the total metasurface area. A maximum spectral tuning of 110 nm is experimentally demonstrated by adopting this design under a small range of bias voltage (1.5–2.7 V), close to the theoretical limit of 9% [169].

Figure 17(d) shows a voltage tunable metasurface as a dynamic plasmonic color filter, fabricated from Al gratings integrated with nematic LC [170]. It is demonstrated that applying a small voltage will convert the transmission from TM mode at 0 V to the TE mode at 4 V due to the change of the state of LC, resulting in dynamic color tunability. Experimentally, dynamic color tuning is obtained across different parts of the visible spectral region. Chen *et al* reported an LC tunable phase gradient metasurface based on gold binary gratings [172]. In their structure, the relative diffraction efficiencies of

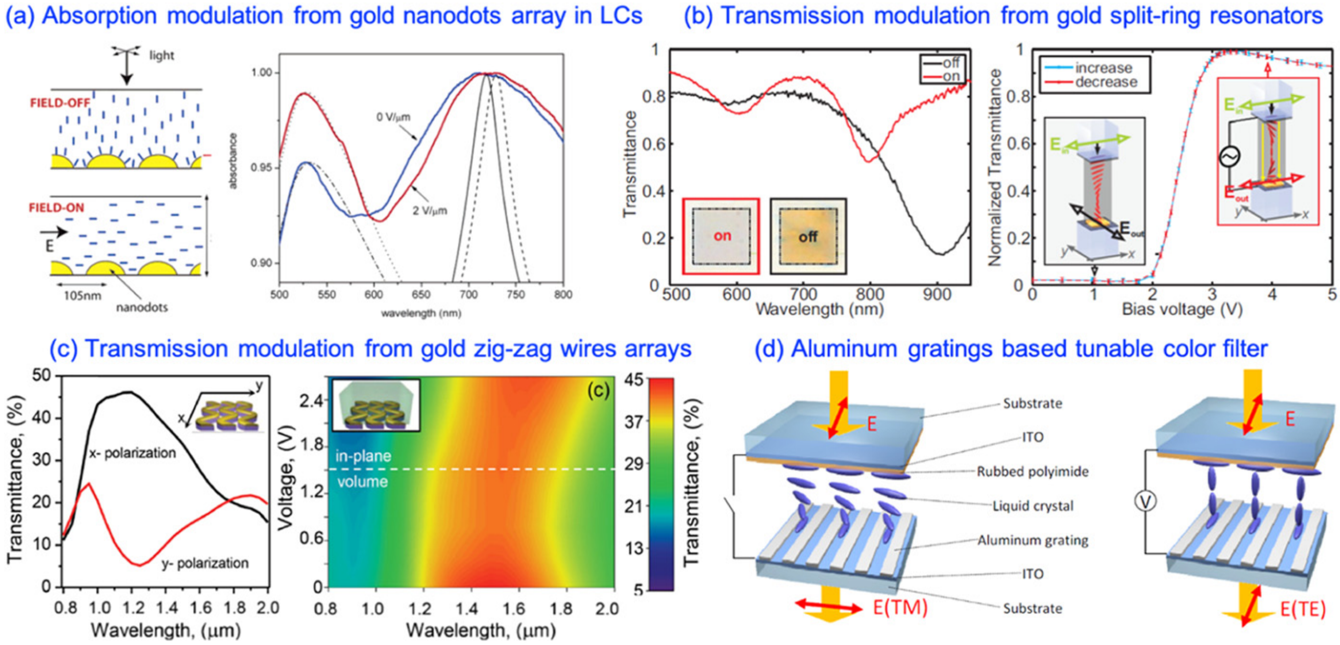

Figure 17. LC-based active metasurfaces with different geometries. (a) Modulation of absorption based on an array of gold nanodots embedded in LC. Reprinted with permission from [167]. Copyright (2005) American Chemical Society. (b) U-shaped SRR based metasurfaces with the switching resonance between electric and magnetic resonant modes. Reproduced with permission from [168]. © The Optical Society. (c) Zig-zag wires array metasurface geometry for spectrum tuning. [169] John Wiley & Sons. © 2015 WILEY-VCH Verlag GmbH & Co. KGaA, Weinheim. (d) Tunable color filters made from aluminum binary gratings based plasmonic metasurface. Reproduced with permission from [170]. © The Optical Society.

+1 and −1 diffraction orders can be electrically controlled due to the change of the polarization of the incident light caused by the LC cell.

The LC infiltered all-dielectric metasurface has also been studied as a promising candidate for the lossless control of electromagnetic waves due to its high transmission efficiency, enabling versatile applications of the optical wavefront, spectrum, and polarization manipulation. Dielectric metasurfaces can also be dynamically modulated by using LCs under applied electric fields, giving rise to a wide range of applications, including light modulators, vortex beam generators, spatial phase modulators, etc. A Mie-resonant metasurface was fabricated from Si nanodisks arrays, which were embedded into LCs (figure 18(a)) [173]. Applying a bias voltage will change the anisotropic permittivity tensor around the metasurface due to the reorientation of the nematic LC molecules, resulting in a large spectral shift of the metasurface resonances. Experimentally, a spectral shift of 50 nm and absolute transmission modulation of 75% was observed at a wavelength of 1550 nm under AC bias of 70 V at frequency of 1 kHz. Besides amplitude modulation, tuning of the transmission phase with a magnitude up to π has also been measured from this structure [173]. The small band gap energy of Si ($E_g \approx 1.1$ eV) causes significant absorption losses in the visible. As an alternative candidate, TiO_2, which has larger band gap energy ($E_g \approx 3.2$ eV), has been widely employed as a lossless building block for metasurfaces suitable for the entire visible spectrum. Figure 18(b) shows an all-dielectric electrically tunable metasurface in the visible (660–690 nm) based on a TiO_2 nanodisks array embedded in a thin LC layer [174]. Upon applying bias voltages of 3–5 V, significant modulation of the resonances associated with large transmission modulation up to 65% has been observed. Wang *et al* reported an efficient vector vortex beam generator by combining an LC phase retarder with dielectric metasurface waveplate (figure 18(c)) [175]. It is shown that the LC phase retarder can introduce phase retardation varying from 0 to 2π with applying voltage. Therefore, it can convert a linearly-polarized Gaussian beam into any desirable vector vortex beams. On the other hand, Li *et al* demonstrated a transmissive SLM based on tunable dielectric metasurface combined with LCs (figure 18(d)). This device has a very small pixel size of ~ 1 μm and can introduce a complete 2π-phase modulation, enabling active beam steering with the efficiency of 36% and a large beam deflection angle of 11° [176].

Besides the electrical tuning approaches, other mechanisms including thermal, and optical control have been successfully implemented active LC metasurfaces with various functionalities and promising performances. Heating the LC cause a change of their internal structure, thus modulating the refractive index [177]. Figure 19(a) shows the LC in the nematic phase, in which the orientation of the LC molecules is parallel to the surface of the LC cell at low temperature (~ -20 °C). Increasing the temperature (~ 60 °C) will change the LC arrangement to the isotropic phase, resulting in a large change in the refractive indices. In this way, dynamic beam switching of a laser beam from 0° to 12° with an efficiency of 50% was demonstrated by heating the LC-based metasurface [177]. With this technique, active tuning of the resonances of

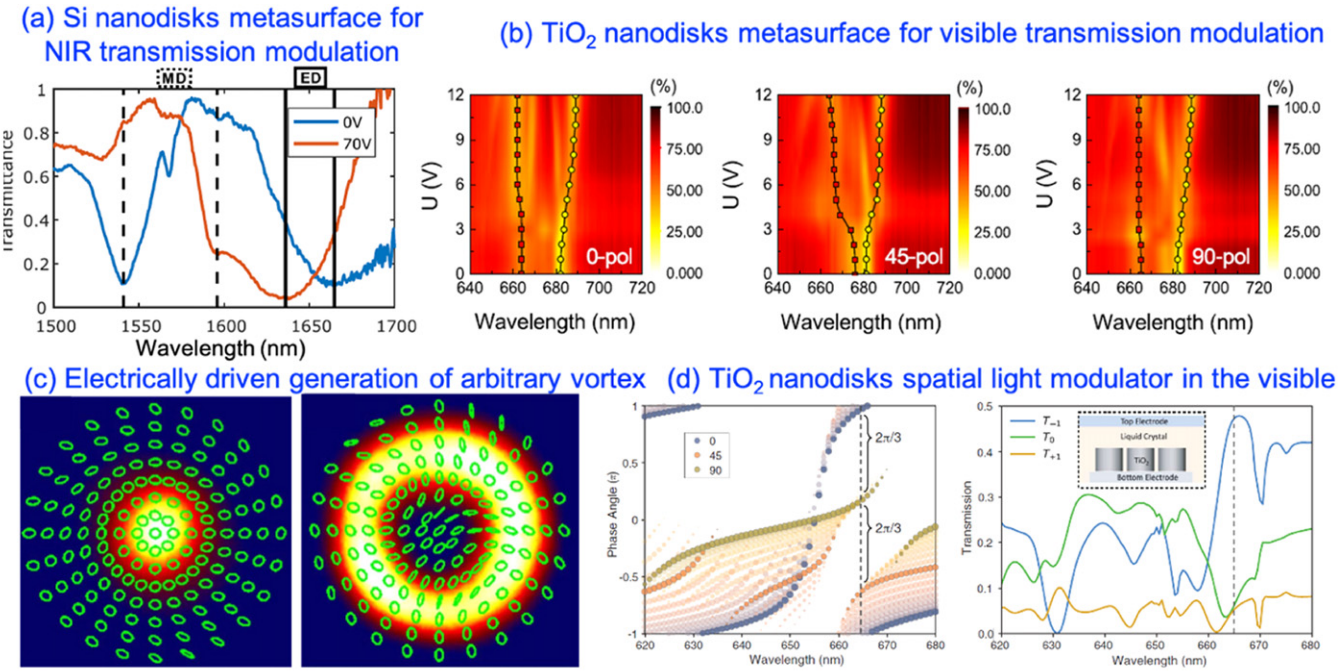

Figure 18. LC-based tunable dielectric metasurface. (a) Mie-resonant based metasurface composed of silicon nanodisks for near-infrared transmission modulation under electrical bias. Reprinted from [173], with the permission of AIP Publishing. (b) The transmission tuning of TiO_2 metasurface for the incidence with polarization directions at 0°, 45°, and 90°, versus applied DC bias. Reprinted by permission from Springer Nature Customer Service Centre GmbH: Springer. Scientific Reports. [174] © 2019. (c) Measured polarization and intensity distributions when the phase retardation is chosen as 2π (left) and π (right), respectively. Reproduced with permission from [175]. © The Optical Society. (d) (Left) Calculated relative phase retardation of the light passing the unit cell, and (right) transmission spectra of the three diffraction orders from a SLM enabled beam-deflecting structure. From [176]. Reprinted with permission from AAAS.

dielectric metasurfaces, which are composed of silicon nanodisk array, has been demonstrated [38]. A maximum resonance tuning range of 40 nm was obtained from this structure, and the transmission change reached up to a factor of 5 (figure 19(b)). Figure 19(c) shows tunable light sources from Mie-resonant dielectric metasurfaces embedded into a LC cell. The spontaneous emission intensity can be increased by two-fold under heating [178]. Liu *et al* demonstrated an optically-tunable plasmonic color filter by integrating gold annular aperture arrays with photo-responsive LCs (figure 19(d)). Due to the change of the photoinduced refractive index, the transmission can be modified up to 18% under UV light exposure [179].

Greatly benefitting from its considerably large optical anisotropy and birefringence ($\Delta n \sim 0.2$), LC-based active metasurfaces have demonstrated both amplitude modulation and a complete 2π phase modulation. Moreover, the LC-based metasurface is compatible with many different tuning mechanisms, including electrical, optical, magnetic, and thermal approaches, according to the needs of various application scenarios. In addition, the LC materials have already been well-developed with mature fabrication technology. Therefore, LCs are one of the most attractive materials platforms for developing active metasurfaces with high efficiency. However, a few key technical challenges need to be addressed for utilizing LC-based active metasurfaces. For instance, one difficulty is to increase the modulation speed of the LC-based devices, as the typical reported switching time of such devices is on the order of tens of milliseconds, which does not meet the typical requirement for fast modulation applications. Moreover, it is highly desirable to individually control both the response of each unit element and reduce the pixel size of the LC-based metasurfaces. However, the spacing of the electrodes and the pixel-size of the reported LC metasurfaces are still in the scale of micrometer, which is far from subwavelength region.

2.4. Electro-optical modulation using III–V semiconductors and multiple-quantum wells

Besides the above-mentioned electrical tuning mechanisms, some other electrically-tunable methods have been reported with remarkable performance and promising potential applications, including electrical control of carrier concentration in a III–V semiconductor substrate and electrical tuning of intersubband transitions in multiple-quantum wells (MQWs).

2.4.1. Electrical control of carrier concentration on III–V semiconductor substrates. The dielectric constant ε of a doped semiconductor substrate can be determined using the Drude model, similar to the conducting oxide materials (section 2.1). Therefore, applying an electrical gate bias onto the semiconductor substrate can control the width of the depletion region within the semiconductor layer, thus causing the modulation of its dielectric constant near the interface. This approach has been taken to create a metallic split-ring-resonators-based active metasurface, fabricated onto a III–V

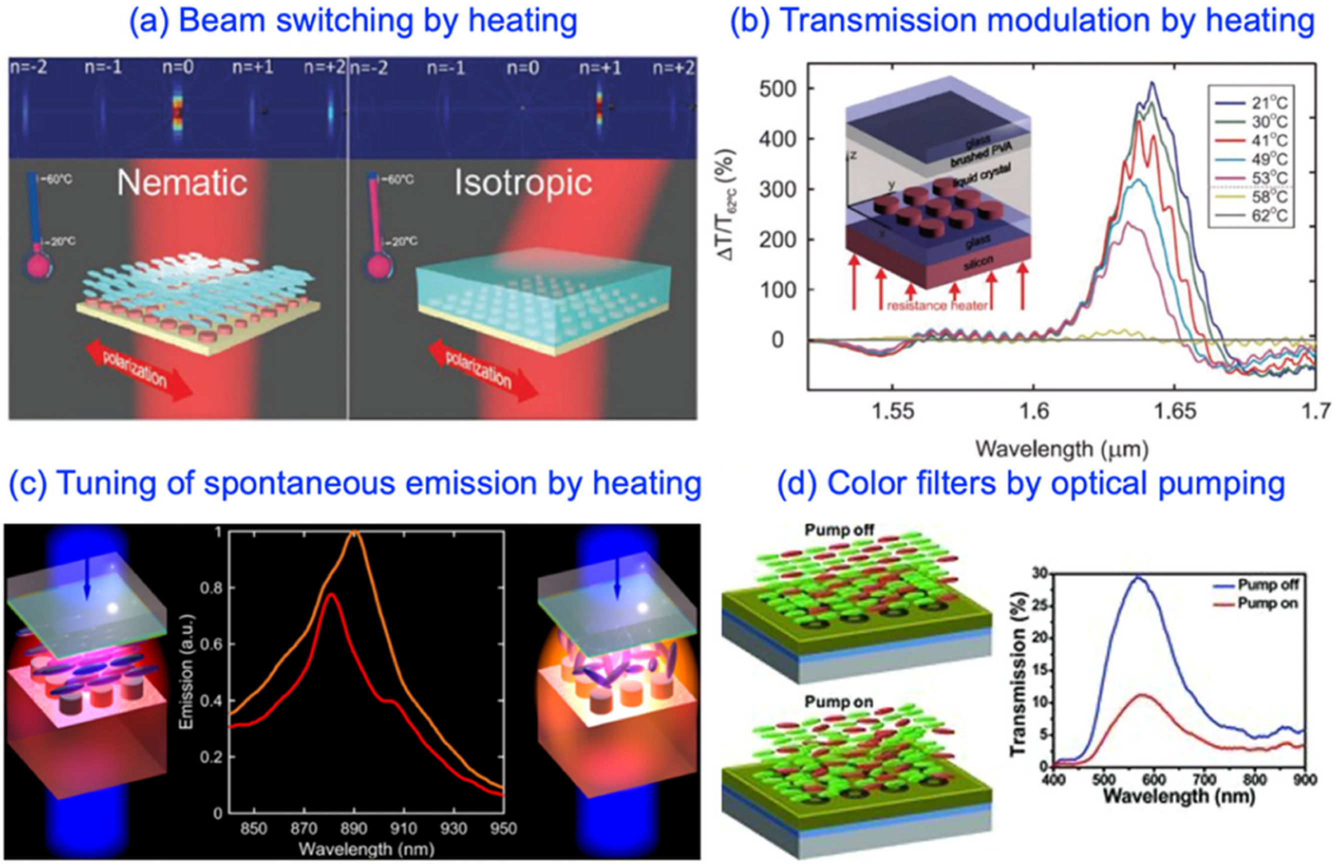

Figure 19. LC tunable metasurfaces through thermal and optical approaches. (a) Dynamic beam switching of a laser beam by heating the metasurface. Reprinted with permission from [177]. Copyright (2018) American Chemical Society. (b) Transmission tunable metasurfaces under different temperature. Reprinted with permission from [38]. Copyright (2015) American Chemical Society. (c) Modulation of spontaneous emissions by heating. Reprinted with permission from [178]. Copyright (2018) American Chemical Society. (d) Light-driven plasmonic color filter. [179] John Wiley & Sons. © 2012 WILEY-VCH Verlag GmbH & Co. KGaA, Weinheim.

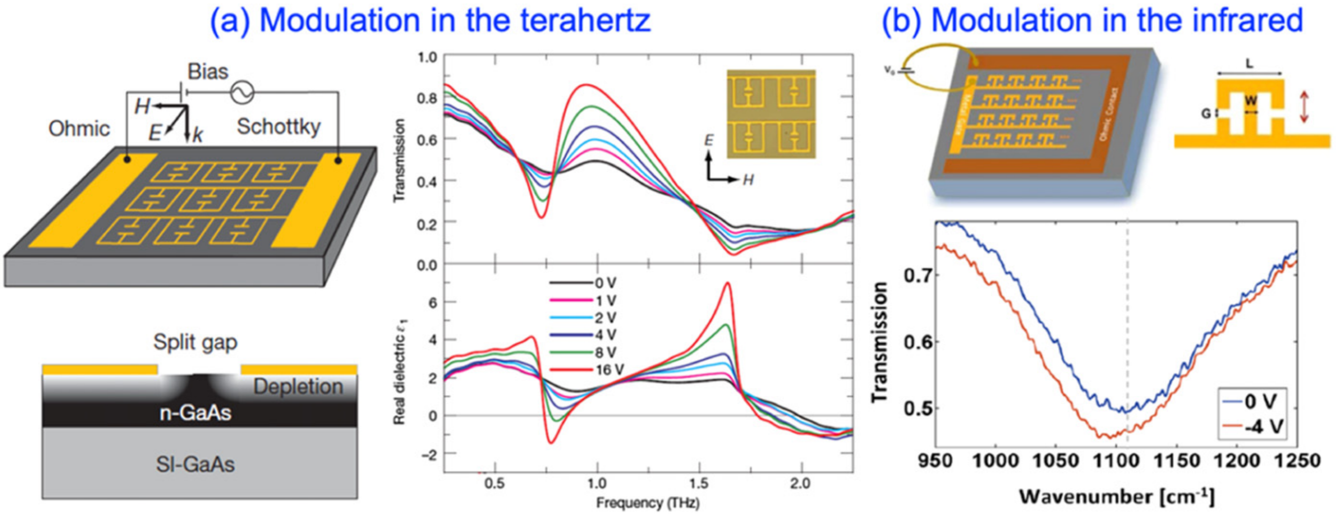

Figure 20. Active metadevice based on carrier density modulation of a III–V semiconductor substrate. (a) Au SRRs array on a GaAs substrate for electrical modulation in the THz region. Transmission and real part of dielectric constant versus reverse gate biases. Reprinted by permission from Springer Nature Customer Service Centre GmbH: Nature. [180] © 2006. (b) Tunable metasurface and the transmission spectra measured under different gate biases. Reproduced with permission from [181]. © The Optical Society.

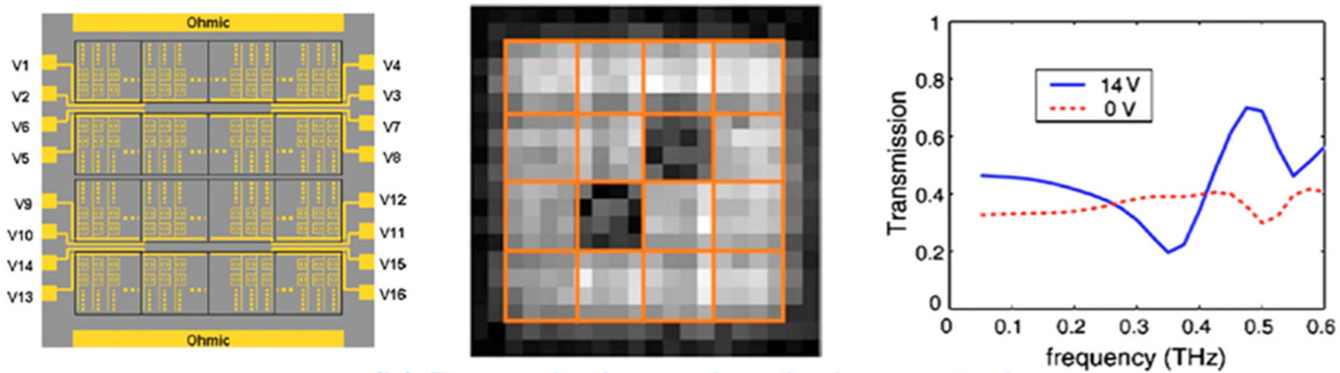
(a) Spatial light modulator

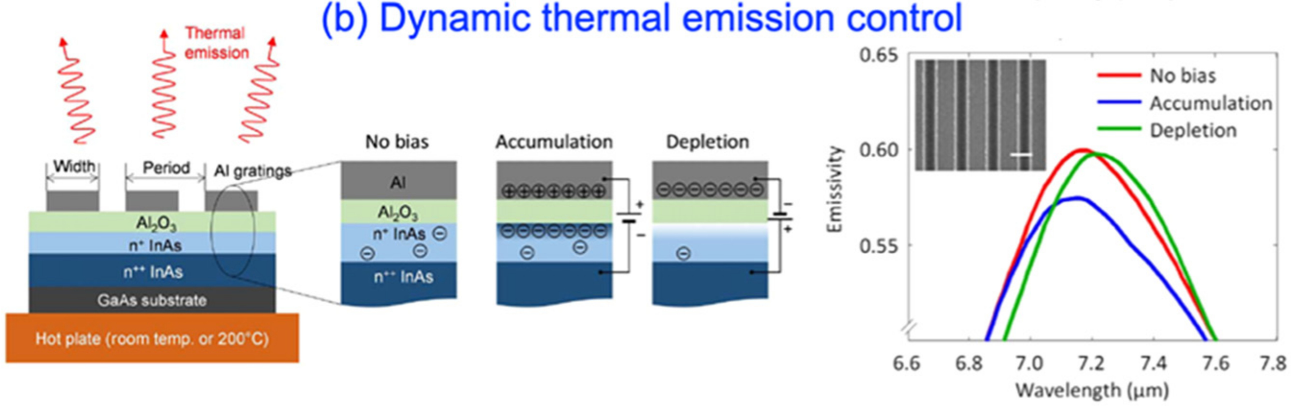
(b) Dynamic thermal emission control

Figure 21. (a) A terahertz SLM, which is composed of (left) a 4 × 4 array of individual pixels, (middle) its transmission image at 0.36 THz, and (right) transmission spectra of the SLM with and without bias. Reprinted from [182], with the permission of AIP Publishing. (b) (Left) Schematic of a tunable metasurface for dynamic control of thermal emission and (right) emissivity spectrum under different conditions. From [183]. Reprinted with permission from AAAS.

semiconductor substrate to tune its plasmonic resonance. The reported structures have a typical size in several microns, giving rise to several active plasmonic devices in the long-wavelength range including the terahertz and mid-infrared regimes (figure 20(a)).

Chen *et al* reported a terahertz active metasurface device created by fabricating an array of gold SRRs on a semiconductor substrate (figure 20(a)) [180]. In this structure, Schottky contacts are formed between the SRRs and the GaAs substrate. The carrier density of the GaAs substrate near the split gaps can be modulated by applying a bias voltage, causing the change of its dielectric constant and thus the resonance strength of the SRRs. Experimentally, a large modulation of transmission intensity up to 50% relative change is demonstrated at a frequency of 0.72 THz using a reverse gate bias of 16 V. Figure 20(b) shows active tuning of planar metamaterial operating in the mid-infrared (∼10 μm), based on an SRR structure fabricated on an n-type GaAs substrate. Upon applying an electrical bias, a large change of the permittivity of GaAs substrate ($\Delta\varepsilon \sim 0.5$) is expected, which significantly shifts the resonance of the metasurface. In this way, the dynamical modulation of the transmission curve with an absolute change of ∼25% is achieved [181].

The modulation of the carrier density of a semiconductor substrate has enabled a few active functional metadevices. Chen *et al* demonstrated a 4 × 4 pixels spatial modulator in the terahertz region which is composed of a gold SRRs array structure fabricated on a GaAs substrate as the unit cell (figure 21(a)). The electrical tuning of the resonance of the SRRs leads to a large amplitude modulation depth in the range between 35% and 50% for all 16 pixels at the resonant frequency of 0.36 THz under a bias voltage (0–14 V) [182]. Figure 21(b) shows an active plasmonic metasurface with dynamic control of the thermal emission. In this structure, the array of plasmonic cavities is epitaxially grown InAs layers. The carrier distribution of the InAs layer can be modulated under the electrical gating bias resulting in either an accumulation layer or depletion layer within the InAs layer. As a result, both the absorption and thermal emission property of the metasurface will be changed. In this way, a polarization-dependent modulation of emissivity up to 3.6% was demonstrated in the mid-infrared range [183].

2.4.2. *Electrical tuning of the intersubband transitions in multiple-quantum wells (MQWs).*

Large electro-optic coefficients can be obtained by engineering the intersubband transitions in MQWs, such as InGaN/GaN systems and AlGaAs/GaAs systems, associated with the quantum-confined Stark effect (QCSE). Such a modulation mechanism purely induced by an electric field opens another feasible approach to realize tunable metasurfaces with low power consumption.

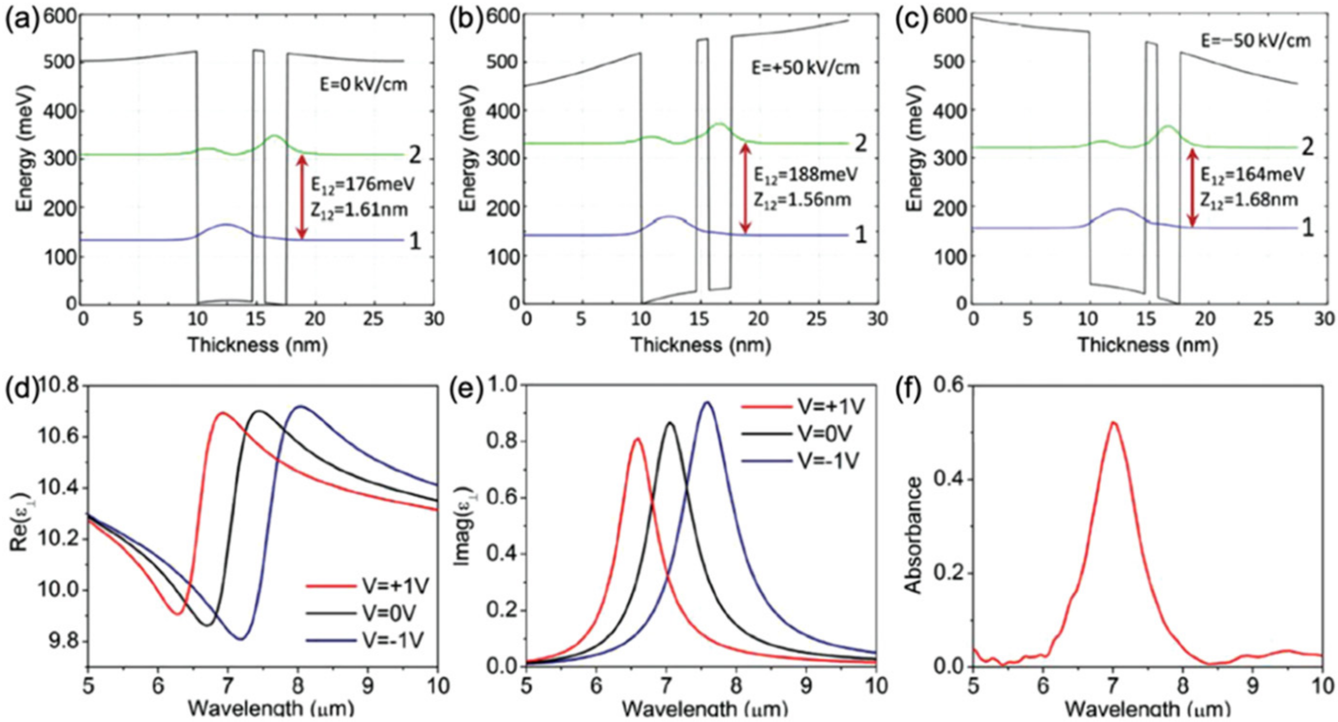

Figure 22. (a)–(c) Calculated conduction band diagram of a coupled MQW structure with different electric fields. (d) and (e) Calculated dielectric constant normal to the surface of MQWs. (f) Measured absorption spectrum of the MQWs measured without applied bias. [184] John Wiley & Sons. © 2014 WILEY-VCH Verlag GmbH & Co. KGaA, Weinheim.

The dielectric constant of electric field polarization perpendicular to the MQWs for the case of TM polarized incidence can be expressed by

$$\varepsilon_{\perp}(\omega) \approx \varepsilon_{\text{core}}(\omega) + \frac{2\pi N_{\text{e}}(ez_{12})^2}{\varepsilon_0 h((\omega_{12}-\omega)-\mathrm{i}\gamma_{12})},$$

where $\varepsilon_{\text{core}}(\omega)$ is the dielectric constant of the semiconductor material, e is the electron charge, N_{e} is the doping concentration in the MQWs, and z_{12}, ω_{12}, and γ_{12} represent the transition dipole moment, frequency, and linewidth broadening factor, respectively (figure 22) [184]. Because of the intersubband transitions in the MQWs are intrinsically TM-polarized, applying a bias can modulate the transition energy ω_{12} or E_{12} (figures 22(a)–(c)), causing a change of $\varepsilon_{\perp}(\omega)$ for the TM polarized light (figures 22(d) and (e)). In contrast, the dielectric constant for the TE polarized light, $\varepsilon_{//}(\omega)$ remains unchanged. Both theoretical and experimental work have proven that an electrically-tunable metasurface can be readily obtained by coupling plasmonic nanoresonators to the TM-polarized modes supported in the MQW layer (figure 22(f)).

Lee *et al* reported an electrically-tunable metasurface in the mid-infrared. It was fabricated by sandwiching an MQW layer between a metallic layer patterned with a two-dimensional array of plasmonic resonators and a ground metallic layer [184]. By coupling the resonance modes of the plasmonic resonators with the intersubband transitions in the MQW layer, strong voltage dependent tuning resulting from the QCSE can be obtained. Figure 23(a) shows the absorption modulation of this structure under different bias voltages with a large relative modulation depth of $>30\%$ at a wavelength of ~ 7 μm. Moreover, this device has a fast operation speed with a response time $<\sim 10$ ns. Benz *et al* demonstrated a tunable metamaterial by combining the intersubband transitions of MQWs with planar metamaterials in the strong light–matter coupling regime [185]. In their device, the resonance frequency of the metamaterial can be tuned due to the intersubband transitions under electric bias, switching the system from an uncoupled regime to a strongly coupled regime. As a result, tuning the resonance of $>8\%$ at the center frequency is realized (figure 23(b)). Figure 23(c) shows a dielectric-active metasurface based on electro-optical modulation of the refractive index of MQWs, $\Delta n \sim 0.01$ [186]. A modulation of reflectance as large as 270% and a large phase shift (0° to $\sim 70°$) are obtained when applying an electric field across the structure. This tunable metasurface further allows the demonstration of electrical switching of the first-order diffracted beam and a dynamic beam steering. The QCSE modulation from the MQWs-based metasurface provides several advantages including fast modulation speeds and low power consumption. For example, fast modulation of reflectance with a response time of <10 ns has been demonstrated [184]. Moreover, the QCSE modulation is pure field-effect with a low value of leakage current density, which can be in the range of $\sim$mA cm^{-2}, leading to low power consumption [186]. However, such a modulation mechanism also suffers from some limitations, such as the minimal change of refractive index ($\Delta n \sim 0.01$), and it modulates not only the phase but also

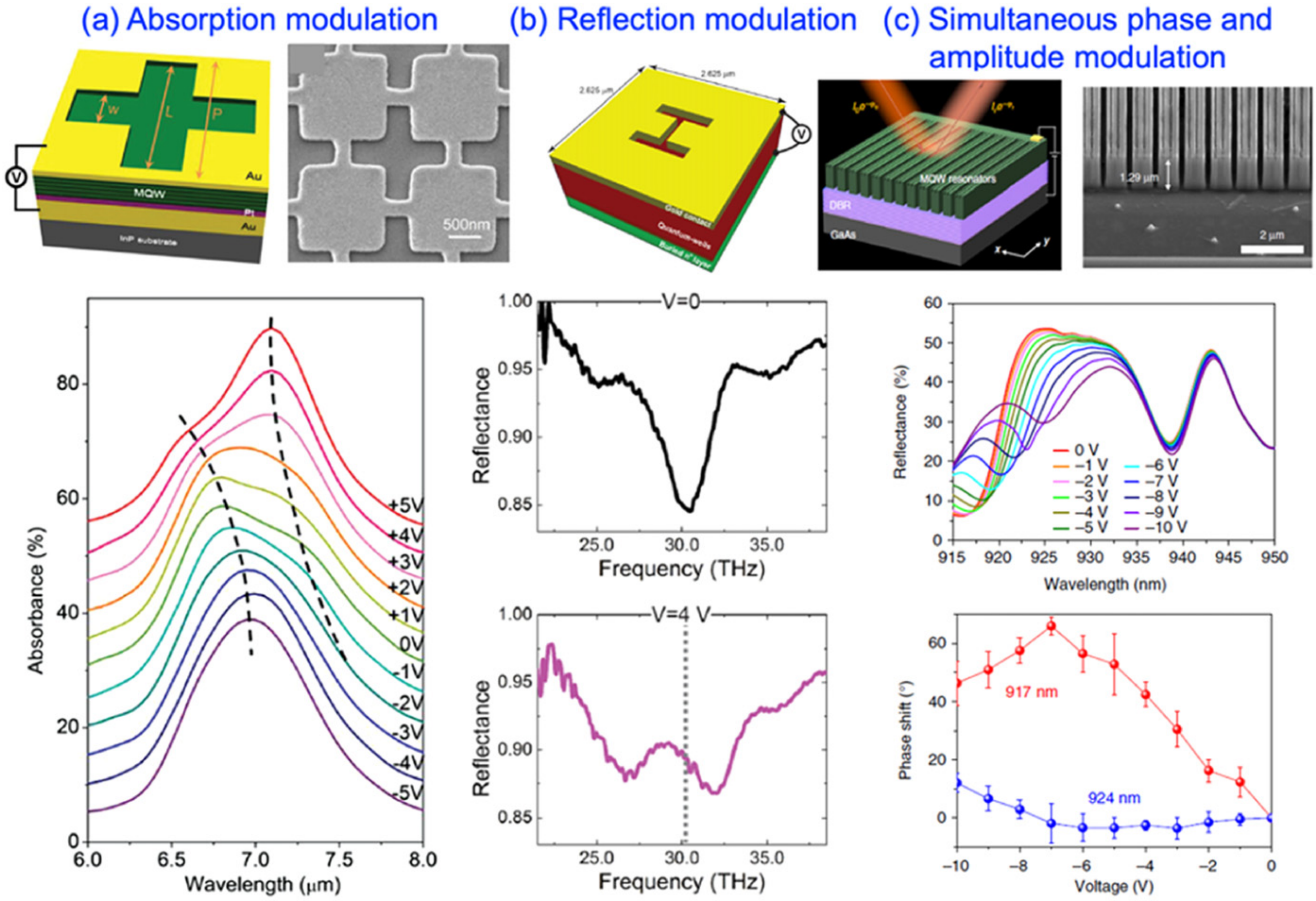

Figure 23. (a) Measured absorption modulation at different bias voltages. [184] John Wiley & Sons. © 2014 WILEY-VCH Verlag GmbH & Co. KGaA, Weinheim. (b) Experimental reflectance spectra under different biases showing a significant tuning of reflectance. Reprinted from [185], with the permission of AIP Publishing. (c) The measured reflectance and phase modulation of the metasurface versus wavelength with applied voltages. Reprinted by permission from Springer Nature Customer Service Centre GmbH: Nature Communications. [186] © 2019.

the amplitude of the structure response. Therefore, optimized designs will be required to implement phase-only modulation.

3. Dynamic metasurfaces with phase-change mechanics

Phase-change or phase-transition materials, already widely employed in optical data storage, have emerged as a class of candidate material for integrating tunability into the optical metasurfaces. In these materials a significant change of the permittivity $\varepsilon(\omega)$, can be achieved during the transition between ordered crystalline and disordered amorphous states due to the change of chemical bonding. Consequently, the optical properties of metasurfaces comprised of phase-change materials can be significantly modulated both reversibly or irreversibly by external stimuli such as electric field application, thermal activation, all-optical excitation, etc. The two most common phase change materials for developing active metasurfaces, chalcogenide glass and vanadium oxide, will be discussed in the following.

3.1. Chalcogenide-glass based metasurfaces

Germanium–antimony–telluride (GeSbTe, also called GST, figure 24(a)) is a kind of nonvolatile phase change material which remains in either the amorphous or crystalline state until an external stimulus is applied [187]. The reversible characteristic of GST makes it suitable for applications in energy harvesting, memory storage, and optical switching. When the temperature approaches to crystalline (∼160 °C)/melting point (∼600 °C), GST transits to a crystalline/amorphous phase (figure 24(b)). The different arrangements of the amorphous state (covalent bonding) and crystalline state (resonant bonding) lead to pronounced variation of the optical properties, such as refractive index (figure 24(c)) and extinction coefficient in the near-infrared and mid-infrared regime (figure 24(d)). For instance, the refractive index of GST in the crystalline phase increases by more than 50% over the refractive index of the amorphous phase [187]. Due to the dramatic contrast of optical properties between the amorphous and crystalline phase, GST is an ideal material candidate for dynamic metasurfaces. The transition between the amorphous and crys-

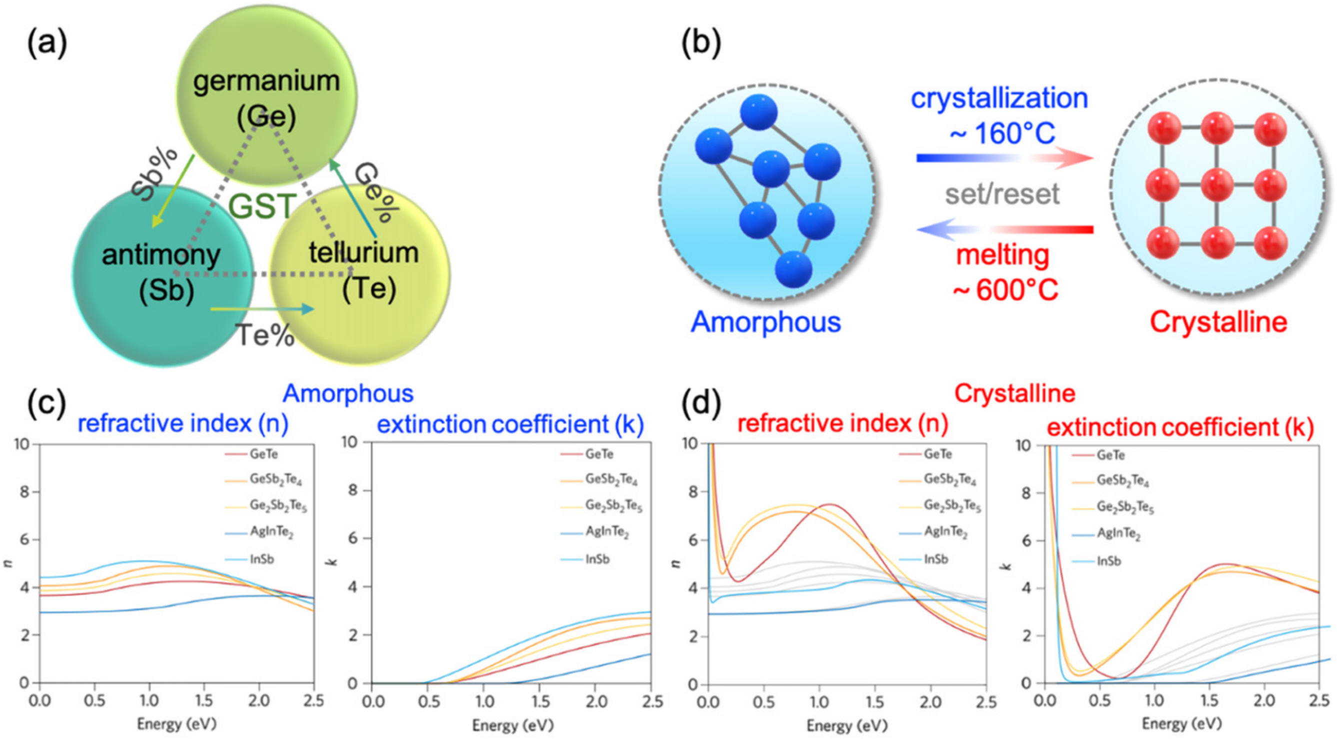

Figure 24. (a) Schematic illustration and (b) the phase transition of GST. Refractive index and extinction coefficient of three different GSTs (GeTe, GST-225 and GST-124) versus photon energy for (c) amorphous and (d) crystalline states. Reprinted by permission from Springer Nature Customer Service Centre GmbH: Nature Photonics. [187] © 2017.

talline states can be realized on the sub-nanosecond timescale, which might lead to GHz optical modulation.

In one of the pioneering works on this topic, Sámson *et al* in 2010 demonstrated the electro-optic switching using a plasmonic planar metasurface which is covered by a layer of gallium lanthanum sulphide (GLS), a type of chalcogenide glass [188]. The phase change of the GLS layer from amorphous state to more conductive crystalline state leads to narrow Fano-resonance blueshift of 150 nm and reflectivity change of 60%. In 2013, an all-optical and bidirectional meta-switch was proposed, which was composed of Au nanostructures coated with GST film sandwiched between two ZnS/SiO$_2$ layers (figure 25(a)) [189]. With laser pulse (amorphous-to-crystalline direction: 100 ns pulses with a peak intensity of 0.1 mW μm^2; crystalline-to-amorphous direction: 50 ns pulses at order 0.25 mW μm^{-2}) switching of the GST, the phase transition (amorphous to crystalline state) red-shifts resonant features by ~200 nm, and the intensity of the transmitted signal decreases with high contrast in the near- to mid-infrared regime. In the same year, Michel *et al* systematically studied the dielectric constant for GST and the resonance tuning of three configurations (with an aluminum (Al) nanoantenna fabricated on top of, inside, and below the GST) (figure 25(b)) [190]. During the thermal annealing, the complex permittivity of GST changed from 12.8 + 0.01i (a-state) to 40.0 + 0.8i (c-state) at a wavenumber of ~3000 cm^{-1} (at a wavelength of ~3.33 μm). The maximum reflectance change (ΔT) was observed in the Al nanoantenna on a bottom layer of GST with a resonance blueshift of 19.3% (610 cm^{-1}). In 2014, they also demonstrated a reversible cycling of infrared switching via femtosecond laser pulses using a structure with GST on top of the Al antenna (figure 25(c)) [191]. In 2015, Yin *et al* demonstrated the first active plasmonic chiral metasurface with GST-326 operating in mid-infrared range (figure 25(d)) [192]. The Born–Kuhn type chiral plasmonic dimer with a GST gap layer sandwiched between corner-stacked Au nanorods, which gave the different spectral responses with left- and right-circularly polarized (LCP and RCP) light as the chiroptical nature. The circular dichroism can be derived by $\theta(\text{deg}) = 33(\log(T_{\text{RCP}}) - \log(T_{\text{LCP}}))$. When the GST layer transfer from a-state ($n_a = 3.5 + 0.01i$) to c-state ($n_c = 6.5 + 0.06i$), the active chiral metasurface offers a large tunability range (4.15–4.90 μm) of circular dichroism response. Furthermore, they also demonstrated a passive chiral layer on an active metasurface to flip the sign of circular dichroism.

Also in 2014, Tittl *et al* proposed a switchable perfect absorber by using a GST-326 layer between an Al nanoblock and a back reflector in the mid-infrared range (figure 26(a)) [193]. The gap surface plasmon mode offers absorption of >90% with incident angle up to 65°. The resonance in the reflective spectrum shifts over 500 nm due to the amorphous-to-crystalline phase transition, which offers multispectral thermal imaging capability. Also, Qu *et al* demonstrated dynamic thermal emission manipulation by using a sandwich structure with GST between a gold nanodisk and a back reflector (figure 26(b)) [194]. By baking at different temperatures with a fixed time period, the bandwidth (up to 6 μm), the thermal emission (30%–100%) and the location of resonance (6.51–9.33 μm) can be tuned accurately according to the different crystallization fraction. Chen *et al*

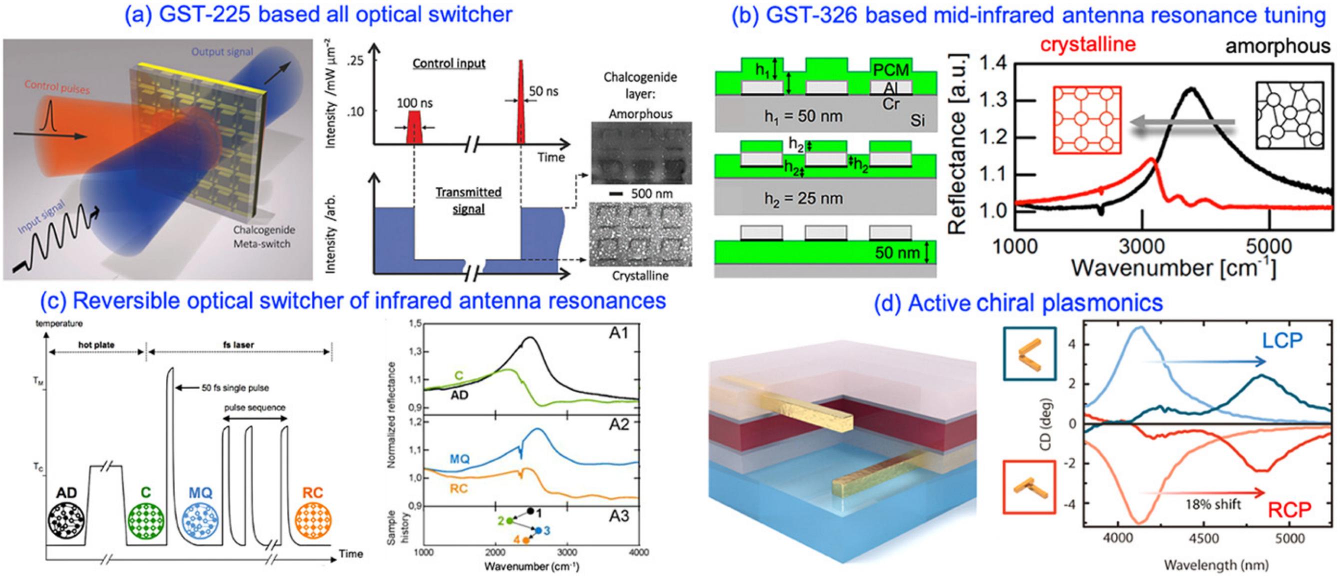

Figure 25. (a) An all-optical and bidirectional meta-switch based on non-volatile GST-225 and single laser pulse control excitations homogenously transit a GST nanolayer between amorphous and crystalline state. [189] John Wiley & Sons. © 2013 WILEY-VCH Verlag GmbH & Co. KGaA, Weinheim. (b) Mid-infrared antenna resonance tuning using low loss GST and experimental antenna resonance shifting. Reprinted with permission from [190]. Copyright (2013) American Chemical Society. (c) Active optical switch based on the reversible phase transition of GST-326 and experimental reflection spectra for Al nanoantenna below GST-326 layer and sample history under different status. Reprinted with permission from [191]. Copyright (2014) American Chemical Society. (d) Active chiral plasmonic dimer stack and circular dichroism spectra of LCP and RCP from the amorphous (light curve) and crystalline (darker curves) states. Reprinted with permission from [192]. Copyright (2015) American Chemical Society.

investigated the active tuning lattice resonance of a hybrid plasmonic crystal incorporating GST sandwiched between a quartz substrate and a gold nanodisk array (figure 26(c)) [195]. The maximum wavelength tuning range of the resonance is ∼500 nm (1.89–2.27 μm). The resonance can be precisely tuned in the above range with a crystallization fraction of GST in different baking times. Several comprehensive simulations were performed on a GST-integrated double Fano resonance [196], an electromagnetically-induced-transparency-like metasurface [197], a tunable near-infrared absorber and modulator [198], and a switchable subwavelength plasmonic structure [199, 200]. Experimentally, Karvounis *et al* exploited the laser-induced structural transitions of GST nanograting on SiO_2 in 2016. The resonance of the grating spectrally shifted by 10% (150 nm) with a contrast ratio of 7 dB (in reflection) and −5 dB (in transmission) in visible/near-infrared wavelength regime [201]. They implied that the extensive chalcogenide family (sulphide, selenide and telluride) with compositional variety and nonvolatile switching functionality offers a wealth of reconfigurable and self-adaptive metasurfaces for potential active 'flat-optic' applications. In 2017, Michel *et al* investigated the performance of nanoantennas with thin films of GST-225, GST-326, and GST-8211 compounds [200] having a wide range of structural and dielectric properties (complex permittivity, carrier concentration and bandgap), suitable for photonic applications in various spectral regimes. In the same year, Shrekenhamer *et al* reported a thermally-tunable infrared metasurface modulator based on GeTe with amplitude modulation of 59% in reflectance [202]. In 2018, Dong *et al* investigated a transmissive metasurface-based gold nanoblock on the top of a Si_3N_4–GST–ITO–Si substrate with a 500 nm concomitant resonance shift in mid infrared range resulting from the huge contrast in the refractive index (n) in the GST phase change (figure 26(d)) [203].

Besides tuning the resonances, Hosseini *et al* first described a unique optoelectronic framework for a display application [204]. The GST-based thin film was inserted between two ITO layers as electrodes on top of a reflective mirror/transparent substrate (figure 27(a)). An array was patterned with an element footprint of 300 × 300 nm^2. The conductive tip of an atomic force microscope (CAFM) was employed to apply the voltage on the top electrode. The display capability with high optical contrast was demonstrated due to the amorphous to crystalline transition of the thin GST elements array. Finally, utilizing the ultrathin GST films, Hosseini *et al* demonstrated a flexible display in both reflective and semi-transparent mode, which could result in foldable ultralight displays. By using a diffraction-limited optical writing laser with different illumination conditions, a thin GST film between two intermediate layers (ZnS–SiO_2) on glass substrate can be selectively switched between amorphous and crystalline phases as a 'rewritable' platform (figure 27(b)) [205]. A variety of devices were realized based on the reconfigurable platform, such as reconfigurable bi-chromatic and multi-focus Fresnel zone plates in visible range, a super-oscillatory lens with subwavelength focus, and a greyscale hologram. Li *et al* used a similar idea but incorporating a polaritonic material platform to demonstrate reversible switching of surface phonon-polaritons (SPhPs) on GST film by a focused nanosecond laser (figure 27(c)) [206]. Their experiments demonstrated that the number of switching events can be improved by attaching a protective layer to suppress film ablation. Alternatively,

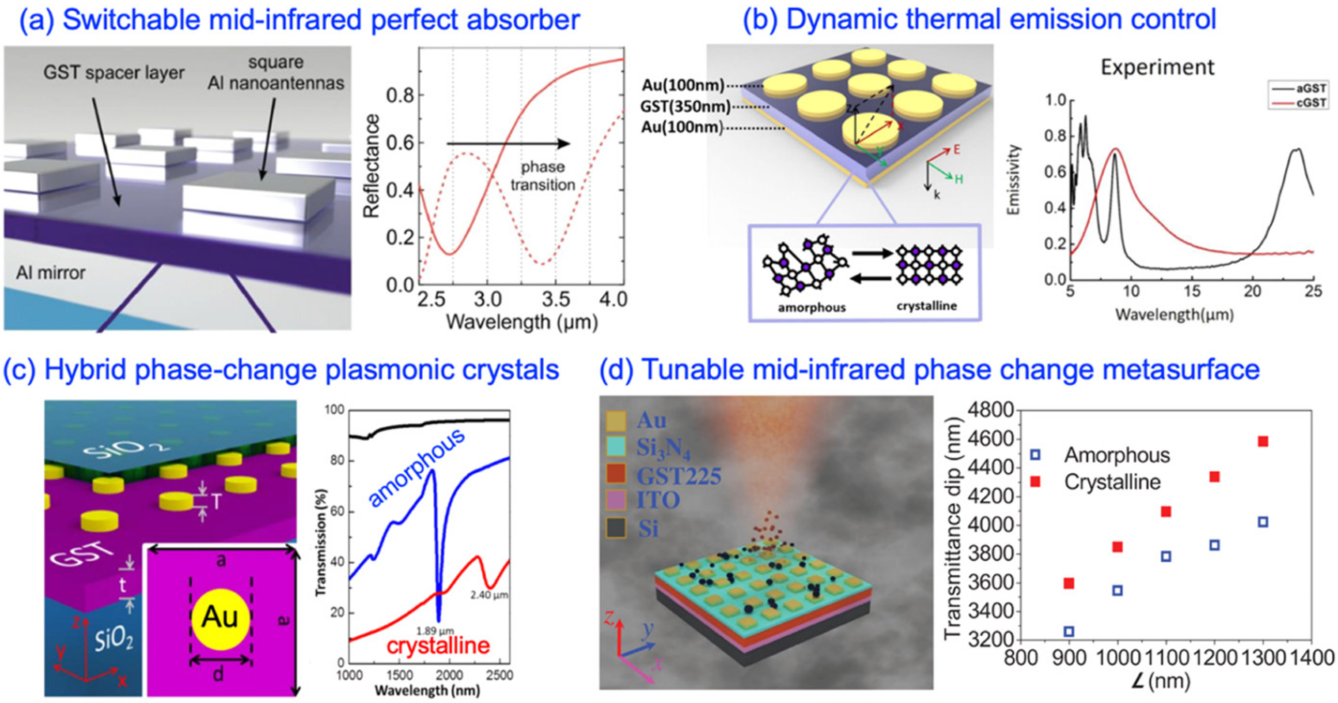

Figure 26. (a) Schematic of a switchable perfect absorber device and experimental measurement of the device in amorphous (solid line) and crystalline state (dashed line). [193] John Wiley & Sons. © 2015 WILEY-VCH Verlag GmbH & Co. KGaA, Weinheim. (b) Sketch of an ultrathin plasmonic thermal emitter and measured spectra in different states. [194] John Wiley & Sons. © 2017 WILEY-VCH Verlag GmbH & Co. KGaA, Weinheim. (c) Active optical switch using the reversible phase change of GST-326. (c) Tuning lattice resonance with hybrid phase-change plasmonic crystals. Reproduced with permission from [195]. © The Optical Society. (d) Tunable mid-infrared GST-225 based metasurfaces and transmittance dip versus gold block pitch for both amorphous and crystalline states. [203] John Wiley & Sons. © 2018 WILEY-VCH Verlag GmbH & Co. KGaA, Weinheim.

the permittivity of the GST can also be modulated reversibly to reduce thermal stresses, and film damage can be avoided by using an fs laser, thus realizing an ultrafast SPhPs optical device. By assigning the different crystallization levels (0%–90%) of GST spatially, Chen *et al* demonstrated that the phase difference of the wavefront can be engineered as large as 0.56π to achieve various functionalities such as a tunable lens [207]. By selective control of phase transition on the composing GST rods, Chu *et al* proposed an active metasurface to realize multiple functionalities, e.g. tuning electromagnetically-induced transparency and tuning anomalous reflection to steer the beam [208]. Meanwhile, Alaee *et al* theoretically suggested a switchable plasmonic GST-nanoantenna with tunable radiation patterns from a dipole-like to a directional pattern with zero backscattering [209].

Moreover, substantial attention has also been paid to metasurfaces with dynamic and reconfigurable functionalities. In 2017, Yin *et al* demonstrated beam switching and bifocal lensing based on geometric phase metasurfaces on the top of a GST layer (figure 28(a)) [210]. Two kinds of nanorods with different plasmon resonances were alternated line-wise, corresponding to the two states of the GST layer. In the case of the GST layer with the amorphous/crystalline phase, only one kind of rods can interact with the incidence, deviating the beam in a deflection angle of 13.23°. They also demonstrated the concept for a bifocal cylindrical lens by incorporating geometric phase metasurfaces with GST film. Due to the phase transition of the GST film, the focal length of the cylindrical lens can be switched from 0.5 mm (amorphous state) to 1 mm (crystalline state). This approach presents an alternative design principle that can be extended in many potential applications, such as a dynamic phase array for aberration correction and dynamic holography. Meanwhile, there has been extensive theoretical work in this area, such as a functional active waveplate [211], dynamic polarization-independent absorber and sensor [212], and active beam control by Mie-resonance based on a geometrically-fixed GST grating under multi-level partial crystallization [213]. Experimentally, de Galarreta *et al* reported a device for beam-steering by a combination of 1D plasmonic Al antennas with a protected GST layer and mirror. The device reflects a normally incident plane wave in the normal direction when the GST layer is in the crystalline state (figure 28(b)) [214], but reflects in an anomalous angle of 33.6° in the amorphous phase with a beam steering efficiency of ∼40%. Furthermore, to improve efficiencies beyond that achieved by typically plasmonic structures, they optimized the structure in a hybrid dielectric/metal plasmonic resonator sandwiched between a gold plane (bottom) and a hybrid silicon/GST cubic resonator (top) with enhanced efficiency of ∼65% in both states [215]. This kind of configuration can be used for switchable absorber, beam steerer, light modulator, tunable filter, etc. In the same year, Zhang *et al* experimentally demonstrated using geometric metasurfaces for tunable photonic spin–orbit interactions (SOIs) (figure 28(c)) [216].

(a) An optoelectronic framework

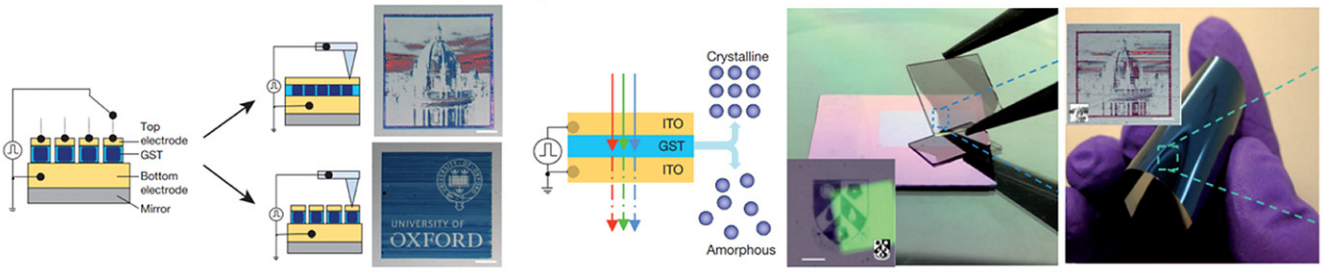

(b) Optically reconfigurable metasurfaces

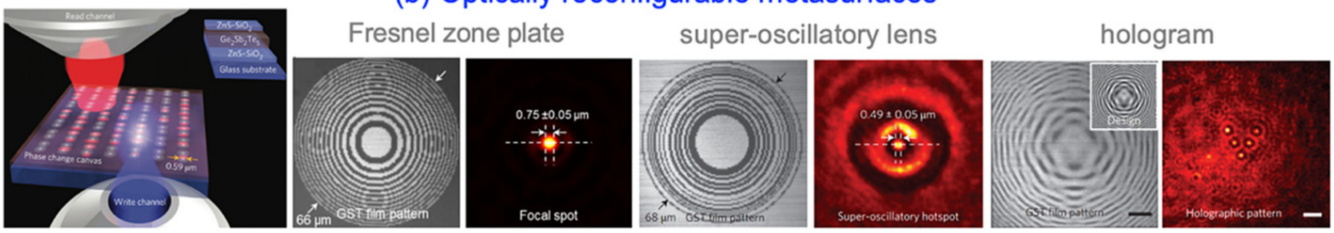

(c) Reversible optical switching based on GST

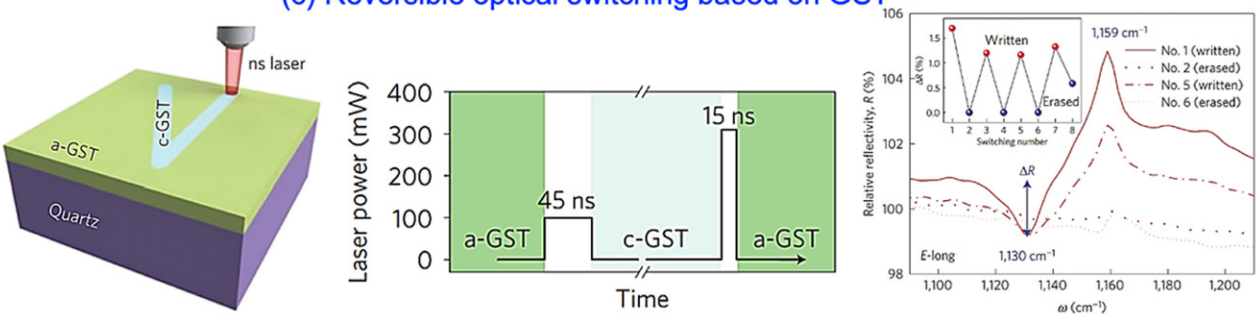

Figure 27. (a) (Left) Schematic of the color changes in an electronic display based on GST, electrically-constructed image of the Oxford Radcliffe Camera and University of Oxford logo, (middle) schematic diagram and demonstration of a semi-transparent device, and (right) flexible display film of electrically-constructed image. Reprinted by permission from Springer Nature Customer Service Centre GmbH: Nature. [204] © 2014. (b) Writable and reconfigurable photonic devices and optical reconfigurable photonic devices as a Fresnel zone plate, binary super-oscillatory lens, and eight-level gray scale hologram. Reprinted by permission from Springer Nature Customer Service Centre GmbH: Nature Photonics. [205] © 2016. (c) Schematic of switching a V-shaped domain by scanning a pulsed laser beam, laser parameters for phase change of the GST films, and measured far-field spectra in reflection of rewritable SPhPs resonators. Reprinted by permission from Springer Nature Customer Service Centre GmbH: Nature Materials. [206] © 2016.

Three metadevices possessing switchable SOIs enable holography, vortex beam generation, and spin Hall effect with the amorphous phase of the GST ('on' state of SOI). When the GST changes to the crystalline phase ('off' state), the phase profiles break down and the phenomena disappear. Experimentation showed a polarization conversion contrast between the 'on' and 'off' states in a broadband operation range (8.5–11.5 μm) with deflection angle of 23.7° and conversion efficiency of 60%.

In 2018, Cao *et al* demonstrated the active control of multispectral thermal emission operating in 2–4 μm based on an array of gold squares on top of a SiO$_2$/GST/Au multilayer (figure 29(a)) [217]. The metadevice enabled a pronounced emissivity modulation with a contrast of 0.65 and a resonance wavelength shift of 425 nm during the phase transition. In addition, reversible switch of multispectral thermal emission can be realized in 300 ns. The configuration shows the possibility of fast control of the thermal radiation and will accelerate the improvement of thermally-emissive devices. In 2019, Gholipour *et al* demonstrated a reconfigurable dielectric metasurface operating in the ultraviolet and high-energy visible spectral range (figure 29(b)) [218]. The nanograting in a composite of ZnS/SiO$_2$ and the GST exhibit a maximum reflection resonance quality factor Q of ~15 at an operation wavelength of 380 nm and a change of Q of >20% with GST phase transition. Recently, Choi *et al* experimentally demonstrated an active wavefront switching metasurface operating in the wavelength range of >500 nm at the near infrared region by utilizing a nonresonant U-shaped GST antenna with different orientation angles (figure 29(c)) [219]. The upper row consists of an antenna which has high cross-polarized light transmittance (CPT) in the amorphous phase, but the bottom row has high CPT in the crystalline phase. The incident light dominantly interacts with the upper row for the amorphous state and the lower row for the crystalline state. The cross polarization of the electrical field is deflected with an angle of 19.5° in +1st diffraction order (amorphous state) and −19.5° in −1st diffraction order (crystalline state). They also demonstrated a dynamic hologram that creates holographic 'S' image for

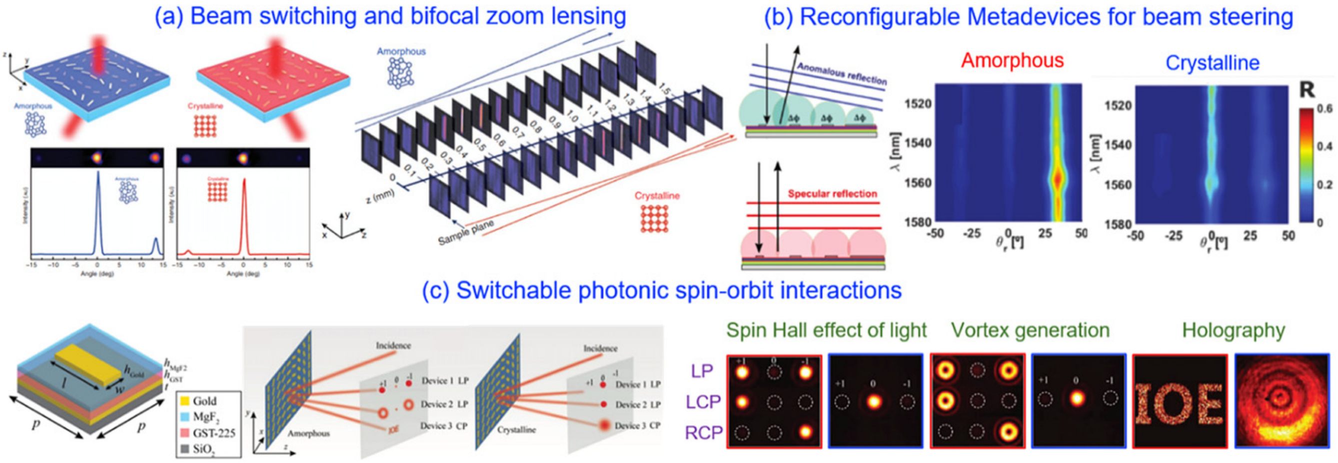

Figure 28. (a) Beam switching and bifocal lensing via dynamic plasmonic metasurfaces, with images and transmission intensity of the beam in the amorphous and crystalline phase; experimental images of the cylindrical bifocal lens at distances z from the metasurface. Reprinted by permission from Springer Nature Customer Service Centre GmbH: Springer. Light: Science & Applications. [210] © 2017.
(b) Reconfigurable metadevices in the near infrared range for beam steering, with experimental angular reflectance in different states. [214] John Wiley & Sons. © 2018 WILEY-VCH Verlag GmbH & Co. KGaA, Weinheim. (c) Reversible switching using an active plasmonic metasurface and the performance of three fabricated metadevices for spin Hall effect of light, vortex generation and dynamic holography. Reproduced from [216]. CC BY 4.0.

the amorphous state and a ‘C’ image in the crystalline state in an operating wavelength from 1300–1700 nm. The proposed device is a potential candidate for all-optical switch, optical routers, and integrated optical storage. Recently, de Galarreta *et al* demonstrated multilevel control of hybrid metasurfaces by embedding GST-225 with the Si sub-wavelength resonators (figure 29(d)) [220]. The dynamic filter and modulation are exhibited at telecommunication wavelengths (1320 nm and 1550 nm) in the amorphous phase, but changes to single band configuration in the crystallization state with a modulation depth of 70% at a wavelength of 1540 nm. The external stimulus of a femtosecond laser gives reversible multilevel states of the GST layer and the capability for fine dynamic manipulation on resonant position and amplitude.

3.2. Vanadium oxide based metasurfaces

Vanadium oxide (VO_2) is a canonical transition metal oxide, which undergoes insulator-to-metal transition (IMT) from a monoclinic state to a rutile state with external thermal, electrical, or optical stimuli (figure 30(a)) [221]. The phase transition of VO_2 between insulating and metallic phase provides access to a wide range of electrical resistivity (figure 30(b)) and complex refractive index (figure 30(c)), and thus VO_2 is attractive for potential applications of active optical devices [222]. In contrast to the phase change of GST, VO_2 will return to the initial state without external stimuli. Therefore, the VO_2-phase transition process is nonvolatile and reversible. In addition, the phase transition temperature of VO_2 is typically ∼68 °C, which is much lower than the crystalline temperature of GST (∼160 °C). Due to the unique properties of VO_2, it has been widely integrated with nanostructures for active metasurfaces.

In an early (2008) demonstration of integration of VO_2 with metasurfaces, Driscoll *et al* proposed a gold split ring resonator (SRR) device on top of 90 nm thick VO_2 for dynamic tuning of resonance in the infrared range (figure 31(a)) [223]. The resonance of the SRR is sensitive to the VO_2 dielectric property due to the external stimuli (temperature). Once the temperature increases to the phase transition temperature of the VO_2 film, the SRR resonance redshifts with a 20% tuning range. Eventually, with higher temperatures, the VO_2 thin film becomes metallic and electrically shorts the SRR, and thus no optical resonance is observed above 343 K (∼70 °C). Instead of realizing the phase transition of VO_2 by external heating, Goldflam *et al* demonstrated a tunable VO_2 memory metasurface with similar SRR structure tuned by electrolyte voltage (figure 31(b)) [224]. The resonance switching is achieved by applied voltage with an ionic gel to trigger the IMT transition of the underlying VO_2 layer. Applying positive and negative voltage can selectively tune the resonance into the on/off state by driving the VO_2 into an insulating/conductive state. In 2013, Kats *et al* reported that the resonance of Y-shaped plasmonic antennas can be switched on/off or tuned with the thermally-driven IMT in the phase of VO_2 (figure 31(c)) [225]. The tunability of the mid-infrared wavelength is ∼10% (shift >1 μm at a wavelength of ∼10 μm). Such demonstration of amplitude and phase responses are promising to realize antenna-based SLMs, thermal labels, emitters, displays and related reconfigurable devices. As with the selective engineering on GST, VO_2 thin film can also be spatially defect-engineered with IMT using selective ion beam radiation in nanoscale (figure 31(d)) [226]. The periodically-patterned slits on the VO_2 film perform like a grating with different responses of incident polarizations at room temperature. The unpolarized light becomes highly polarized with a degree of linear polarization (∼90%) upon reflection from the patterned film. With the temperature above the IMT point, reflectance becomes constant with respect to various incident polarization angles due to the contrast of the VO_2 fading away.

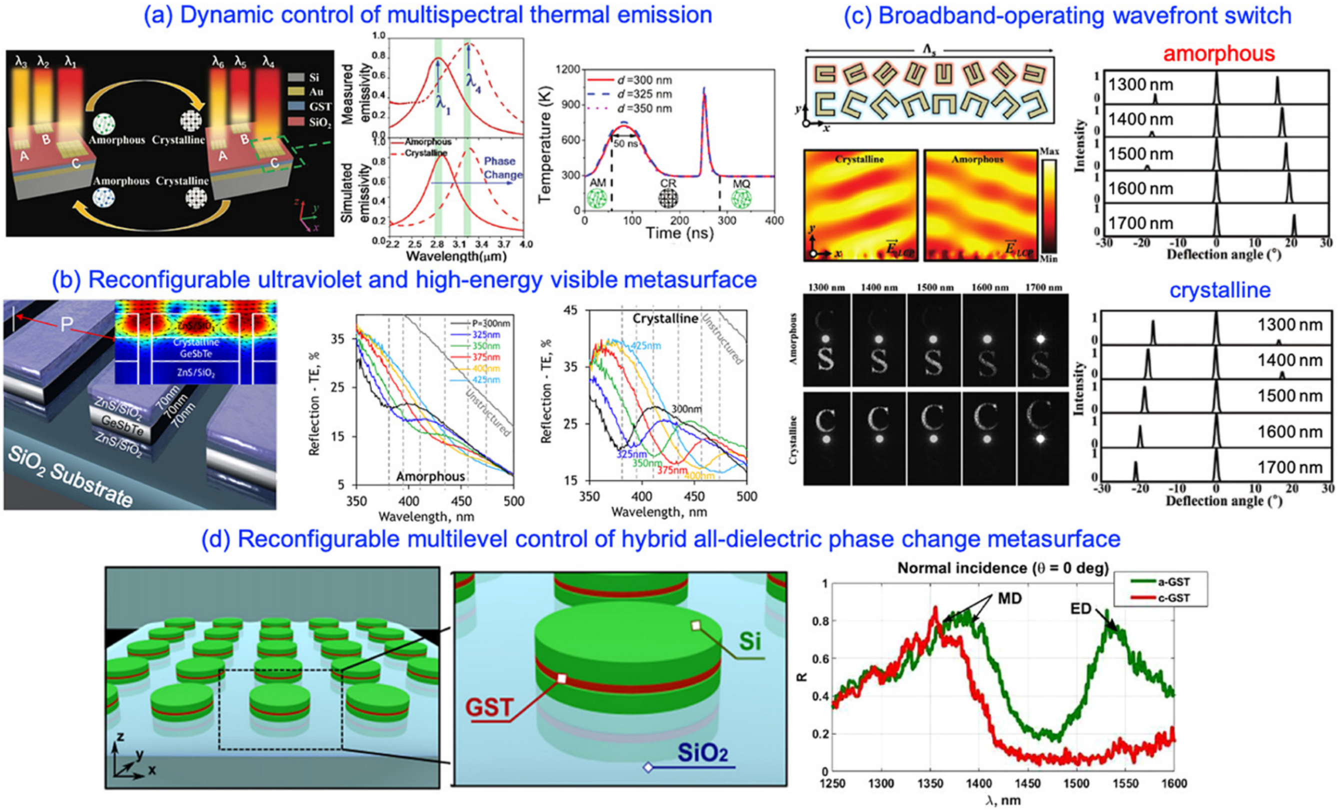

Figure 29. (a) Schematic of tunable thermal emission GST-based metasurfaces, experimentally measured and simulated emissivity of pixel C for the both amorphous and crystalline phase and time-dependent temperature distributions. [217] John Wiley & Sons. © 2018 WILEY-VCH Verlag GmbH & Co. KGaA, Weinheim. (b) Reconfigurable dielectric metasurfaces in the ultraviolet and high-energy visible and measured spectra of ZnS/SiO$_2$/GST/ZnS/SiO$_2$ grating with incident TE in reflection for selected grating periods. Reprinted with permission from [218]. Copyright (2019) American Chemical Society. (c) Supercell structure schematic of a beam steering active hologram, simulated cross electric field profile at a wavelength of 1550 nm, with the plots of Fourier plane images for beam steering and Fourier plane images for an active hologram in 1300–1700 nm in amorphous and crystalline states. [219] John Wiley & Sons. © 2019 WILEY-VCH Verlag GmbH & Co. KGaA, Weinheim. (d) Schematic and reflected spectra of hybrid all-dielectric phase change metasurfaces. Reproduced with permission from [220]. © The Optical Society.

By using the IMT, the hybrid gold–VO$_2$ nanostructure arrays can also be functionalized as a tunable near-infrared resonant absorber (figure 32(a)) [227]. The modulation of absorption is up to 70% and is 64% using hybrid gold–VO$_2$ nanowire and nanodisc arrays with linear polarized and unpolarized incident light, respectively. In 2016, Earl *et al* demonstrated a reversibly-switchable polarizer with a silver nanorods array on top of VO$_2$ thin film (figure 32(b)) [228], leading to rotation of the primary polarization axis of light in the visible wavelength. The orientation of the principal linear polarization axis of the reflected signal is rotated by 90° at the operation wavelength with reflected efficiency of 42.4% and 22.6% in the insulating and metallic VO$_2$, respectively. In 2017, Ma *et al*, presented a dynamic composite left/right-handed metasurface operating in the mid-infrared, which consists of H-shaped Au pads separated from a metallic ground plane by a thin VO$_2$ film [229]. Due to the triggered IMT by heat, both RCP and LCP modes redshifted with decreased absorbance before switching off. In 2018, a thermally-reconfigurable optical switch using an aluminum nanohole array on quartz utilizing the IMT of VO$_2$ was designed by Sun *et al* (figure 32(c)) [230]. The fabricated switch exhibits an operating bandwidth >650 nm with maximum transmission modulation of 20%, 23% and 26% in the C, L and U band respectively with an extinction ratio of ~5 dB in the operation wavelengths.

With the advancement of nanotechnology, there are various fabrication methods of VO$_2$ which benefit the integration with metasurfaces. For instance, VO$_2$ can be fabricated by ALD with conformal coating on plasmonic indium-tin-oxide nanorod arrays (figure 33(a)) [231]. The seamlessly-conformal coating enables strong interplay between the intrinsic plasmonic nanostructure and phase transition induced permittivity change of VO$_2$. It enables all-optical modulation from the visible to infrared spectral ranges. In 2018, Ligmajer *et al* presented an alternative approach for a dynamic metasurface comprised of epitaxially-grown VO$_2$ nanobeams (figure 33(b), left) [232]. Instead of extensive nano-lithographic fabrication, the large-area metasurface (>1 cm^2, with thickness of ~40 nm) can be tuned with strong transmission modulation (>9 dB) in the telecommunication band. Particularly, the transmission in 'on' state remains as high as >80% in near- to mid-infrared wavelengths (figure 33(b), right).

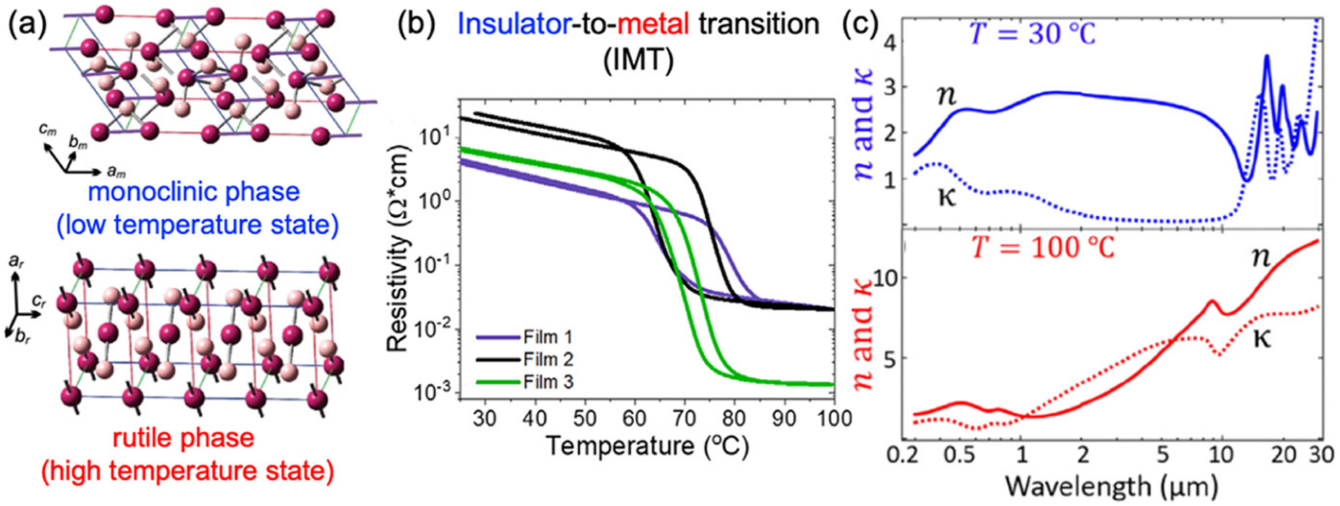

Figure 30. (a) Schematic illustration of the monoclinic phase (insulator) at low temperature and the rutile phase (metal) at high temperature of VO_2. Reprinted from [221], with the permission of AIP Publishing. (b) Resistance and (c) complex refractive index of VO_2 against the temperature [222] John Wiley & Sons. © 2019 WILEY-VCH Verlag GmbH & Co. KGaA, Weinheim.

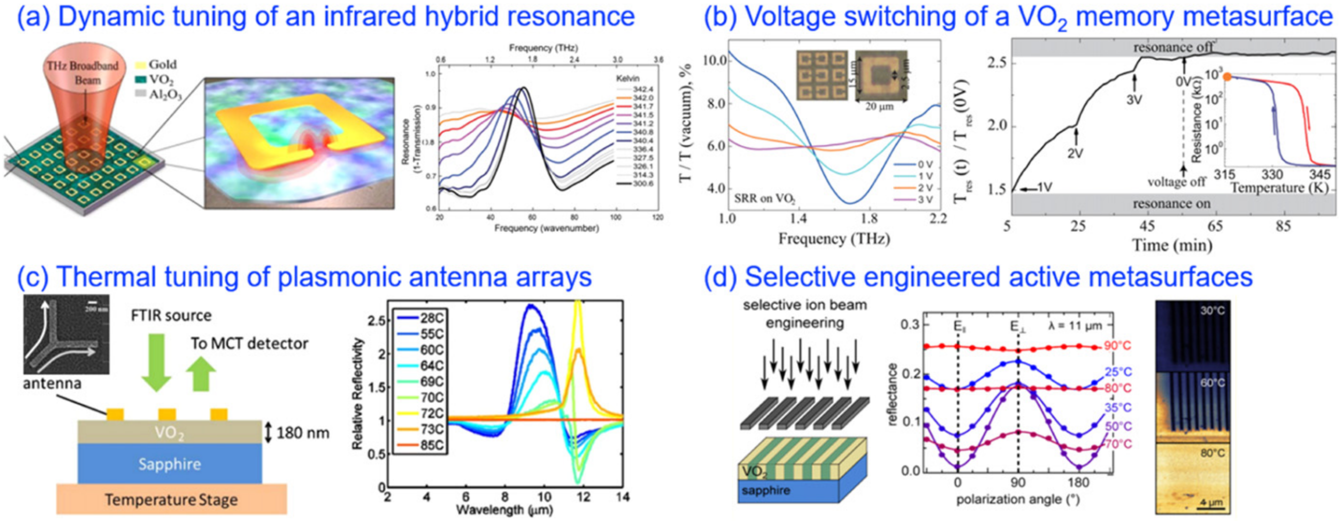

Figure 31. (a) Sketch of vanadium dioxide split ring resonator hybrid metasurfaces and dynamic tuning of the SRR resonance with temperature. Reprinted from [223], with the permission of AIP Publishing. (b) Voltage-dependent transmission of VO_2 memory metasurfaces at temperature of 315 K and time dependence on transmission change at the resonance versus positive voltage at 315 K. Reprinted from [224], with the permission of AIP Publishing. (c) Thermal tuning of plasmonic antenna arrays in mid-infrared wavelengths and reflectivity spectra of the antenna array for increasing temperatures. Reproduced with permission from [225]. © The Optical Society. (d) Spatially-selective defect engineered active metasurface with polarization-dependent reflectance at 11 μm for increasing temperature from 25–90 °C, and near-field scattering amplitude of the switchable polarizer obtained by scattering-type scanning near field infrared microscopy. Reprinted with permission from [226]. Copyright (2016) American Chemical Society.

The phase transition of VO_2 can be also triggered in an electrically controllable fashion. Hashemi *et al*, reported a strategy for making tunable metasurfaces. They were able to deflect the phase front via a 2D array of resonant metasurface unit elements embedded with electrically-tunable VO_2 (figure 34(a)) [233]. The proof-of-concept device offers a phase shift of 59°, transmitted intensity modulation of 50%, and beam deflection of 44° in horizontal and vertical directions. In 2017, Zhu *et al* demonstrated a dynamically reconfigurable metadevice capable of spectral control by placing VO_2 at the feed gap of a bow-tie field antenna (figure 34(b)) [234]. The device has a measured tuning range of ∼360 nm in near infrared range, a modulation depth of 33% at resonance, fast switching (with modulation speed of 1.27 ms), and precise spatial control with 21 nJ switch energy per pixel. In 2018, Takeya *et al* demonstrated the photodetection of a stoichiometric VO_2 thin film integrated with silver nanorods (figure 34(c)) [235]. The nanorods convert light to heat and suppress the resistivity of the VO_2 via localized surface plasmon resonance (LSPR). Incorporation of the thermo-plasmonic effect into bolometric photodetection allows for wavelength and polarization sensitivity. Recently, Kim *et al* reported a dynamical metasurface capable of continuous phase modulation in the near-infrared region with a VO_2 active film integrated into

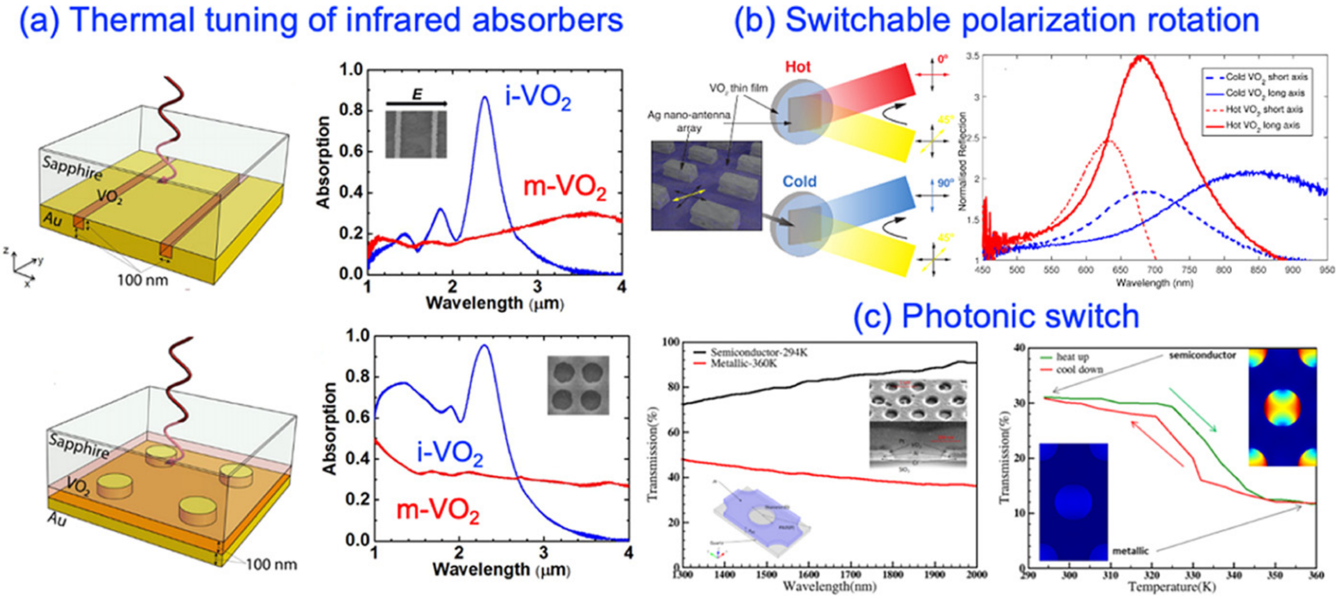

Figure 32. (a) Schematic representations and measured spectra of grating and cylinder hybrid gold–VO_2 design. Reprinted from [227], with the permission of AIP Publishing. (b) Visualization of switchable polarization rotation and normalized reflectance for 45° incident light for the analyzing polarizer with both parallel (solid lines) and orthogonal (broken lines) to the long axis of the rods. Reprinted from [228], with the permission of AIP Publishing. (c) Measured transmission spectrum of pristine VO_2 layer and temperature hysteresis of the photonic switch in transmission at a wavelength of 1550 nm. Reprinted by permission from Springer Nature Customer Service Centre GmbH: Springer. Scientific Reports. [230] © 2018.

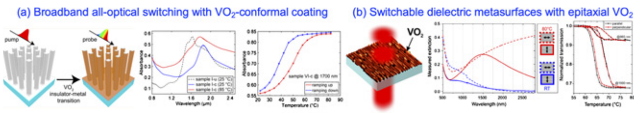

Figure 33. (a) (Left) Schematic of broadband all-optical switching with VO_2-conformal coating, (middle) Fourier-transform infrared spectra of ITO rods array before coating (sample I-u) and after coating (sample I-c) at 25 °C and 85 °C, and (right) temperature-dependent absorbance of VO_2-coated ITO nanorod arrays at a wavelength of 1700 nm. Reprinted with permission from [231]. Copyright (2016) American Chemical Society. (b) (Left) Schematic and AFM images of switchable metasurfaces with epitaxial VO_2 nanostructures, (middle) extinction spectra with incident polarization parallel (dashed lines) and perpendicular (solid lines) with nanobeams, and (right) hysteresis in transmission at wavelengths of 965 nm and 1500 nm for polarized light parallel and perpendicular to nanobeams. Reprinted with permission from [232]. Copyright (2018) American Chemical Society.

the dielectric gap of antenna (figure 34(d)) [236]. By electrically controlling the volume fractions of dielectric and metallic states in the VO_2 film, they obtained a continuous phase shift of 250° in reflected light with a modulation in reflection of 23.5% and a resonance shift of 175 nm. The response time of this VO_2-based metasurface is ∼15 ms for 'on' and ∼100 ms for 'off' states, respectively, which can be improved by the optimization of thermal engineering. Recently, Howes *et al* demonstrated a Huygens metasurface (silicon rod array) capped with a VO_2 layer (figure 35(a)), which enabled on-state transmission (−4.8 dB) at an operation wavelength of 1.24 μm and large turndown ratio (7.7 dB) by ultrafast laser as the optical limiter (figure 35(b)) [237]. The incident intensity for the VO_2 phase transition temperature (67 °C) is 3.2 kW cm^{-2} and the relaxation time (cooling from metallic to semiconducting state) within ∼1 ps (figures 35(c) and (d)). Note that there are several comprehensive simulation works on active metasurfaces based on the phase transition of VO_2, such as dynamic wave-front engineering [238], a tunable optical switch [239] in near-infrared spectral regime, a reflective polarization converter [240] and a switchable metalens [241].

Combining the phase-change materials with metasurfaces is a rising direction that gives high-contrast, near-infrared, electronically-, optically-, and thermally-addressable switching or modulation. Especially for GST, the technological importance lies in the broad availability of the material family with different compounds, which offers non-volatile change between the amorphous and crystalline phases. The large refractive index change in the entire active layer ($\Delta n \approx 2$ in near infrared and mid-infrared range) during the phase change offers opportunities for stable, dramatic light modulation in amplitude and phase. On the other hand, VO_2 has the volatile phase transition. However, there is room for improvement on the modulation speed for both phase-change materials. Up to now, the demonstrated switching frequency for dynamic metasurfaces is relatively low (up to 1 kHz) due to the constraints of electrically- and thermally-induced phase change/transition. The optical stimuli via laser pulse gives decent modulation for the individual unit element but it is energy- and time-consuming to alter the whole metasurface. In addition, the required external laser makes it less compatible for compact device applications. Recent work demonstrated that the cooling from metallic to semiconducting state of VO_2 is $<\sim$1 ps [237], which is a new modulation speed record for a phase change/transition material.

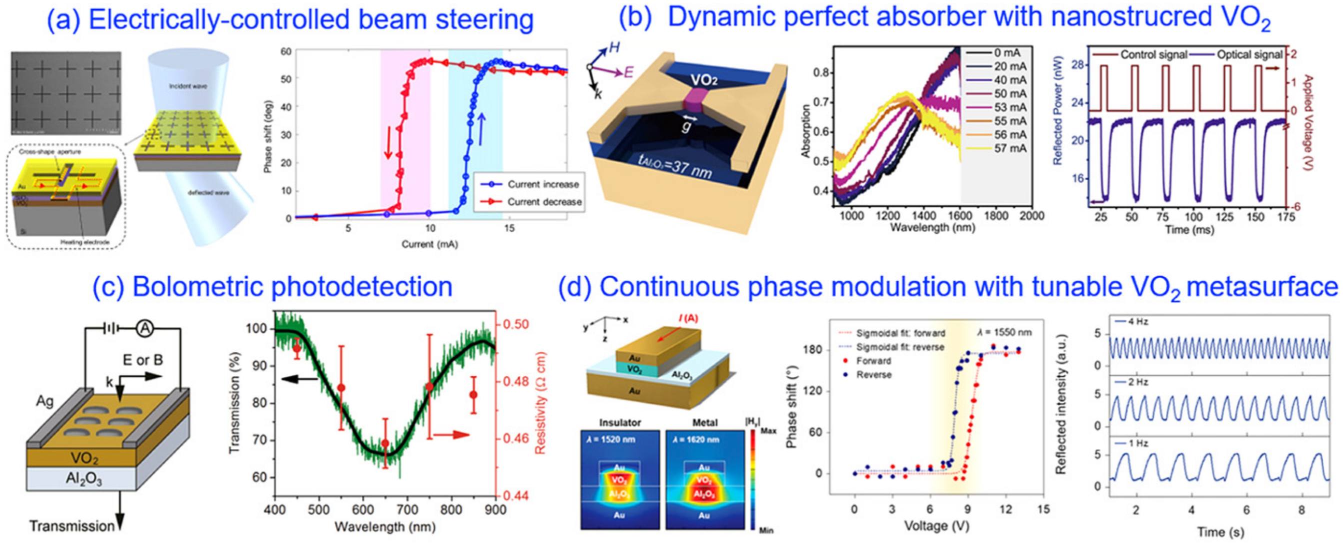

Figure 34. (a) Schematic of an electrically-controlled beam-steering metasurface and measured phase response versus the applied current. Reprinted by permission from Springer Nature Customer Service Centre GmbH: Springer. Scientific Reports. [233] © 2016. (b) Sketch of the dynamic perfect absorber structure. Measured absorption spectra versus input current, trigger signal and monitored reflection over multiple modulation cycles. Reprinted with permission from [234]. Copyright (2017) American Chemical Society. (c) Schematic of a VO$_2$ bolometer integrated with silver nanorods and (left) its measurement configuration, (right) measured transmission and resistivity versus wavelength. Reprinted by permission from Springer Nature Customer Service Centre GmbH: Springer. Scientific Reports. [235] © 2018. (d) Schematic of an electrically-tunable VO$_2$ metasurface unit element, continuously tunable phase shift versus applied voltage, and measured temporal response at a wavelength of 1550 nm. Reprinted with permission from [236]. Copyright (2019) American Chemical Society.

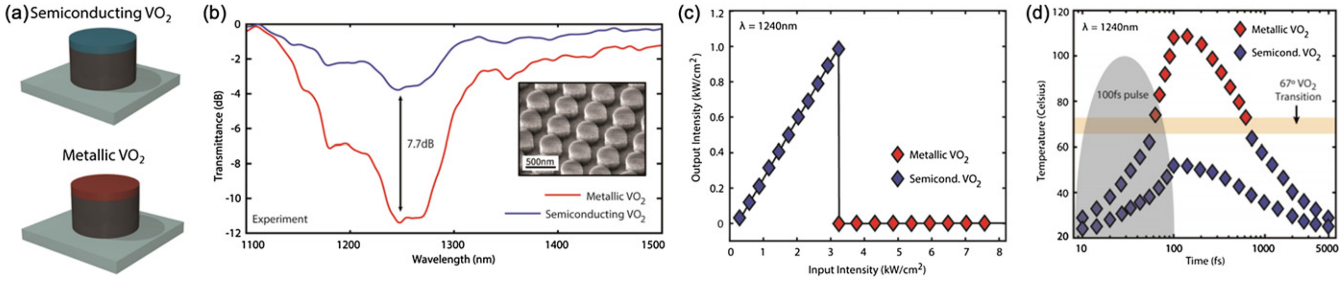

Figure 35. Optical limiting based on VO$_2$–Huygens metasurfaces. Reprinted with permission from [237]. Copyright (2020) American Chemical Society. (a) Schematic of VO$_2$–Huygens metasurfaces for optical limiting. (b) Measured transmittance of the limiter in the on and off states. (c) Nonlinear response of the output versus input intensity. (d) Temporal thermal characteristics of the optical limiter.

Overall, the phase change/transition mechanism provides significant potential for practical applications in novel metasurface devices, for instance all optical switching, thermal modulation, beam steering devices, bifocal lens and reconfigurable display and holograms for imaging, sensing, and communication technologies.

4. Active metasurfaces via nano-mechanical structural reconfiguration

The electromagnetic properties of a metasurface can also be modified by reconfiguring the structures of its building blocks. This can be realized by changing the balance of forces at micro/nanoscale. Various types of forces acting at micro/nanoscale between the constituting unit elements defining the metasurface, such as the electrostatic force (Coulomb force), magnetic forces (Lorentz and Ampère forces), optical force, or thermal stimulation (figure 36), have been used to modify the distances between the adjacent elements or to deform the elements and hence dynamically change the geometry of the metasurface. As the size of the unit cell decreases, these externally-induced micro/nano-scale forces grow in magnitude and strongly compete with the restoring elastic forces, which decrease with decreasing structural dimensions. Due to an unbalance between these mutually competing forces (externally excited vs. restoring), the metasurface geometry can be tuned, and, consequently, their optical response (reflection, transmission, and/or absorption) can be modulated. Therefore, precise dynamic tuning of the optical response of a metasurface can be achieved by controlling these micro/nano-scale forces precisely using external stimuli such as electric field, magnetic field, electric current, heating/cooling, or electromagnetic field. More details related to

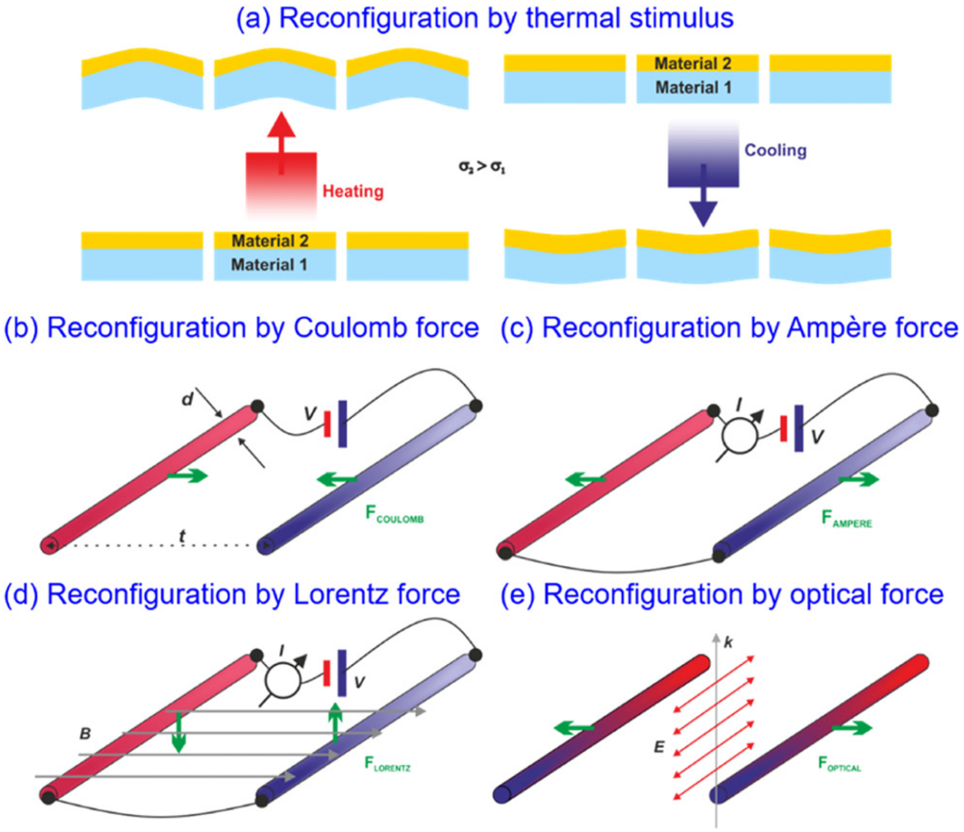

Figure 36. (a) Mechanism of thermally-reconfigurable metasurfaces. Reprinted with permission from [243]. Copyright (2011) American Chemical Society. (b)–(e) Forces acting on a pair of nanowires. The pair of nanowires can be considered as unit element of a metasurface. These forces at the nanoscale can be exploited for reconfiguration of the metasurfaces with (b) Coulomb force [244], (c) Ampère force [245], (d) Lorentz force [246], and (e) optical force [242].

reconfigurable metasurfaces based on the mechanical reconfiguration of nano-cantilevers or nanorods via different forces can be found in a recent review paper [242].

Microelectromechanical systems (MEMS) or nanoelectromechanical systems technology are some of the most promising techniques for dynamic reconfiguration of metasurfaces, where the building blocks of the metasurface can be reconstructed by micro/nano actuators through electrostatic, electromagnetic, piezoelectric, and electrothermal actuation. These micro/nano-actuators can transform electrical signals into mechanical actuations, hence reconfiguring the structure geometry. Figure 37 shows a schematic illustration of an example of electrostatic micro-actuators that consists of an array of curled actuator fingers which are connected to the ground electrode and a bottom electrode separated by an insulation layer between these two electrodes [247]. When applying an electrical bias, the actuator fingers can be pulled down by the acting electrostatic forces, which at higher voltages will be further pulled to a maximum position in which the fingers become flat. The actuator fingers will curl up back to their previous positions once the electrical bias is removed [247]. Such electrically-controllable micro-movements thus enable precise control of the functions of the MEMS components.

Figure 38(a) represents a thermo-mechanical reconfigurable metasurface operating in the THz regime, consisting of a SRR array integrated on cantilevers. In this structure, significant tuning of both the electric and magnetic response was obtained by bending the cantilevers upwards out of the plane under the thermal stimuli, leading to a large transmission modulation (∼70%) at a frequency of 0.5 THz [248]. The use of electrostatic forces to deform the lattice structure of metasurfaces offers another feasible approach to tailor their optical properties due to the near field coupling between adjacent unit cells. Figure 38(b) shows an example of a reconfigurable metasurface driven by electrostatic force. The meta-unit of the proposed metasurface contains two identical aluminum resonators, one located on an isolated substrate, the other one on a frame substrate. The permeability of this metamaterial can be tuned from −0.26 to 0.29 at ∼2 THz at the time scale of ∼500 μs [249]. Zhu *et al* reported a terahertz metamaterial with tunable anisotropy. The structure can be tuned between the anisotropic and isotropic state by MEMS-based actuators. Phase change with a magnitude of ∼30° and large transmission modulation up to 120% were demonstrated (figure 38(c)) [250]. Figure 39(a) shows a reconfigurable terahertz metasurface, composed of electromechanically-actuated micro-cantilever arrays, which functions as a quarter-wave plate. A large tuning range of the resonance frequency up to ∼230 GHz is demonstrated under the electrostatic actuation. High transmission modulation up to 34% and large phase change with a magnitude of 85° was achieved at a frequency of 0.81 THz [251]. Figure 39(b) shows tuning in the THz

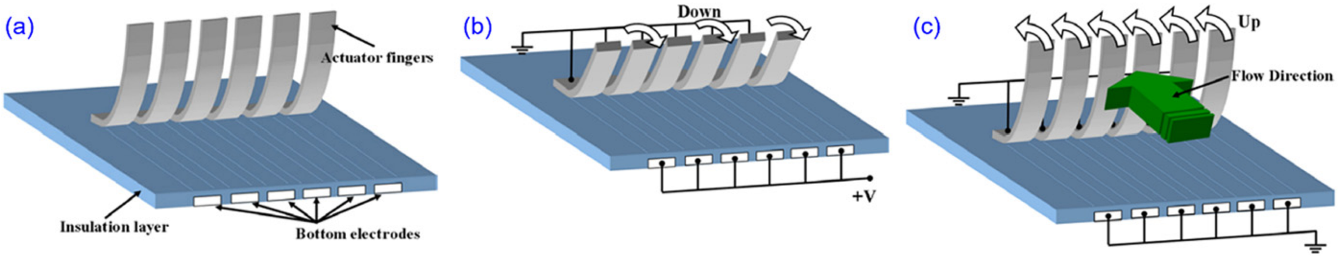

Figure 37. Schematic of a micro-actuator operated by the electrostatic force. Reproduced from [247]. © IOP Publishing Ltd. All rights reserved. (a) Overview of the structure. (b) The fingers are bending down under bias voltage. (c) The fingers return to their original position once the bias is removed.

(a) Reconfigurable metasurface by thermal stimulus

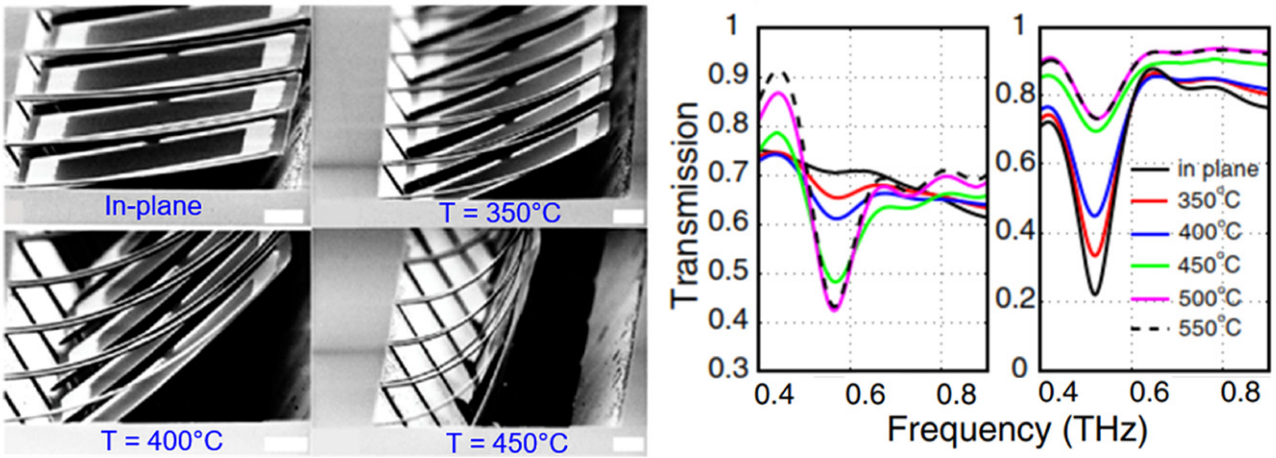

(b) Switchable magnetic metasurface (c) Maltese-cross metasurfaces with tunable THz anisotropy

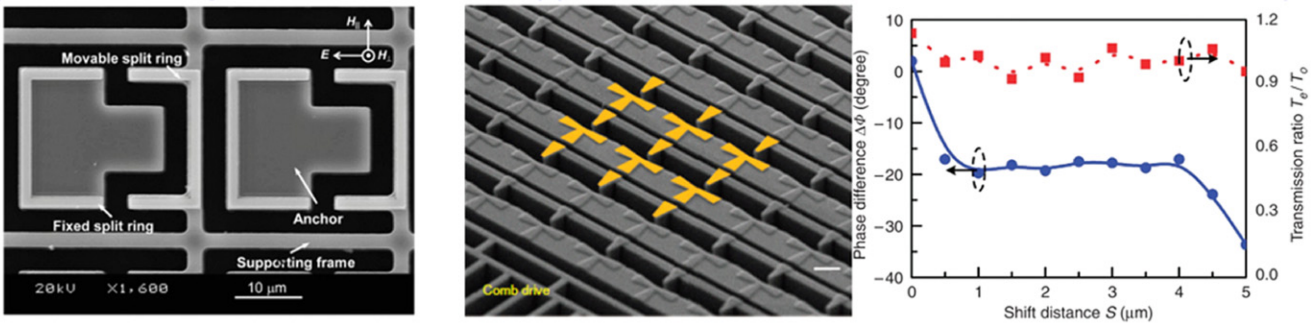

Figure 38. MEMS-based reconfigurable metasurfaces working at the THz frequency. (a) Split-ring-resonators based thermally reconfigurable metamaterial bended at different temperatures. Reprinted figure with permission from [248], Copyright (2009) by the American Physical Society. (b) Switchable magnetic metamaterial via micromachined actuators. [249] John Wiley & Sons. © 2011 WILEY-VCH Verlag GmbH & Co. KGaA, Weinheim. (c) Microelectromechanical Maltese-cross tunable metasurface. Reprinted by permission from Springer Nature Customer Service Centre GmbH: Nature Communications. [250] © 2012.

regime, with a T-shaped metasurface with out-of-plane movable microstructures [252]. By gradually increasing the electrical bias, the cantilevers could be continuously bent toward the substrate due to the increasing magnitude of the electrostatic forces. Tuning of the resonant frequencies by 0.27 THz and 0.50 THz for TM and TE polarized incidence could be achieved experimentally. Furthermore, Zhang *et al* experimentally demonstrated control over both transmission and reflection at 0.76 THz and 1.16 THz respectively, with a metasurface consisting of an aluminum split-ring-resonator and two free-hanging Si slabs (figure 39(c)) [253]. A change in reflection of 59% and 34%, respectively, at these two frequencies was achieved by dual mode resonance switching because of the metamaterial reconfiguration. Figure 39(d) shows a micro-ring metamaterial operating in the THz regime. In this structure, the polarization-dependent state can be switched to a polarization-independent state by reconfiguring the lattice of the metamaterial. By doing this, shifts of the resonant transmission up to 25.8% for the TE polarized incident and 12.1% for the TM polarized incident were achieved [254]. Most active metasurfaces operate in a single-input–output design; however, achieving multiple controls of metasurfaces will

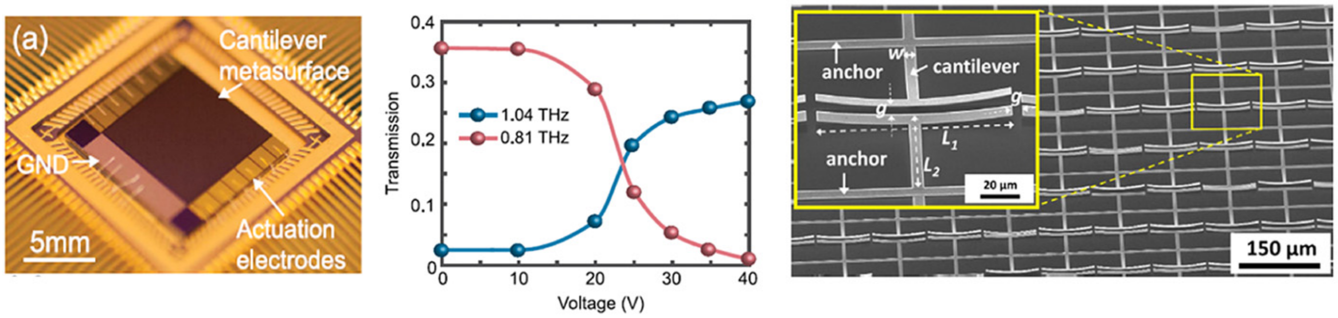

(a) Reconfigurable metasurface waveplate

(b) T-shaped terahertz metasurface

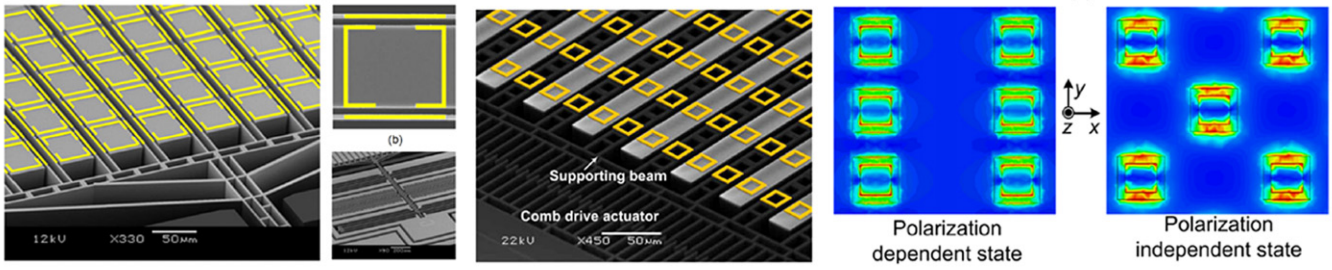

(c) Dynamic dual mode switching

(d) Polarization dependence tunable metasurface

Figure 39. MEMS-based reconfigurable metasurfaces working at the THz frequency regime. (a) Tunable metasurface functioning as transmission waveplate, and the electromechanical modulation of the transmission amplitude. Reproduced with permission from [251]. © The Optical Society. (b) SEM image of a T-shaped metasurface with building blocks that can be reconfigured by electrostatic forces. Reprinted from [252], with the permission of AIP Publishing. (c) SRR-based electrostatic reconfigurable metasurface supporting dual-mode resonances. Reprinted from [253], with the permission of AIP Publishing. (d) Micro-ring metamaterial for polarization control using micromachined actuators. Reprinted from [254], with the permission of AIP Publishing.

facilitate the development of extremely versatile devices in which multi-valued correlations are established between the input controls and the output response. To this end, Manjappa *et al* demonstrated a reconfigurable MEMS metasurface exhibiting multiple-input–output states. Their device was composed of two split ring resonators, which can be independently controlled by two bias voltage channels, respectively, to increase and/or decrease the out-of-plane asymmetry of the metasurface resonator. Such variation of anisotropy gives rise to the hysteresis loop of the systems, allowing for the formation of multiple-input–output characteristics of the metasurface, which can be used for logic operations in THz frequencies [255].

Further extending the operational frequency region of the reconfigurable metasurfaces from the long wave regime to the optical regime will require improved tuning of the nanoscale inner unit elements. Advancement of fabrication technologies in the last several years has helped to overcome this issue. Liu and Padilla demonstrated a tunable thermal emitter in the mid-infrared regime based on an MEMS metasurface (figure 40(a)) [256]. In this structure, electrostatic force is employed to actuate the device for the control of the free-standing parts. By doing this, the energy emitted from the surface can be tailored at a modulation speed up to 110 kHz. The modulation index of this structure is ~23.7%. Figure 40(b) shows a metalens integrated onto a two-dimensional scanning MEMS platform. The angular rotation of the integrated metalens can be electrically controlled by the movements of the MEMS elements, tuning the angle of the focal line up to 2.5° [257]. Miao *et al* reported a tunable metasurface which is composed of an array of three-dimensional nano-split rings as the meta-element. The unit cells can be deformed in multiple directions under the injection of currents (figure 40(c)). In this way, the device can be switched between a closed and an open state, leading to the shift of the resonance absorption between the long wave ($\sim$10.4 μm) and the mid infrared ($\sim$6.3 μm) region with a modulation depth up to 95% and a phase tuning of 260° [258]. Figure 40(d) depicts an example where thermal reconfigurability is exploited to experimentally demonstrate a smart mid-infrared metasurface, which can passively control its own temperature [259]. A difference of emissivity of >30% was achieved due to thermal stimulus-induced reconfiguration.

For the near-infrared regime, Qu *et al* constructed a reconfigurable metasurface composed of alternating straight- and meandering-patterned gold nanowires manufactured on a Si_3N_4 membrane (figure 41(a)) [260]. When an electrical bias of a few volts is applied to the neighboring strings, they attract each other by an electrostatic force of magnitude of a few nanonewtons. As a result, the strings move closer to each other in the plane of the metasurface, modifying the excitation condition for the plasmonic mode supported by the meandering pattern, and consequently the resonant optical response of the metasurface. Reversible transmission and a reflection change with a maximum of 8% modulation depth and with megahertz bandwidth were demonstrated on application of an electrical bias up to 2.4 V (figure 41(a)). Furthermore, high-contrast (transmission change of $\sim$250% at a wavelength of 1.2 μm and reflectivity change of 110% at a wavelength of 1.6 μm) irreversible switching of the

(a) Reconfigurable metasurface mid infrared emitter

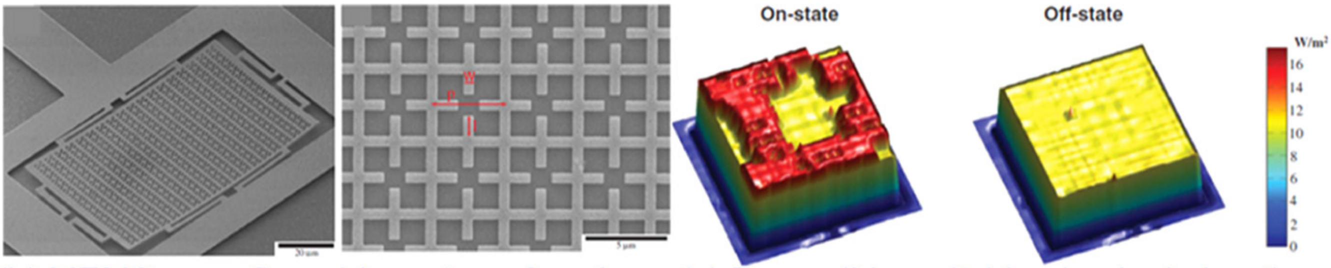

(b) MEMS reconfigurable metasurface lens

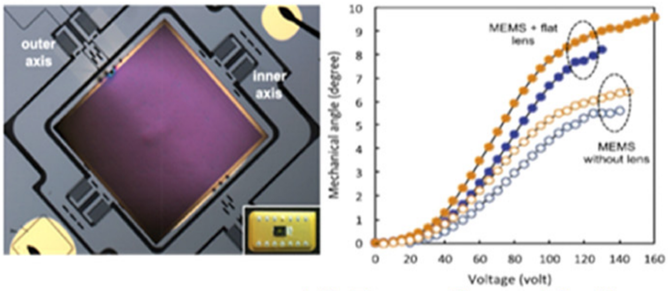

(c) Reversible switching by Joule heating

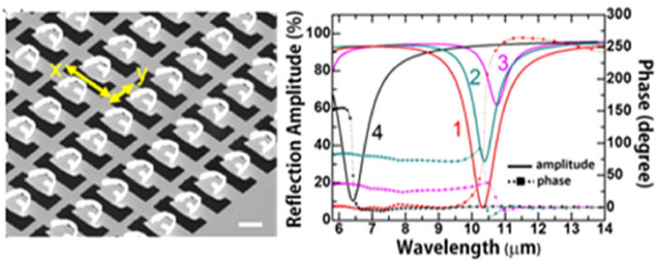

(d) Reconfigurable thermochromic metausrface

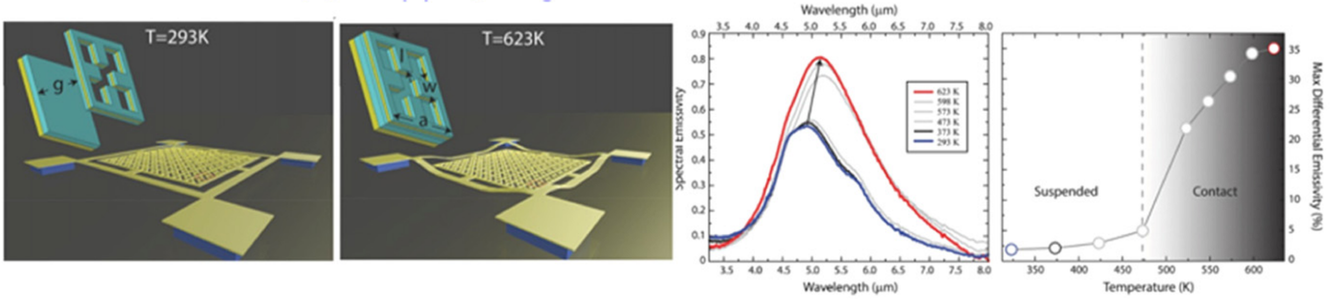

Figure 40. Nano-structural reconfigurable metasurfaces working in the mid-infrared. (a) Tunable emitter based on metamaterial and its emitted power density at on and off state. Reproduced with permission from [256]. © The Optical Society. (b) Optical microscope image of a metalens integrated with MEMS scanner and angular displacement of the MEMS scanner under different bias. Reprinted from [257], with the permission of AIP Publishing. (c) Tunable metasurface based on SRRs array and the dependency of reflectance response under different currents. Reprinted with permission from [258]. Copyright (2016) American Chemical Society. (d) A thermochromic metasurface working in the mid infrared. The blue and the red curves show emission spectra for temperatures of 293 K and 623 K. The right-most curve shows maximum difference of emissivity as a function of temperature. [259] John Wiley & Sons. © 2016 WILEY-VCH Verlag GmbH & Co. KGaA, Weinheim.

metasurface could be achieved without any external polarizer/analyzer. The effective electro-optical coefficient of such a metasurface is typically $\sim 10^{-5}$ to 10^{-6} m V^{-1} which is several orders of magnitude higher than that observed in a natural electro-optic media such as lithium niobate (3×10^{-11} m V^{-1} at a wavelength of 633 nm). A similar tuning mechanism was utilized in a metasurface absorber showing a very high switching contrast of 1500% at a wavelength of 2.1 μm [261]. Thermal stimulus has also been exploited to reconfigure and/or tune a metasurface in the near infrared. In this regard, Qu *et al* reported a reconfigurable photonic metamaterial, where plasmonic split rings resonators (SRRs) are placed on a thermally-reconfigurable bi-material scaffold (figure 41(b)) [243]. The structure was constructed with two strings. One string (asymmetric bi-layer) of the pair exhibits temperature-dependent deformation while the other string (symmetric tri-layer) remains intact. Heating causes relative displacement of the neighboring strings which results in a change in the electromagnetic coupling of the adjacent SRRs. Up to 50% transmission change was demonstrated in the spectral range from 1200 nm to 1700 nm by increasing the temperature from 76 K to 270 K. Furthermore, the change in the optical properties was found to be reversible. However, note that such type of tuning mechanism is relatively slow.

Nanomembrane-based metasurfaces can also be reconfigured by engaging Lorentz forces. The first reported work where the structural reconfiguration in the near-infrared is carried out by F_{Lorentz} was based on a chevron nanowire structure fabricated on an elastic membrane (figure 41(c)) [246]. Upon simultaneous application of external electric and magnetic fields, the metasurface exhibited strong magneto-electro-optical effects that caused changes of its optical properties. The chevron nanowire array was constructed with gold where the alternating wires were electrically connected to the electrical terminals at both ends. Hence, the electric field applied across the array induced a current I in every second wire.

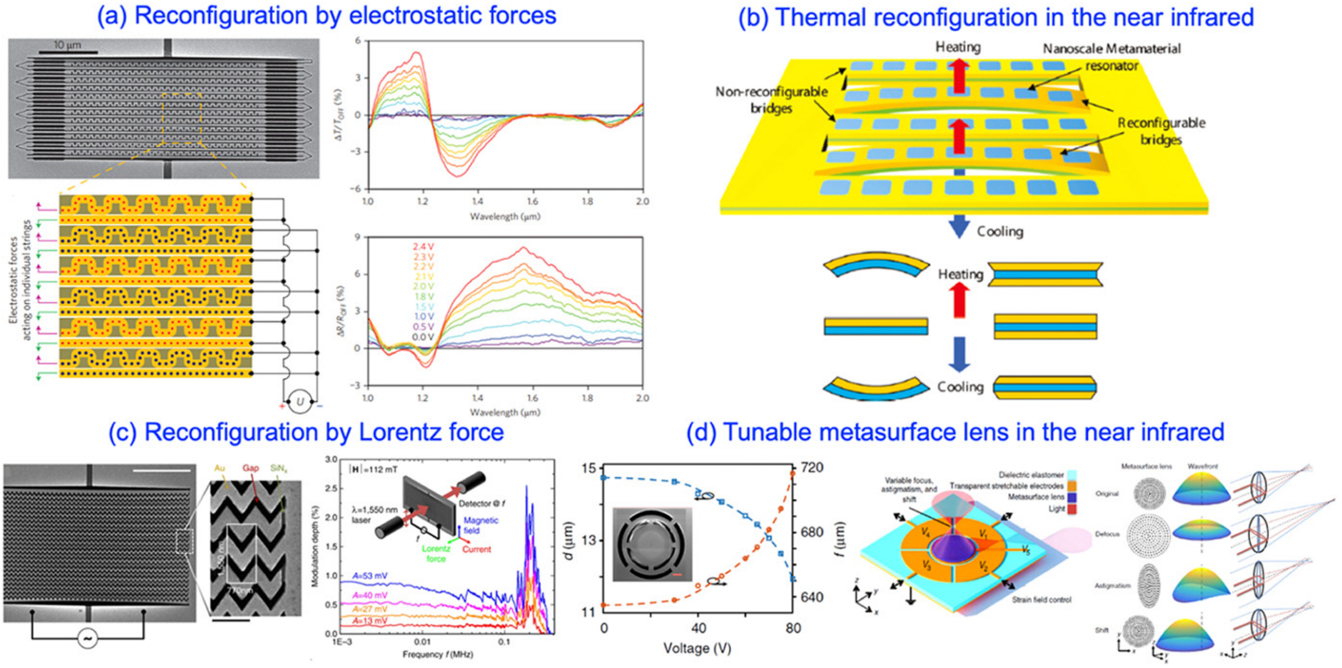

Figure 41. Nano-structural reconfigurable metasurfaces in the near-infrared. (a) (Left) Electromechanically-tunable metasurface placed on a silicon nitride membrane. (Right) The transmission and reflectance of the device under different biases. Reprinted by permission from Springer Nature Customer Service Centre GmbH: Nature Nanotechnology. [260] © 2013. (b) Thermally-controlled reconfigurable photonic metamaterial and its transmission at different temperature. Reprinted with permission from [243]. Copyright (2011) American Chemical Society. (c) (Left) A membrane-based magneto-optical modulator: nanowire structural reconfiguration by the Lorentz force. Reproduced from [246]. CC BY 4.0. (Right) Modulation of transmission spectra for different electrical biases at a fixed magnetic field of 112 mT. (d) (Left) A MEMS-based tunable lens in the infrared region and the dependency of the focal length of the tunable lens on the applied bias. Reproduced from [265]. CC BY 4.0. (Middle and right) A tunable metalens fabricated on artificial muscles-based dielectric elastomer actuators, and the dependency of its focal length and astigmatism on the applied bias. From [266]. Reprinted with permission from AAAS.

Several hundreds of modulation frequencies could be achieved in the near infrared, and the effective magneto-electro-optical susceptibility χ, reached $\chi_{yyxy}/n \approx 10^{-4}$ mV^{-1} T^{-1}, where n is the refractive index of the wire material. This remarkable magneto-electro-optical effect, which is not attainable in natural materials, caused a maximum transmission modulation of 2.5% with an electrical bias of only 53 mV and a magnetic field of 112 mT (figure 41(c)). Moreover, the reconfigurable properties were reversible. In another work with a similar type of structure, electrically-controlled transmission changes of up to 50% at sub-milliwatt power level were realized [262]. Magneto-electro-optical modulators and field sensors at nanotesla levels could be realized via optimizing the design of the metasurface. Optical forces in the membrane-based metasurfaces also become significant in the near-infrared and allow reconfiguration driven by light which leads to optical nonlinearity. Optical force-activated reconfiguration using an all-dielectric optomechanical metasurface was theoretically predicted by Zhang *et al* [263]. Later, an experimental demonstration exhibiting optomechanical nonlinearity allowing optical modulation of light at a frequency of 150 MHz with an all-dielectric metasurface was reported. Metasurfaces based on plasmonic nanoantenna were also exploited to achieve tunability based on optical force-actuated reconfiguration. Qu *et al* used π-shaped resonators made with horizontal and vertical bars of gold placed on top of adjacent silicon nitride strips to achieve optical reconfiguration in the near-infrared at milliwatts power level. At higher pump frequencies (>100 kHz), the optical forces on the gold bars dominate over heat-induced forces. Hence, a net repulsion force acts between adjacent strips along the in-plane direction (figure 36(e)), reconfiguring the structural geometry of the unit cell and in turn changing the optical properties of the metasurface. Plasmonically-enhanced nano-optomechanical nonlinearity can be as strong as $\chi^{(3)}/n^2 \approx 10^{-12}$ m^2 V^{-2}. Furthermore, the nonlinear response time can be three orders of magnitude faster than what could be anticipated from the universal trend linking the response speed and the magnitude of $\chi^{(3)}$ nonlinearities [264]. Figure 41(d) (left) shows a tunable dielectric metasurface lens which can be controlled by the integrated MEMS device. In this structure, the relative positions of two pieces of the metasurface lenses can be tuned by applying voltages. As a result, the effective focal length of the metalens can be changed from 672 μm to 824 μm at an operation wavelength of 915 nm, with a high absolute focusing efficiency of 40%–45% throughout the tuning range. Moreover, such a tunable metalens can be operated at a modulation speed up to 4 kHz [265]. Figure 41(d) (middle and right) shows a tunable large area metalens at an operation wavelength of 1550 nm, fabricated on artificial muscles-based dielectric elastomer actuators. This tunable metalens has a high efficiency (~62.5% throughout the tuning range) and a large focal length modulation (as high as 107%). The total thickness of this device is only 30 μm with a fast operation speed with a response time of ∼33 ms [266].

Recently, nano-structural reconfigurable metasurfaces have been further demonstrated in the visible. Holsteen *et al* reported tunable metasurfaces with various functions, of which the pixels can be individually controlled to impose a complete 2π phase control and a large amplitude modulation [267]. In their structure, Mie-type resonators are suspended using the Si-on-insulator technology. The metasurfaces can be tuned mechanically by the MEMS part. Figure 42(a) shows the structural color tuning of a letter 'S' under different voltages as a demo of the color tuning function. Moreover, the arrays of the metasurface with different widths can continuously impose phase shifts to the scatting light in a complete 2π range, allowing dynamic wavefront shaping. The beam steering performance of the metasurface can continuously deflect the incident light from 2° to 12° under different voltages (figure 42(b)) [267]. Furthermore, a tunable metalens is also demonstrated by this technique (figure 42(c)). By applying a voltage up to 2.2 V, the focal length of the metalens can be tuned from 26–5 μm at a wavelength of 600 nm [267]. Note that the operation speed of the demonstrated metalens is very fast due to the compactness of the metasurface pixels (up to 1 MHz). Thermal stimulus was also exploited to tune the response of metasurfaces in the visible. In a work by Karvounis *et al*, a whopping change in relative transmission of 197% at a wavelength of 654 nm was demonstrated from a metasurface constructed by subwavelength nanowires made of $MoS_2/MoO_{3-x}/Si_3N_4$ (figure 42(d)) [268]. The giant tunability of this device results from stress-induced structural deformations and a stress-induced large change in the refractive index of the MoS_2. Moreover, by using a faster heating/cooling rate of $\sim$15 K min^{-1}, a hysteretic behavior of the transmission was observed. A maximum difference in optical transmission of 45% between the two states could be achieved at a wavelength of 675 nm.

The integration of a metasurface with MEMS technologies for active modulation offers several advantages, including low power consumption, large modulation depth, and the possibility of individual control of meta-atoms even in the visible. Impressively large phase modulation up to 2π is also demonstrated in the visible. However, it is technically challenging (and has not been demonstrated so far) to individually pixelize each meta-resonator with nanoscale dimension and thickness for multi-functional tunable MEMS metasurface devices. In addition, the current MEMS-based active metasurfaces are limited by their relatively slow modulation speed in the range from kHz to MHz, which is much slower than reported tens of GHz modulation speeds of the other mechanisms, such as electrical injection of free carriers. However, the modulation speed of the MEMS-based active metadevice might already meet the requirements of certain practical applications, for instance a tunable metalens where kHz modulation speed would be acceptable. Therefore, the MEMS-based active metasurface is still one of the most promising mechanisms to further develop for reconfigurable metasurface devices. On the other hand, nanomechanical metasurfaces, which allow for dynamic light modulation in ultracompact nanoscales, also have potential for reconfigurable metasurface devices. Note that the recent advancement of high refractive index dielectric/semiconductor resonators, which have the advantage of much lower loss and larger optical force as compared to plasmonic nanostructures, have very significant promise for practical applications. Moreover, the emerging diamond membrane, which features higher mechanical resonances as well as superior thermal properties over the silicon and silicon nitride membranes, will be a promising candidate as supporting structures, enabling the significant performance improvement of an MEMS system.

5. Flexible metasurfaces

Another promising technique to realize a functional tunable metasurface is to embed nano-antennas on a flexible substrate. The performance of nano-antennas imbedded on elastic substrates is highly sensitive to structural parameters. By mechanically stretching a flexible metasurface, the periodicity (space between resonators) can be precisely changed (figure 43). This affects interaction between neighboring resonators and can be used to manipulate the resonant wavelength as well as phase. This enables large resonance tunability and can be applied to sense small changes in dimensions [269, 270]. Flexible metasurfaces with tunable plasmonic and diffractive properties have been demonstrated with flexible substrates [271–274]. The performance of flexible metasurfaces depends strongly on the choice of substrate. An ideal flexible substrate has a low refractive index (typically $n = 1.43$) and low loss to maintain high transmittivity and resonance strength [275]. It should also possess low Young's modulus to exhibit high flexibility and elasticity. Thus, polymers like polydimethylsiloxane (PDMS), polymethylmethacrylate, and polystyrene are preferred as the flexible substrates [271]. Flexible tunable metasurfaces have been demonstrated to introduce new aspects and functionalities of optical devices such as highly tunable metasurface lenses [272], flexible absorbers in terahertz frequencies [265, 276], tunable diffraction gratings [277], and highly sensitive sensing devices [269]. In addition, flexible metasurfaces can be conformally applied on curved surfaces which could enable novel applications such as a flexible display and an integrated sensor on human body [278, 279].

Mechanical deformation of a flexible substrate by modifying the spacing between the resonant elements has been demonstrated since 2010. Pryce *et al* demonstrated a highly tunable SRR coupled with a nanowire resonator with resonant wavelength shift of 400 nm [270, 280]. When the substrate is mechanically stretched, the neighboring resonators are pulled apart, modifying both the capacitance of the SRR gap and the coupling strength between neighboring resonators, thus achieving high tunability (figure 44(a)). By patterning plasmonic antennas on stretchable polymer films, Aksu *et al* demonstrated active tuning of the optical responses of a flexible and non-planar metasurface via mechanical stretching (figure 44(b)) [281]. In their design, they incorporated the metasurface with bow-tie structures on a stretchable and flexible PDMS substrate with an average interparticle distance of 40 nm. By stretching the metasurface, inter-particle distance was varied which resulted in fine tuning of the resonance wavelength. As gap distance decreases, a clear

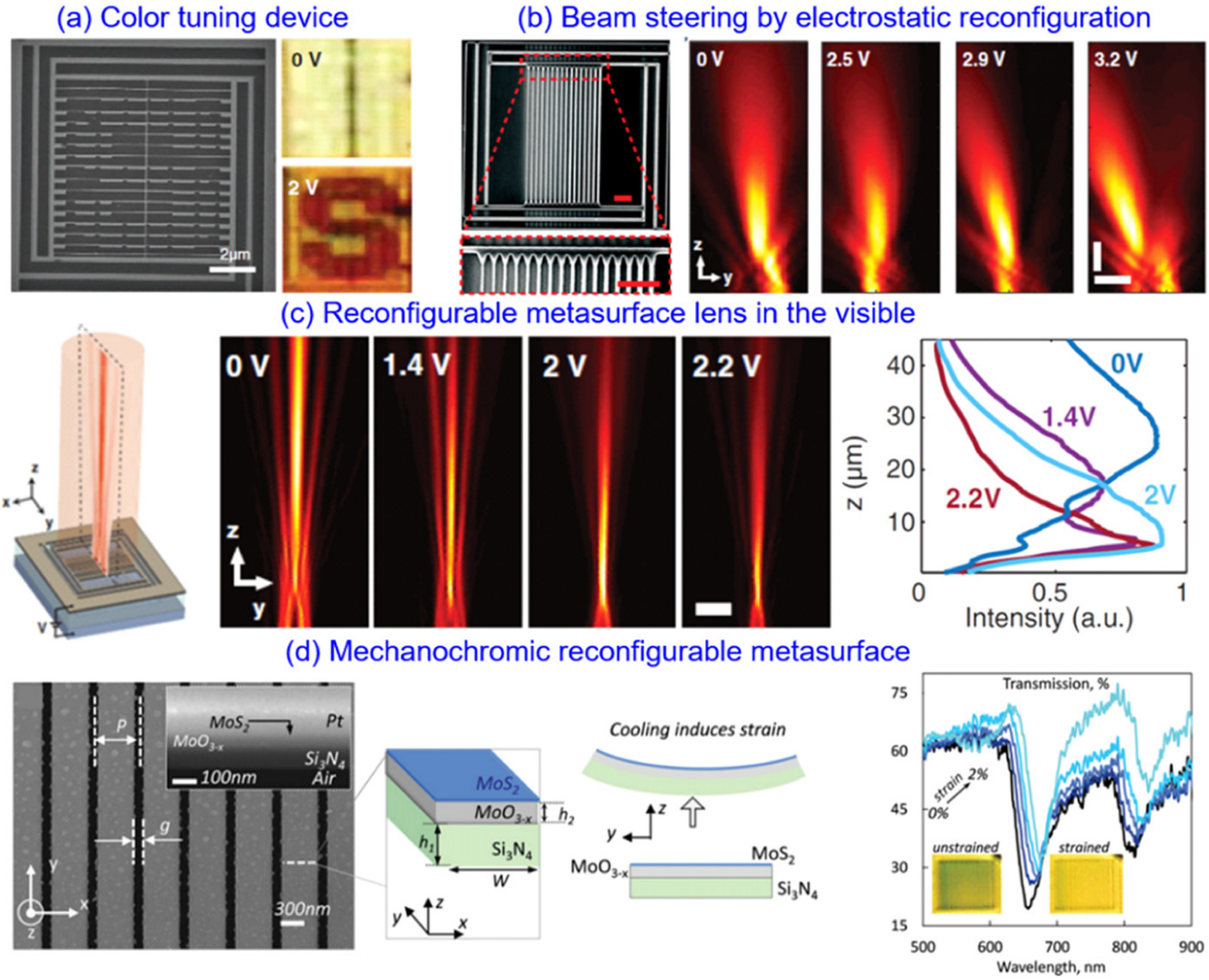

Figure 42. Reconfigurable nano-mechanical metasurfaces in the visible. (a) SEM image of the structure and color tuning of a character of letter 'S' is realized by applying voltage. (b) Beam-steering device and the intensity profiles of the beam steered at different angles. (c) Schematic of an MEMS-tunable lens and its focusing performance under different voltages. (a–c) From [267]. Reprinted with permission from AAAS. (d) (Left) A mechanochromic metasurface and (right) its tunable transmission properties in the visible. Reproduced from [268]. CC BY 4.0.

resonance red shift is observed due to the strong near-field interaction described by the hybridization model [274]. Gutruf *et al* demonstrated an all-dielectric, mechanically-tunable metasurface that operates in the visible [282]. The flexible metasurface is made of an identical array of TiO_2 cylindrical resonators embedded in PDMS. When a uniaxial strain was applied, the metasurface shows a clear red shift in resonance wavelengths. The resonant peak shifted 5.08% to a longer wavelength and 0.96% to a shorter wavelength from the original resonance wavelength when measured under TE and TM polarizations, respectively. By incorporating high-contrast metastructures (HCMs) on flexible substrates, Zhu *et al* demonstrated a new flexible HCM whose color can be controlled by stretching the substrate [277]. HCMs are made up of high-refractive index materials with periodic structures and are surrounded by low index material. The periodicity of the HCMs is made nearly one wavelength length [283, 284]. By applying a small deformation in the HCMs, the first order diffraction can be enhanced while annihilating other diffraction orders, showing abilities as a highly tunable diffraction grating with tunable coloration and beam steering.

Another promising feature of the flexible metasurface is its ability to collectively control the phase without any significant change in transmission. It is well known that the geometry [9] and orientation [285] of the meta-atoms govern the phase discontinuity at each position of the metasurface. Hence, the phase discontinuity of a metasurface can be manipulated by changing the position and the orientation of meta-atoms via mechanical deformation. A flexible metasurface has been used to demonstrate a metalens with a tunable focal length. The phase profile of the lens can be written as, $\phi(\rho, \lambda) \approx \pi\rho^2/\lambda f$, where λ is the operating wavelength, ρ is the distance to the center of lens, and f is the focal length. By stretching the flexible substrate, the distance (ρ) of each meta-atom can

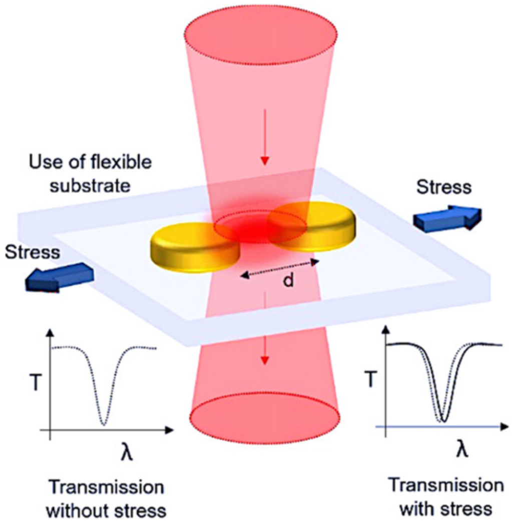

Figure 43. Schematic of tunability on a flexible metasurface.

be changed, leading to a new phase profile and focal length (figure 45). If the substrate is stretched by distance '*s*', the new focal length becomes $f' = s^2 f$. Ee and Agarwal demonstrated a continuously tunable, focal length flexible metalens by incorporating an Au nanorod array on a stretchable PDMS substrate (figure 45(a)) [286]. By changing the lattice constant of the Au nanorod array, the focal distance of the metalens can be continuously varied. The metalens was designed to operate at a wavelength of 632.8 nm, and the focal length can be continuously tuned from 150–250 μm. However, this flexible metalens can only work with circularly-polarized light, and the efficiency is relatively low due to the incorporation of the plasmonic Au antenna. The efficiency of a tunable metalens can be greatly enhanced using a dielectric metasurface on a flexible substrate. Kamali *et al* demonstrated a highly tunable elastic dielectric metalens via radial strain. The metalens is designed to operate at a wavelength of 915 nm, and the focal length can be tuned from 600–1400 μm with a focusing efficiency of $>$50% (figure 45(b)) [272]. High refractive index amorphous silicon square nano-posts were encapsulated in a low refractive index elastic PDMS membrane. Due to this high index contrast between the silicon nano-post and the elastic PDMS, a high localization of energy density resides inside the nano-posts giving rise to weak coupling between them. Consequently, the phase transformation depends largely on the width and position of the nano-post and not the distance between them. Thus, a uniform stretch ratio of $(1 + \varepsilon)$ on the radius of the metalens scales its focal length by a factor of $(1 + \varepsilon)^2$, where ε is a minute change in the position of meta-atom from its original position (figure 45(b)).

Mechanical tuning is one of the promising approaches to make active metasurfaces. It offers simplicity in the design and fabrication process and is one of the simplest techniques to achieve dynamic tuning of a metasurface. Also, the flexible metasurface offers advantages of integration on non-planar and curved structures. Flexible metasurfaces are highly dependent on structural parameters, which can be beneficial for designing tunable color filter, diffraction grating, metalens, sensor, etc. However, the disadvantages of the flexible metasurface include the slow tuning speed, it is highly sensitive to the environment (e.g., temperature), and it is incompatible with complementary metal-oxide semiconductor (CMOS) technology. Also, it is not possible to individually control each meta-resonator, making it a challenge to integrate into device components.

6. Nonlinear optical metasurfaces

In nonlinear optics, the optical response of materials can be expressed as a power series expansion of the nonlinear material polarization

$$P = \varepsilon_0(\chi E + \chi^{(2)}E^2 + \chi^{(3)}E^3 + \cdots + \chi^{(n)}E^n),$$

where ε_0 is the vacuum permittivity; E is the electric field; and $\chi^{(2)}$, $\chi^{(3)}$, and $\chi^{(n)}$ are the 2nd, 3rd, and nth order of nonlinear susceptibilities, respectively [288]. At large intensities, the nonlinear terms, $\chi^{(2)}E^2$, $\chi^{(3)}E^3$, $\cdots$, $\chi^{(n)}E^n$ can become sufficiently large, inducing the nonlinear optical responses. The nonlinear terms in this expansion also leads to the generation of new frequencies. Second and third harmonic generation (SHG and THG), four-wave mixing (FWM) processes, and optical Kerr effect (OKE) are some of the physical phenomena that are related to $\chi^{(2)}$ and $\chi^{(3)}$. Natural materials have intrinsically very low nonlinear responses; hence, to observe a strong nonlinear response, optically bulky materials and complex phase matching conditions must be satisfied [288, 289]. To acquire strong nonlinear properties from an optically thin metasurface, one could utilize a high $\chi^{(n)}$ material and optical resonances of meta-atoms that can exhibit strong local field enhancement and can provide strong light–matter interaction in ultrathin metasurfaces. In addition, the phase matching condition can be relaxed in ultrathin metasurfaces since the interaction takes place in the subwavelength thickness (figure 46). Furthermore, the concepts of metasurfaces for controlling the amplitude and phase of light could be adapted to nonlinear metasurfaces. Hence, nonlinear metasurfaces benefit from unique advantages such as complete control of the nonlinear tensor, optical resonances leading to strong field localizations, and phase-mismatch-free interactions. In this section, nonlinear metasurface techniques used to efficiently generate higher harmonics, phase control, and tuning of nonlinear processes will be discussed with the following three subsections: metallic, dielectric/semiconductor, and hybrid nonlinear metasurfaces.

6.1. Metallic nonlinear metasurfaces

Conventional metallic metasurfaces consist of metal unit elements that exhibit large local field enhancement due to localized surface plasmon resonance (LSPR). The highly-confined field along with the high $\chi^{(3)}$ value of metal (e.g. gold) itself facilitates strong THG, which has been demonstrated in single plasmonic nano-antennas [290–292]. Moreover, using non-centrosymmetric metal nanoparticles, enhanced second order harmonic responses have been experimentally demonstrated [293–298]. By properly choosing suitable asymmetry of the meta-atom, strong mode overlap between the nonlinear polarization mode and its harmonics can be achieved, leading to

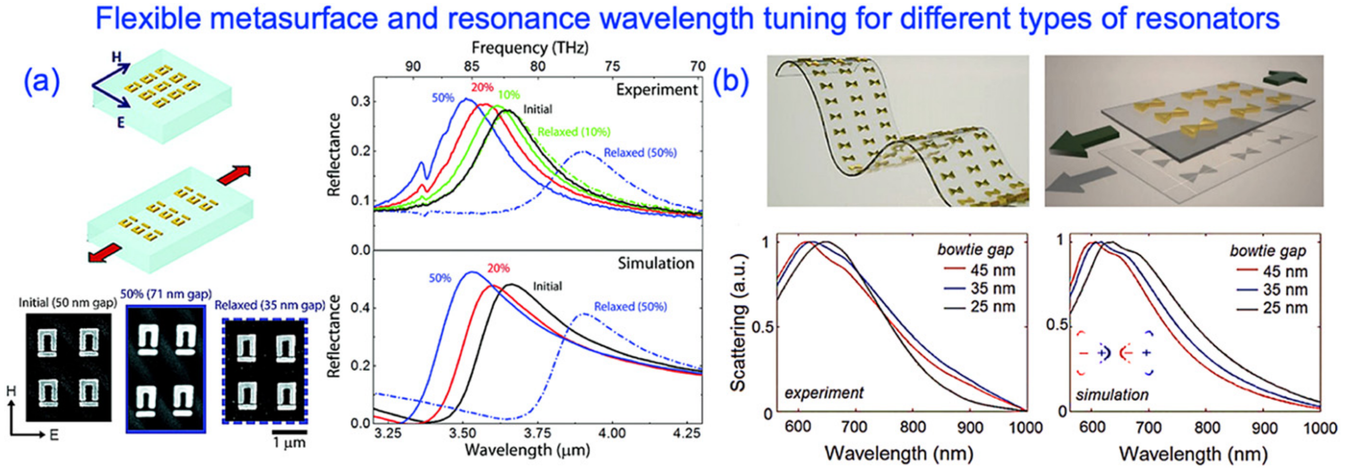

Figure 44. Flexible and non-planar metasurfaces with different types of resonators. (a) Split ring resonator coupled with bar resonators. Reprinted with permission from [270]. Copyright (2010) American Chemical Society. (b) Bowtie resonators; the gap between individual bowtie antenna governs scattering. [271] John Wiley & Sons. © 2015 WILEY-VCH Verlag GmbH & Co. KGaA, Weinheim.

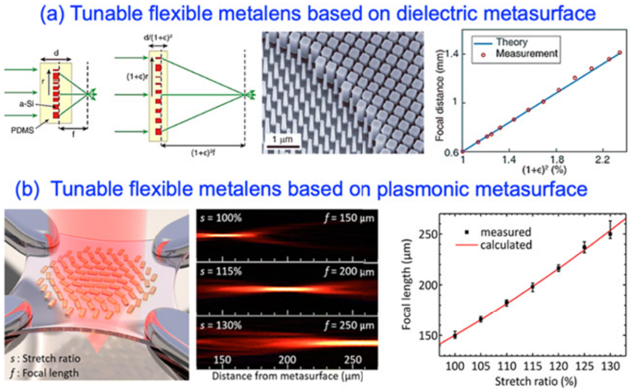

Figure 45. (a) Schematic of flexible metalens based on Au plasmonic meta-atoms. The focal length of the flexible metasurface is tuned using mechanical deformation. [272] John Wiley & Sons. © 2016 WILEY-VCH Verlag GmbH & Co. KGaA, Weinheim. (b) Schematic of a dielectric metasurface microlens encapsulated in a low index elastic membrane. Inset: scanning electron microscope image of dielectric antenna array. Reprinted with permission from [286]. Copyright (2016) American Chemical Society.

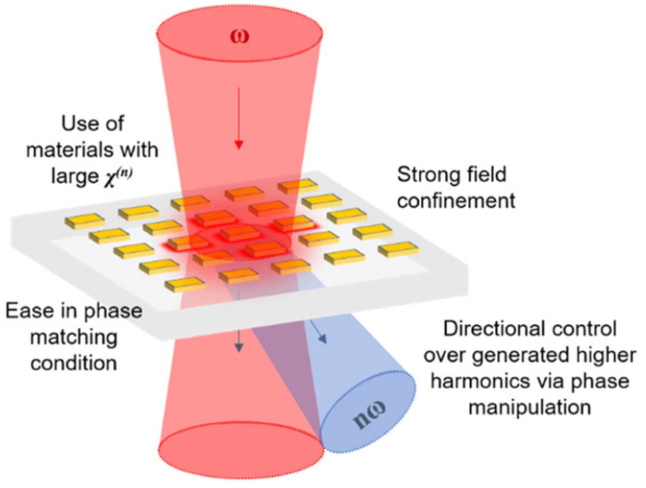

Figure 46. Schematic of nonlinear metasurfaces with phase controlled high harmonic generation.

high far-field nonlinear emission [299]. Further, the efficiency and the emission properties of generated HHG can be significantly enhanced and controlled using a well-engineered metasurface. Czaplicki *et al* demonstrated five-fold enhancement of SHG from metasurfaces by reducing the density of a V-shaped gold unit element (figure 47) [300]. This enhancement can be attributed to the favorable interparticle interaction of the metasurface that supports SLR. SLR can be achieved when the product of refractive index (n) of the surrounding homogenous dielectric medium and the periodicity of the metasurface (P) is larger than the LSPR wavelength of the unit element. SLR exhibits spectral narrowing and enhanced local field confinement that leads to enhanced SHG.

Quasi-phase matching, known as the poling technique, is a common scheme for enhancing nonlinear interaction in nonlinear metasurfaces. In this poling technique, unit elements are stacked in a specific spatial pattern in such a way that it reverses the sign of χ^2 alternately to imprint a momentum along specific direction. This technique is implemented to enhance and control the direction of generated higher harmonics [301–304]. Segal *et al* used tightly packed SRRs to create nonlinear PhCs and demonstrated diffraction and focusing of SHG (figure 48) [301]. Periodic inversion of the effective $\chi^{(2)}$ is achieved by periodic inversion of the SRRs' orientation. The phase of SHG at each SRR unit is used to manipulate the diffraction angle and to achieve a focusing effect. The diffraction angle of SHG at normal incidence is given by $\sin(\theta_{\mathrm{SH}}) = m\lambda_{\mathrm{FH}}/2\Lambda$, where m is an integer, λ_{FH} is the fundamental harmonic (FH) wavelength, and Λ is the modulation period of the metasurface. Using a similar binary nonlinear metasurface consisting of SRR unit elements, nonlinear vortex beam generation has been realized experimentally (figure 49(a)) [304]. A similar Pancharatnam–Berry (PB) phase technique can be used to control the phase of generated higher harmonics [285, 305–307]. A similar technique used to control the phase of generated higher harmonics involves rotating an antenna by an angle of θ with respect to its adjacent neighbor [308]; the

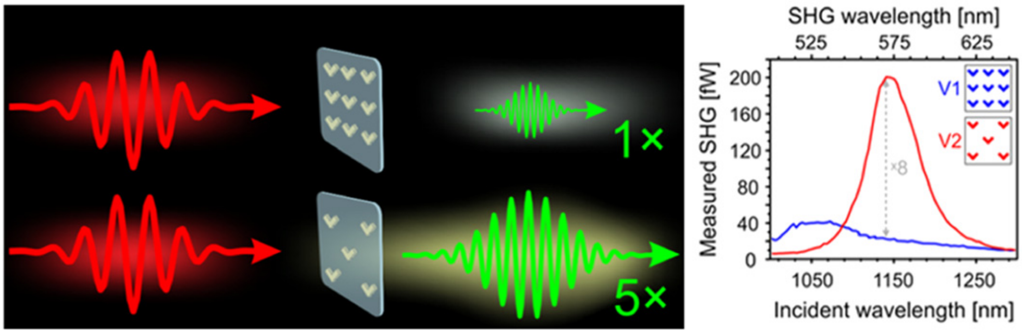
Second harmonic generation via surface lattice resonance metasurface

Figure 47. (Left) Schematic of SHG in a non-centrosymmetric V-shaped gold metasurface due to SLR. (Right) Red and blue curves represent the SHG signal from the metasurface with and without SLR. Reprinted with permission from [300]. Copyright (2018) American Chemical Society.

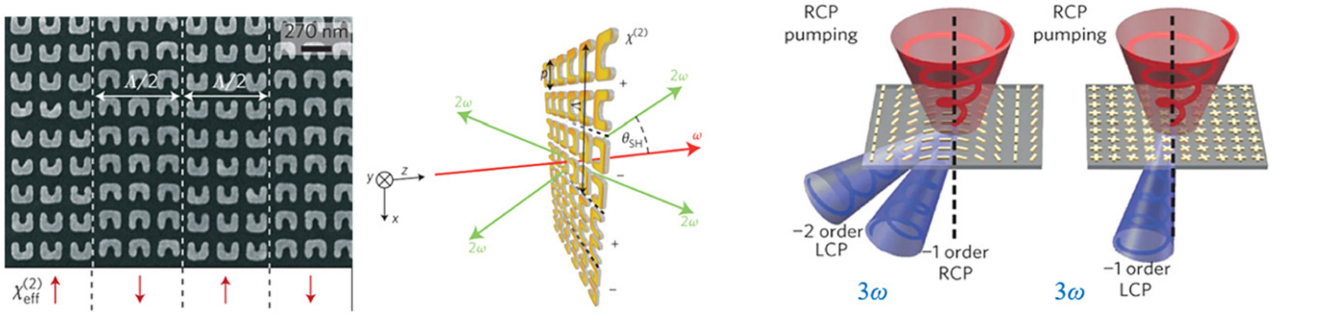
(a) Metasurface poling using π-phase shift for second harmonic generation

(b) Continuous phase control using PB phase

Figure 48. Phase manipulation on nonlinear metallic metasurfaces. (a) One-dimensional modulation of $\chi^{(2)}$ and controlled far-field SH emission. Reprinted by permission from Springer Nature Customer Service Centre GmbH: Nature Photonics. [301] © 2015. (b) Schematic of nonlinear phase-controlled diffraction for a circularly-polarized fundamental wave. Reprinted by permission from Springer Nature Customer Service Centre GmbH: Nature Materials. [307] © 2015.

nano-antenna introduces a nonlinear geometric phase variation $(n+1)\,\sigma\theta$ or $(n-1)\,\sigma\theta$, where $\sigma = \pm 1$ represents a right and left hand circularly-polarized fundamental wave, and n is the generated nth harmonic. Also, the generated higher harmonics obey certain selection rules. According to the selection rule, when a circularly-polarized fundamental wave interacts with a single nanostructure with m-fold rotational symmetry, only harmonic orders with $n = lm \pm 1$ are generated, where m is the rotational symmetry number, l an integer, and the '+' and '−' signs correspond to harmonic generation of the same and opposite circular polarization, respectively (see table 10) [309]. As an example, a meta-atom with one-fold rotational symmetry, such as SRRs, can generate SH waves with a phase shift of $\sigma\theta$ and $3\sigma\theta$, TH waves with a phase shift of $2\sigma\theta$ and $-4\sigma\theta$, and higher harmonic waves with phase as tabulated below [310].

Similarly, for a nanorod which has two-fold symmetry, only odd harmonics are allowed for both circular polarizations. The THGs have phases of $2\sigma\theta$ and $4\sigma\theta$ in the forward direction. Li and Shen *et al* implemented a PB phase metasurface with two-, three-, and four-fold symmetry meta-atoms to demonstrate nonlinear continuous phase control of SHG and THG, respectively (figure 48(b)) [307, 311]. Upon further investigation, Gennaro *et al* realized the presence of higher diffraction orders that were not predicted by the generalized law of nonlinear refraction (figure 49(b)) [312]. These higher diffraction orders can only be obtained by the adaptation of higher order antenna modes. Thus, the simple adaptation of higher order modes extends the interpretation of geometric phase nonlinear metasurfaces with complex composite unit elements and explains the observation of apparently symmetry-forbidden nonlinear processes.

By an introduction of additional phase mismatches among neighboring meta-atom, the HHG signal in the far field can be enhanced or canceled because of constructive and destructive interference. Walter *et al* used an ultrathin nonlinear photonic metasurface to demonstrate nonlinear optical encryption for securing information (figure 49(c)) [313]. An optical image remained hidden under fundamental wave illumination which can be read from the generated SHG signal. Similarly, using the concept of P–B phase and symmetry selection rule, Schlickriede *et al* demonstrated simultaneous generation and focusing of SHG from a metasurface made up of three-fold symmetry tristar gold meta-atoms (figure 49(d))

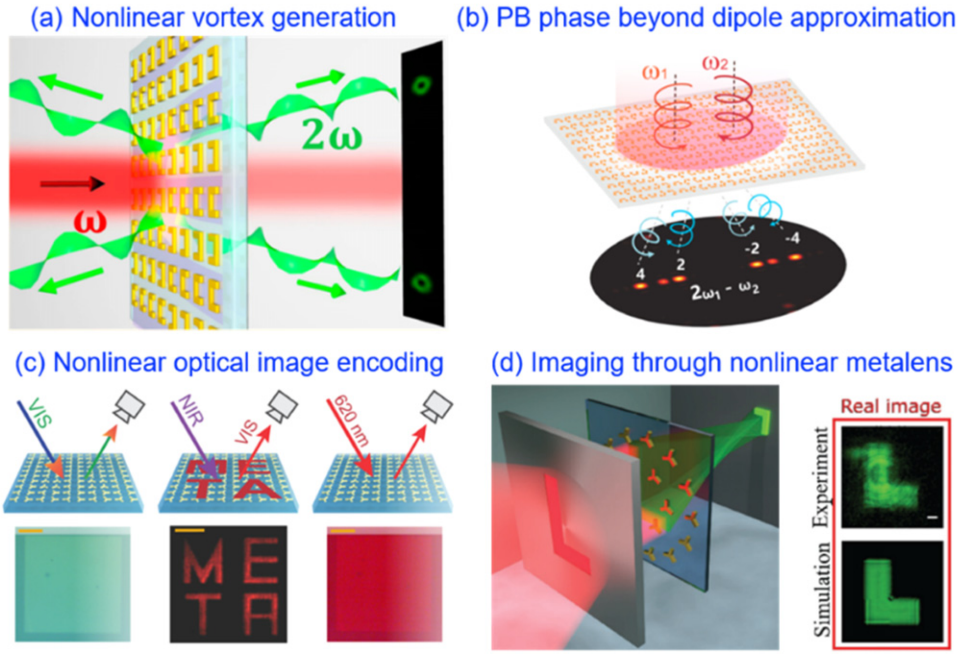

Figure 49. Nonlinear metallic metasurfaces. (a) Illustration of second harmonic vortex generation and diffraction. Reprinted with permission from [304]. Copyright (2016) American Chemical Society. (b) Illustration of PB phase-induced nonlinear FWM diffraction of a gradient metasurface. The higher diffraction orders are associated to the higher order multipole modes. Reprinted with permission from [312]. Copyright (2019) American Chemical Society. (c) Working principle of the nonlinear metasurface for nonlinear optical encryption for securing information. Reprinted with permission from [313]. Copyright (2017) American Chemical Society. (d) Schematic concept and optical properties of the nonlinear metalens. [314] John Wiley & Sons. © 2018 WILEY-VCH Verlag GmbH & Co. KGaA, Weinheim.

[314]. The nonlinear metalens acts like a regular lens but controls the beam propagation of the SHG signal. Prior *et al* finely adjusted the aspect ratio of rectangular gold nano-apertures to demonstrate anomalous phase matching as well as a nonlinear metalens [308]. The existence of the nonlinear PB phase in the FWM process was demonstrated by Li *et al* [315]. The polarization state of the FWM signal was controlled by choosing an appropriate combination of the polarization of the excitation beams. This effect of FWM intensity on the polarizations of excitation beams could be useful in designing polarization-controlled nonlinear metasurfaces.

6.2. Dielectric and semiconductor nonlinear metasurfaces

All-dielectric metasurfaces incorporate high-index materials with a negligible extinction coefficient. Furthermore, an all-dielectric metasurface can exhibit Mie-type resonance, i.e., both electric and magnetic dipole resonances, and it possesses negligible losses, allowing excitation at high light intensities. Though field enhancement is lower compared to using a plasmonic nanoantenna, enhancement inside the overall volume can lead to higher nonlinear conversion efficiency [316–319]. Dielectric nano-antennas can also support another form of localized electromagnetic mode known as the anapole resonance [320]. Anapole resonance is a nonradiative mode caused by the destructive interference between a toroidal dipole and an electric dipole mode (figures 50(a) and (b)) [321]. Anapole modes have been shown to provide strong field enhancements in metasurfaces designed for THG (figure 50(c)). Semmlinger *et al* demonstrated THG from visible to vacuum ultraviolet (VUV) utilizing the anapole resonance in cylindrical TiO_2 [321] and ZnO (figure 50(d)) [322].

On the other hand, recent demonstrations of the bound state in continuum (BIC) in high index dielectric metasurfaces have led to high-Q resonance devices [323–325]. The BICs are waves that remain localized even though they coexist with a continuous spectrum of radiating waves that can carry energy away. The Q-factor and the lifetime of a true BIC is infinite, and true BICs can only be achieved in systems with at least one dimension extending to infinity [325]. However, a perturbation in the ideal system can cause the BIC to collapse to a Fano resonance with a finite lifetime, which is usually called quasi-BIC. It has been shown that a finite but high Q-factor quasi-BIC resonance can be tailored by introducing asymmetric factors into the system (figure 51(a)) [326]. The Q factor consists of the radiative part (Q_r) and nonradiative part (Q_{nr}) where $1/Q = 1/Q_r + 1/Q_{nr}$. Here, Q_{nr} arises from the fabrication factors like surface roughness, structural disorder, deviation from the fabrication design, etc and hinders the overall Q-factor of the metasurface. In contrast, Q_r can be tailored by introducing asymmetry to the meta-atoms. Liu *et al* demonstrated high SHG and THG conversion efficiency with an ultrahigh-Q resonance (Q factor = 18 511) made up of an asymmetric T-shaped Si metasurface [327]. In general, a high Q factor indicates a high field intensity enhancement (FIE) within the Si meta-atom; thus, the THG conversion efficiency ($\eta_{THG} \sim 10^{-6}$) of this metasurface is at least five orders magnitude higher than that of bare silicon. Koshelev *et al* introduced and demonstrated a critical coupling condition ($Q_{nr} = Q_r$) to

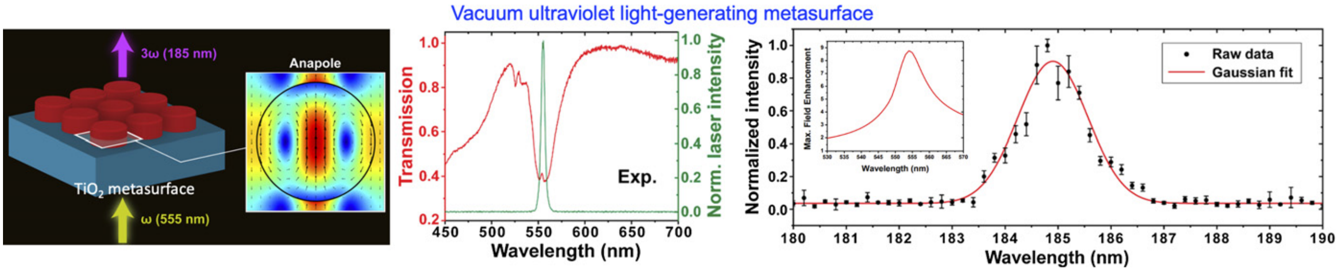

Figure 50. VUV light-generating metasurface. Reprinted with permission from [321]. Copyright (2019) American Chemical Society. (a) Schematics of VUV light generation in high refractive index metasurface. (b) The presence of sharp resonance at a wavelength of 555 nm (green line) is associated with anapole resonance. (c) FIE inside the TiO_2 nanodisc. (d) The increase in THG at VUV (185 nm) from silicon metasurface can be associated with the strong field enhancement due to anapole resonance.

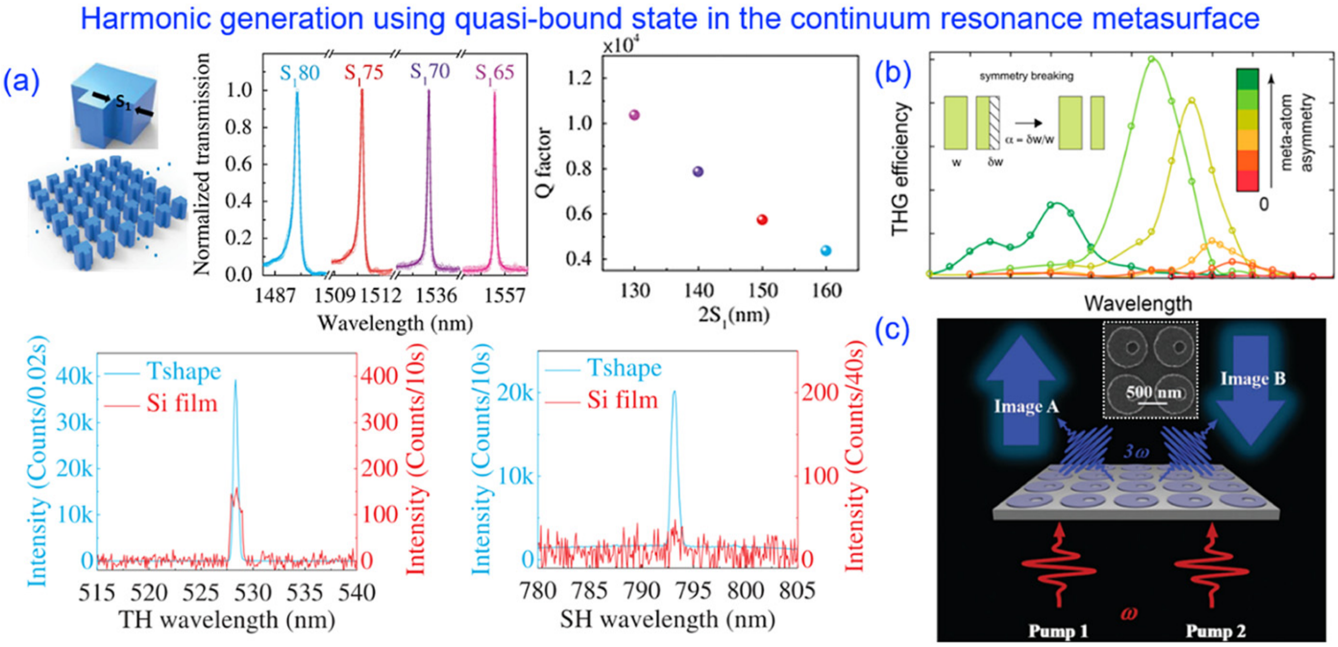

Figure 51. Harmonic generation using quasi-BIC resonance on a high index asymmetric metasurface. (a) Q-factor dependence on the asymmetric factor (S_1). Enhanced SHG and THG intensity from the metasurface and same thickness Si film. Reproduced from [327]. CC BY 4.0. (b) Enhanced THG using an in plane broken symmetry metasurface. Reprinted with permission from [328]. Copyright (2019) American Chemical Society. (c) Pump wavelength and/or polarization dependent THG image tuning via a quasi-BIC resonance metasurface. Inset: meta-atoms with asymmetric nano-holes. Reproduced from [329]. CC BY 4.0.

tailor the most effective THG from the asymmetry of a dielectric metasurface within plane broken symmetry (figure 51(b)) [328]. By incorporating meta-atoms onto a Si disc with off-center nano holes, Xu *et al* demonstrated dynamical switching of images generated by a nonlinear metasurface that supports the quasi-BIC state (figure 51(c)) [329].

In addition to the single frequency HHG conversion, dielectric/semiconductor metasurfaces can incorporate different parametric mixing processes. Lui *et al* observed seven different nonlinear processes (SHG, THG, fourth-harmonic generation, sum-frequency generation (SFG), two-photon absorption-induced photoluminescence, FWM, and six-wave mixing) in a GaAs-based dielectric metasurface (metamixer) (figure 52) [330]. This gave rise to 11 new frequencies that span the ultraviolet to NIR spectral range. The enhanced electromagnetic fields at the metasurface resonant frequencies, along with large optical nonlinearities of non-centrosymmetric GaAs and relaxed phase-matching conditions due to the subwavelength dimensions of the metasurface, led to the simultaneous HHG. Similarly, frequency conversion processes have been demonstrated from a Si metasurface [331] and plasmonic antenna on a crystalline Si substrate [332].

In addition to HHG, precise control of the wavefront over the HHG is also possible using metasurfaces for nonlinear phase profiles engineering. Wang *et al* demonstrated beam deflection and vortex beam generation of the third harmonic signal (figure 53). The metasurface was designed with circular and elliptical unit elements that could achieve a phase variation between 0 and 2π for the third harmonic signal while maintaining a constant conversion efficiency [333]. Gao *et al* realized nonlinear holograms using a similar approach with C-shaped silicon resonators. The phase variation of the third harmonic signal was controlled by changing the width of the opening of the C-shaped Si meta-atoms [334]. Löchner *et al* used an

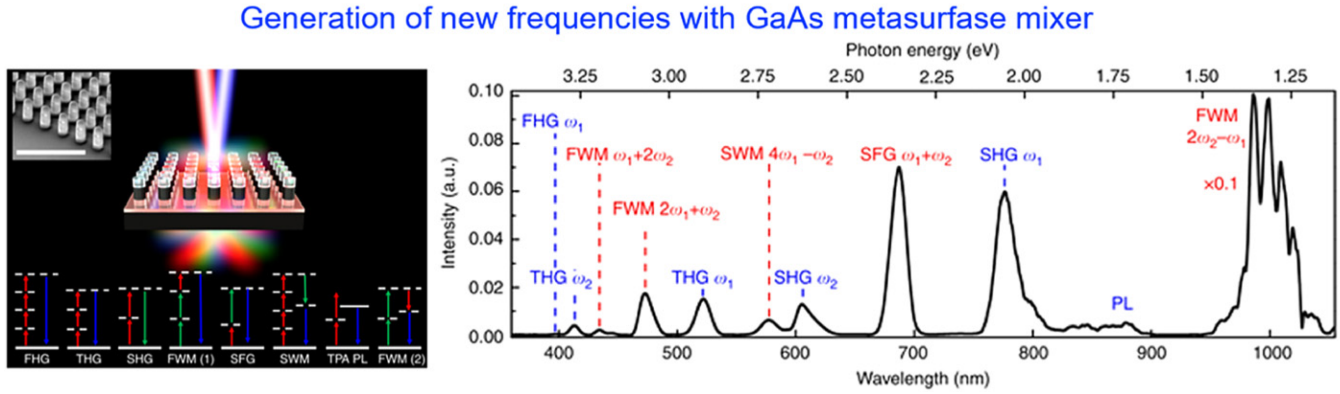

Figure 52. (Left) Schematic of an optical metamixer and multiple nonlinear optical processes in GaAs dielectric resonators. Inset: a side-view scanning electron microscope image of the GaAs metamixer (scale bar: 3 μm). (Right) Spectrum of generated new frequencies. Reprinted by permission from Springer Nature Customer Service Centre GmbH: Nature Communications. [330] © 2018.

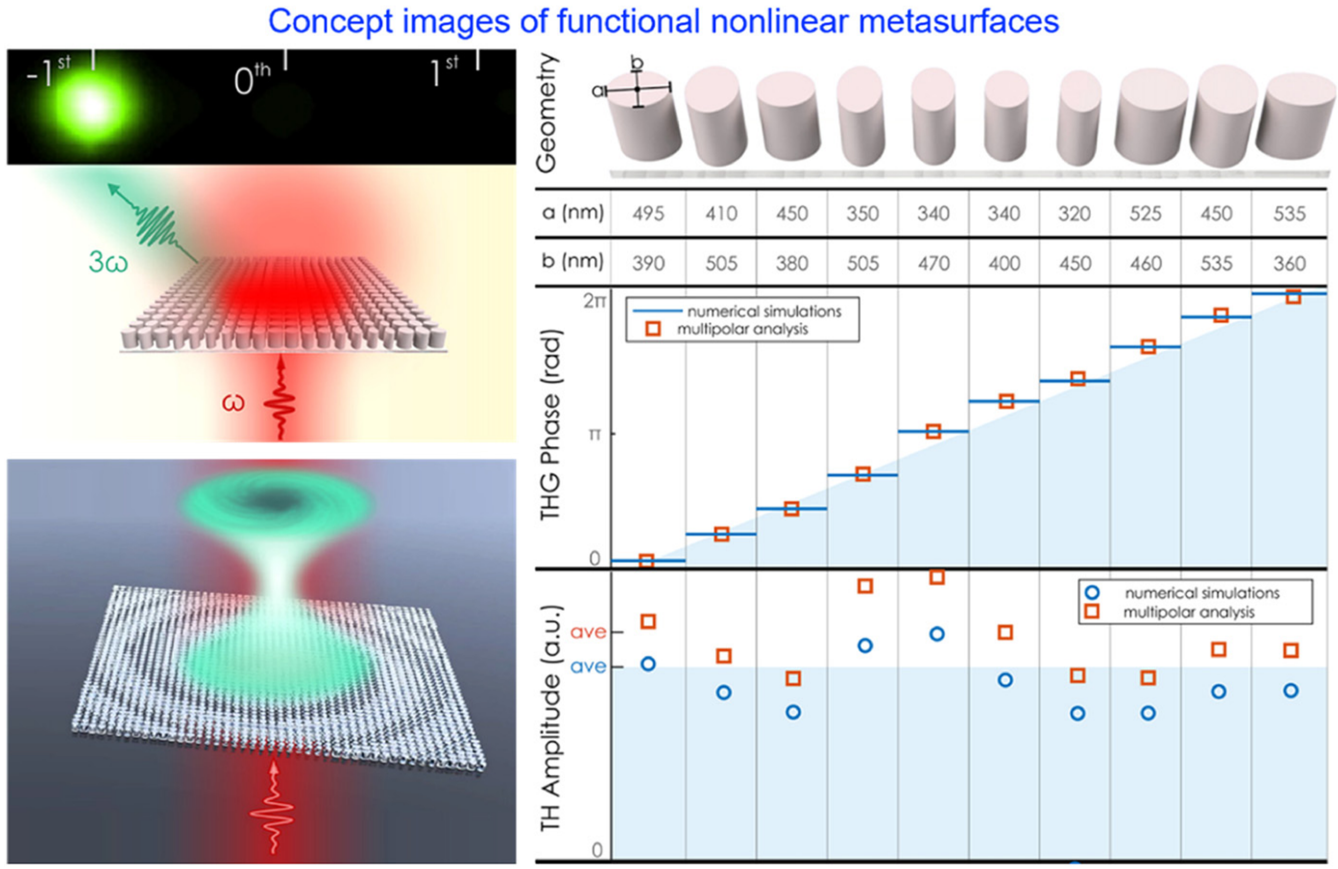

Figure 53. A nonlinear beam deflector and vortex beam generator, with dependence of third harmonic amplitude and phase on geometries and size of nanopillar meta-atoms. Reprinted with permission from [333]. Copyright (2018) American Chemical Society.

AlGaAs metasurface to demonstrate that the emission power of the SHG depended on the polarization and mode of the FH beam [335]. Applying the PB phase approach, Reineke *et al* demonstrated polarization-dependent wavefront control and reconstruction of an encoded hologram at the third-harmonic wavelength [336]. Amorphous silicon nanofins meta-atoms with a two-fold rotational symmetry were implemented to encode phase information utilizing the rotation orientation. By building arrays of resonators, anomalous diffraction and complex beam shaping (e.g., hologram) for the TH signals was realized.

Another demonstration from nonlinear metasurfaces is the reshaping of a conventional Hermite–Gaussian beam. Xu *et al* demonstrated introduction of optical angular momentum (OAM) into a Hermite–Gaussian beam (figures 54(a) and (b)) [337]. After passing through a metasurface, the Hermite–Gaussian beam acquired OAM at low intensity levels, while preserving the original beam's amplitude and phase

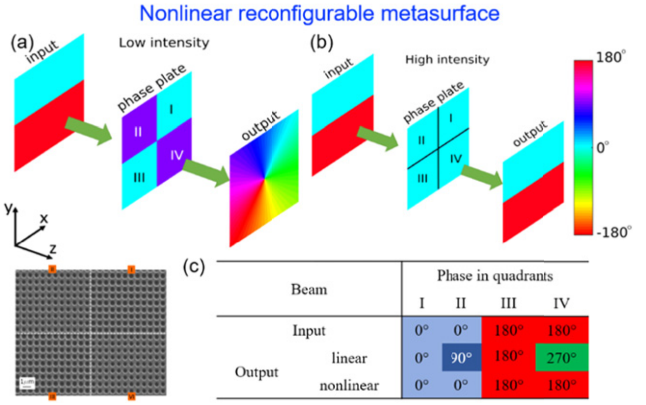

Beam		Phase in quadrants I	II	III	IV
Input		0°	0°	180°	180°
Output	linear	0°	90°	180°	270°
	nonlinear	0°	0°	180°	180°

Figure 54. Conceptual illustration of a nonlinear As_2S_3 metasurface with reconfigurable output beam. (a) Generation of OAM at low intensity. Inset: scanning electron microscopy image of the fabricated metasurface. (b) Absence of OAM at high intensity. (c) Phase introduced by the metasurface on the beam after passing through the four quadrants of the metasurface at low intensity and high intensity. Reproduced from [337]. CC BY 4.0.

characteristics at high intensity levels. The metasurface was constructed with nano-holes on arsenic trisulfide (As_2S_3) chalcogenide glass in such a way that the phase acquired in the even quadrants (II and IV) is larger than in the odd quadrants (I and III) at low intensities. The phase distribution of the metasurface at different quadrants and the phase of the transmitted beam before and after passing through the metasurface for low intensity (linear regime) and high intensity (nonlinear regime) are given in figure 54(c). The highly nonlinear chalcogenide glass ($n_2 = 7.9 \times 10^{-13}$ cm^2 W^{-1}) provided a large Kerr nonlinear response ($\Delta n \sim 0.04$ at 1.2 GW cm^{-2}) for the phase manipulation at the 3rd and 4th quadrants. In addition, since the reconfigurability is enabled by the strong Kerr effect in chalcogenide glass, the metasurfaces can possess an ultrafast response time of 120 fs [338].

In dielectric media, nonlinear refraction and two-photon absorption depend on instantaneous $\chi^{(3)}$ effect, also known as the optical Kerr effect. These processes can be manipulated for ultrafast all optical tuning. Shcherbakov *et al* were the first to demonstrate the ultrafast nonlinear response of an all-dielectric metasurface based on amorphous silicon nanodisks [339]. They demonstrated low-power, 65 fs all-optical switching because of the strong localized magnetic Mie resonances. Later, Yang *et al* demonstrated an ultrafast all-optical switch of 490 fs ($\sim$2 THz) using a Fano-resonant Si metasurface with a high quality factor Q of 466 (figure 55) [317]. The metasurface was comprised of a periodic lattice of coupled rectangular bars and disk resonators (figure 55(a)). An incident electric field along the length of the rectangular bar resonators excited dipole resonance (bright mode). Because of near field interaction between the resonators, magnetic dipole resonance (dark mode) was excited within the disc resonator to produce strong Fano resonance (figure 55(b)). The strong field enhancement due to the Fano resonance led to large optical nonlinearity (figures 55(c) and (d)). Using a degenerate pump-probe experiment with a 1 kHz optical pump laser with a fluence of $\sim$60 mJ cm^{-2}, a switching time of 490 fs was observed. However, the modulation depth for this experiment was merely 0.2%. Using an 80 MHz laser with an FH wavelength designed at the Fano-resonance wavelength (1348 nm) and a peak pump intensity of 3.2 GW cm^{-2}, a five-fold enhancement in THG with respect to an un-patterned silicon film was observed. The metasurface demonstrated an absolute conversion efficiency of 1.2×10^{-6} along with transmission modulation depth of 36%.

One promising way to control the SHG in a metasurface is using an external static electric field. Inversion symmetry forbids second-order nonlinear processes in centrosymmetric media under the electric dipole approximation. However, application of a bias voltage across an optical medium can break the symmetry and can enable electric-field-induced second harmonic (EFISH) generation. EFISH is a third-order nonlinear effect enabled by an externally-applied static or low-frequency field

$$\chi_{\mathrm{eff}}^{(2)} \approx \chi^{(3)} \times E_{\mathrm{c}},$$

where, ${\chi_{\mathrm{eff}}}^{(2)}$ is the induced second order susceptibility, $\chi^{(3)}$ is third order susceptibility, and E_{c} is the applied electric field. As a result, induced nonlinear processes are not limited to non-centrosymmetric materials. Thus, by coupling strong field enhancement with the induced ${\chi_{\mathrm{eff}}}^{(2)}$ within the non-centrosymmetric material, SHG can be achieved. Kang *et al* demonstrated EFISH in an amorphous dielectric layer of an Al_2O_3 metamaterial absorber (figure 56(a)) [340]. Utilizing the strong electric field enhancement inside the Al_2O_3 from the metamaterial resonance and application of the external electric field, controllable SHG was realized. The generated EFISH intensity was linearly dependent on the applied external electric field, and nearly one order of magnitude enhanced signal was achieved with an external voltage of 10 V. EFISH was also demonstrated in an all-dielectric metasurface consisting of a rectangular Si grating. Strong magnetic Mie resonances intensified the nonlinear interaction of light with silicon (figure 56(b)) [341].

Shcherbakov *et al* demonstrated a tunable upconverted THG using a photon-accelerating semiconductor infrared metasurface (PASIM) (figure 57) [342]. Photon acceleration is a time-dependent nonlinear phenomenon where rapidly generated plasma produced by an intense laser can increase the energy of individual photons and generate tunable HHG pulses [343, 344]. A mid-infrared laser with an FH wavelength of 3.62 μm was used to tune the THG signal from 1.1–1.17 μm [342]. PASIM was engineered with nearly-touching rectangular Si nano-antennas to exhibit high Q factor and enhanced multi-photon absorption. The generated THG signal from the PASIM showed up to eight-fold stronger than the one without the pattern.

Dielectric and semiconductor metasurfaces provide a strong nonlinear response, low dissipative losses, and high damage threshold. In addition, the presence of higher order electric and magnetic responses makes it possible to tune the amplitude and phase of higher harmonics. Also, due to the presence of the instantaneous Kerr effect, it could be used for ultrafast switchable flat optical devices and generation of femtosecond pulses. Owing to the high nonlinearity of III–V semiconductors, a strong second order nonlinear process is possible

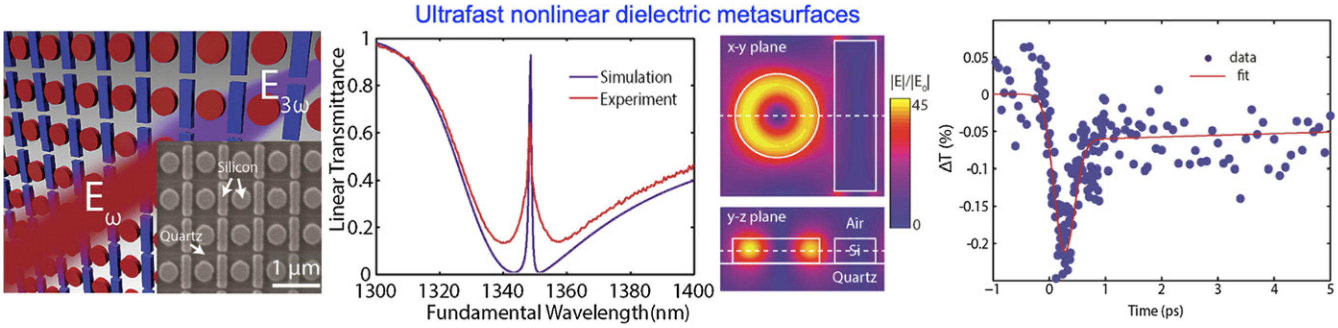

Figure 55. (a) Schematic of ultrafast all-optical switching using a silicon metasurface. (b) Simulated electric field amplitude at Fano resonance wavelength. (c) Strong field enhancement results from the Fano-type with large transmission modulation, and (d) sub picosecond temporal response of the dielectric metasurface. Reprinted with permission from [317]. Copyright (2015) American Chemical Society.

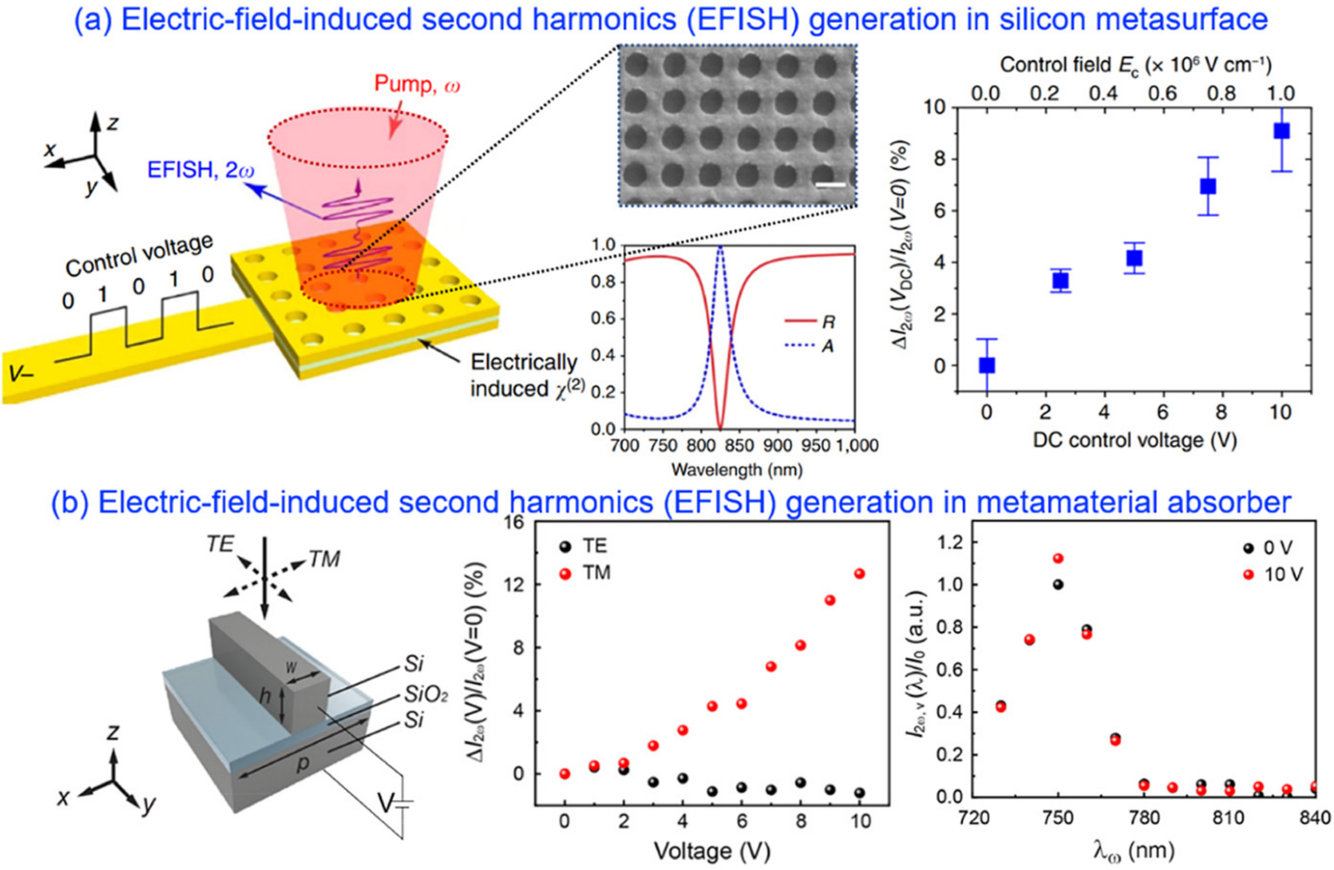

Figure 56. EFISH generation metasurface. (a) Schematic illustration of silicon nanohole metamaterial. Reprinted by permission from Springer Nature Customer Service Centre GmbH: Nature Communications. [340] © 2014. (b) Electrically-controlled SHG in a metamaterial absorber. The TM polarized excitation induced a magnetic Mie resonance mode that enhanced to EFISH generation. Reprinted with permission from [341]. Copyright (2019) American Chemical Society.

which extends its use to both even and odd higher harmonic processes. These advantages make dielectric and semiconductor metasurfaces a potentially powerful platform for modern ultrafast nonlinear nanophotonics.

6.3. Hybrid nonlinear metasurfaces

Strong nonlinear light conversion (nonlinear effects) could be enabled by combining strong field enhancement with large intrinsic nonlinear materials in hybrid metallic-dielectric/semiconductor metasurfaces [294, 345–349]. The emerging ENZ materials with high nonlinearity (refractive index changes of ±0.8 at ENZ wavelength) have been integrated with plasmonic antennas to induce strong nonlinear properties. As a proof of concept, Alam *et al* demonstrated an enhanced Kerr nonlinearity in an Au/ENZ metasurface with an absolute change in refractive index as high as 0.8 and a modulation speed of sub-picoseconds [350]. The metasurface

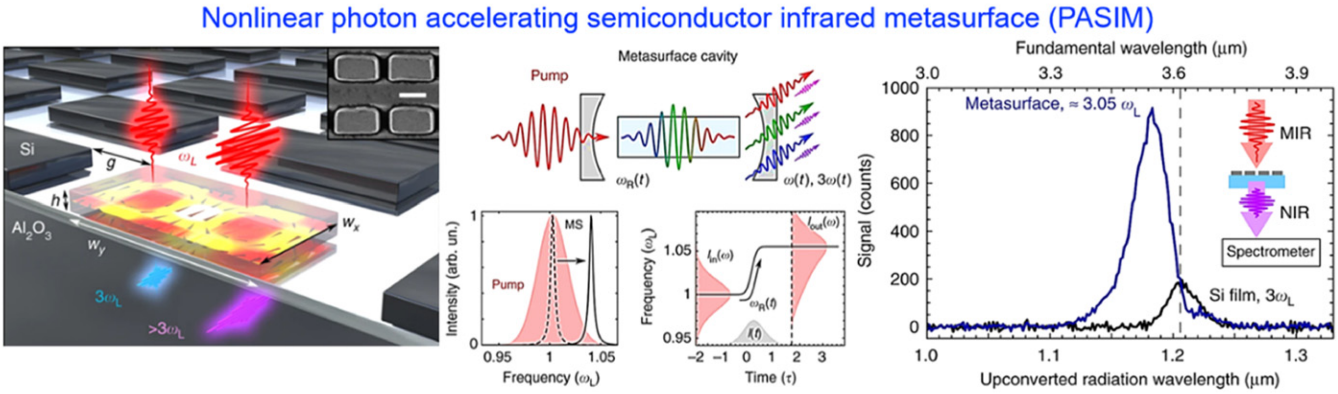

Figure 57. (Left) Self-induced blue-shift of incident light via a nonlinear photon accelerating semiconductor infrared metasurface (PASIM). (Middle) Illustration of the working principle and (right) experimental measurement of self-induced blue-shift of incident in PASIM. Reprinted by permission from Springer Nature Customer Service Centre GmbH: Nature Communications. [342] © 2019.

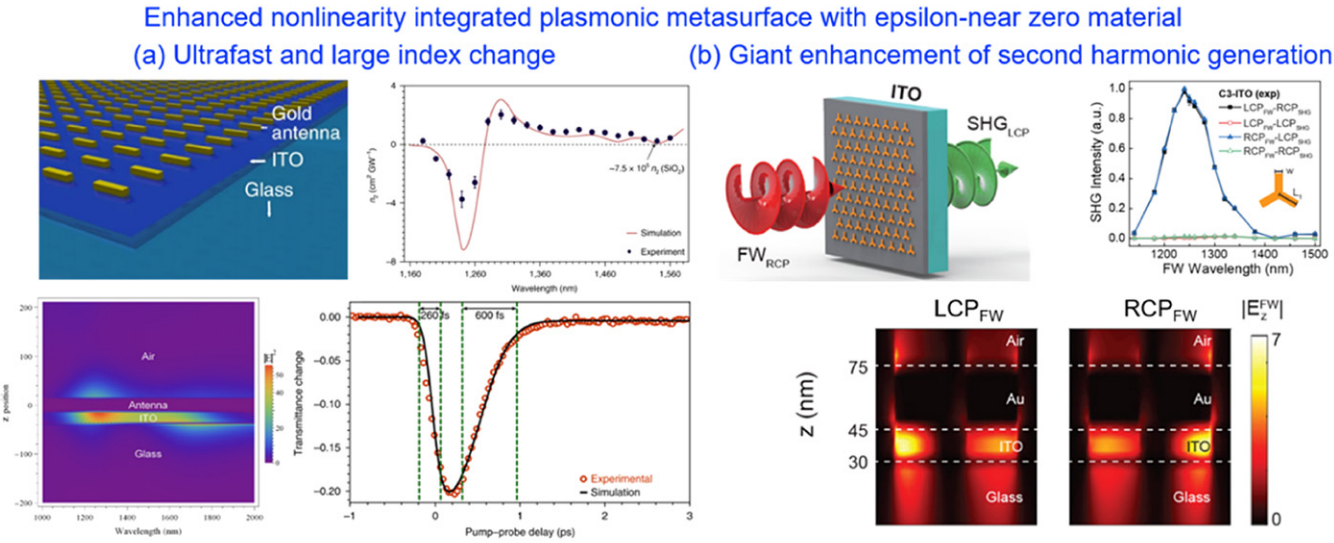

Figure 58. (a) Ultrafast-nonlinear response of an ENZ-integrated plasmonic metasurface. Reprinted by permission from Springer Nature Customer Service Centre GmbH: Nature Photonics. [350] © 2018. The large change in effective refractive index can be attributed to the large FIE inside the ITO because of strong coupling between the fundamental mode of each antenna and the ENZ mode. (b) Giant enhancement of second-order nonlinearity in ENZ-integrated plasmonic metasurface. Reprinted with permission from [351]. Copyright (2020) American Chemical Society.

consists of 23 nm ITO on a glass substrate with arrays of gold bar antennas placed on top (figure 58(a)). Due to strong coupling between the fundamental mode of the antenna and the ENZ mode, the electric field is confined within the ENZ medium, thus increasing the change in refractive index of the ITO. Recently, Deng *et al* demonstrated enhanced SHG at normal incidence using an ENZ-integrated plasmonic metasurface [351]. Their design incorporated tristar-shaped plasmonic (Au) meta-atoms placed on top of a 15 nm ITO ENZ layer (figure 58(b)). These meta-atoms provided the necessary strong electric field and symmetric breaking condition to the ENZ layer to achieve SHG. When the metasurface is illuminated with a circularly-polarized light, a strong *Z*-component of the near field is confined inside the ENZ layer. Since the SHG from an ENZ layer can be described by the leading second-order nonlinear susceptibility component χ_{zzz} [352], this strong confinement of the *z*-component of the electric field inside the ENZ medium gave rise to strong SHG. A similar approach to enhancing the SHG and SFG was demonstrated by Yuan *et al* where highly nonlinear two-dimensional gallium selenide ($\chi^{(2)}$ of GaSe $\sim$1000 pm V^{-1}) flakes were integrated with an L-shaped Si metasurface [353]. The L-shaped meta-atoms are designed to support Fano resonance at a wavelength of $\sim$1541 nm. Second-order nonlinear processes in the GaSe flake could be strongly enhanced by pumping the metasurface at resonance wavelength. This enhancement is due to the effective interaction of GaSe flakes with the evanescent field of the resonance.

Although semiconductor-loaded plasmonic metasurfaces provide higher nonlinear conversion efficiency than that of conventional highly-nonlinear materials, the conversion efficiency is still very low for practical applications. This can be attributed to the small light–matter interaction length. As an example, to accomplish efficient frequency conversion in

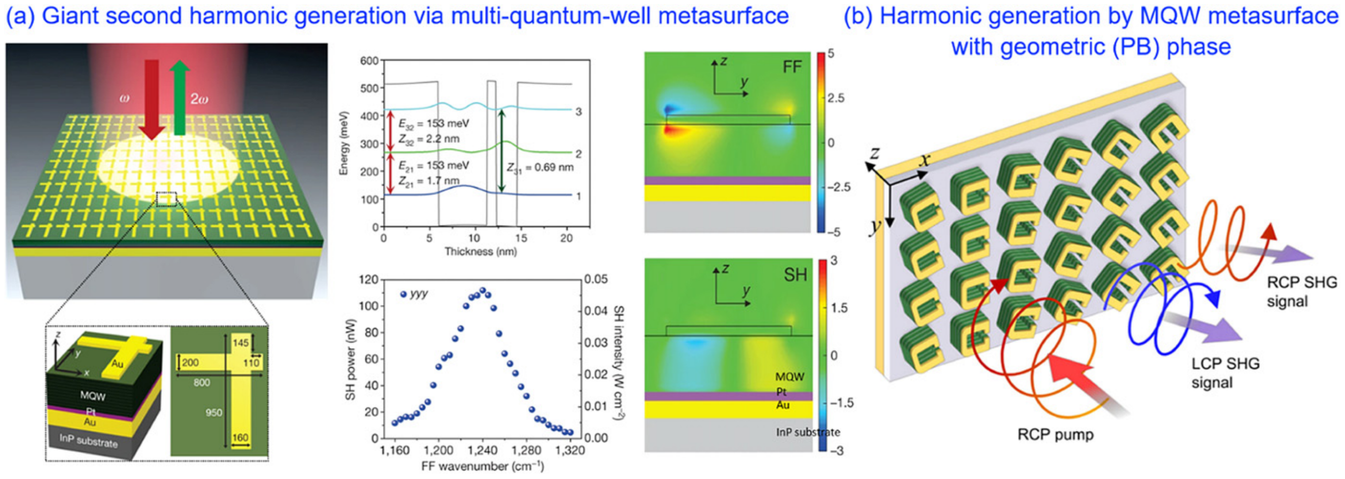

Figure 59. (a) Schematic of the MQW metasurface design for enhanced SHG. Conduction band diagram of an InGaAs/AlInAs coupled quantum well. Z-component of electric field at FH and SH frequency. Reprinted by permission from Springer Nature Customer Service Centre GmbH: Nature. [346] © 2014. (b) Multi-quantum well (MQW) metasurface with SRR meta-atoms exhibiting a PB phase for SHG. Both right- and left-hand circularly polarized second harmonic signals are generated along different directions as a consequence of the geometric phase gradient of the gold capped MQW meta-atoms along the x direction. Reprinted figure with permission from [310], Copyright (2015) by the American Physical Society.

a nonlinear metasurface, the product of the second order nonlinear response $\chi^{(2)}$ and the pump electric field intensity E_{pump} must be $|\chi^{(2)}E_{\text{pump}}| \sim 1$. However, the value of $\chi^{(2)}$ is extremely small in almost all materials, and thus E_{pump} needs to be infinitely large. However, because of the damage threshold of the materials used, the electric field is constrained with a certain finite value. This inadequacy of the metasurface could be compensated using a multi-quantum-wells (MQWs)-integrated metasurface. MQWs have high nonlinear susceptibilities and are made by stacking several III–V semiconductor layers. These layers serve as a set of potential wells and barriers for charge carriers which leads to discretization of energy levels along a transverse direction. MQW with desired inter-band and inter-sub-band transition rates and frequencies, and optical susceptibility, can be engineered by adding more semiconductor layers with different doping levels and adjusting their widths [354, 355]. However, due to lack of effective coupling of light with MQW, the large MQW nonlinearities have not been commonly utilized. This is because optical transitions between subbands are intrinsically polarized along the surface normal to the MQW layers. Plasmonic resonators placed on top of MQW allow the coupling, as it induces a z-polarized electric field inside the MQW and enhances the sub-band nonlinear response. Lee *et al* experimentally demonstrated well-designed plasmonic metasurfaces on top of MQW layered substrates (figure 59(a)) [346]. The MQW was made up of multi-layers of InGaAs/InAlAs [356]. The metasurface was designed to have highest second order susceptibility (χ_{zzz}) at 8064 nm with two distinct absorption peaks at wavelengths of 8064 nm and 16 128 nm. From a 400 nm-thick metasurface, strong SHG with a conversion efficiency of $\sim 2 \times 10^{-6}$ was achieved at a wavelength of ~ 8 μm at normal incidence. Thus the efficiency of generated higher order harmonics can be significantly increased by a suitable choice of metasurface.

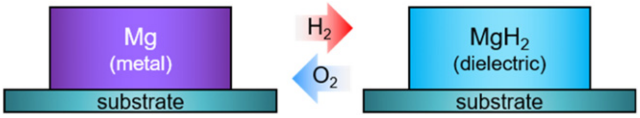

Figure 60. Schematics of the hydrogenation/dehydrogenation for Mg with hydrogen/oxygen exposure. Reprinted with permission from [363]. Copyright (2019) American Chemical Society.

Gomez-Diaz *et al* proposed T-shaped gold meta-atoms deposited on the grounded MQW with a back reflector to demonstrate 0.8% SHG conversion efficiency at 52 THz [357]. Also, they estimated the difference frequency generation (DFG) conversion efficiency of 0.01% at 5.5 THz. The conversion efficiency of DFG was increased slightly by implementing a similar T-shaped gold coated MQW unit element to achieve approximately 0.3% conversion efficiency ($\lambda = 5.4$ μm photons down converted to $\lambda = 12.9$ μm photons) [358]. Similar work has been done using plasmonic metasurfaces with dog-bone or SRR-shaped gold meta-atoms placed on top of MQWs [359, 360]. MQW metasurfaces have also been implemented to demonstrate THGs. Lee *et al* used an MQW metasurface to demonstrate high THG at a wavelength of 8.9 μm [361]. A THG conversion efficiency of 1.8×10^{-3}% was realized in 400 nm thick metasurfaces. High conversion efficiency was achieved because of a good mode overlap between the MQW and the plasmonic antennas at the fundamental and third harmonic frequencies. The concept of nonlinear continuous phase control using PB phase as discussed in section 6.1 can also be implemented in an MQW metasurface. Tymchenko *et al* purposed full control over the phase and amplitude of the SHG via implementation of gold-capped MQW split ring resonators (SRR) (figure 59(b)) [310]. Nookala *et al* demonstrated continuous phase control of the giant nonlinear second harmonic with the implementation of gold-capped MQW (SRR) gradient metasurfaces [362].

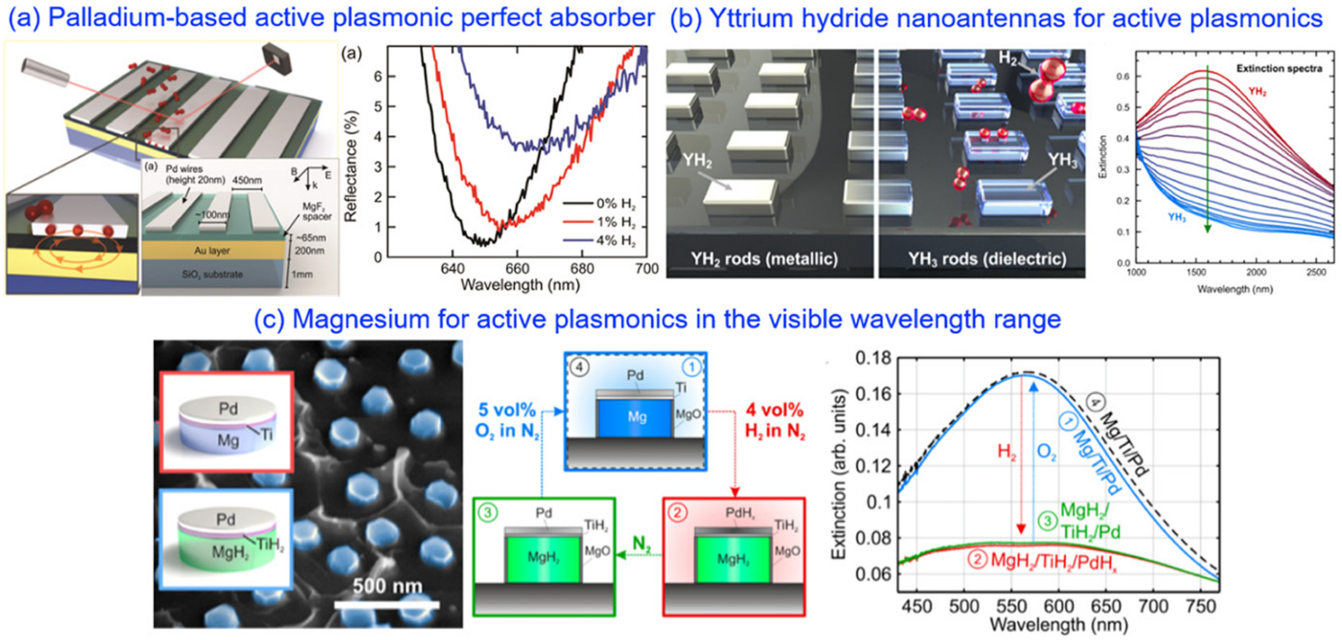

Figure 61. (a) Schematics of active plasmonic perfect absorber based on palladium and reflectance of the absorber for different hydrogen concentrations. Reprinted with permission from [364]. Copyright (2011) American Chemical Society. (b) Schematics of yttrium dihydride (YH_2)/trihydride (YH_3) nanorods on glass substrates and extinction spectra recorded every 4 s in the phase transition from YH_2 (red lines) to YH_3 (blue lines) when exposed to hydrogen. Reprinted with permission from [365]. Copyright (2014) American Chemical Society. (c) Schematic of Mg-based active plasmonics in the visible, switching between Mg and MgH_2 with the catalytic of a 10 nm Pd layer and 5 nm Ti buffer layer and extinction spectra of Mg/Ti/Pd unit element. Reprinted with permission from [366]. Copyright (2015) American Chemical Society.

Plasmonic metasurfaces integrated with MQW provide giant nonlinear conversion efficiency and can be designed to operate from near infrared to terahertz region. However, the main limitation in these metasurfaces comes from the relatively low saturation intensities. The saturation occurs at low input intensity due to very strong local fields in MQW volumes. The fundamental idea behind the integration of plasmonic metasurfaces is to maximize the mode overlapping, keeping a uniform z-component of the electric field distribution to lessen the impact of saturation. Further optimization of the metasurface geometry and the QW region could lead to larger higher harmonic conversion efficiency. Therefore, MQW integrated with plasmonic metasurfaces have high potential in achieving efficient nonlinear processes and could have significant impact on a variety of applications such as THz generation/detection, frequency conversion, and phase conjugation.

Active nonlinear metasurfaces possess a unique ability to generate new frequencies of light and to modulate the complex refractive index via nonlinear optical processes under high intensity pulsed excitation. As with linear metasurfaces, the phase and wavefront of the generated new frequencies can be controlled by using the geometric phase variation of the metasurfaces. In addition, ultrafast all-optical nonlinear switching could be achieved due to the efficient modulation of the complex refractive index of the nonlinear metasurfaces. Such modulation has been demonstrated with speed in the terahertz frequency. Although nonlinear metasurfaces show several distinct advantages over other tuning mechanisms, they have some intrinsic drawbacks, for instance, low conversion efficiency for frequency conversion and the requirement of ultra-high excitation intensity. Furthermore, although large Kerr nonlinearity and refractive index change can be achieved in nonlinear metasurfaces, it is almost impossible to individually alter properties of each meta-atom. In addition, a high-power external light source is required in most of the nonlinear metasurface applications, which makes this approach less practical for compact device applications. However, there is significant room to improve on the power requirement for the nonlinear metasurfaces (such as integrating with MQW material). With the discovery of new material with intrinsic higher nonlinearity and well-designed nonlinear metasurfaces, most of the challenges can be addressed, and practical novel applications such as dynamic holography and ultrafast laser pulse shaping can be developed (see section 9).

7. Tunable metasurfaces based hydride-loading transition metal

Besides the mentioned phase change/transition materials in section 3, there is another kind of active material that has metal to dielectric transition with exposure to hydrogen (H_2). The dynamic optical properties caused by the transition between metal and dielectric can be utilized to enable active metasurfaces with a variety of functionalities. Here we take magnesium (Mg) as an example to illustrate the hydride-loading mechanism [363] (figure 60). Mg nanostructure exhibits LSPRs. Meanwhile, Mg can be hydrogenated to MgH_2 with

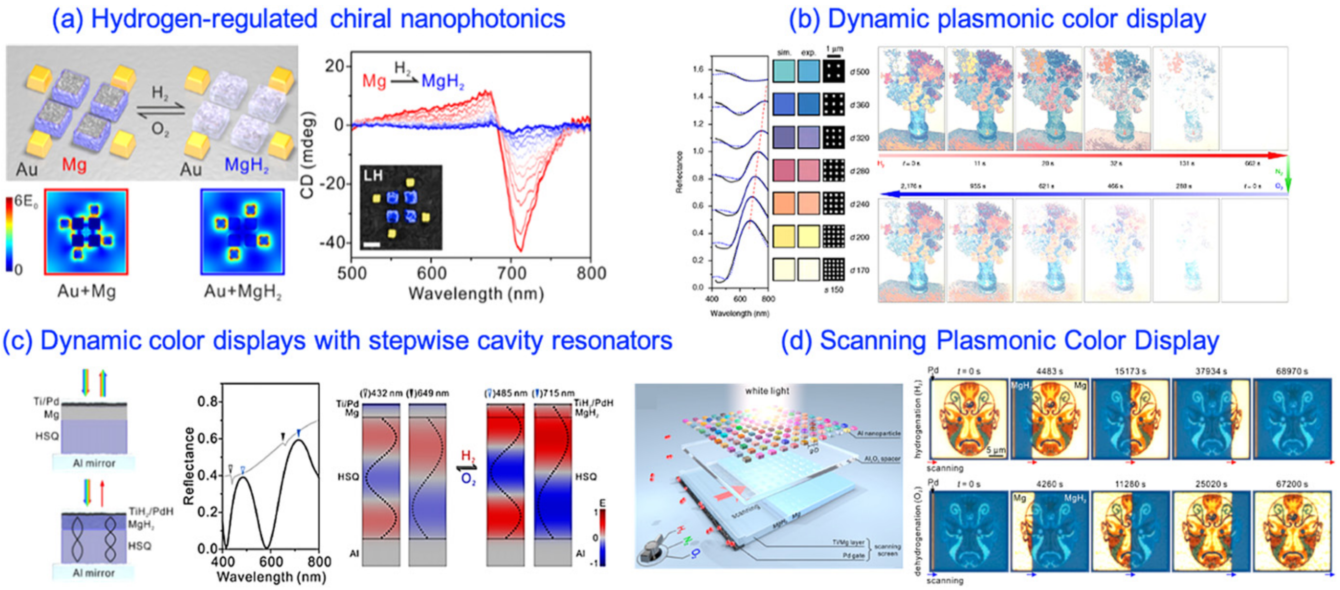

Figure 62. (a) Schematic of the chiroptical response in the hydrogenation/dehydrogenation cycle, with simulated electrical field of the hybrid structure before and after H_2, and measured circular dichroism spectra of the left-handed sample upon H_2 interacting against time. Reprinted with permission from [367]. Copyright (2016) American Chemical Society. (b) Schematic of a dynamic plasmonic color display, reflectance spectra, white light images and corresponding SEM images of the selected color pixels, and dynamic display evolution of arbitrary images with hydrogenation/dehydrogenation. Reprinted by permission from Springer Nature Customer Service Centre GmbH: Nature Communications. [368] © 2017. (c) Schematic of dynamic color displays with cavity resonators and simulated reflectance spectra of tile in the blank and color states, and the electric field intensities of the different Fabry–Pérot resonances in H_2 and O_2. Reprinted with permission from [369]. Copyright (2017) American Chemical Society. (d) Sketch of the scanning plasmonic color display and the optical micrograph displays in time evolution. Reprinted with permission from [370]. Copyright (2018) American Chemical Society.

H_2 exposure. MgH_2 can be treated as dielectric with low loss and refractive index $n + ik = 1.95 + 0.01i$ ($\varepsilon_r = 1.97$) at visible and near-infrared wavelengths. The transition of Mg to MgH_2 is reversible in H_2/oxygen (O_2) atmosphere. The large permittivity contrast between Mg ($\varepsilon_r = -2$) and MgH_2 ($\varepsilon_r = 1.97$) offers an opportunity to develop dynamic metasurfaces.

For an early demonstration in 2011, Tittl *et al* experimentally realized a plasmonic perfect absorber based on palladium (Pd) in the visible range (figure 61(a)) [364]. The Pd exhibits significant changes in dielectric function under hydrogen exposure due to phase transition from a metal to a dielectric, the lattice expansion, and a change in the Fermi level of the conduction electrons. They demonstrated a reversible increase in reflectance (0.5%–4.9%) with a maximum spectral shift of 19 nm in the presence of 4% H_2 concentration and response time of 10–50 s at an operation wavelength of 650 nm. The Pd-based plasmonic perfect absorber was able to reliably detect the low concentration of H_2 in the air, exhibiting the possibility for realization of tunable metasurface with exposure to hydrogen. In 2013, Strohfeldt *et al* fabricated an array of yttrium nanorods and exploited the transition between metallic yttrium dihydride (YH_2) and insulating YH_3 due to hydrogen exposure (figure 61(b)) [365]. The plasmon resonance of YH_2 nanostructure at 1580 nm completely vanished in 50 s after the transition to YH_3 with 5% vol. H_2 in N_2. In 2015, Sterl *et al* demonstrated that Mg nano-disks with a palladium (Pd) cap and a titanium (Ti) buffer layer can be reversibly switched between the metallic Mg to dielectric MgH_2 with the exposure to hydrogen/oxygen gas (figure 61(c)) [366]. When the Mg/Ti/Pd unit element is exposed to hydrogen gas (4% vol. in N_2), the Pd cap catalyzes the splitting of the H_2 into atomic hydrogen so that the atomic hydrogen can diffuse into the Ti layer and Mg nanodisks. The transition of metallic Mg to dielectric MgH_2 results in the almost complete disappearance of the plasmonic resonance at the visible wavelength in a few minutes. Reversibly, with the exposure of O_2 diluted in N_2 to the MgH_2/Ti/Pd unit element, the resonance is fully restored in ∼15 min. Note that Mg has better plasmonic performance with excellent extinction efficiencies in UV to visible range (blue) compared to Y and Pd. In particular, compared to hydrogenation of Y and Pd that release the stored H_2 once its pressure drops off, Mg can be partially hydrogenated, preserving the hydrogen and retaining at any states between Mg and MgH_2 (in absence of O_2) by methods of regulating the duration and the concentration of the H_2/O_2.

As mentioned before, Mg with its reversible transition from metal to dielectric is one of active material candidates for realizing dynamic metasurfaces with a variety of functionalities. In 2016, Duan *et al* proposed that hybrid plasmonic metamolecules with gold (Au) and magnesium elements can realize dynamically-controlled plasmonic chirality in the hydrogenation process (figure 62(a)) [367]. The Mg blocks with satellite Au elements are designed to generate sharp circular dichroism spectra in the visible range. However, when the Mg hydrogenates to MgH_2, the hybrid metamolecule becomes achiral with a featureless circular dichroism spectrum. Therefore, the chiroptical response can be switchable in the hydrogenation or dehydrogenation process of Mg/MgH_2. In 2017, they also

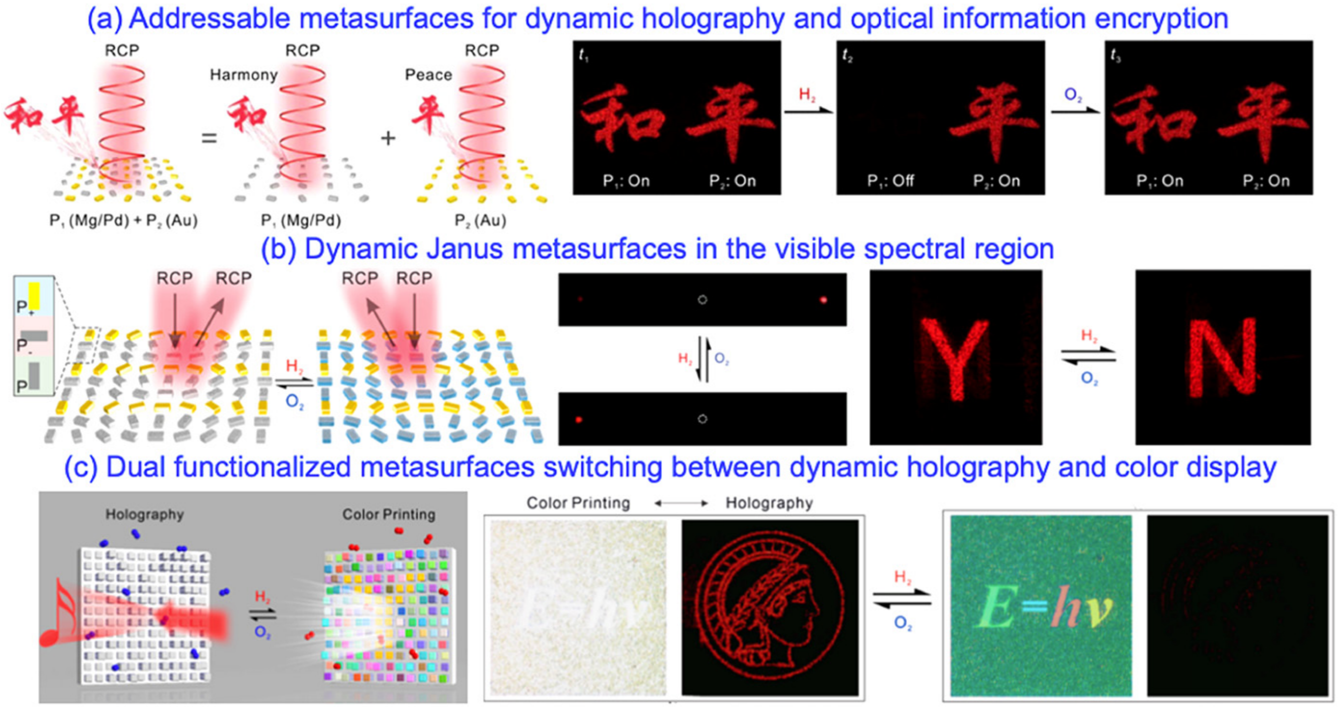

Figure 63. (a) Two holographic images reconstructed from two independent phase profiles including Mg/Pd (P_1) and Au (P_2) as dynamic and static pixels and evolutions of P_1 and P_2 in the hydrogenation/dehydrogenation cycle. From [371]. Reprinted with permission from AAAS. (b) Schematic of dynamic beam steering with Janus metasurfaces, with representative snapshots of the reflected anomalous light and holographic 'Y' and 'N' at the same spatial location after hydrogenation and dehydrogenation. Reprinted with permission from [372]. Copyright (2018) American Chemical Society. (c) Schematic of the dual function switching between dynamic holography and dynamic color display by hydrogenation (H_2) and dehydrogenation (O_2), switching between dynamic color display and dynamic hologram during hydrogenation and dehydrogenation. Reprinted with permission from [373]. Copyright (2020) American Chemical Society.

demonstrated a dynamic plasmonic color display using Mg metasurfaces between capping Ti/Pd layers and a Ti adhesion layer (figure 62(b)) [368]. The brilliant colors can be generated by LSPRs of individual Mg pillars by a lattice with periodicity *s* and diameter *d*. The phase transition of Mg to MgH_2 due to hydrogen exposure on the carefully designed metasurfaces can enable the active behaviors of the plasmonic display, such as plasmonic subwavelength animations, highly secure information encryptions, and dynamic display of arbitrary vivid images. In the same year, they implemented the dynamic color displays by using Mg-based pixelated Fabry–Pérot cavities with various heights by a method of gray scale nanolithography (figure 62(c)) [369]. The Fabry–Pérot cavities are composed of the Mg/Ti/Pd capping layers, stepwise pillars, and the Al mirrors. Firstly, the capping layers reflect the visible light, leading to the blank state, without color generation. When Mg is hydrogenated and transformed to MgH_2, the Fabry–Pérot cavities are formed and reflect narrow spectrum of light to generate the high-contrast colors. Note that the dynamic display switching processes between black/white initial state and final color state takes 78 and 35 s, respectively. In 2018, inspired by the macroscopic scanning devices, they realized the scanning control over plasmonic pixels (i.e., Al nanoblocks) on top of a Mg layer as a scanning screen (figure 62(d)) [370]. The scanning process is triggered by the Pd gate which can catalyze the transition process of Mg/MgH_2 as mentioned in [366]. Moreover, they demonstrated the potential application for information encryption with a quick response code.

In 2018, Li *et al* from the same group demonstrated addressable Mg-based metasurfaces for dynamic holography and optical information encryption (figure 63(a)) [371]. The dynamic plasmonic pixel can be utilized to control the phase of wavefronts by the method of the PB phase (i.e., geometric phase). The whole metasurface pattern is multiplexed with two independent phase profiles with dynamic Mg/Pd (P_1) and static Au (P_2) pixels. Two holographic images (Chinese characters, 'harmony' and 'peace') are encoded into left and right phase profiles, respectively. In the atmosphere of H_2, the two Chinese words are merged, but with O_2, the word 'harmony' vanished due to the metal to dielectric transition of the Mg/MgH_2, but the word 'peace' remains. In the same year, they also proposed the dynamic Janus metasurfaces that offer a variety of optical functionalities (beam steering, bifocal lensing, dynamic holography, and dual optical function switching) at visible wavelengths with different orientations of the triple-pixel unit (one Au rod and two Mg rods) (figure 63(b)) [372]. Very recently, they demonstrated the multifunctionalities of dual-function switching between dynamic holography in white light and dynamic color display at an operation wavelength of 633 nm on a single piece of Mg-based metasurfaces (figure 63(c)) [373].

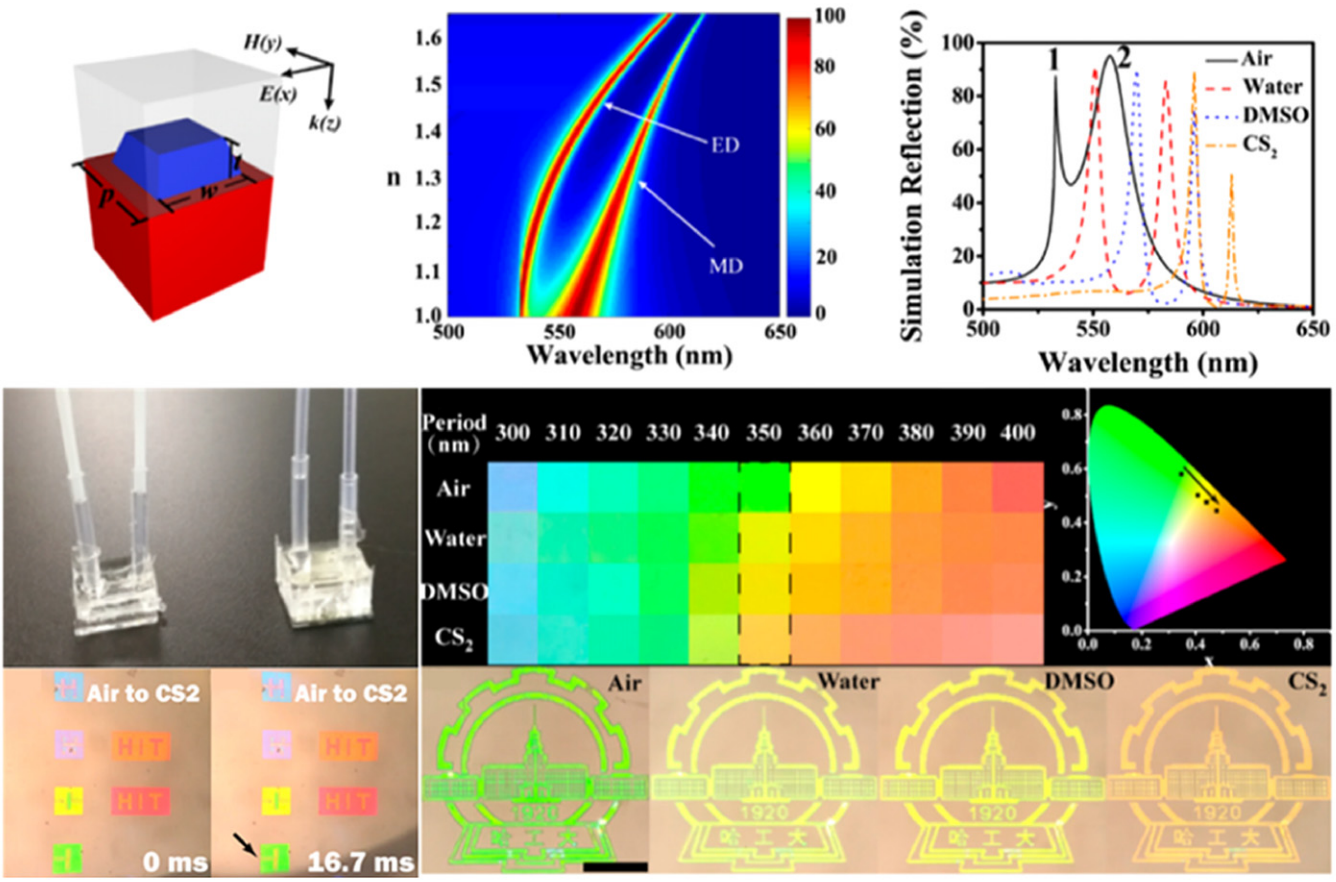

Figure 64. (Top) Schematics of the TiO_2 metasurface unit element, with reflection spectra against external refractive index and reflection spectra of TiO_2 metasurfaces immersed into different refractive index liquids. (Middle) Image of TiO_2-based metasurfaces with microfluidic channels and the measured reflection color for TiO_2 metasurfaces under a bright microscope in different refractive index liquids. (Bottom) Time evolution of the structural colors and color logo of university of Harbin Institute of Technology. Reprinted with permission from [374]. Copyright (2018) American Chemical Society.

Hydride-loading transition metals (Pd, Y and Mg) have higher chemical reactivity than conventionally utilized plasmonic material candidates (e.g., Au, Ag, and Al). The reversible reactivity offers the unique phase transition from metal to dielectric and large refractive index for the realization of dynamic metasurfaces with a variety of functionalities, for instance, active color display, beam steering, bifocal lens, dynamic holography, etc. The downside of this tunable mechanism is that the hydrogenation and dehydrogenation processes require a specific environment with purified H_2 and O_2 flow. In addition, although the response time of this mechanism has been improved to as quick as ∼25 s for hydrogenation (75 s for dehydrogenation), it is a slower than that of other mechanisms used for active metasurfaces. However, there are still some interesting topics and applications utilizing the mechanism of hydride-loading transition metals (see prospective applications in section 9).

8. Microfluidic tunable metasurfaces

Besides the tunable methods mentioned above, there are some other mechanisms for tuning the metasurface properties dynamically. One of active mechanisms is to change the external refractive index surrounding the metasurfaces to modulate the optical responses including spectral shift, amplitude, and phase. In 2018, Sun *et al* experimentally demonstrated real-time tunable colors spanning the visible spectrum (500–650 nm) [374]. The metasurface unit element fabricated on a 15 nm ITO coated glass is composed of TiO_2-based nanoblocks embedded into a polymeric PDMS microfluidic channel (figure 64, top). The resonances of the electric dipole and magnetic dipole with period of 350 nm and gap of 60 nm exhibit resonance wavelength shift toward longer wavelength for 60 nm (530–590 nm) and 50 nm (560–610 nm), respectively, when the ambient refractive index gradually changes from 1.0 to 1.6. The microfluidic channels can be fabricated (<100 nm in width) and offer the precise control of liquid droplets. The two resonances of electric/magnetic dipole shift toward longer wavelengths and their simulated reflection is preserved with the external environment changing from air ($n = 1.0$) to water ($n = 1.33$), dimethyl sulfoxide ($n = 1.4795$), and CS_2 ($n = 1.6276$). By designing the period of unit element, the reflection peak can be selected in the whole visible wavelength (figure 64, middle). By injecting various kind of microfluid, the atmosphere of the TiO_2-metasurface

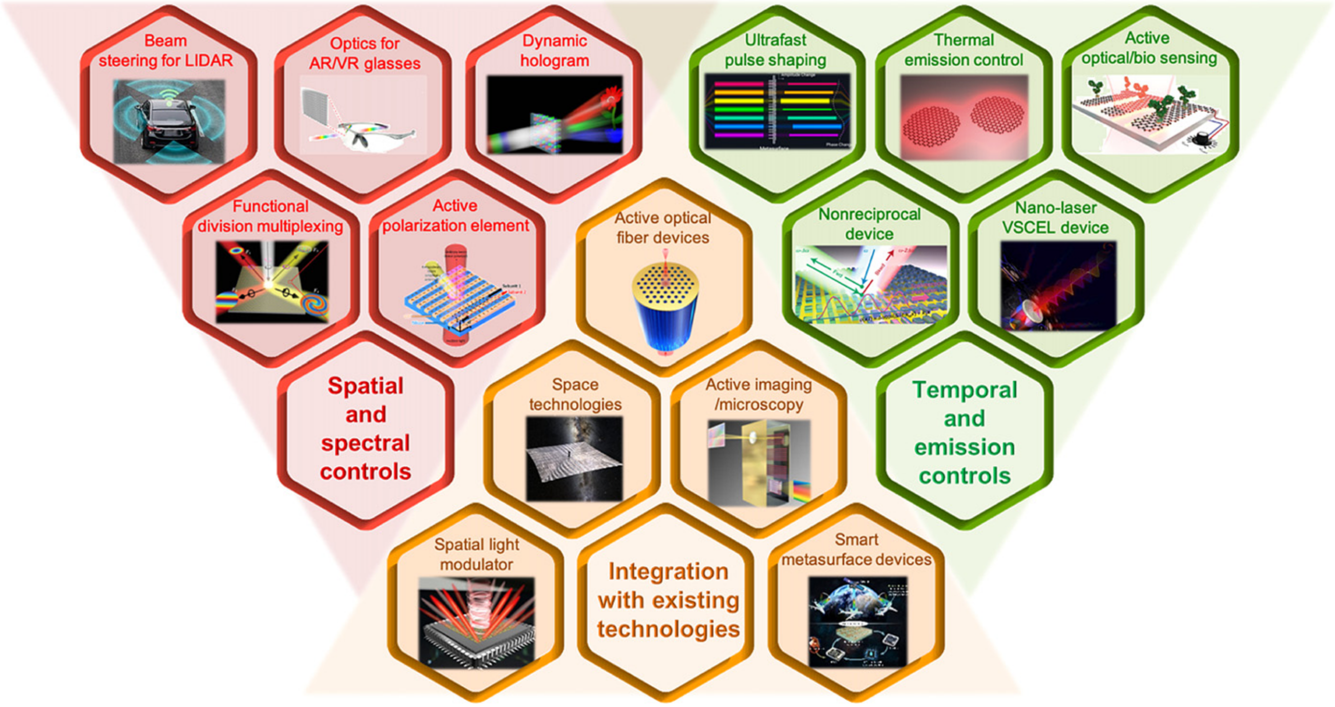

Figure 65. Overview of prospective applications. (I) Prospective applications based on the spatial and spectral controls of active metasurfaces, (II) prospective applications based on the temporal and emission controls of active metasurfaces, and (III) prospective applications based on integrating tunable metasurfaces with existing technologies.

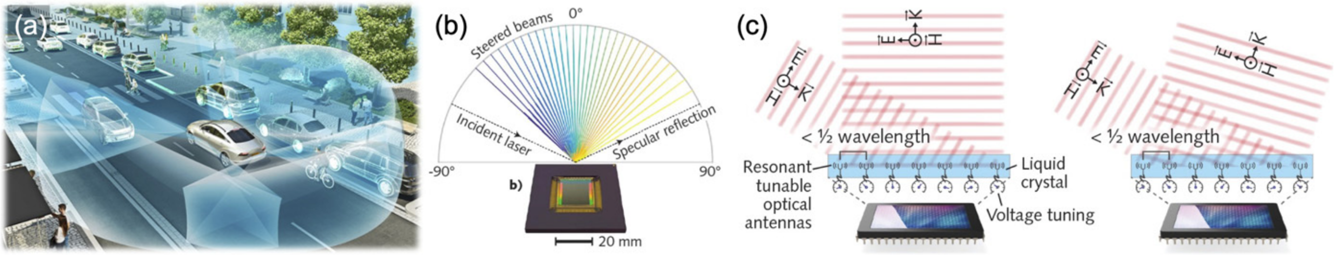

Figure 66. Tunable metasurfaces as the beam steering element for LIDAR applications. (a) Schematic of LIDAR for self-driving cars. Reproduced with permission from [375]. © Laser Focus World [Continental Automotive] and (b) on-chip beam steering element based on tunable metasurfaces. (c) An illustration of the operation of LC metasurface beam steering with TM-polarized incidence. The LC metasurface steers light to two different output angles, determined by the spatial frequency of the phase-modulation pattern applied to the array of tunable resonators on the LC metasurface. (b and c) Reproduced with permission from [376]. © Laser Focus World.

is changed to a different refractive index and the corresponding reflected color can be precisely modulated with response time of ∼16.7 ms (figure 64, bottom). The proposed microfluidic reconfigurable all-dielectric metasurface has the capability of erasing and restoring the information encoded in the metasurfaces, which can find potential applications in optical information encryption and functional color display.

This microfluidic approach offers an alternative way in designing active metasurfaces. The distinct colors can be produced via injecting various solvents. Compared with the previous techniques, the response time is only in millisecond scale. Although the microfluidic method increases the complexity of the fabrication process and tuning operations, it can benefit sensing applications as a 'lab on a chip.' Moreover, the use of high-resolution microfluidic channel and metasurface can potentially further development of a pixel-size color transition display.

9. Prospective applications for active optical metasurfaces

Various mechanisms to realize the dynamic control of electromagnetic waves with active metasurfaces have been summarized and presented in this article. Active metasurfaces provide control of both the amplitude and phase of optical waves with subwavelength spatial resolution, high operation speed, and low power consumption (figure 3), thus exhibiting significant promise for the next generation of ultracompact, lightweight, high-efficiency applications, including imaging/display, remote/bio-sensing, and communication

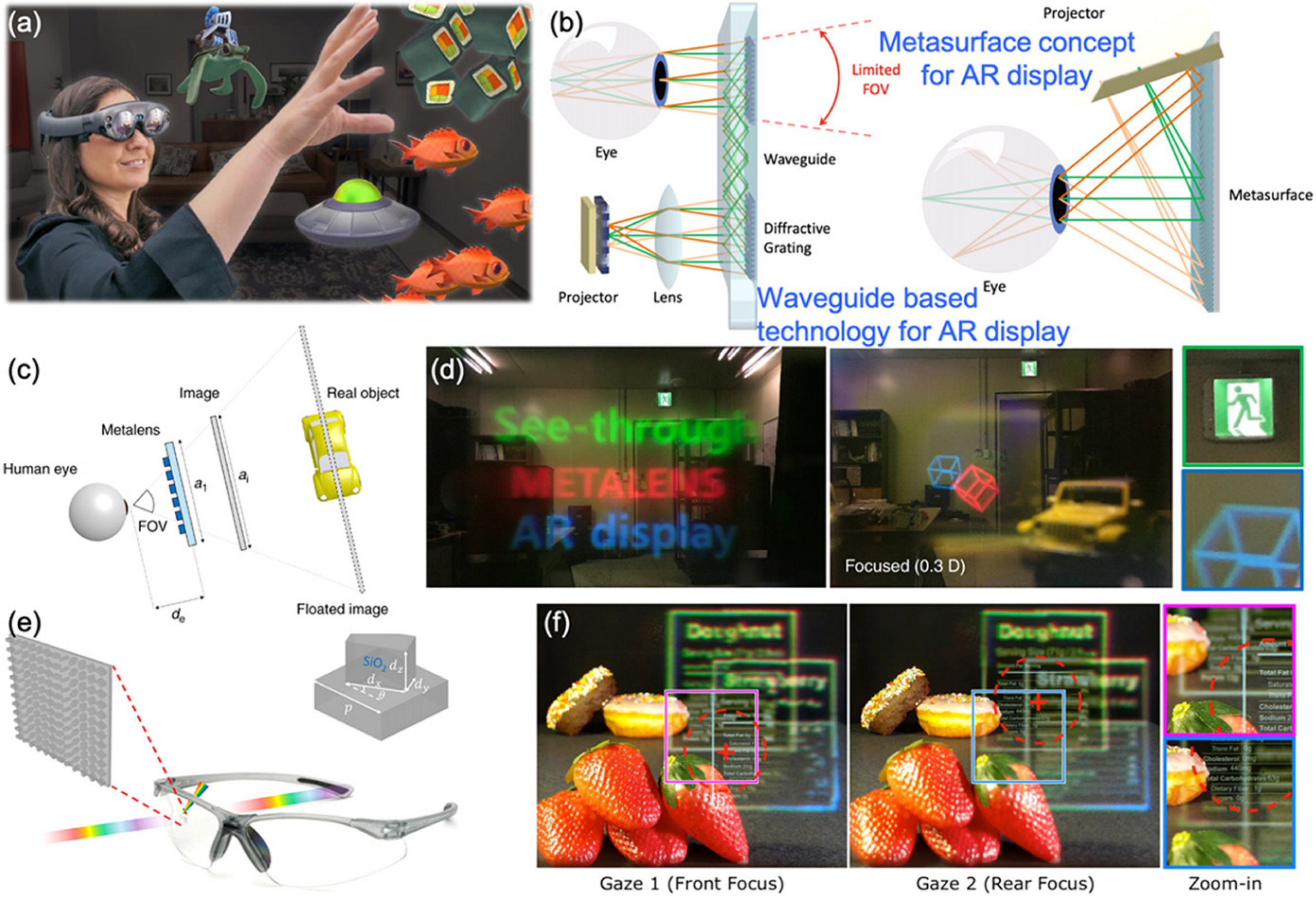

Figure 67. Metasurfaces for VR/AR display applications. (a) Image of AR glass (@Magic Leap Inc.). Reproduced with permission from [384]. © The Wall Street Journal. (b) Schematic of (left) key technology for AR near-eye display based on diffraction grating and optical waveguide and (right) metasurface concept for AR display. Reproduced with permission from [385]. © SPIE. (c) Schematic of the see-through near-eye display system with a metalens as a transmission-type eyepiece. (d) (Left) Single-color AR images with real objects for red, green, and blue colors. (Right) Demonstration of the floating depth of the image. Side images in green and blue boxes are part of the original, showing that the emergency light and blue cube are at the same depth. (c and d) Reproduced from [382]. CC BY 4.0. (e) Conceptual diagram of eyewear integrated with a silica metasurface where a small portion of an incident light is redirected toward a photodetection/imaging unit that is built into the frame of a pair of glasses. Reprinted with permission from [383]. Copyright (2017) American Chemical Society. (f) Display results from Foveated AR prototype with tunable lens. By tracking the user's gaze direction (red cross), the system dynamically provides high-resolution inset images to the foveal region and low-resolution large-FOV images to the periphery. Reproduced with permission from [386]. Copyright © 2019 ACM.

technologies. However, most of the active metasurfaces discussed in the previous sections are limited on the realization of basic optical functions, such as control of optical phase and amplitude, light steering, tunable focal length, etc, and advanced device functionalities and new technologies from active metasurfaces are yet to be developed.

In this section, we will discuss several prospective applications and emerging technologies based on the use of tunable optical metasurfaces. Some proof-of-concept applications based on tunable optical metasurfaces have been demonstrated and will be presented in the section. While some of the other applications have not been realized so far, we anticipate significant new advances when the tunable mechanisms are further developed in the coming years. We will focus in particularly on prospective applications based on three aspects (figure 65): (I) prospective applications based on the spatial and spectral controls of active metasurfaces, (II) prospective applications based on the temporal and emission controls of active metasurfaces, and (III) prospective applications based on integrating tunable metasurfaces with existing technologies.

9.1. Prospective applications with spatial and spectral control of active metasurfaces

9.1.1. Beam steering element for light detection and ranging applications (LIDAR). Light detection and ranging (LIDAR), an active remote sensing system, is one of the most important technologies for driver-assisted and fully autonomous vehicles. The LIDAR system in autonomous vehicles typically illuminates the surrounding area with a steerable and tightly-focused beam focused in all directions by spinning the light via a mechanical moving mirror or MEMS-mirrors and measuring more than one million points per second of the reflected light with a sensor to monitor static or moving objects nearby

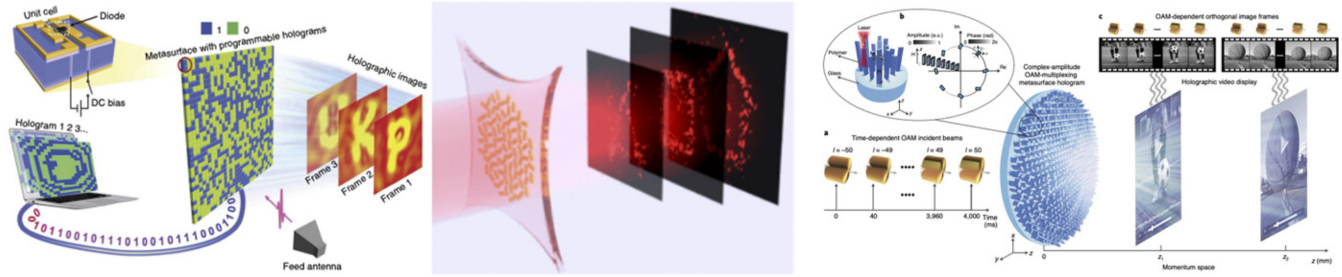

(a) Reprogrammable metasurface hologram composed of semiconductor diode

(b) Multiplexed metasurface hologram on a flexible substrate

(c) Orbital angular momentum holography in momentum space

Figure 68. Active holography based on metasurfaces. (a) Dynamic metasurface hologram composed of a semiconductor diode with binary modulation in the microwave region. Reproduced from [85]. CC BY 4.0. (b) Reconfigurable holographic imaging realized on a flexible substrate by mechanical strain. Reprinted with permission from [388]. Copyright (2017) American Chemical Society. (c) Complex-amplitude metasurface-based orbital angular momentum holography in momentum space. Reprinted by permission from Springer Nature Customer Service Centre GmbH: Nature Nanotechnology. [389] © 2020.

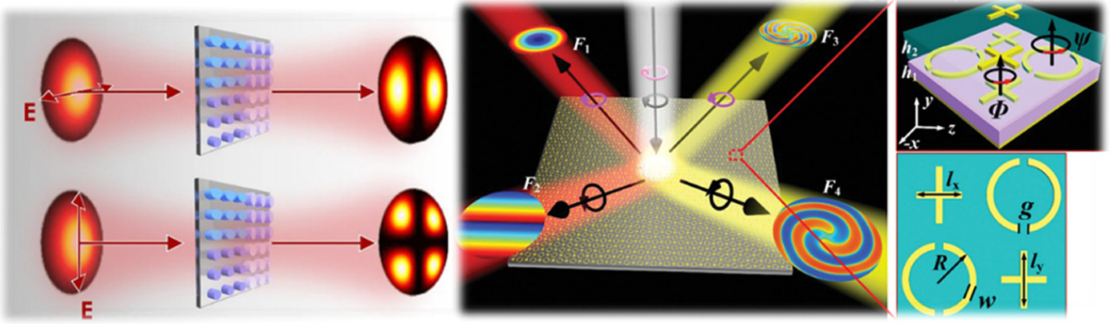

(a) Mode multiplexing in spatial domain

(b) Mode- and spin-decoupling for wavevector and frequency multiplexing

(c) Multi-channel vortex beam generation using optical metausrface

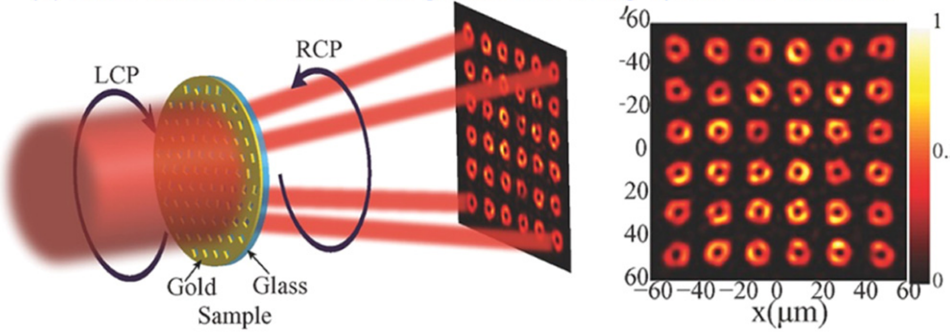

Figure 69. Concept of space, mode, spin, and frequency division multiplexing using metasurfaces. (a) Schematic of mode multiplexing in spatial domain with ultrathin metasurfaces that convert incoming Gaussian LP_{01} modes into LP_{11} and LP_{21} modes, enabling mode multiplexing. [393] John Wiley & Sons. © 2018 WILEY-VCH Verlag GmbH & Co. KGaA, Weinheim. (b) Schematic of the quad-port metasurface for mode- and spin-decoupling for wavevector and frequency multiplexing. [394] John Wiley & Sons. © 2019 WILEY-VCH Verlag GmbH & Co. KGaA, Weinheim. (c) Illustration of multi-channel vortex beam generation using optical metasurfaces. [396] John Wiley & Sons. © 2017 WILEY-VCH Verlag GmbH & Co. KGaA, Weinheim.

($<$200–300 m) in a real-time environment (figure 66(a)) [375]. However, current LIDAR systems are typically bulky and slow, and they have low spatial resolution for large field of view (FOV) applications due to the mechanical counterparts. Therefore, there is a need for developing non-mechanical, compact, and efficient beam steering elements for LIDAR applications (e.g., in figures 66(b) and (c)).

Tunable metasurfaces with phase and amplitude control on individual elements providing ultrafast and low-power consumption responses are a promising solution for development of a lightweight non-mechanical LIDAR device with enhanced resolution. As discussed in the previous sections, several proof-of-concept beam steering elements have been demonstrated with active metasurfaces based on different mechanisms, including via electrical conducting oxide field-effect dynamic metasurfaces [116, 124, 131], electronically-driven LC based reconfigurable metasurfaces [177], and MEMS-controlled metasurfaces [267] (see overview in table 1). For

(a) Electrical control of the light polarization

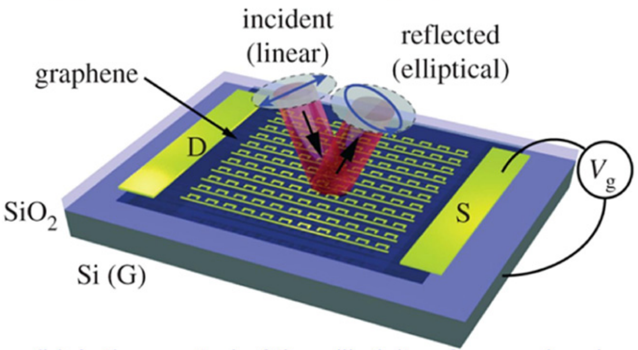

(b) Active control of the ellipticity of anomalously diffracted beam

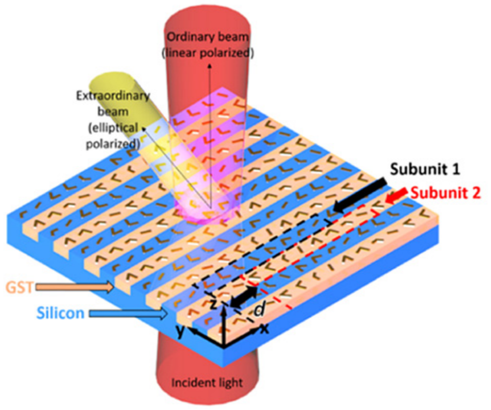

Figure 70. Active metasurfaces for tunable polarization control devices. (a) Schematic of the electric control of the polarization state of light using graphene-integrated anisotropic metasurfaces. The active metasurface converts linearly polarized incident light to elliptical polarization by electrical gating. Reproduced from [401] with permission of The Royal Society of Chemistry. (b) Schematic of the GST-based dynamic metasurface for active tunability of the ellipticity of anomalously diffracted beams. Reproduced from [211]. CC BY 4.0.

application as a beam steering device, the gate-tunable conducting oxide metasurfaces have significant potential advantages in term of large phase modulation, high operation speed, a small pixelized element which should allow better spatial resolution, and lower energy consumption. However, the low efficiency and difficulty with integration into large-dimension devices due to leakage current of the insulating dielectric oxide need to be significantly improved for actual device application. MEMS-based metasurfaces show promise for large phase modulation and high device efficiency; however, the limiting factors are low operation speed (few hundred kHz) and difficulty in pixelating individual unit elements. The LC based metasurfaces provide an efficient way to modulate phase and amplitude with moderate efficiency and operation speed, but the micron-size pixelized dimension limits the resolution of steering angle, and there is slow switching speed (1 kHz). Further research is required to improve the performance metrics of tunable metasurfaces as the beam steering elements for commercial LIDAR devices.

Despite the challenges, the startup company Lumotive has recently developed a reflective LC based metasurface to serve as the beam steering element for its LIDAR technology (figures 66(b) and (c)) [376]. The company demonstrated a device with uniform steering efficiency across a large FOV of 120° (uniform efficiency across the FOV), an aperture size of 25×25 mm^2, and a switching speed of 25 μs operating at a wavelength of 980 nm, demonstrating a significant promise for a viable active-metasurface-based LIDAR system with low cost, high reliability, and small size.

9.1.2. Tunable metasurfaces for augmented reality/virtual reality applications.

Augmented reality (AR)/virtual reality (VR) is a rapidly growing technology that involves integration of computer-generated virtual information into real-world perceptions (figure 67(a)). The near-eye display, which typically consists of microdisplay and imaging optics, is the core hardware for the AR/VR experience. Among different near-eye display methods, a diffractive waveguide consisting of an optical waveguide and a diffraction grating is a common technique. Light (the image) from the microdisplay (e.g., from the side of the glass) couples in the optical waveguide through the diffraction grating and reaches the eye (figure 67(b)) [377, 378]. However, the AR glasses utilizing the waveguide coupler technology typically exhibit a small FOV. In addition, limitations might arise to achieving the best compromise between performance metrics such as transmission/reflection coupling efficiency, transparency of the glass, color uniformity and resolution over the eyebox and FOV, spectral dispersion, form factor, and device dimensions (see details about waveguide coupler technologies for AR glasses in [378]).

Metasurfaces provide an alternative solution for developing ultrathin optical components for AR/VR glasses due to their unique ability to bend and shape the light, e.g., their highly efficient diffraction with large incidence angle (figure 67(b), right) [379–381]. Several attempts have been made to combine metasurface optics for AR/VR applications [379–383]. Using a see-through metalens with high numerical aperture and broadband characteristics, Lee *et al* demonstrated a compact near-eye display system for AR with a wide FOV (figures 67(c) and (d)) [382]. Li *et al* demonstrated an all-silica beam information detector that not only affords robust phase manipulation for signal generation, but also preserves the original incident wave fronts, showing promise for AR technologies by monitoring and optical signals *in situ* (figure 67(e)) [383].

AR/VR technologies might be further advanced with the use of tunable metasurfaces. With their controllable focal length and variable FOV, active metasurfaces might enable natural focus depth by dynamic focal length with a resolution that matches human visual acuity and wide FOV, thus solving the current challenging trade-offs between the eye box and FOV because of the compact nature of the metasurface (figure 67(f)) [386]. Moreover, active metasurfaces might allow functions for near-eye gaze tracking that help to enable a dynamic position and varifocal AR/VR system [387]. There is certainly a bright future for integrating active metasurfaces into AR/VR glasses. However, significant progress needs to be made on developing high transmissive and large area active metasurfaces with large tunability, high efficiency, high switching rate, low cost, and low external power consumption. Currently none

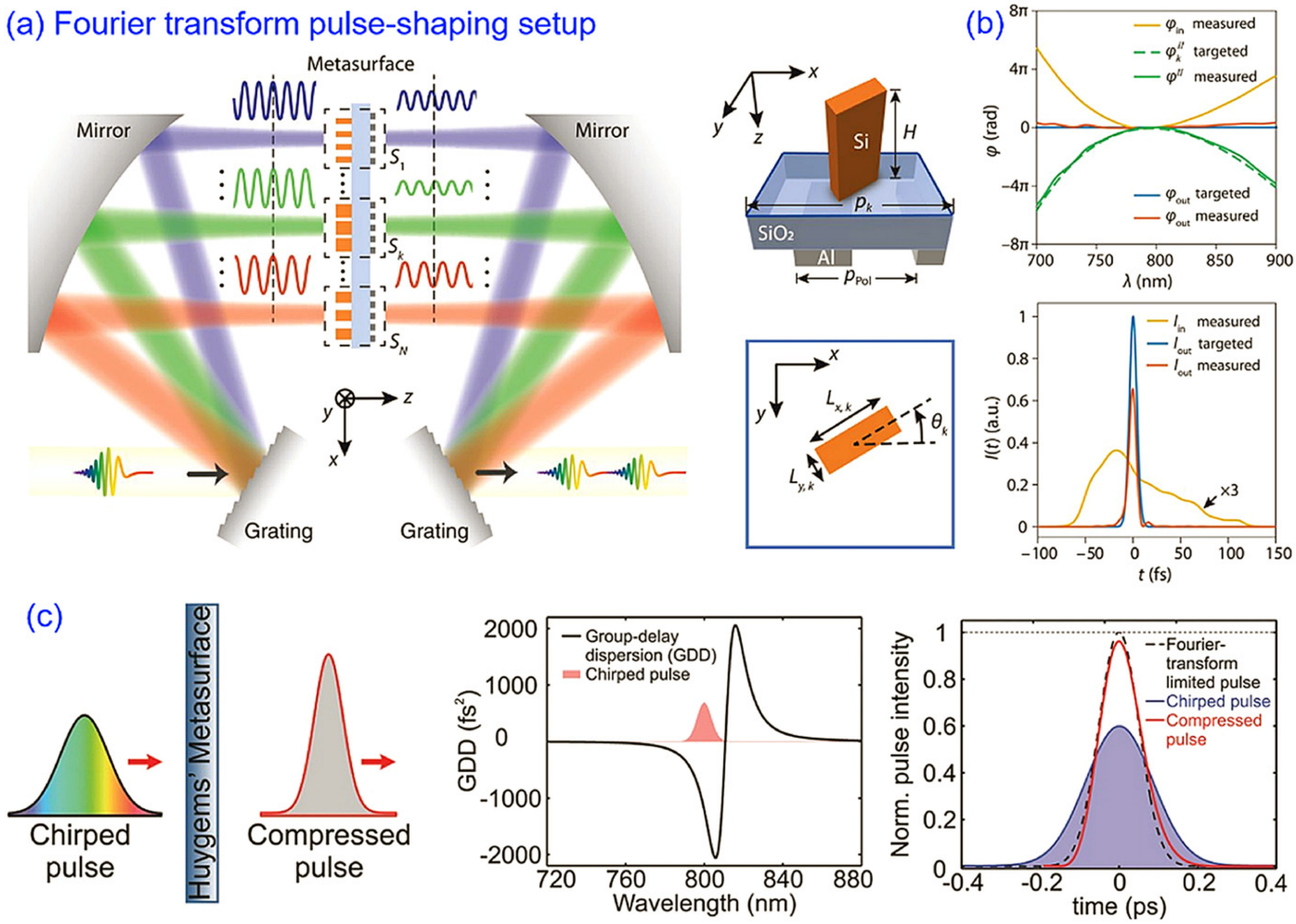

Figure 71. (a) Schematic of a Fourier transform pulse-shaping setup using pulse-shaping Si nanopillar metasurfaces. (b) (Top) Characterization of salient spectral phases of pulse compression enabled by the metasurface. (Bottom) Temporal profile of the targeted and measured output pulse (solid blue and solid red line) emerging from the pulse-shaper incorporating metasurface given the positively chirped input pulse (solid yellow line). (a and b) From [62]. Reprinted with permission from AAAS. (c) (Left) Conceptional image showing the recompression of a chirped pulse after passing a Huygens metasurface, (middle) group delay dispersion of the ideal Huygens metasurface. (Right) Simulated temporal profile of a 120 fs Fourier-limited pulse, of the chirped pulse, and of the recompressed pulse after propagation through six layers of the Huygens metasurface. [405] John Wiley & Sons. © 2015 WILEY-VCH Verlag GmbH & Co. KGaA, Weinheim.

of the reported mechanisms fulfill these requirements, but we believe some of these goals could be achieved with the significant advancement of tunable metasurfaces in the coming few years.

9.1.3. Dynamic holography. A hologram is a physical recording of an interference pattern of light, which makes use of light diffraction to reproduce a three-dimensional field of image. Holography has been widely employed in a large variety of applications such as 3D displays, data storage, metrology, biological image processing, etc. However, traditional holography technologies consist of bulky components with relatively large pixel sizes, which results in several fundamental physical limitations, including narrow bandwidth, small viewing angle, multiple diffraction orders, etc. Metasurfaces have demonstrated unparalleled advantages in the holography, e.g., subwavelength spatial resolution, ultra-thin thickness, large FOV, and high reconstruction efficiency [16, 71, 72, 91]. It is worth pointing out that the significantly reduced (subwavelength) pixel size of metasurface-based holography helps to eliminate the undesired diffraction orders, significantly improving the efficiency and quality of the image compared to traditional holograms. Furthermore, with flexible tunability of metasurfaces, the capacity and functionality of the holography can be further expanded to their practical applications in dynamic display, information processing, and data storage, etc.

Pioneering approaches have been employed to realize active metasurface hologram with promising results. Figure 68(a) shows a reprogrammable hologram metasurface in the microwave region [85]. In this structure, an electric diode is employed as the unit cell of the metasurface, which can be individually switched between 'on' and 'off' by applying voltages, enabling the generation of 1 bit coding holographic images. The theoretical reflection efficiency of this structure can reach >90%, and the phase difference between the '1' and '0' states is ∼180°. Although the hologram in their work is designed for much longer wavelengths (microwave) rather than in the optical wavelength, this early demonstration of an electrically-tunable metasurface-based

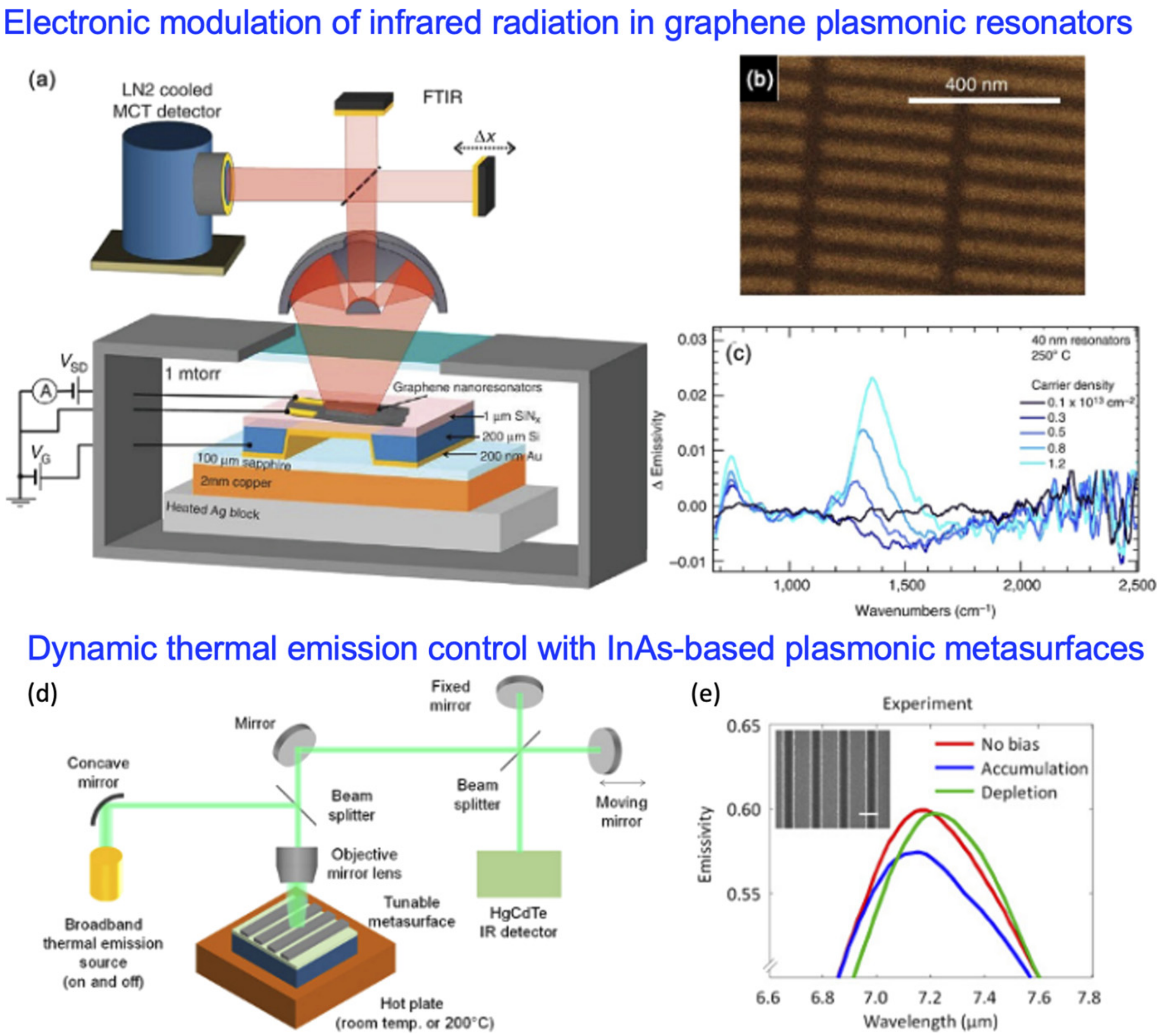

Figure 72. Control of thermal emission by active metasurfaces. (a) Schematic of thermal emission measurement setup. (b) A representative SEM image of 30 nm graphene nanoresonators on a 1 mm-thick SiN_x membrane. (c) Carrier density dependence of change in emissivity with respect to the charge neutral point for 40 nm graphene nanoresonators at 250 °C. Reprinted by permission from Springer Nature Customer Service Centre GmbH: Nature Communications. [417] © 2015. (d) Device schematic of an active metasurface with a high-doped (n++) InAs layer epitaxially grown on top of a GaAs substrate and used as a metallic mirror with a negative real dielectric constant. A low-doped (n+) InAs layer functions as an active layer for controlling emissivity. Corresponding SEM image of the structure is shown in right of figure. (d) FTIR microscope with reflectivity and emissivity measurement modes. (e) Emissivity spectrum for no bias (red curve), depletion (green curve) (+10 V), and accumulation (blue curve) (−7 V). From [183]. Reprinted with permission from AAAS.

hologram reveals an ultrafast modulation speed with a reconfiguration time of ∼33 ns. Malek *et al* reported reconfigurable metasurface holograms in the visible by patterning gold nanorods based geometric phase elements on a stretchable PDMS substrate (figure 68(b)). In this work, the hologram image can be modified by applying an isotropic strain to the flexible substrate by changing the position of image plane. In this way, multiplexed metasurface holographic images can be realized mechanically [388]. Furthermore, metasurface holograms can be dynamically controlled by chemical reactions [371] as discussed in section 7. Recently, Ren *et al* demonstrated a complex-amplitude metasurface-based orbital angular momentum (OAM) holography technology in momentum space (figure 68(c)) [389].

Currently there are several technical challenges that hinder the development of a tunable metasurface hologram, especially for the applications in the visible regime, including the difficulties in reducing the size of the electrodes into nanoscale for

(a) Electrically tunable plasmonic biosensor

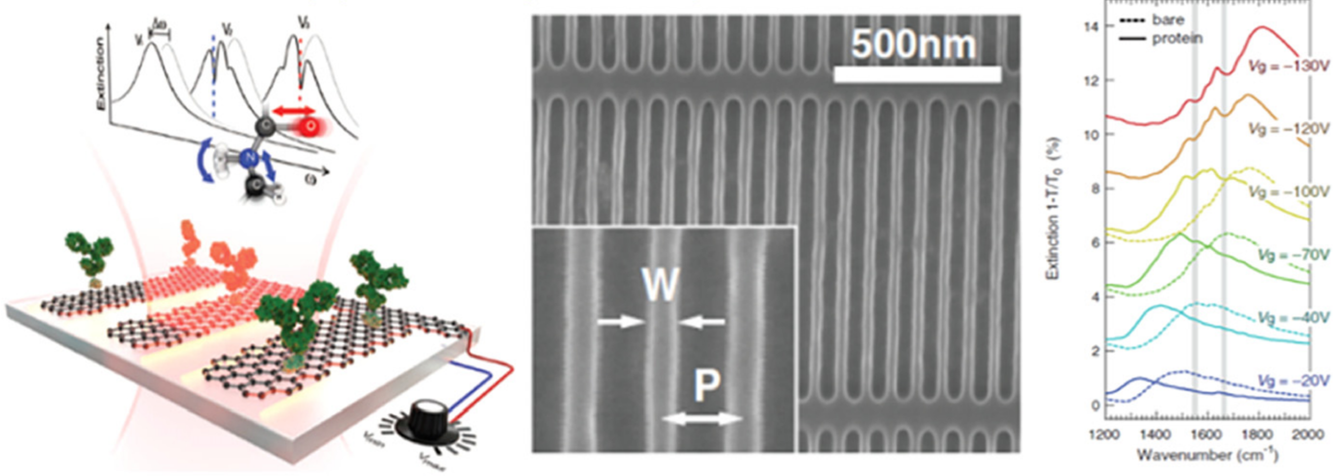

(b) High-index dielectric metasurface biosensor

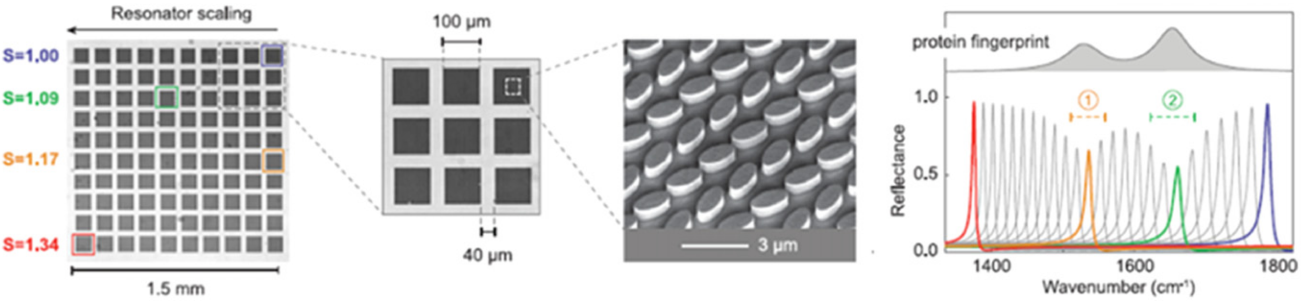

Figure 73. Metasurfaces-based biosensors. (a) Graphene-based plasmonic tunable biosensor in the mid infrared, and its extinction spectra under different biases. From [420]. Reprinted with permission from AAAS. (b) Two-dimensional array of high-index dielectric metasurface biosensing elements. From [422] . Reprinted with permission from AAAS.

electrical tuning of the metasurface hologram with pixel-level control of the metasurface elements with fast speed, due to the limitations of nanofabrication.

9.1.4. Space-, mode-, spin-, and frequency-division multiplexing for optical communications. Controlling the properties of light (e.g., spin and mode) allows an additional degree of freedom to enhance data transmission in optical communication. For instance, free-space based and optical-fiber based optical communication via orbital angular momentum and mode-division multiplexing have been recently demonstrated [390–394]. Metasurfaces provide a unique opportunity to engineer and convert the optical modes in a compact platform. For example, Kruk *et al* experimentally demonstrated the conversion of LP_{01} optical modes into LP_{11} and LP_{21} modes for a free-space optical communication system using highly transparent dielectric metasurfaces (figure 69(a)) [393]. The single metasurface is capable of mode multiplexing with an extinction ratio of >20 dB over the telecommunication C-band for data transfer signal of 100 Gb s^{-1}. Researchers have been able to utilize metasurfaces not only for mode-division multiplexing but also for spin-, space-, and frequency-division multiplexing (e.g., figure 69(b)) [80, 394, 395] and multichannel vortex beams (figure 69(c)) [396].

Having the ability to individually alter the optical phase and amplitude of the metasurface unit element, tunable metasurfaces provide an extra degree of freedom to dynamically convert the polarization, spin, and spatial domain for tunable multiplexing with controllable working states and tunable output (e.g., active conversion of orbital angular momentum modes and spatial optical modes). Although active multiplexing functions with coverable spin and spatial modes have not been demonstrated so far (other than ordinary beam steering and switching), we expect that reconfigurable metasurfaces will play an important role in developing integrated multiplexing metasurfaces with structured light for optical communication and imaging technologies.

9.1.5. Active polarization control elements. Optical metasurfaces provide a unique ability to spatially tailor the polarization state of light on a subwavelength scale optical element. Such control of the polarization state leads to unique properties such as polarization conversion and rotation, which in turn can lead to the development of a polarization-dependent hologram, multiplexer, detector, polarimeter, and even a polarization-based camera [55, 397–400]. Active control of the polarization state for each optical element will further advance polarization-based metasurface devices for imaging, sensing, communication, and spectroscopy applications.

To date, there are limited reports on the active control of the polarization state in dynamic metasurfaces. Dutta-Gupta

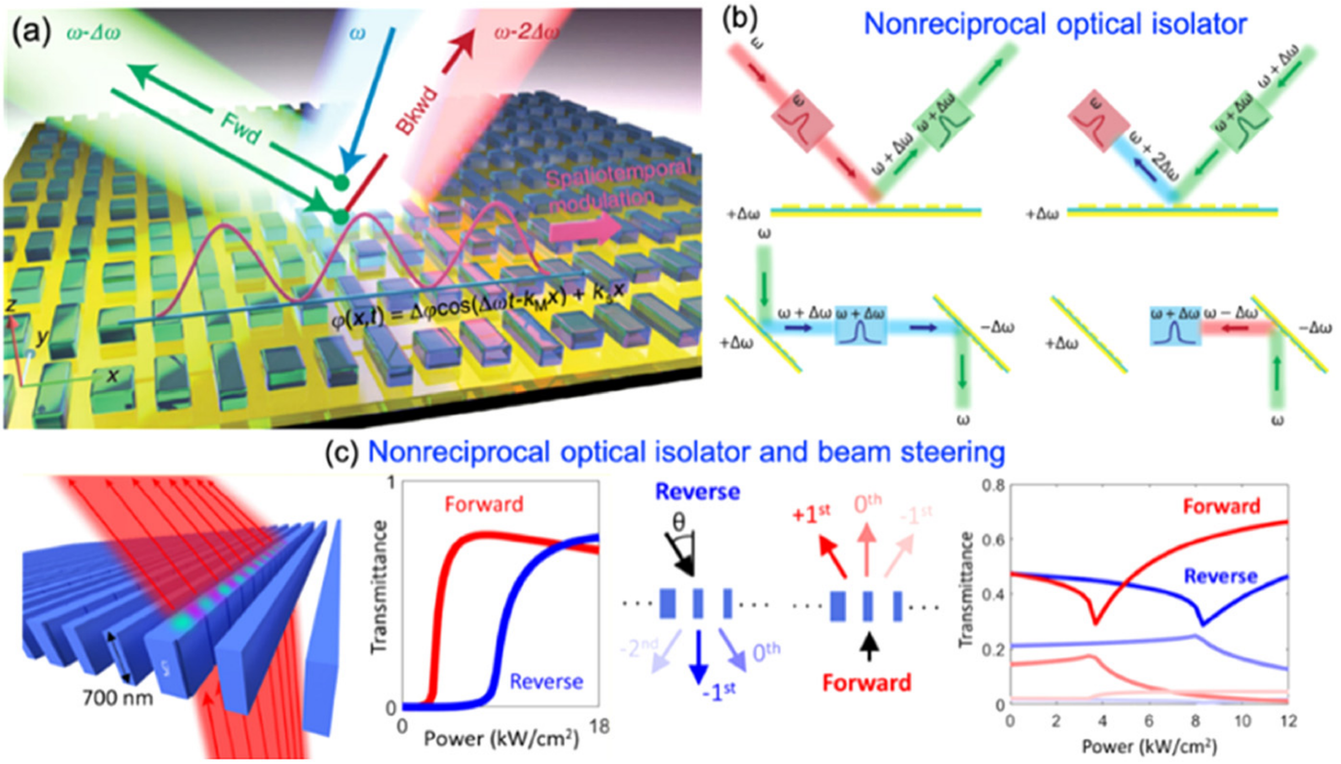

Figure 74. (a) Schematic of nonreciprocal metasurfaces. Reprinted by permission from Springer Nature Customer Service Centre GmbH: Springer. Light: Science & Applications. [423] © 2019. (b) (Top) Schematics of an optical isolator with unidirectional light flow using a time-varying metasurface and two high quality resonators and (bottom) an optical isolator with same input/output frequency using two time-varying metasurfaces and a high-quality resonator. Reproduced from [424]. CC BY 4.0. (c) Schematic of nonreciprocal silicon metasurfaces and transmittance as a function of input power, and schematic of diffraction setup through metasurfaces with incident angle for reverse illumination matching +1st diffraction angle for forward illumination and diffraction intensity versus input power. Reprinted with permission from [427]. Copyright (2018) American Chemical Society.

et al demonstrated a polarization convertor using a graphene-integrated anisotropic metasurface (figure 70(a)) [401]. The metasurface device could change the linear polarization to elliptical/circular polarization by inducing carriers into graphene using field-effect doping. However, the device required an applied voltage of ±250 V and operated at mid-infrared wavelength (∼7.8 μm). Using a similar structure, they demonstrated graphene-based laser interferometry for motion detection with nanoscale precision based on phase measurement for two orthogonal polarizations by modulating the carrier injection into the graphene metasurfaces [402]. Li *et al* proposed a tunable wave plate based on active GST metasurfaces (figure 70(b)) [211]. They numerically reported that the device could gradually tune the ellipticity of light and reach all intermediate elliptical polarization states in the mid-infrared regime. Using a VO_2-based metasurface, Earl *et al* demonstrated active rotation of the linear polarization axis of the reflected light for 90° [235] as discussed in section 3.2.

However, a powerful polarization-dependent reconfigurable metasurface could potentially lead to the next-generation nanophotonic applications, e.g., polarization-dependent detection/imaging, polarization encoding/multiplexing, and a polarization-based metasurface camera [61].

9.2. Prospective applications with temporal and emission controls of active metasurfaces

9.2.1. Ultrafast laser pulse shaping. Most of the reports on wavefront engineering using metasurfaces are limited to the spatial domain. Recently, efforts have been made to use metasurfaces to tailor the temporal response of the ultrafast optical pulse for pulse shaping and compression [62, 403–408]. The most common technique for pulse shaping employs several different programmable mask or SLM technologies and an acousto-optic dispersive filter [408–414]. However, the SLM techniques have slow response, and the number of control pixels is limited by the interconnect due to the difficulty in integrating more than few hundred separated electrode connections in the optically active region. A recent study by Divitt *et al* demonstrated a successful integration of dielectric metasurfaces into the ultrafast technologies to shape the temporal profile of an ultrafast femtosecond pulse [62]. By carefully tailoring the amplitude and phase specifically to each frequency of the spectrally-dispersed pulse, they demonstrated precise pulse-shaping operations (splitting, compression, chirping, and higher-order distortion) via a Fourier-transform setup (figures 71(a) and (b)). Decker *et al* also analytically reported that an all-dielectric Huygens metasur-

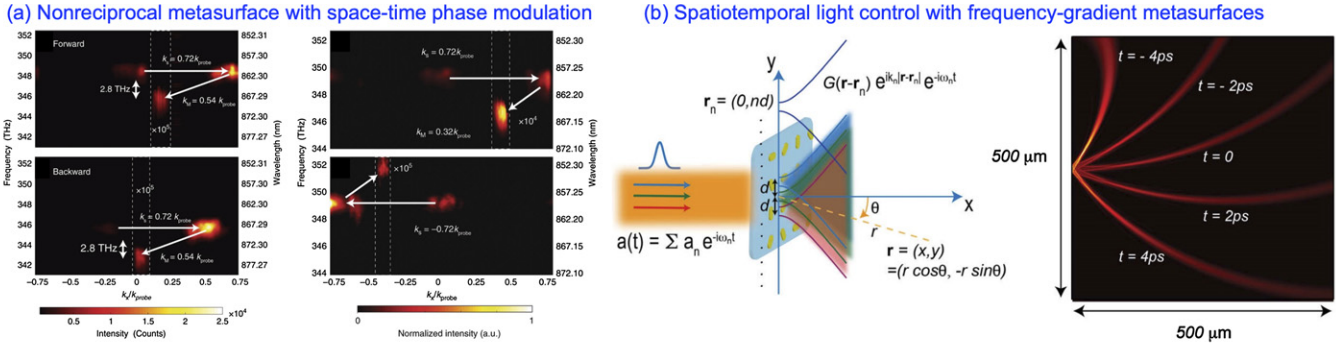

Figure 75. (a) Experimental demonstrations of nonreciprocal light reflection on a space–time phase modulated metasurface and direction selectivity of the photonic transitions. Reproduced from [423]. CC BY 4.0. (b) Illustration of the light–matter interaction between a frequency-comb source and a passive metasurface, and light generated at different time instants by a designed frequency-gradient metasurface. From [428]. Reprinted with permission from AAAS.

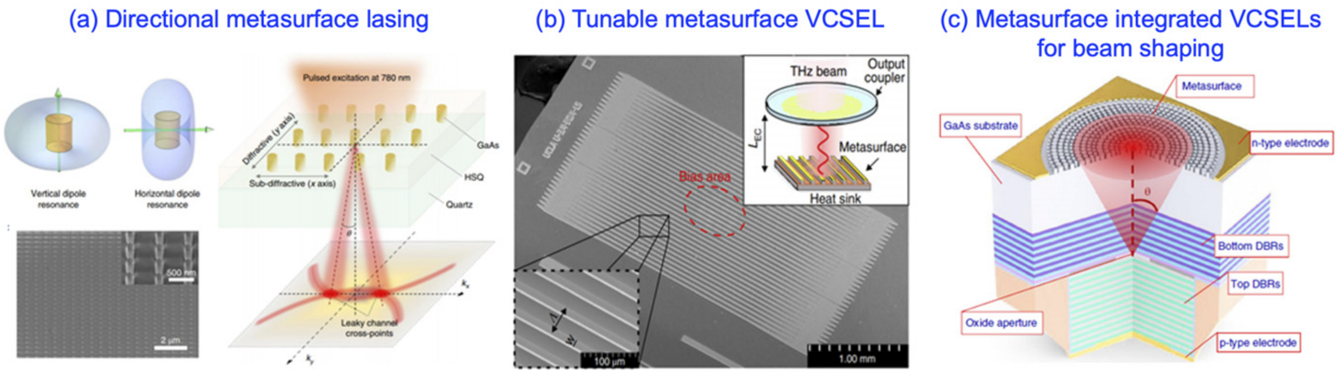

Figure 76. Metasurface lasers. (a) A directional laser, composed of GaAs nano pillars. Reprinted by permission from Springer Nature Customer Service Centre GmbH: Nature Nanotechnology. [432] © 2018. (b) A tunable THz metasurface vertical surface emitting laser. Reprinted by permission from Springer Nature Customer Service Centre GmbH: Nature Photonics. [433] © 2019. (c) Metasurface-integrated surface emitting laser with arbitrary phase shaping properties. Reprinted by permission from Springer Nature Customer Service Centre GmbH: Nature Nanotechnology. [57] © 2020.

face can be functionalized as a compact, highly efficient and thin pulse-compression device due to its strong group-delay dispersion of >-2000 fs^2 in combination with unity transmission, showing recompression to the initial chirped pulse after transmission through six layers of Huygens metasurfaces (figure 71(c)) [405].

Tunable metasurfaces could open up exciting opportunities for ultrafast technologies. The fully active spatiotemporal control of light by active metasurfaces would lead to an increased amount of information that can be induced in the short laser pulse due to the subwavelength feature of the metasurface element. In addition, tunable metasurfaces could also be employed to shape incident pulses and wavefronts simultaneously, leading to the arbitrary ultrafast manipulation of spatiotemporal light fields [406]. Active metasurface pulse shaping would have the advantages of faster response time and smaller and more pixelized elements over the SLM techniques. For inducing such pulse manipulation and arbitrary ultrafast spatiotemporal light fields, it will be necessary to develop a programmability feature based on a separable array of the dynamic metasurfaces. The electrical tunable metasurfaces (e.g., TCO/graphene-based metasurfaces) might be favorable for this application due to the fast response and low power consumption, but the efficiency will certainly need to be improved. The LC based and MEMS metasurfaces are other possible options since they provide large phase and amplitude manipulation, but the pixelized size and the ability to individually control elements would need to be further improved.

9.2.2. Thermal emission control. Controlling thermal emission/radiation is important for thermal imaging, gas/chemical sensing, and energy applications. Metasurfaces and nanostructures have been applied to break the thermal radiation characteristics which could be more efficient than conventional thermal radiators. They also provide possibility to achieve enhanced, coherent, unidirectional, and tunable thermal radiation [415, 416]. Progress has further been made to dynamically control the thermal emission using active metasurfaces.

Brar *et al* experimentally demonstrated electrically-tunable control of blackbody emission from graphene plasmonic resonators on a silicon nitride substrate (figures 72(a) and (b)) [417]. By applying bias to tune the carrier density of the graphene, the resonators show a change of 2%–3% of emissivity with respect to the charge neutral point for 40 nm graphene

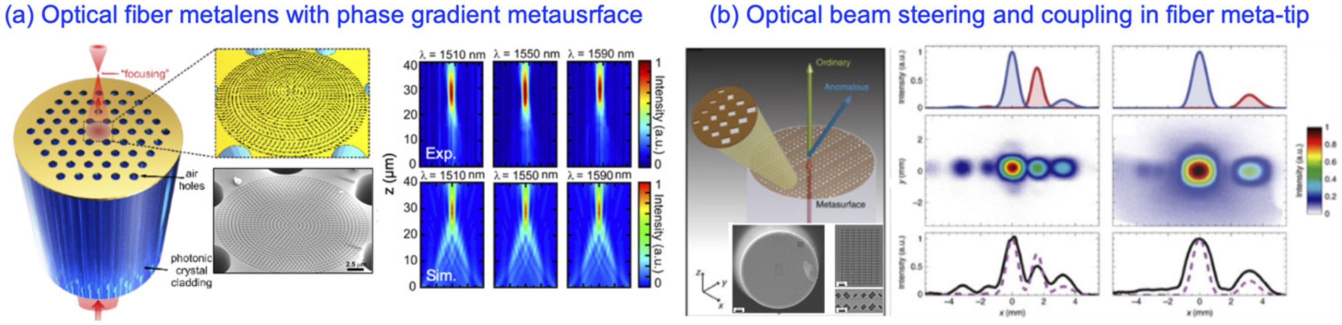

Figure 77. (a) In-fiber optical metalens developed on a large mode area PhC fiber, showing the focusing effect the telecommunication wavelength. Reproduced from [444]. CC BY 4.0. (b) (Left and middle) Optical fiber meta-tips for beam steering and coupling. The far-field characterizations are shown in the right image with (right) (top) simulated electric field–intensity profiles of the ordinary and anomalous beams (blue and red curves, respectively); (middle) measured field–intensity map; and (bottom) comparison of the measured (black-solid curve) and simulated (magenta-dashed curve) results. Reproduced from [445]. CC BY 4.0.

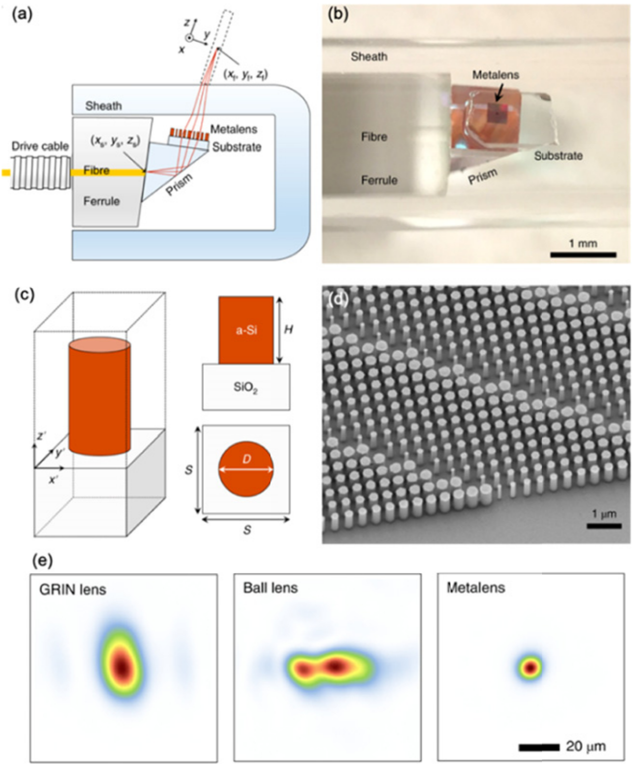

Figure 78. (a) Schematic and (b) photographic image of the nano-optic endoscope. (c) An individual metalens building block consisting of an amorphous silicon nanopillar on a glass substrate. (d) SEM image of a portion of the fabricated metalens. (e) Focal spot profiles of a graded-index (GRIN) OCT catheter, a ball lens OCT catheter and the nano-optic endoscope at a wavelength of 1310 nm. The incorporation of the metalens as the focusing element enables tighter focus with negligible astigmatism. Reprinted by permission from Springer Nature Customer Service Centre GmbH: Nature Photonics. [447] © 2018.

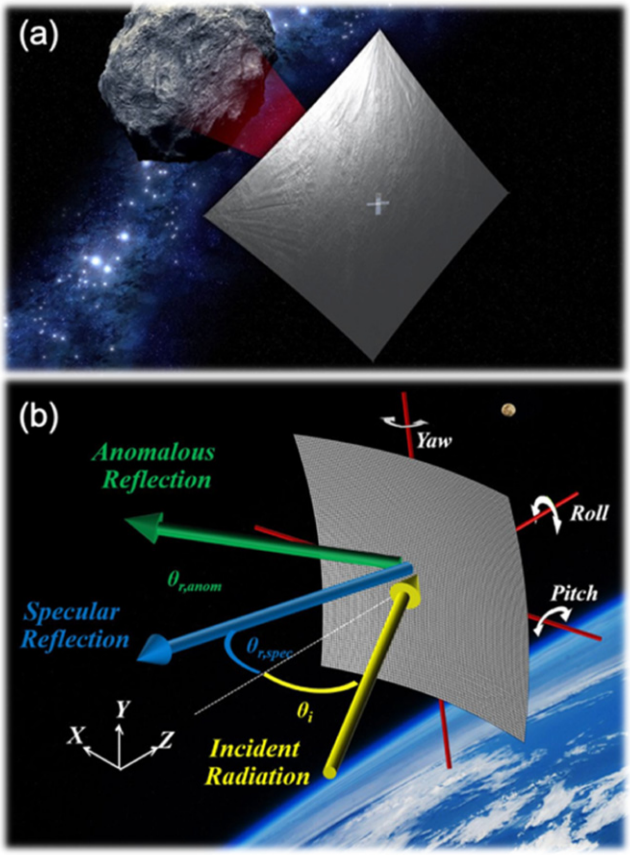

Figure 79. (a) An artist's depiction of NASA's NEA Scout mission and lightsail. Reproduced with permission from [448]. © The Optical Society. (b) Sketch of solar sail system interacting with oncoming TE polarized light. Angle of incidence is varied along the x–z plane. Reprinted by permission from Springer Nature Customer Service Centre GmbH: Springer. Scientific Reports. [457] © 2018.

resonators at a temperature of 250 °C due to the combination of plasmon–phonon and plasmon–electron interactions (figure 72(c)). Park *et al* reported active tailoring of thermal emission using an InAs-based plasmonic metasurface. The emissivity is controlled by electrical biasing and changing the carrier density of the active low-doped (n^+) InAs layer (figure 72(d)) [183]. Dynamic control of emissivity for a few percent at a wavelength of 7.3 μm was achieved by forming the depletion layer (+10 V) and accumulation layer (−7 V) of the active layer (figures 72(e) and (f)). Using an MEMS, Liu and Padilla reported dynamic control of emission at room temperature [256] as discussed in section 4.

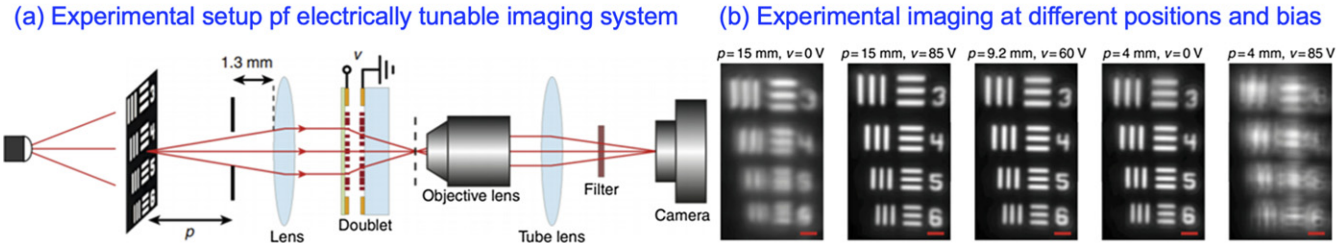

Figure 80. Electrically-tunable metasurface imaging system. Reproduced from [265]. CC BY 4.0. (a) The experimental setup for the imaging characterization. (b) Experimental imaging results show that the distance of the imaging plane can be tuned from 4 mm to 15 mm by applying the bias of 85 V. The scale bars are 10 μm.

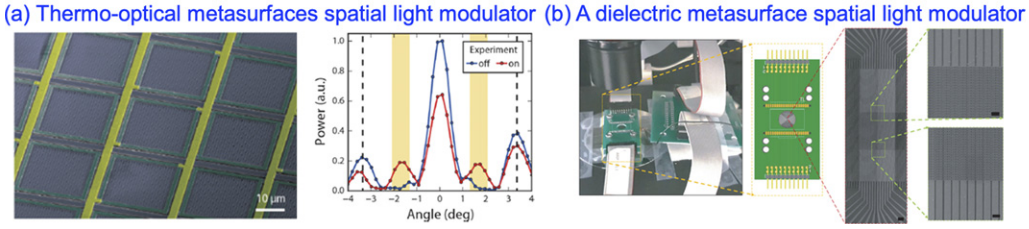

Figure 81. (a) (Left) SEM image of a 6 × 6 silicon antenna array-based SLM and (right) the measured far-field power distribution profile of the deflected beam from the SLM. Reprinted with permission from [287]. Copyright (2017) American Chemical Society. (b) The optical image and SEM image of a one-dimensional dielectric SLM mounted onto a PCB which can operate in the visible. From [176]. Reprinted with permission from AAAS.

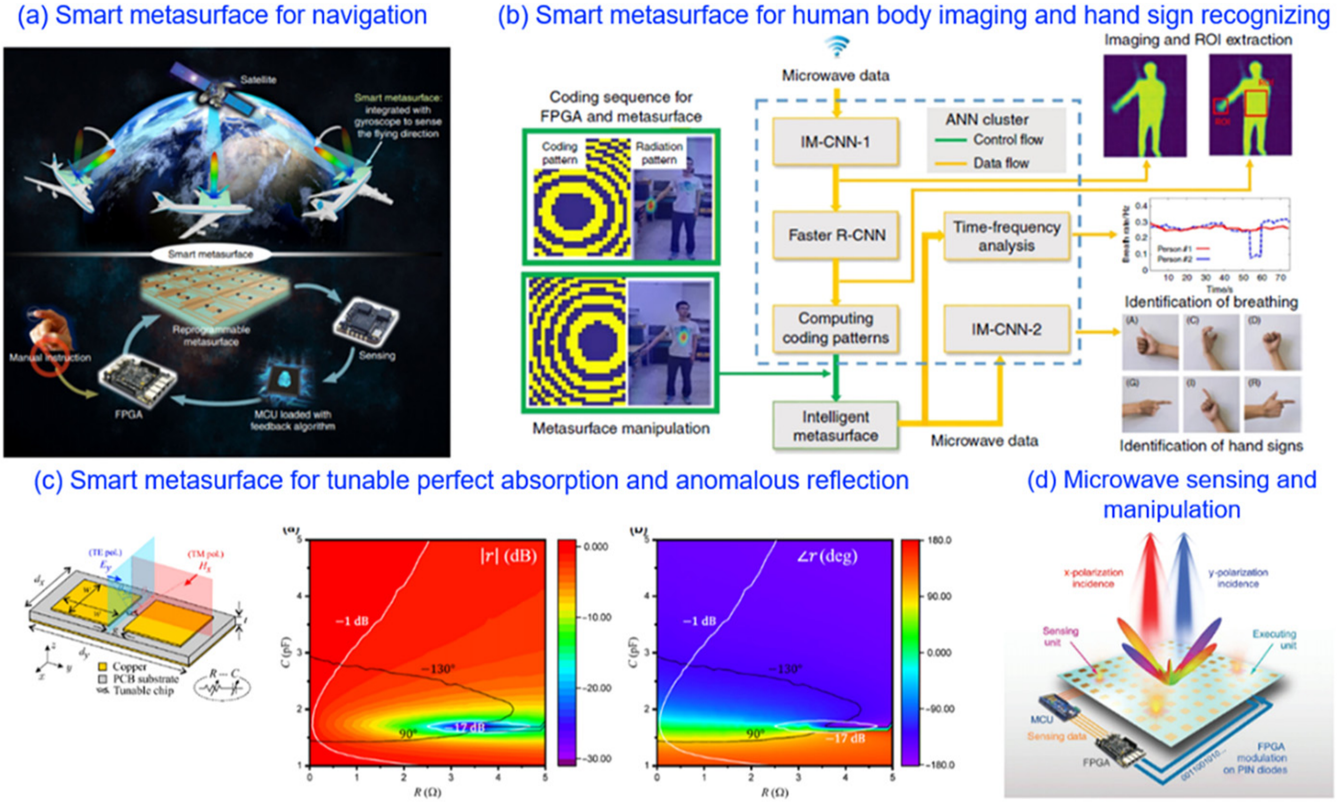

Figure 82. (a) Schematic of a smart metasurface with self-adaptively reprogrammable functions. Reprinted by permission from Springer Nature Customer Service Centre GmbH: Springer. Light: Science & Applications. [466] © 2019. (b) Digital coded metasurface trained by deep learning for human body imaging and recognition of hand signs. Reproduced from [469]. CC BY 4.0. (c) Schematic of the unit cell for the intelligent metasurface (left), and their independent control over reflection amplitude and phase as a function of load resistance and capacitance, respectively (right). Reprinted figure with permission from [468], Copyright (2019) by the American Physical Society. (d) Schematic of a smart metasurface for simultaneously sensing and manipulating microwaves. Reproduced from [470]. CC BY 4.0.

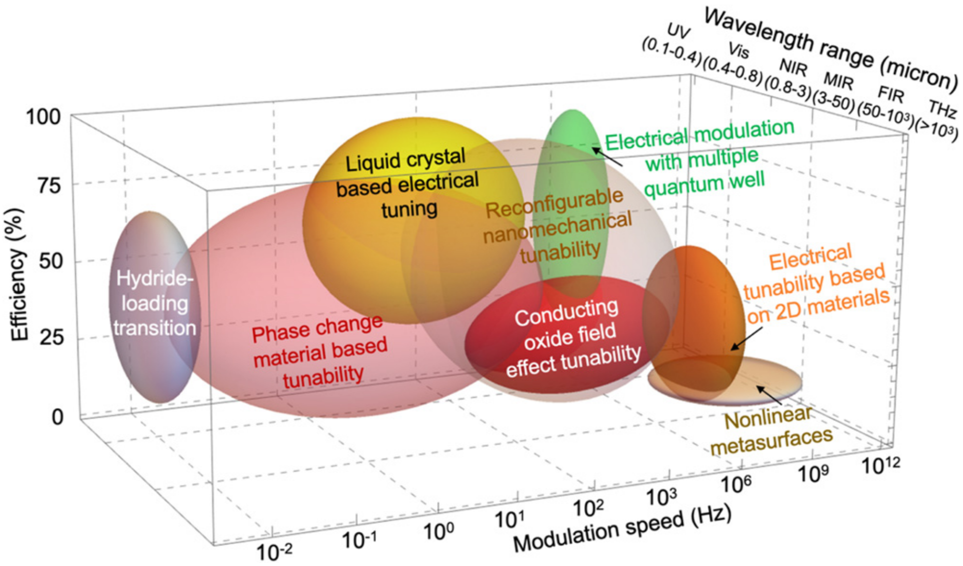

Figure 83. Performance map on reported active metasurfaces. Ellipsoids represent the range of key parameters (operation wavelength range, modulation speed and efficiency) summarized from various tunable metasurface mechanisms which can provide $>0^\circ$ optical phase shift. The performances are summarized from tables 2–14.

From these demonstrations, active metasurfaces have shown significant promise for nanophotonic control of thermal emission. However, these initial demonstrations are limited for practical applications because they involve weak modulation strength, applying relatively large external voltages, and limited thermal control in the active devices. With further efforts, tunable metasurfaces could provide the opportunity for ultrafast and low power individual control of emissivity, allowing angular, polarization, nonreciprocal, and spatial/temporal control of thermal radiation for various applications such as chemical/bio-sensing, thermophotovoltaics, hyperspectral imaging, and infrared spectroscopy/camera.

9.2.3. Active optical sensing and biodetection. The rapidly increasing demands in personalized medicine, global health care, and diagnostics require various types of chemical and bio-sensors suitable for rapid, low-cost, on-chip detection and analysis. Conventional bulky spectroscopy techniques do not have the sensitivity required to detect small amounts of biomolecules. Plasmonic metasurfaces are capable of tightly confining the light into the subwavelength region due to field enhancement of the surface plasmon resonance, which can greatly enhance the light–matter interaction to increase the sensitivity [418, 419]. However, note that the plasmonic resonance-enhanced detection usually comes at the expense of reduced spectral bandwidth. If this limitation can be overcome, the use of active metasurfaces could greatly boost the capacities of biosensing chips and extend their bandwidth, promoting the next generation of sensing and detection systems on a chip. For instance, active metasurfaces have the advantage of tracing and detecting multiple fingerprint resonances of different biomaterials in a dynamic way, allowing for real-time multi-analysis and selective detection over a broad spectral range with a single device.

In this regard, Rodrigo *et al* demonstrated an electrically-tunable biosensor using graphene nanoribbon arrays in the mid-infrared regime (figure 73(a)) [420]. In this structure, the unique electro-properties of graphene allow for the continuous tuning of their plasmonic resonance from 1450 cm^{-1} to above 1800 cm^{-1} under different applied biases, enabling selective detection of proteins at different frequencies. On the other hand, the large resistive loss of the metallic/plasmonic metasurface results in a low-quality factor, limiting their performance. In contrast, high-index dielectric metasurfaces, featuring low intrinsic loss and compatibility with CMOS technologies, have aroused considerable interest as a platform for high performance biosensing applications [421, 422]. For example, Tittl *et al* reported a two-dimensional pixelated dielectric high-Q metasurface-based sensor array in the mid-infrared (figure 73(b)) [422]. The resonance position of each individual metasurface element is designed to be linearly varied within a broad fingerprint range of a specific target so that the device can detect the absorption signatures at multiple spectral points. Although only passive dielectric metasurfaces have been implemented for biosensing to date, we envision that the rapid development of tunable dielectric metasurfaces will provide great opportunities to advance their applications in dynamic biosensing.

9.2.4. Dynamic nonreciprocal metasurface devices. Most metasurfaces are constrained by the Lorentz reciprocity theorem that exhibits time-reversal symmetry, indicating the forward and backward signals are consistent when exchanging the input and output. Recent studies show that breaking the time-reversal symmetry can introduce nonreciprocity to metasurfaces. The nonreciprocal metasurfaces with dynamic phase modulation can convert incident light with a frequency of ω to forward reflectance with a frequency of $(\omega-\Delta\omega)$ [423]

Table 2. Performance of gate-tunable conducting oxide metasurfaces.[a]

	Reference	Year	Journal	Cite	Stimuli	Active material	Unit cell	Element size (nm)	Fabrication	Operation range (μm)	Spectral shift	Modulation depth	Phase shift	Energy consumption	Speed	Efficiency	Application/function
1	[116]	2016	Nano Lett.	358	Electrical	ITO	Au bar	400	EBL	1.55	—	$\Delta R/\Delta T = 4$ dB	184°	∼2.5 V, 2.5 fJ (est.)	10 MHz	∼20%	Beam steering
2	[123]	2018	Nano Lett.	91	Electrical	ITO	Au cross	400	EBL	1.55	—	$\Delta R/R = 89\%$	303°	6.5 V	—	∼13%–30%	Phase modulation
3	[124]	2020	ACS Nano	5	Electrical	ITO	Au cross	400	EBL	1.522	—	$\Delta R/R = 12\%$	270°	−6 to 6 V	—	∼7%–19%	Beam steering, active metalens
4	[125]	2017	Nano Lett.	164	Electrical	ITO	Au bar	2200	EBL	5.94	—	$\Delta R/R = 72\%$	180°	−40 to 40 V	—	1.4%–2.4%	Phase/amplitude modulation
5	[126]	2015	Sci. Rep.	163	Electrical	ITO	Au bar	750	EBL	3–5	—	$\Delta R/R = 15\%$	—	−5 to 5 V	—	50%	Active absorber
6	[128]	2017	Adv. Mater.	45	Electrical	Ag/ITO	Ag/Al_2O_3/ITO dolmen	400	FIB	0.5–0.8	—	$\Delta R/R = 30\%$, $\Delta R/R = 78\%$	—	5 to 100 mV	600 Hz	∼30%	Amplitude modulation
7	[129]	2013	Appl. Phys. Lett.	99	Electrical	ITO	ITO/Au stripe	600	EBL	4.1–4.6	∼10 nm	$\Delta A/A = \sim 4\%$	—	10 V	—	—	Active absorber
8	[130]	2017	Appl. Phys. Lett.	9	Electrical	AZO	AZO grating	915	Two beam interference	0.532	—	Δdiffraction = 4%	—	4 V	0.95 GHz (est.)	Diffraction = 2.1%	Active grating
9	[131]	2018	Optica	65	Electrical	AZO/Si	Huygens resonators	800	EBL	1.4–4.55	—	$\Delta T/T = 75\%$	—	−10 to 10 V	—	40%	Beam steering
10	[127]	2019	Nanophotonics	2	Electrical	ISO	Au bar	1000	EBL	1.6–8	620 nm	$\Delta R/R = 57\%$	—	−10 to 10 V	—	∼25%–60%	Active absorber

[a] EBL: electron-beam lithography; FIB: focused ion beam milling.

(figure 74(a)). Meanwhile, the backward reflectance with a frequency of $(\omega - \Delta\omega)$ is converted to $(\omega - 2\Delta\omega)$, instead of ω.

The unique properties of nonreciprocal metasurfaces open up the opportunity for significant functionalities. In 2015, Shaltout *et al* proposed nonreciprocal metasurfaces using time-gradient phase discontinuities. Furthermore, nonreciprocal metasurfaces can be paired with resonators (filters) to realize magnetic-free isolation in an ultrathin interaction distance with spatiotemporal modulation which is impossible for traditional optical isolators based on bulky magneto-optical materials (figure 74(b)) [424]. In the same year, Hadad *et al* proposed a space–time gradient metasurfaces to demonstrate a nonreciprocal electromagnetic induced transparency by introducing a spatiotemporal modulation with a sinusoidal impedance [425]. In 2016, Shi and Fan proposed dynamic non-reciprocal metasurfaces with arbitrary phase reconfigurability [426]. Each unit element of the metasurfaces is subject to temporal refractive index modulation between photonic transitions of the different states, which gives nonreciprocal response without the need for a magneto-optical active element. In 2018, Lawrence *et al* designed a passive metasurface with nonreciprocity for direct and anomalously-refracted light in the near-infrared region [427]. The metasurface consists of a 100 nm-thick, periodically-patterned Si grating acting as an optical diode for an intensity of ∼kW cm^{-2} (figure 74(c), left). The same platform but with a three-element phase gradient metasurface can achieve nonreciprocal beam steering with a large angle of ∼45° (figure 74(c), right). In 2019, Guo *et al* experimentally demonstrated nonreciprocal light reflection at visible wavelength (∼860 nm) by the spatial and temporal phase modulation from a nonlinear Kerr metasurface (figure 75(a)) [423]. A nonlinear metasurface carrying travelling-wave modulation can create spatial phase gradient and multi-terahertz temporal phase wobbling. The proposed metasurface with space–time phase modulation exhibits completely asymmetric reflections in forward and backward light propagations with a large bandwidth of ∼5.77 THz. Recently, Shaltout *et al* experimentally reported a novel approach of continuous beam steering by creating a virtual frequency-gradient via a passive metasurface with a frequency-comb source (figure 75(b)) [428]. The frequency-gradient metasurface exhibits a continuous steering angle of >25° in 8 ps.

Most nonreciprocal metasurfaces have been realized with judicious design and an active light source, which enables topological isolation, ultrafast beam steering, one-way lensing, holography, etc. The dynamic nonreciprocal metasurfaces require fast response of tunability. The fast phase reconfigurability for individual elements is not only a challenge but also an opportunity for controllable nonreciprocal metasurfaces with practical applications.

9.2.5. Nano-laser/vertical-cavity surface-emitting laser tunable devices.

The unique characteristics of metasurfaces, such as ultra-thin thickness, planar configuration, and subwavelength precision of wavefront control, make them ideal candidates to be integrated with semiconductor lasers. In this context, plasmonic metasurfaces have been integrated on the facet of edge-emitting quantum cascade lasers and vertical-external-cavity surface-emitting lasers (VCSELs) to

Table 3. Performance of two-dimensional materials enabled active metasurfaces.[a]

	Reference	Year	Journal	Cite	Stimuli	Active material	Unit cell	Element size (nm)	Fabrication Fabrication	Operation range (μm)	Spectral shift	Modulation depth	Phase shift	Energy consumption	Speed	Efficiency	Application/ function
1	[150]	2015	Optica	41	Electrical	Graphene	Graphene anti-dot	2–6 μm	Photolithography	33–200	—	$\Delta T/T < 15\%$	—	−60 to −210 V	—	—	Transmission modulation
2	[149]	2011	Nat. Nano	2461	Electrical	Graphene	Micro-ribbon	2 μm	Optical lithography	1.1–3.3, 25–100	0.8 μm	$\Delta T/T < 5\%$	—	−0.5 to 2.2 V	—	—	Transmission modulation
3	[156]	2014	Nano Lett.	450	Electrical	Graphene	Au plasmonic structure	600	EBL	4–9	0.8 μm	$\Delta R/R = 95\%$	—	0 to 80 V	20 GHz	10%	Active perfect absorption
4	[152]	2013	Nano Lett.	490	Electrical	Graphene	Au dimer	2600	EBL	4–8	600 nm	$\Delta T/T \sim 30\%$	—	0 to −26 V	—	—	Modulation
5	[151]	2012	Nat. Mater.	707	Electrical	Graphene	Hexagonal metallic atom	60 μm	Photolithography	0.1–0.6 THz, 1.2–2.5 THz	—	$\Delta T \sim 47\%$	32.2°	−300 to 300 V	—	—	Transmission switching
6	[155]	2018	Nano Lett.	111	Electrical	Graphene	Graphene plasmonic ribbon	200	EBL	5–8 (7.2)	—	$\Delta R/R = 95.8\%$	—	2.4 V	~1 MHz	95.9%	Active perfect absorption
7	[153]	2014	Nano Lett.	185	Electrical	Graphene	Au fano resonator	900 × 600	EBL	1.7–2.5	—	$\Delta R/R \sim 22\%$	—	0 to 2 V, −30 to 30 V	—	~25%	Reflectance modulation
8	[142]	2018	Light Sci. Appl.	65	Electrical	Graphene	Dog bone U antenna	1000	EBL	5–12	~1 μm	$\Delta R/R = 90\%$ (−4.5 dB)	—	−4 to 8 V	~1 GHz	~10%	Modulation; pixel imaging
9	[157]	2017	Nano Lett.	175	Electrical	Graphene	Au bar	$1.2 \times 0.4\ \mu\mathrm{m}^2$	EBL	8–9 (8.7)	510 nm	—	237°	−80 to 90 V	MHz to GHz (est.)	23%–30%	Beam steering
10	[154]	2014	Nano Lett.	187	Electrical	Graphene	Au ring aperture	150 μm	EBL	0.2–0.9 THz (0.44 THz)	—	$\Delta T/T = 50\%$	—	−20 to 20 V	—	50%	Transmission modulation
11	[158]	2020	ACS Nano	7	Electrical	Graphene	Graphene plasmonic ribbon	1295/2454	EBL	7 mid infrared	—	$\Delta R/R \sim 100\%$	360°	—	—	60%	Modulation; beam steering
12	[159]	2018	Nano Lett.	12	Electrical/ optical	MoS_2	SiN nanohole	620–680	EBL	580–750 nm infrared	—	$\Delta T/T \sim 3\%$	—	0 to 30 V, 120 $\mu\mathrm{W}\ \mu\mathrm{m}^{-2}$	~0.8 s	<20%	Tunable exciton–trion conversion
13	[160]	2017	Nano Lett.	82	Electrical	MoS_2	Ag nano disc	460	EBL	580–690 nm	10 nm	$\Delta R/R \sim 100\%$	—	0 to 80 V	—	—	Active coupling strength
14	[161]	2019	Nano Lett.	4	Electrical	WS_2	Ag bar	430	EBL	560–680 nm	—	$\Delta R/R \sim 40\%$	—	0 to 80 V	—	—	Coupling modulation
15	[162]	2019	ACS Photonics	8	Electrical	MoS_2	Au grating	445	EBL	550–750 nm	—	$\Delta E/E \sim 200\%$	—	−30 to 30 V	~Ns	—	Tunable emission
16	[163]	2020	Nat. Photonics	9	Electrical	WS_2	Zone plate	20 μm	EBL	625 nm	—	Enhanced focusing ~33%	—	0 to 3 V	20 Hz	Focusing ~0.08%	Atomically thin lens

[a] EBL: electron beam lithography; $\Delta E/E$: Δemission/emission.

Table 4. Performance of LC based reconfigurable metasurfaces.[a]

	Reference	Year	Journal	Cite	Stimuli	Active material	Unit cell	Element size (nm)	Fabrication Fabrication	Operation range (μm)	Spectral shift	Modulation depth	Phase shift	Energy consumption	Speed	Efficiency	Application/ function
1	[167]	2005	Nano Lett.	273	Electrical	LCs	Au nanodot	105	Anodization of Au film	500–800	3/34 nm	$\Delta A = 4\%$	—	50 V	1 kHz	97%	Tunable absorber
2	[171]	2013	Opt. Express	96	Electrical	LCs	Au V-shaped resonator	490	FIB	1550	0.25 μm	$\Delta T/T = 500\%$	—	7 V	—	55%	Optical switching
3	[168]	2013	Opt. Express	118	Electrical	LCs	Au SRR	300	EBL	600–1600	7 nm	$\Delta T \sim 60\%$	—	6 V	—	90%	Resonance modulation
4	[170]	2017	Opt. Express	19	Electrical	LCs	Al bar	300–460	EBL	400–800	—	$\Delta T \sim 50\%$	—	4 V	—	60%	Tunable color filter
5	[172]	2016	Opt. Express	19	Electrical	LCs	Au binary-grating	240	EBL	450–800	—	$\Delta T \sim 30\%$	—	10 V	—	65%	Transmission modulation
6	[169]	2015	Adv. Opt. Mater.	108	Electrical	LCs	Au V-shaped resonator	390 × 580	FIB	800–2000	110 nm	$\Delta T \sim 40\%$	—	2.7 V	—	45%	Transmission modulation
7	[173]	2017	Appl. Phys. Lett.	127	Electrical	LCs	Si nanodisk	909	EBL	~1550	29/55 nm	$\Delta T = 75\%$	180°	70 V	—	90%	Transmission modulation
8	[174]	2019	Sci. Rep.	10	Electrical	LCs	TiO_2 nanodisk	360	EBL	660–690	26/6 nm	$\Delta T = 65\%$	—	5 V	—	80%	Transmission modulation
9	[175]	2018	Opt. Lett.	23	Electrical	LCs	Dielectric metasurfaces			635	—	—	360°	10 V	—	—	Active vortex generation
10	[176]	2019	Science	60	Electrical	LCs	TiO_2 nanodisk	360	EBL	620–680	—	—	360°	8 V	—	36%	Spatial light modulation
11	[177]	2018	ACS Photonics	85	Thermal	LCs	Si nanodisk	430	EBL	700–800	—	$\Delta T = 30\%$	—	Temperature change 35 °C	—	50%	Beam steering
12	[38]	2015	ACS Nano	249	Thermal	LCs	Si nanodisk	919	EBL	1370–1550	40 nm	$\Delta T/T = 500\%$	—	Temperature change 41 °C	—	80%	Transmission modulation
13	[178]	2018	Nano Lett.	53	Thermal	LCs	Si nano-cylinder	560	EBL	900	—	$\Delta\text{emission} = 200\%$	—	Temperature change 42 °C	—	—	Tunable light sources
14	[179]	2012	Adv. Mater.	129	UV exposure	LCs	Au annular aperture	800	FIB	400–1000	—	$\Delta T = 18\%$	—	—	—	30%	Active color filter

[a] EBL: electron-beam lithography; FIB: focused ion beam milling; LC: liquid crystal.

Table 5. Performance of electro-optical metasurfaces using III–V semiconductors and MQWs.[a]

	Reference	Year	Journal	Cite	Stimuli	Active material	Unit cell	Element size (nm)	Fabrication Fabrication	Operation range (μm)	Spectral shift	Modulation depth	Phase shift	Energy consumption	Speed	Efficiency	Application/ function
1	[182]	2009	Appl. Phys. Lett.	321	Electrical	GaAs	Au SSR	7600	Photolithography	0.36 THz	—	$\Delta T = 50\%$	—	14 V	3 kHz	70%	SLM
2	[180]	2006	Nature	2102	Electrical	GaAs	Au SSR	50 μm	Photolithography	1–2 THz	—	$\Delta T = 50\%$	—	16 V/160 mW	—	85%	Transmission modulation
3	[181]	2012	Opt. Express	52	Electrical	GaAs	Au SSR	2000	Optical lithography	10 μm	10 cm^{-1}	$\Delta T = 25\%$	—	4 V/100 mW	—	50%	Transmission modulation
4	[183]	2018	Sci. Adv.	14	Electrical	InAs	Al bar	1200	EBL	7.3 μm	—	Δemission = 3.6%	—	−15 V–15 V	600 kHz	60%	Dynamic emission
5	[185]	2013	Appl. Phys. Lett.	46	Electrical	MQWs	Au nanocross	2625	EBL	~30 THz	—	$\Delta R = 5\%$	—	4 V/~140 mW	—	90%	Reflection modulation
6	[184]	2014	Adv. Opt. Mater.	73	Electrical	MQWs	Au nanocross	1730	EBL	6–8 μm	300 nm	$\Delta A = 30\%$	—	4 V/~130 mW	100 MHz	90%	Absorption modulation
7	[186]	2019	Nat. Commun.	60	Electrical	MQWs	MQWs bar + double slits	910	EBL	915–950 nm	—	$\Delta R/R = 270\%$	~70°	10 V/1 mW cm^{-2}	1 MHz	50%	Beam steering

[a] EBL: electron-beam lithography; MQW: multiple-quantum well.

control the beam quality, light transmission, and polarization states of the emitting beam [429, 430]. Recently-developed high-index dielectric metasurfaces, of considerable interest for various applications, have demonstrated the advantages of low absorption loss and the ability to control both the electric and the magnetic optical responses for an on-chip laser device [22, 431].

Figure 76(a) shows directional lasing in active GaAs nanoantenna arrays achieved by partially breaking a bound state in the continuum [432]. The emitting light from this structure has both high directionality and a quality factor as large as 2750. The lasing directivity and emitting wavelength of this structure can be tuned either by changing the geometry of the nanoantenna array or by modifying the gain spectrum of the GaAs nanopillars with temperature. Curwen *et al* reported a continuous tuning of metasurface-based THz quantum-cascade VCSELs (figure 76(b)) [433]. The reflecting metasurface in this work is composed of narrow metallic ridge waveguides loaded with gain material, which allows for broadband tuning and simultaneously enables high power and good beam quality. Continuous tuning (larger than 20%) of a single laser mode is demonstrated by changing the external length using a piezoelectric stepper motor. Xie *et al* proposed a wafer-level non-intrusive approach for arbitrary beam-shaping VCSELs with programmable controllability by directly sculpturing the emitting surfaces into metasurfaces (figure 76(c)) [57]. This technique enables arbitrary manipulating the wavefront of the laser beams. Furthermore, the large scale of two-dimensional arrays of the metasurface VCSELs allows for programmable control of emitting beams on a chip.

To date, there is no experimental demonstration of tunable nano-laser/VCSEL devices based on active metasurfaces. However, we envision the integration of tunable metasurfaces, and nano-lasers could promote the development of a next-generation multi-functional ultra-compact laser and spectroscopy system due to the ability to actively control the laser emission properties including focusing spot diameter, emission wavelength, the directionality of the emitting beam, and the polarization states, which would advance a large variety of applications in manufacturing, communication, ultra-compact LIDAR, etc.

9.3. Prospective applications integrated with existing technologies

9.3.1. Active meta-optical fiber devices. Optical fiber is a well-developed technology used in numerous of photonic applications. However, the optical properties of the optical fiber waveguide such as phase, amplitude, polarization state, and mode profile cannot typically be altered after the fiber drawing fabrication, and its functionality is somewhat limited by the dielectric materials of the core and cladding. Attempts have been made to fabricate metasurface structures on the optical fiber facets to modify the optical properties of the fiber. Compact optical components such as diffraction grating [434] and plasmonic sensors [435–437] have been realized with periodical metallic nanostructures (i.e., slits, holes and bars) on

Table 6. Performance of chalcogenide-glass based metasurfaces.[a]

	Reference	Year	Journal	Cite	Stimuli	Active material	Unit cell	Element size (nm)	Fabrication Fabrication	Operation range (μm)	Spectral shift	Modulation depth	Phase shift	Energy consumption	Speed	Efficiency	Application/ function
1	[188]	2010	Appl. Phys. Lett.	311	Electrical	GLS	Au split rings	375	FIB	750–1750	150 nm	$\Delta R = 60\%$	—	0 to 45 V	50–100 ns	40%	Reflection modulation
2	[189]	2013	Adv. Mater.	318	Optical	GST-225	Au split rings	400	FIB	0.4–2, 5–7	200 nm	$\Delta R/\Delta T = 4$ dB	—	0.1–0.25 mW μm^{-2}	50–100 ns	<70%	Optical switching
3	[190]	2013	Nano Lett.	208	Thermal	GST-326/ InSb	Al bar	(1.2 × 2.6) μm^2	EBL	2–10	19.3% (610 cm^{-1})	—	—	—	—	—	Optical switching
4	[204]	2014	Nature	423	Electrical/ optical	GST-226	ITO/GST/ITO	300	EBL	0.35–0.75	—	—	—	0 to 2.2 V, 15 pJ/pixel	125 ns	—	Display/ framework
5	[191]	2014	ACS Photonics	139	thermal/ optical	GST-326	Al bar	500 × 100	EBL	2–10	560 cm^{-1}	$\Delta R = 21\%$	—	51 mJ cm^{-2}, 31 mJ cm^{-2}	50 fs; 1s	63%	Reversible switching
6	[207]	2015	Sci. Rep.	106	Optical	GST-225	GST slit + Au	500	FIB	1.55	—	—	101°0.56π	4 mW CW laser	—	—	reconfigurable platform
7	[192]	2015	Nano Lett.	170	Thermal	GST-326	ZnS/SiO$_2$ + Au rod	1600/1800	EBL	4–6	0.75 μm (18%)	ΔCD $= \pm 5°$, $\Delta T = \sim 10\%$	—	—	—	~60%	Active chiral plasmonics
8	[193]	2015	Adv. Mater.	301	Thermal	GST-326	Al square/GST/Al	800	EBL	3–5	0.7 μm (25%)	$\Delta R = 60\%$	—	—	—	>90%	Active perfect absorber
9	[205]	2015	Nat. Photon.	577	Optical	GST-225	Reconfigurable element	600	Laser direct writing	1.5–2.5	—	$\Delta R = 100\%$	—	31.2 nJ/pixel; 140 mJ cm^{-2}	0.0068 ns	—	Reconfigurable platform
10	[206]	2016	Nat. Mater.	213	Optical	GST-326	SPP resonator	5000	Laser direct writing	8.3–9.1	943–1135 cm^{-1}	$\Delta R = 6\%$	—	Pulse laser: 100–310 mW	15–45 ns	—	Optical switching
11	[195]	2016	Opt. Express	117	Thermal	GST-225	Au disk	1200	Laser direct writing	1.0–2.5	500 nm	$\Delta T = 56\%$	—	—	—	—	Transmission modulation
12	[201]	2016	Appl. Phys. Lett.	152	Optical	GST-225	Grating	750–950	FIB	1.0–1.8	(~150 nm) 10%	$\Delta R = 7$ dB; $\Delta T = -5$ dB	—	~3 mW μm^{-2}	—	—	Optical switching
13	[200]	2017	Adv. Opt. Mater.	27	Thermal	GST-225, 326, 8211	Rod metal antenna	836–1256	EBL	1–6	—	—	—	—	—	—	Polarization conversion
14	[210]	2017	Light Sci. Appl.	151	Thermal	GST-326	Nanorod + GST layer	900	EBL	2–5	950/870 nm	$\Delta T = \sim 30\%$	—	—	—	40%–50%	Beam switching
15	[194]	2017	Laser Photon. Rev.	91	Thermal	GST-225	Au/GST/Au MIM disc	5000	Photolithography	5–25	0.77–4.08 μm	Δemissivity $= 80\%$	—	—	—	—	Active thermal emission
16	[202]	2017	Conference paper	1	Optical	GeTe	Nano block	1600	EBL	4–12	—	$\Delta R = 59\%$	—	0.12 mJ cm^{-2}	20 ps	—	Modulator
17	[214]	2018	Adv. Funct. Mater.	104	Optical/ thermal	GST-225	Al slit + GST-MMI	700	EBL	1.0–1.6	—	—	300°	—	10 min	40%	Beam steering
18	[203]	2018	Adv. Opt. Mater.	44	Thermal	GST-225	Au pillar + GST layer	1100	EBL	3–6	500 nm	—	—	—	30 min	<60%	Resonance modulation
19	[217]	2018	Adv. Opt. Mater.	28	Optical	GST-225	Au square/SiO$_2$/ GST/Au	450	EBL	2–4	270–425 nm	$\Delta A = 65\%$	—	33–105 mW	300 ns	—	Active thermal emission
20	[216]	2018	Adv. Sci.	45	Thermal	GST-225	Au rod	4200	FIB	8.5–11.5	—	—	180°	—	20 min	60%	Optical switching
21	[218]	2019	Nano Lett.	26	Optical	GST-225	ZnS/SiO$_2$/GST/ ZnS/SiO$_2$ slit	300–400	FIB	0.2–0.5	—	$\Delta T = 23\%$;	—	~140 mJ cm^{-2}	4.68 ps	10%–40%	Transmission modulation
22	[219]	2019	Adv. Opt. Mater.	26	Thermal	GST-225	U-shaped GST antenna	550	EBL	1.3–1.8	—	—	39°	—	—	—	Beam steering; active hologram
23	[220]	2020	Optica	9	Optical	GST-225	Si/GST/Si disc	850	EBL	1.2–1.6	~40 nm	$\Delta R = 70\%$	—	~19.2 mJ cm^{-2}	12.5 ns	40%–75%	Dynamic filter; modulation

[a] EBL: electron-beam lithography; FIB: focused ion beam milling; CD: circular dichroism.

Table 7. Performance of vanadium oxide based metasurfaces.[a]

	Reference	Year	Journal	Cite	Stimuli	Active material	Unit cell	Element size (nm)	Fabrication Fabrication	Operation range (μm)	Spectral shift	Modulation depth	Phase shift	Energy consumption	Speed	Efficiency	Application/ function
1	[223]	2008	Appl. Phys. Lett.	314	Thermal	VO_2	Au split ring resonator	20	EBL	83–500	20%	$\Delta T = 20\%$	—	—	—	—	Transmission modulation
2	[225]	2013	Opt. Lett.	172	Thermal	VO_2	Y-shaped antennas	3	EBL	2–14	10% (1.2 μm)	$\Delta R/R = 150\%$	—	—	—	—	Reflection modulation
3	[224]	2014	Appl. Phys. Lett.	49	Electrical	VO_2	U-shaped antenna	20	EBL	136–222	—	$\Delta T = 3\%$, $\Delta T/T = 150\%$	—	−3 to 3 V	20 min	—	Optical switching
4	[227]	2015	Appl. Phys. Lett.	104	Thermal	VO_2	Hybrid Au–VO_2 slit/disc	1	EBL	1–4	1 μm	$\Delta A = 64\%–70\%$	—	—	—	—	Tunable absorber
5	[226]	2015	Nano Lett.	151	Thermal	VO_2	Checkerboard/slit	1	Selective ion beam	2–15	300 nm	$\Delta R = 50\%$	—	—	—	—	Tunable dichroism
6	[233]	2016	Sci. Rep.	91	Electrical	VO_2	Cross-shape aperture	817	EBL	80–100 GHz	—	$\Delta T = 50\%$	±57°	0.36 mA mm^{-1}	—	—	Beam steering
7	[228]	2016	APL Photonics	26	Thermal	VO_2	Ag nanorod	0.25	EBL	0.45–0.95	58/162 nm	—	—	—	—	23%–42%	Polarization rotator
8	[231]	2016	ACS Nano	35	Optical	VO_2	VO_2-coated ITO rod	0.6–1	EBL	0.4–0.75; 2.5–6.5	—	$\Delta A = 20\%–30\%$	—	9.55 mJ cm^{-1}	3 ps	—	Broadband switching
9	[234]	2017	Nano Lett.	125	Electrical	VO_2	Bow-tie field antenna	0.264×0.3	EBL	0.9–1.6	360 nm	$\Delta A = 33\%$	—	0 to 2.2 V, 21 nJ/pixel	1.27 ms	—	Tunable display
10	[229]	2017	Mater. Res. Express	3	Thermal	VO_2	H-shaped Au pad	3×2.6	EBL	7.5–15	300–400 nm	—	—	—	—	—	Beam steering
11	[232]	2018	ACS Photonics	16	Thermal	VO_2	Epitaxial metasurface	$(1–2) \times (0.1–0.2)$	Laser-assist sputter	0.5–3	—	$\Delta T > 9$ dB	—	—	—	80%	Optical switching
12	[230]	2018	Sci. Rep.	16	Thermal	VO_2	Al nanohole	1.01	EBL	1.3–2	—	$\Delta T = 39\%$	—	—	>1 ms	38%	Photonic switching
13	[235]	2019	Sci. Rep.	9	Thermal	VO_2	Ag rod	0.3	EBL	0.4–0.9	—	$\Delta T = 15\%$	—	—	—	∼70%	Bolometric photodetection
14	[236]	2020	Nano Lett.	44	Electrical	VO_2	Au/VO_2/ Al_2O_3/Au slit	0.4	EBL	1.2–2.0	175 nm	$\Delta R = 24\%$	250°	0 to 14 V	15–100 ms	5%–25%	Beam steering
15	[237]	2020	Nano Lett.	1	Optical	VO_2	VO_2/Si disc	0.656/0.66	EBL	1.1–1.5	—	$\Delta T = 7.7$ dB	—	3.1 kW cm^{-2}	∼1 ps	−4.8 dB	Optical limiting

[a] EBL: electron-beam lithography; FIB: focused ion beam milling.

Table 8. Performance of nano-mechanical structural reconfigurable metasurfaces.[a]

	Reference	Year	Journal	Cite	Stimuli	Active material	Unit cell	Element size (nm)	Fabrication Fabrication	Operation range (μm)	Spectral shift	Modulation depth	Phase shift	Energy consumption	Speed	Efficiency	Application/ function
1	[249]	2011	Adv. Mater.	237	Electro-static	Si	Al semi split ring resonator	27	Ion etching	1.0–3.0 THz	—	Δpermeability = 211%	—	—	500 μs	70% TE; 90% TM	Switchable metamaterial
2	[248]	2009	Phys. Rev. Lett.	479	Thermal	SiN_x/Au	Au split ring resonator	100	SMT	0.3–0.7 THz	—	$\Delta T = 55\%$	—	—	—	90%	Transmission modulation
3	[265]	2018	Nat. Commun.	201	Electro-static	SiN	Si nanopost	320 nm	EBL	915 nm	—	Focal length $\Delta f/f = 23\%$	—	80 V	4 kHz	45%	Tunable metalens
4	[258]	2016	Nano Lett.	22	Electro-thermal	SiN	Au split ring	4.8 × 3.2	FIB	6–14	6.3–10.4 μm	$\Delta R = 95\%$	260°	0.32 V, 6.4 mW	50 kHz	55%	Reflectance modulation
5	[256]	2017	Optica	56	Electro-static	Al_2O_3	Au cross	4.6	Micro-machining	6–16	—	Δemission = 23.7%	—	15 V	110 kHz	—	Dynamic emitter
6	[259]	2016	Adv. Mater.	60	Thermal	SiN	Au cross	1.8	EBL	3.5–8	—	Δemission = 31%	—	—	—	81%	Thermal emission
7	[287]	2017	ACS Photonics	30	Thermal	Si	Si bar	675 nm	EBL	1.5–1.55	—	—	360°	3.5 mW	~15 kHz	40%	Beam deflection
8	[267]	2019	Science	30	Electro-mechanical	Si	Si nanowire	400 nm	EBL	0.6	—	—	360°	3.2 V	1 MHz	—	Beam steering, tunable lens
9	[260]	2013	Nat. Nano	316	Electro-static	SiN	Au nanowire	625 nm	FIB	1–2	~20%	$\Delta R/R = 8\%$	36°	1 V; 2.5 μW	0.5 MHz	68%	Modulation, active absorber
10	[257]	2018	APL Photonics	66	Electro-static	Si	Au nanodisk	2.5	Photolithography	4.6	—	—	—	160 V	1 kHz	83%	Beam steering
11	[266]	2018	Sci. Adv.	131	Elastomer	Elastomer	Si nanopost	1.46–1.64	Photolithography	1.55	—	Focal length $\Delta f/f = 107\%$	—	1–2.5 kV	33 ms	62.5%	Varifocal metalens
12	[251]	2018	Optica	47	Electro-static	Cu	Au cantilever	>1 (est.)	Photolithography	~1 THz	230 GHz	$\Delta R = 0.2$–0.4, $\Delta T = 0.34$	85°	38 V	—	25%	Tunable waveplate
13	[250]	2012	Nat. Commun.	198	Electro-static	Si	Al trapezoid stripe	28	Ion etching	1–5 THz	—	$\Delta T = 120\%$	180°	10 V	10 kHz	~80%	Active control of anisotropy
14	[254]	2011	Appl. Phys. Lett.	63	Electro-static	Si	Al micro-ring	56 × 28	Ion etching	2–4 THz	25.8% TE, 12.1% TM	—	—	~55 V	—	~80%	Polarization switching
15	[243]	2011	Nano Lett.	338	Thermal	SiN	Au split ring	390 × 490 nm^2	FIB	1.18–1.735	20 nm	$\Delta T/T = 51\%$	—	—	—	15%	Reconfigurable transmission
16	[246]	2015	Nat. Commun.	92	Magneto-electro-optical	SiN	Au nanowires	35 × 20	FIB	1.55	—	~2.5%	—	53 mV	—	~10%	Modulation and sensor
17	[268]	2019	Adv. Sci.	6	Thermal	SiN	Binary gratings	—	FIB	0.5–0.9	24 nm	197%	—	—	—	197%	Color display

[a] EBL: electron-beam lithography; FIB: focused ion beam milling; SMT: surface micromachining technology; TE: transverse electric; TM: transverse magnetic.

Table 9. Performance of flexible metasurfaces.[a]

	Reference	Year	Journal	Cite	Stimuli	Active material	Unit cell	Element size (nm)	Fabrication Fabrication	Operation range (μm)	Spectral shift	Modulation depth	Phase shift	Energy consumption	Speed	Efficiency	Application/ function
1	[277]	2015	Optica	127	Mechanical	PDMS	Au grating	630	EBL	0.55–0.65	39 nm	—	—	—	—	80%	Tunable coloration
2	[281]	2011	Adv. Mater.	215	Mechanical	PDMS	Au dimer	1500	EBL	0.6–1	160 nm	—	—	—	—	~50%	Flexible plasmonics
3	[270]	2010	Nano. Lett.	418	Mechanical	PDMS	Au asymmetric antenna	1600	EBL	3–4.5	400 nm	$\Delta R/R \sim 160\%$	—	—	—	~30%	Resonance modulation
4	[282]	2015	ACS Nano	178	Mechanical	PDMA	TiO_2 cylinder	400	EBL	0.591	31 nm	$\Delta T/T \sim 40\%$	—	—	—	~77%	Resonance modulation
5	[272]	2016	Laser Photon. Rev.	196	Mechanical	PDMA	Si nano pillar	380	EBL	0.915	—	—	360°	—	—	>50%	Varifocal lens
6	[286]	2016	Nano Lett.	236	Mechanical	PDMS	Au antenna	520	EBL	0.6328	—	$\Delta T/T \sim 22\%$	360°	—	—	~90%	Varifocal lens
7	[269]	2011	Nano Lett.	209	Mechanical	PDMS	Au split ring resonator	504 × 480	EBL	1.5	436 nm/RIU	—	—	—	—	~25%	Biosensing

[a] EBL: electron-beam lithography; FIB: focused ion beam milling; PDMA: polydimethylsiloxane; PDMS: polydimethylsiloxane.

the facets of conventional fibers. A method to apply a metallic structure to a polymeric membrane on the facet of a hollow core PCF has been functionalized as a nanoplasmonic filter [438]. With the phase flexibility and functionality of metasurfaces, several in-fiber metasurface optical components (316) have been demonstrated, for instance, an in-fiber optical filter and amplifier [439], linear polarizer [440], focusing lens [441], efficient fiber optical tweezer [442], and efficient in-fiber modulator [443]. Optical fiber tips with a phase-gradient metasurface could be functionalized for developing a metalens on a PhC fiber that enables light focusing in the telecommunication regime (figure 77(a)) [444] and beam steering and coupling elements for light manipulation (figure 77(b)) [445]. Compared with metasurfaces on planar substrates (such as Si and SiO_2 glass etc), metasurface-optical fiber provides advantages such as minimization and portability of nanophotonic in-fiber devices [446].

Optical endoscope devices integrated with metasurfaces have developed including an endoscopic optical coherence tomography catheter achieving near diffraction-limited imaging through negating non-chromatic aberrations (figure 78) [447]. Instead of directly fabricating the metasurface on the end face of the optical fiber, the metalens and prism are bonded on the angle-cleaved optical fiber facet using optical adhesive. The metasurface-integrated nano-optic endoscope outperforms the commercial GRIN lens and ball lens catheters with increased imaging depth-of-focus and flexible chromatic dispersion for high resolution imaging. This device demonstrated improved endoscopic imaging in resected human lung specimens and in sheep airways *in vivo* [447].

Integration of active metasurfaces into optical fiber will take the optical fiber devices to the next level because of their capability for controlling the focus, polarization, and mode properties of the light in real time. We anticipate that tunable metasurface fiber devices will advance in-fiber imaging technologies such as endoscopy, in-fiber sensing, optical trapping/molecules manipulation, and in-fiber Raman/coherent Raman/fluorescence spectroscopy. Furthermore, the spectral and spatial control of the light in optical fiber will be favorable for the development of optical fibers for particles trapping and sorting as well as dispersion control and mode control for optical fiber lasers. However, no active optical fiber metasurface functions have been reported so far due to the technical challenge of fabricating functional metasurface nanostructures on the small cross-section of the optical fiber. Electrically-tunable conducting oxide/2D/LC mechanisms, phase change mechanisms, and nonlinear optical mechanisms will probably be the first feasible mechanisms for exploring the functional properties of in-fiber metasurfaces.

9.3.2. Dynamic metasurfaces for lightsail and space technologies. Proposals have been reported recently to incorporate advanced photonic structures such as metasurfaces into solarsail or lightsail applications. Light-driven sails are usually a large, flexible, and reflective surfaces. When a light source (the Sun or a laser) shines on the surface, momentum transfer occurs due to the radiation pressure described by the laws of

Table 10. Symmetric selective high harmonic generation [309].

		Harmonic response				
Antenna shape	Symmetry	1st	2nd	3rd	4th	5th
U haped	1-fold	-2θ	$\theta, -3\theta$	$2\theta, -4\theta$	$3\theta, -5\theta$	$4\theta, -6\theta$
Bar shaped	2-fold			$2\theta, -4\theta$		
Tristar shaped	3-fold		3θ		3θ	-6θ
Cross shaped	4-fold			4θ	4θ	

reflection of diffraction, and thus driving the lightsail with relativistic speeds (figure 79(a)) [448, 449]. Metasurfaces offer a potential to create thin and lightweight metafilm that will provide high momentum transfer efficiency and control of the diffraction and reflection properties. Initial experimental and modeling results show that a lightsail comprised of two opposing diffraction gratings with self-stabilizing attributes could be achieved by the radiation-pressure-induced restoring force created by the bigrating [450, 451]. Several groups also demonstrated the use of thin and low-mass metasurfaces for efficient propulsion and self-stabilizing lasersail or solarsail applications [452–457].

Active metasurfaces could provide a unique opportunity to actively control the reflection and diffraction of light, and thus the radiation pressure and the lateral/normal forces acting on the lightsail. The dynamic control of phase gradient of the active metasurfaces will allow real time adjustment of the torque and normal forces for rolling or pitching of the lightsails and provide attitude control (e.g., in figure 79(b)). Such improved control is of great interest since the current technologies for lightsail control are limited to the use of bulky mechanical components translating the center of mass of the lightsail [457, 458]. In addition, a tunable metasurface might also provide active control of the thermal emission for radiative cooling of the lightsail [42, 452, 459, 460]. Such cooling would be an important consideration for a laser-induced lightsail due to the absorption and thermal issues associated with the materials used. However, the challenge for lightsail and space applications include the large-scale fabrication of large area active metasurfaces, which we will discuss in the following section.

9.3.3. Active imaging and microscopy. Metasurfaces have been widely applied in various imaging applications such as microscopy, polarization imaging, hyperspectral imaging, etc. For instance, Khorasaninejad *et al* demonstrated an ultrathin metalens which can focus the incident light down to a diffraction-limited spot as small as $\sim 0.64\lambda$, allowing for high-resolution imaging [461]. Moreover, the capability of metasurfaces for manipulating both polarization and phase of the electromagnetic fields could allow polarization analysis and functional imaging, which can be used to obtain morphology information such as shape and texture of a surface [399]. Metasurfaces could also be employed to extract molecular composition by hyperspectral imaging, giving rise to an ultrasensitive label-free analytical platform for biosensing combined with imaging optics [60].

However, the passive metalens typically has a fixed optical response and limited depth of focus, which is not suitable to adaptive focusing and imaging applications. The implementation of dynamic imaging based on an active metasurface opens an entirely new solution for multifunctional imaging, which could help to further reduce the number of optical components required for the system, leading to an ultracompact, low cost, low weight platform for high performance imaging applications. For example, active metalenses with multiple foci have been demonstrated, and their capability of adaptive focusing is suitable to imaging complex three-dimensional objects over multiple image planes. In this regard, Arbabi *et al* demonstrated dynamic imaging from a tunable metalens with electrically-controlled focusing based on MEMS in the near infrared (figure 80) [265]. This tunable metalens allows for changing the object distance from 4–15 mm by electrically-controlled refocusing. With this device, they experimentally demonstrated that the image of the object is out of focus without applying bias when the object is placed at 15 mm, while the image comes into focus under a bias of 85 V. Furthermore, they discuss the capability of their device for electrically-tunable microscopy by simulation results. Tunable metalenses have also been successfully demonstrated by other approaches, including by stretching a flexible substrate [286], electrical control [266] and optical control [205], providing diverse options for various application scenarios.

9.3.4. Active metasurface based spatial light modulator for dynamic wavefront control. The capability of a SLM to dynamically control the wavefront of light is of fundamental importance to redistribute or beam steer the light, which is highly desired for many applications including LIDAR, AR, adaptive imaging, and scanning microscopy [210, 462, 463]. However, current widely-implemented diffractive optical components (LC-based SLMs and digital micromirror-based SLMs) have several drawbacks, including slow modulation speeds in the range of a few kHz, complex manufacturing process, and large pixel size [464, 465]. For instance, the pixel size of a typical reflective LC SLM is larger than 3 μm and tens of micrometers for transmissive SLMs, resulting in a small FOV [176]. Metasurface-based SLMs offer the advantage of subwavelength spatial resolution which is essential for wide angle applications. To date, metasurface-based SLMs have been realized from different materials using different tuning mechanisms.

As discussed in section 2.4, Chan *et al* reported a metasurface SLM in the terahertz region which is composed of 4×4 pixels fabricated from a gold SRRs array structure on a GaAs substrate (figure 21(a)) [182]. However, such a configuration relies on the control of the carrier density in the

Table 11. Performance of nonlinear metasurface via frequency conversion and nonlinear frequency mixing.[a]

	Reference	Year	Journal	Cite	Stimuli	Active material	Unit cell	Element size (nm)	Fabrication	Operation range (nm)	Spectral shift	Modulation depth	Phase shift	Energy consumption	Pulse duration	Speed	Efficiency	Application/ function
1	[358]	2018	Adv. Opt. Mater.	5	Optical	MQW	T-shaped Au and MQW antenna	2050×950	EBL	5.4 μm	—	—	—	$\sim$3 GW cm^{-2}	—	—	0.3%	DFG
2	[359]	2014	Appl. Phys. Lett.	68	Optical	MQW	C-shaped Au antenna	1300	EBL	30 THz	—	—	—	$\sim$12 kW cm^{-2}	$\sim$600 fs	—	$\sim 3 \times 10^{-4}$%	SHG
3	[361]	2019	Adv. Opt. Mater.	8	Optical	MQW	T-shaped Au antenna	2100×1600	EBL	8.9 μm	—	—	—	$\sim$210 kW cm^{-2}	—	—	1.8×10^{-3}%	THG
4	[347]	2016	Adv. Opt. Mater.	66	Optical	MQW	T-shaped Au antenna	1900×900	EBL	10 μm	—	—	—	0.1 GW cm^{-2}	400 ns	—	0.08%	SHG
5	[346]	2014	Nature	457	Optical	MQW	L-shaped Au antenna	100×1300	EBL	8.0 μm	—	—	—	0.5 GW cm^{-2}	400 ns	—	0.02%	SHG
6	[357]	2015	IEEE Conference	3	Optical	MQW	T-shaped Au antenna	2×1 μm^2	EBL	26 THz	—	—	—	1 W	—	—	0.8%	SHG
7	[349]	2018	Opt. Express	4	Optical	ITO	Au grating	250	EBL	1500	—	—	—	0.25 mW	150 fs	—	8.7×10^{-4}%	THG
8	[342]	2019	Nat. Commun.	33	Optical	Si	Si rectangular antenna	900	EBL	3600	$<$120 nm	—	—	$<$30 GW cm^{-2}	200 ± 30 fs	—	—	Frequency conversion
9	[330]	2018	Nat. Commun.	96	Optical	GaAs	GaAs nano cylinder	840	EBL	1570	—	—	—	$\sim$78 mJ cm^{-2}	40–45 fs	—	$\sim 2.3 \times 10^{-4}$% SHG	Frequency mixer
10	[331]	2018	Nat. Phys.	90	Optical	Si	Si bar + disc	1280	EBL	2320	—	—	—	71 GW cm^{-2}	$\sim$60 fs	—	$\sim 5 \times 10^{-7}$% SHG	HGG (9th harmonics)
11	[332]	2017	Nat. Phys.	125	Optical	Si	Si rectangular antenna	840	EBL	2100	—	—	—	$\sim$30 GW cm^{-2}	100 fs	—	$\sim 2.3 \times 10^{-5}$% SHG	HGG (11th harmonics)
12	[350]	2018	Nat. Photon.	111	Optical	ITO	Au bar antennas	600	EBL	1250	—	—	—	0.1 GW cm^{-2}	140 fs	$\sim$2 THz	—	Switch/ modulation
13	[339]	2015	Nano Lett.	270	Optical	Si	Si nano disc	300	EBL	755	—	$\Delta T/T = 60\%$	—	27 GW cm^{-2}	45 fs	$\sim$15 THz	—	Switch/ modulation
14	[317]	2015	Nano Lett.	319	Optical	Si	Si nano cylinders	750	EBL	1350	—	$\Delta T/T = 36\%$	—	3.2 GW cm^{-2}	250 fs	$\sim$kHz	1.2×10^{-6}%	THG
15	[341]	2019	ACS Photonics	6	Optical	Si	Si grating	280	EBL	750	—	$\Delta T/T = 10\%$ SHG	—	0–10 V	100 fs	—	—	Electrically tunable SHG
	[340]	2014	Nat. Commun.	73	Optical	Au	Au nano holes	370	EBL	820	—	$\Delta T/T = 130\%$ SHG	—	0–10 V	100 fs	—	—	Electrically tunable SHG

Table 11. Continue

16	[318]	2016	Nano Lett.	255	Optical	GaAs	SiO_x + GaAs + $(Al_xGa_{1-x})_2O_3$ nanorod	600	EBL	1020	—	—	—	3.4 GW cm^{-2}	120 fs	—	~2 × 10^{-3}%	SHG
17	[316]	2014	Nano Lett.	424	Optical	Si	Si nano disc	2850	EBL	1260	—	—	—	~5.5 GW cm^{-2}	200 fs	—	~2 × 10^{-5}%	THG
18	[293]	2006	Science	723	Optical	Au	Split ring Au antenna	100 × 1300	EBL	1550	—	—	—	0.25 GW cm^{-2}	120 fs	—	—	SHG
19	[294]	2015	ACS Photonics	99	Optical	MgF_2	Au/MgF_2/ Au disc	400	EBL	732	—	—	—	~0.3 GW cm^{-2}	100 fs	—	9.1 × 10^{-5}%	SHG
20	[335]	2018	ACS Photonics	34	Optical	GaAs	SiO_2/ GaAs/AlGaO cylindrical antenna	755	EBL	1030	—	—	—	<1 GW cm^{-2}	100 fs	—	—	Frequency conversion
21	[345]	2018	Opt. Express	7	Optical	Au	Dimer + SiO_2 + Si buried oxide layer	540	EBL	1410	—	—	—	7.5 GW cm^{-2}	150 fs	—	—	THG
22	[362]	2016	Optica	75	Optical	MQW	C-shaped Au antenna	1800	EBL	9830	—	—		2 kW cm^{-2}	CW laser	—	~0.1%	SHG
23	[321]	2019	Nano Lett.	13	Optical	TiO_2	TiO_2 cylinder	332	EBL	555	—	—		~10 GW cm^{-2}	—	—	~1 × 10^{-5}%	VUV generation
24	[322]	2018	Nano Lett.	38	Optical	ZnO	ZnO cylinder	222 × 236	EBL	394	—	—		~15 GW cm^{-2}	—	—	~1 × 10^{-7}%	VUV generation
25	[300]	2018	Nano Lett.	34	Optical	Au	V-shaped Au antenna	500, 707	EBL	1000–1300	—	—		12 MW cm^{-2}	200 fs	—	~2.5 × 10^{-9}%	SHG
26	[353]	2019	ACS Photonics	10	Optical	GaSe	L-shaped Si antenna	830	EBL	~1541	—	—		14.61 mW	8.8 ps		~3.6 × 10^{-8}%	SHG
27	[351]	2020	Nano Lett.	2	Optical	ITO	Tristar Au antenna	550	EBL	1160	—	—		~112 MW cm^{-2}	250 fs	—	~10^{-7}%	SHG
28	[328]	2019	ACS Photonics	28	Optical	Si	Asymmetric Si double antenna	720	EBL	1588	—	—		~0.1 GW cm^{-2}	5 ps	—	~2 × 10^{-5}%	THG
29	[327]	2019	Phys. Rev. Lett.	24	Optical	Si	Symmetric defect Si antenna	720	EBL	1556	—	—	—	3 mW	5 ps		~10^{-7}% SHG, ~10^{-5}%THG	SHG, THG
30	[329]	2019	Adv. Sci.	13	Optical	Si	Si disc hole Si antenna	840	EBL	1345	—	—	—	1 GW cm^{-2}	200 fs		~10^{-5}% THG	Dynamic image

[a] EBL = electron-beam lithography; DFG: difference frequency generating; SHG: second harmonic generation; THG third harmonic generation; HHG: high harmonic generation. The efficiency here is related to harmonic generation.

Table 12. Performance of nonlinear metasurface with phase control via self-action effects.[a]

	Reference	Year	Journal	Cite	Stimuli	Active material	Unit cell	Element size (nm)	Fabrication	Operation range (nm)	Spectral shift	Modulation depth	Phase shift	Energy consumption	Pulse duration	Speed	Efficiency	Application/function
1	[301]	2015	Nat. Photonics	248	Optical	Au	U-shaped Au antenna	400	EBL	1300	—	—	—	150 mW	140 fs		5.4×10^{-8}% SHG	SHG beam deflection
2	[306]	2013	Nat. Commun.	886	Optical	Au	Au bar antenna	500	EBL	810	—	—	—	—	—		—	3D holography
3	[310]	2015	Phys. Rev. Lett.	117	Optical	MQW	U-shaped Au antenna	1500	EBL	8000	—	—	—	∼15 kW cm^{-2}	—		—	SHG beam deflection
4	[305]	2015	Adv. Funct. Mater.	149	Optical	Au	Dual-layer Au rectangular holes	400 × 530	EBL	900	—	—	—	—	120 fs		—	—
5	[333]	2018	Nano Lett.	67	Optical	Si	Si nano disc	550	EBL	1615	—	—	—	300 mW	300 fs		10^{-4} THG	Beam steering
6	[304]	2015	ACS Photonics	118	Optical	Au	U-shaped Au antenna	270	EBL	1250	—	—	—	0.85 GW cm^{-2}	140 fs		—	Nonlinear metalens
7	[307]	2015	Nat. Mater.	260	Optical	Au	Au rectangular + cross antenna	400	EBL	1200	—	—	—	50 kW cm^{-2}	200 fs		—	SHG/THG beam deflection
8	[334]	2018	Nano Lett.	30	Optical	Si	C-shaped antenna	660	EBL	1400	—	—	—	33 GW/cm^2	100 fs		1.1×10^{-6}% THG	Nonlinear hologram
9	[336]	2019	Nano Lett.	16	Optical	Si	Si bar antenna	575	EBL	1240			—	300 mW	200 fs		∼10^{-9}% THG	Multiplexed holography
10	[337]	2018	Opt. Express	11	Optical	As_2S_3	Circular nano holes	660	EBL	1255			90°	1.2 kW cm^{-2}	100 fs		—	OAM generation
11	[314]	2018	Adv. Mater.	52	Optical	Au	Tristar shaped antenna	500	EBL	1085			—	250 mW	200 fs		—	Nonlinear metalens
12	[313]	2017	Nano Lett.	82	Optical	Au	Tristar shaped antenna	500	EBL	1240	—	—	—	52 mW	200 fs	—	—	Image encoding

[a] EBL = electron-beam lithography; MQW: multiple-quantum well; SHG: second harmonic generation; THG third harmonic generation. The efficiency here is related to harmonic generation.

Table 13. Performance of hydride-loading transition metal based tunable metasurfaces.[a]

	Reference	Year	Journal	Cite	Stimuli	Active material	Unit cell	Element size (nm)	Fabrication	Operation range (μm)	Spectral shift	Modulation depth	Phase shift	Speed	Efficiency	Application/function
1	[364]	2011	Nano Lett.	342	H_2/O_2	Pd	Grating	450	EBL	0.6–0.85	19 nm	$\Delta R = 3.5\%$	—	10–50 s	$A \approx 99\%$	Absorber, sensing
2	[365]	2014	Nano Lett.	73	H_2/O_2	YH_2	Nanoblock	700 × 400	EBL	1–3	—	$\Delta T = 23\%$	—	50 s to 20 min	—	Active plasmonics
3	[366]	2015	Nano Lett.	119	H_2/O_2	Pd/Ti/Mg	Nanodisk lithography	80–200	Colloidal hole-mask	0.4–1	—	Δemission = 10%	—	15 min	—	Active plasmonics
4	[367]	2016	Nano Lett.	63	H_2/O_2	Mg/Ti/Pd	4 particles + 4 Au satellite	~800	EBL	0.5–0.8	—	ΔCD = 40%	—	100 min	—	Plasmonic chirality
5	[368]	2017	Nat. Commun.	231	H_2/O_2	Ti/Pd/Mg/Ti	Nanoblock	280–640	EBL	0.4–0.8	~50 nm	$\Delta R = 50\%$	—	10–37 min	—	Color display
6	[369]	2017	Nano Lett.	90	H_2/O_2	Mg/Ti/Pd	Stepwise pillar	500	EBL	0.4–0.8	53–66 nm	$\Delta R = \sim 40\%$	—	35–75 s	$R \approx 10\%–70\%$	Color display
7	[370]	2018	ACS Nano	38	H_2/O_2	Pd/Mg	Al nanoblock antenna	160–410	EBL	0.4–0.8	—	$\Delta R = 30\%$	—	5–40 min	—	Scanning display
8	[371]	2018	Sci. Adv.	116	H_2/O_2	Pd/Mg	Nanodisk	300	EBL	0.5–0.95	—	$\Delta R = 30\%$	—	25–1000 s	—	Dynamic holography
9	[372]	2018	Nano Lett.	46	H_2/O_2	Mg	Nanoblock	300–600	EBL	0.633	—	$\Delta R \approx 30\%$	—	30 s to 2 h	$R \approx 35\%$	Beam steering active holography
10	[373]	2020	ACS Nano	1	H_2/O_2	Mg/Ti/Pd	Nanoblock	500	EBL	0.4–0.8	—	$\Delta R \approx 5\%–50\%$	180°	25–75s	$R \approx 58\%$	Active holography color display

[a] EBL: electron-beam lithography; CD: circular dichroism.

Table 14. Performance of microfluidic active metasurfaces.[a]

	Reference	Year	Journal	Cite	Stimuli	Active material	Unit cell	Element size (nm)	Fabrication	Operation range (nm)	Spectral shift	Modulation depth	Phase shift	Energy consumption	Speed	Efficiency	Application/function
1	[374]	2018	ACS Nano	55	Micro-fluidic	Refractive index liquid	TiO_2 nanoblock	300–400	EBL	500–650	50–60 nm	—	—	—	16.7 ms	0.55–0.95	Color display

[a] EBL: electron-beam lithography.

conventional semiconductor substrate. It is difficult to scale up in the optical region. To overcome this limitation, Zeng *et al* demonstrated a hybrid graphene metasurface SLM in the mid infrared as discussed in section 2.2. The large thermo-optic coefficient $\sim 2 \times 10^{-4}$ K^{-1} of the amorphous silicon (a-Si) makes it a promising material for thermal tunable metasurface applications. Horie *et al* reported a 6 × 6 array of a-Si active antennas based SLM with beam deflection capability at the telecom wavelength of ∼1500 nm (figure 81(a)). In their structure, an asymmetric Fabry–Perot resonator was employed as the individual antenna, which was composed of a silicon-based subwavelength grating and a distributed Bragg reflector, which allows for 2π coverage phase modulation. Experimentally, beam deflection up to 1.7° was demonstrated with an efficiency of ∼40%. Moreover, this device exhibited a fast modulation speed with a response time of ~ 70 μs, which is almost an order of magnitude faster than the LC based SLMs [287]. By combining a metasurface with LCs, Li *et al* demonstrated an SLM in the visible with a small pixel size of ~ 1 μm as discussed in section 2.4 (figure 81(b)) [176]. As a result, their SLM is capable of phase-only modulation of the laser in transmission. Furthermore, beam steering was demonstrated with an efficiency of 36% and deflection angle of $<11^\circ$.

Despite the encouraging progress that has been made in developing a metasurface SLM in the optical region, there are several technical challenges to be addressed for practical applications. For instance, the pixel number needs to be significantly scaled up to meet the requirements of realistic applications. Also, the one-dimensional configuration of the current metasurface SLM in the visible undermines its applicability. We believe the extension of the SLM function into two-dimensional operations and small pixel size will be important aspects with active metasurfaces.

9.3.5. Self-adaptive metasurfaces for smart optoelectronic devices. The rapid development of modern electronic and photonic devices, wireless technologies (i.e., Bluetooth, Wi-Fi, LiFi, 4G, etc), and artificial intelligence, have given rise to a new type of smart/intelligent optoelectronic devices which can operate interactively and autonomously. The advancement of active metasurfaces with unprecedented tunability and programmability would open up a great opportunity for the application of metasurfaces as the basis for smart/intelligent devices with self-adaptive functionalities, programmability, and/or multiple tunability. Despite the various mechanisms that have been employed for the implementation of active metasurfaces, the tunability/functionality of the current active metasurfaces mainly rely on manual control. Further integration of external control components, such as sensors [466], light collectors [467], and integrated circuits [468] with active metasurfaces could allow adaptively programming their functionality through an unmanned feedback system, allowing for operations based on ambient environment changes. For instance, Ma *et al* proposes a smart metasurface integrated with a three-axis gyroscope which is motion-sensitive and capable of adjusting the EM radiation beams self-adaptively via changing different rotations of the metasurface (figure 82(a)) [466]. Single/multibeam steering and other dynamic reactions have been achieved adaptively from this smart metasurface by developing an online feedback algorithm as the control. Moreover, intelligent metasurfaces driven by artificial neutral networks were proposed by Li *et al* at a Wi-Fi frequency of 2.4 GHz. Their device consists of 32 × 24 meta-atoms with a total size of 54 × 54 mm^2 [469]. A PIN diode was incorporated into the unit element to act as the electrically-active component by employing deep learning techniques into the programmable metasurfaces. Their devices are capable of high-resolution imaging of the human body and high-accuracy recognition of hand signs and vital signs in real time (figure 82(b)). Liu *et al* demonstrated an intelligent metasurface with programmability and multiple reconfigurable functions at the radio frequency (∼5 GHz) [468]. The independent control over the capacitance and resistance of the integrated circuits by varying the bias voltage enables local tuning of both the reflection amplitude and phase of the metasurface (figure 82(c)), allowing for the demonstrations of tunable perfect absorption and tunable anomalous reflection. Figure 82(d) illustrates a digital coding metasurface capable of smart sensing in the radio frequency, which is composed of metallic patches connected by PIN diodes [470]. Note that this device contains both sensing units and executing units; the sensing unit can detect and convert the incident polarization-dependent electromagnetic wave into transmittable data, and the executing unit will reprogram the function of the metasurface to produce the target scattering fields upon receiving the data. The capability of such a device to simultaneously sense and manipulate microwaves has potential in intelligent imaging and communication applications.

The functionalities of the smart/intelligent metasurface can be further extended to detect humidity, temperature, illuminating light, and so on, greatly expanding the application scenarios of active metasurfaces as intelligent optical components. However, it worth pointing out that the operation frequency of the current reported smart/intelligent metasurfaces is mainly limited to the microwave region, due to the large feature size of the unit cell, which usually contains a diode, varactor, or integrated circuit as the active component to implement local tuning. Despite the great progress that has been made with optical active metasurfaces by various tuning mechanisms as discussed in previous sections, it is still very challenging to realize local control of the unit cell of a metasurface in nano scale, preventing the application of smart metasurfaces in the optical regime using current configurations.

10. Conclusion and outlook

Active optical metasurfaces are paving the way toward the development of next-generation flat optical components and devices. In the last few years, successful demonstrations have been made of efficient control of optical properties (e.g., phase, amplitude, spatial/spectral/temporal responses) and early-stage device functions (e.g., beam steering, tunable focusing, tunable color filters/absorber, dynamic hologram, etc) based on the ten major tunable mechanisms described in this review. Since tunable metasurfaces have been investigated extensively only in the last five years, it is difficult to pick a single mechanism as being most promising for developing efficient active metasurfaces. All ten major mechanisms show their own pros and cons for various properties and performance characteristics (see table 1 for details).

Among these mechanisms, **electrically-tunable conducting oxide metasurfaces** have the advantage of a large gate-tunable refractive index modulation within the Debye length of the accumulation/depletion layer, leading to large optical phase modulation (300°). In addition, they could provide high operation speed (>10 GHz) and low power consumption (estimated 2.5 fJ bit^{-1}). Since they are operated in an electronic chip and the conducting oxide materials are CMOS technology compatible, they have a great potential for developing compact and integrable flat optical devices. The disadvantages are that they exhibit low efficiency (<40%), and they are not accessible in the visible. There is a limitation on the device dimensions (<4000 μm^2) due to the dielectric breakdown within the thin insulator layer. Proof-of-concept applications (beam steering elements, a tunable metalens, and tunable absorbers) have been realized from this mechanism.

Two-dimensional materials incorporated into electrically-dynamic metasurfaces have shown promise for large phase modulation (203°), high speed operation (20 GHz), ultrathin device dimensions, and potentially low energy operation (applied voltage <3 V). However, they are currently limited to the THz and mid-infrared regime, with low efficiency (<50%). They pose a challenge regarding the required nano-patterning, and device dimensions are currently in millimeter size. Tunable absorbers, modulators, and metalenses have been initially demonstrated.

LC based active metasurfaces have demonstrated both outstanding amplitude modulation ($\Delta T/T = 500\%$) and a complete 2π range of phase modulation. Moreover, the devices exhibit high efficiency (97%), they have low power requirements (applied voltage < 4 V), and they can be operated in visible and near-infrared regime. However, the main drawbacks are the slow modulation speed (up to 1 kHz) and limited pixel size/thickness due to the size of the LCs. Demonstrated device functions include beam steering, color filtering, and spatial light modulation.

Electrically-modulated metasurfaces based on III–V semiconductor/quantum wells show the benefits of fast modulation speed (100 MHz) and low power consumption (1 mW cm^{-2}). The limitations include limited phase modulation due to small change of the refractive index ($\Delta n \sim 0.01$), large unit element size (∼910 nm), and operation only in the near infrared wavelength. Beam steering and absorption/reflection modulation have been demonstrated with this type of active metasurface.

Dynamic metasurfaces based on phase change/transition materials show excellent phase modulation (300°) and amplitude modulation ($\Delta R = 100\%$) due to large refractive index change ($\Delta n \approx 2$) during the material phase transition. However, device efficiency is moderate (typically <50%), and the switching speed is relatively slow (<1 kHz) due to the heating and cooling in the transition processes. Initial applications such as all optical switching, thermal modulation, beam steering devices, bifocal lens, and reconfigurable display/holograms have been demonstrated with the phase change/transition materials based tunable metasurfaces.

Dynamic nano-mechanical metasurfaces offer large phase modulation (360°), large amplitude modulation ($\Delta R = 95\%$), low power consumption (1 V/2.5 μW) with high efficiency ($\sim$90%), and large operation range (from the visible to THz). The disadvantages of this tunable mechanism are the moderate modulation speed ($\sim$1 MHz) and challenges to individually pixelize each meta-resonator with nanoscale dimensions. Applications including beam steering, tunable filters, and tunable metalenses have been demonstrated with this mechanism with high efficiency.

Flexible metasurfaces provide good performance with large phase modulation (360°), large amplitude modulation ($\Delta R/R = 180\%$), device efficiency of 90%, and operation in the visible to near infrared. However, the disadvantages of flexible metasurface include the slow tunable speed, they are highly sensitive to the environment (e.g., temperature), they are incompatible with on-chip device applications, and it is barely possible to individually control each unit element. Tunable metalenses and color filters have been demonstrated as initial device functions from flexible metasurfaces.

Nonlinear optical metasurfaces provide different functionalities since new frequencies of light could be generated and manipulated in the nonlinear processes. Moreover, a large nonlinear refractive index could be induced, leading to efficient optical phase modulation (360°) and amplitude modulation (optical switching, $\Delta R/R = 60\%$) with high switching speed (in the order of THz). However, high power optical excitation produced by an expensive ultrafast laser is normally required in inducing the nonlinear optical effects in nonlinear metasurfaces, and the conversion efficiency of harmonic generation is relatively low. It is also less practical for compact device applications because of the requirement of a high-power laser. Ultrafast optical switching, manipulation of harmonic generation, nonlinear holography, and a frequency comb have been reported from the development of nonlinear metasurfaces.

For the **hydride-loading transition metal tunable metasurfaces**, the performance characteristics are good with demonstrated phase modulation of 180°, reflectance change (ΔR) of 60%, and device efficiency up to 75%. The main drawback for this tunable metasurface is the low modulation speed ($<$0.1 Hz). Moreover, it requires specific gas environments for the efficient tuning, making it less practical for device applications. Active device functions such as dynamic color filters, holograms, and beam steering elements have been demonstrated.

Microfluid-based active metasurfaces provide a special functionality based on the well-developed microfluidic chip. It shows decent amplitude modulation ($\Delta R = 40\%$) and efficiency of 55%–95% but a generally slow response time (in the millisecond scale). Tunable color displays have been demonstrated by using microfluidic active metasurfaces.

Each different mechanism has its unique properties and optical performance metrics. Judicious designs will have to be developed depending on the target functionality of the device. To help researchers gain important insights into the three potentially most important performance metrics (e.g., operating wavelength, efficiency, and speed) of the different mechanisms, we have summarized the operational wavelength, device efficiency, and operation speed from reported literatures (see tables after each session) for various mechanisms that are capable of providing $>$90° optical phase shift (figure 83). For applications requiring high modulation speed ($>$kHz), the electrical tunable metasurfaces (e.g., with conducting oxide, 2D materials, multiple quantum-well) are the best currently-available option (red, orange, and green regions). However, the device efficiency and specific operation wavelength will need to be further engineered since they are limited to certain operational wavelength range. Nonlinear optical metasurfaces (brown region) is a very different mechanism since it could potentially modulate the optical response in high speed, but the nonlinear conversion efficiency (e.g., harmonic generation conversion efficiency and efficiency for optical switching) is generally low. LC-based active metasurfaces (yellow region) and dynamic nano-mechanical metasurfaces (gray region) provide high efficiency and large operational spectral range but are limited by slow modulation ($<$1 kHz).

Most of the reports on active metasurfaces are ‘proof-of-concept’ demonstrations without significant integration into actual device applications. We expect significant progress in application development in the next few years. Nevertheless, in this review article, we speculate on 15 prospective applications for active optical metasurfaces for the field of next-generation flat optics technologies (figure 65). The prospective applications are based on metasurface with (i) active spatial and spectral controls (e.g., beam steering elements for LIDAR, active optics components for AR/VR glasses, dynamic hologram, functional multiplexer for communications, and active polarization elements), (ii) active temporal and emission controls (e.g. ultrafast pulse shaping, active optical sensing and biodetection, thermal emission control, dynamic nonreciprocal metasurface devices, and novel tunable laser devices), and (iii) active integration with existing technologies, e.g., active meta-optical fiber devices, nano-dynamic metasurfaces for lightsail and space technologies, active imaging and microscopy, metasurface SLM for dynamic wavefront control, and self-adaptive metasurface devices.

In the longer term, to further extend the science and application of active optical metasurfaces, will require advancements in both materials and engineering approaches. Particularly, we speculate that the following areas are important for advancing active metasurfaces and further exploring emerging applications and technologies.

New materials: precise control of the material properties of active metasurfaces is one of the keys to enhance and tune optical performance and functionalities. Novel active materials (conducting oxide materials, two-dimensional materials, phase change materials, etc) integrated with metasurfaces have opened the door to dynamic control of the optical properties. However, significant material science research is needed to explore better material candidates that exhibit a large refractive index in contrast with external stimuli, lower optical absorption, high response speed, and compatibility with nanofabrication technologies. Novel materials including new conducting oxide materials and metallic nitrides [97, 471, 472], unexplored III–V materials, optoelectrical few-layer black phosphorus [473–476], transdimensional materials with thicknesses of a few tens of atomic layers [94, 477], and conducting polymers [478] are yet to be explored in the context of tunable metasurfaces. We envision that extensive material science research on novel active materials and improvement of current existing materials are important directions for active metasurfaces.

Large area nanofabrication and nanoscale pixelization: fabrication of large scale metasurfaces with sufficient device dimensions (e.g., >100 cm^2) and small element features is another challenge for the field of metasurfaces. Since current nanofabrication processes for metasurfaces involve expensive techniques (e.g., electron beam lithography and focused ion beam milling), it is difficult to mass produce large area metasurfaces with sub-wavelength meta-elements because of the slow processing time and frequent stitching errors in the lithography process. For instance, most of the reported visible/near infrared metalenses are limited in the diameter of <300 μm [44, 52, 479] due to the practical challenges mentioned. Developing a metalens with a larger diameter is an urgent research need. As with applications involving passive metasurfaces, many applications using active metasurfaces will also require large active device dimensions (>10 cm^2), e.g., LIDAR devices (figure 66), AR/VR components (figure 67), dynamic holograms (figure 68), and space optical components (figure 69). Significant challenges remain regarding fabricating and mass-producing large area active devices since multilayer and multi-materials fabrication is involved. In addition, pixelization on each unit element with separately-controllable optical response is a currently unrealized goal for tunable metasurfaces and another obstacle for the realization of large area dynamic metasurfaces. Attempts have been made since 2018 to fabricate large area metasurfaces using scalable photolithography and nanoimprinting approaches [480], such as fabricating a few square millimeters metasurface filter using nanoimprinting technology [481], a 2 cm diameter near-infrared a-Si metalens using stepper photolithography [482], a large-area Alvarez-enabled metalens with controllable focal length by stepper photolithography [483], a large-area pixelated a-Si metasurface beam deflector (2.5×2.5 mm^2) based on 12 inch immersion lithography [484], and an all-glass large metalens array (diameter of 1 cm) on a 4 inch fused-silica wafer using deep-UV lithography [485]. However, there has been no experimental realization of large-area active metasurfaces so far. We believe that design and fabrication of large area tunable metasurfaces using large scale fabrication technologies with nanoscale pixelization will be an important step toward realistic functional nanodevices.

Machine learning assisted design: machine learning and other optimization approaches have been successfully adapted for the inverse design of optical metasurfaces in the last three years. These approaches have been utilized for enhancing the target optical responses of metasurfaces, such as improved transmission/reflection efficiency; optimization of color and spectral responses; development of a high-efficiency, high numerical aperture metalens; high-efficiency beam steering; and high efficiency thermal emission [486–498]. The inverse design approaches are powerful for efficient metasurfaces in specific device applications. However, only few attempts have been made to utilize the machine learning for designing functionalities of tunable metasurfaces. Studies on inverse design of active metasurfaces have been reported recently, for instance, enhancing the efficiency of beam steering with LC based metasurfaces [499], object recognition using dynamic metasurface apertures capable of transceiving programmable microwave patterns [500], real-time machine-learning-guided imaging and compressed-domain object recognition using reconfigurable microwave metasurfaces [502], and array-level inverse design for enhancing beam steering directivity. We believe that inverse design algorithms will be an important factor for optimizing the efficiency and functionalities of active optical metasurfaces for practical applications.

We have witnessed important advances and early-stage device development of active optical metasurfaces in recent years. With further research, we envision that more novel materials/tunable mechanisms, mature device applications, and industry involvement will be realized in the future. We hope this comprehensive review article will provide insights for researchers in this field. We have every expectation that active metasurface research will lead to the full control of optical properties and the widespread integration of metasurfaces into multifunctional metaphotonic devices.

Acknowledgments

This work was supported in part by the CAREER Award Program from National Science Foundation (Grant Number: 1752295) and AFOSR-AOARD (Award Number: FA2386-18-1-4099; FA2386-21-1-4057).

Data availability statement

All data that support the findings of this study are included within the article (and any supplementary files).

ORCID iDs

Jingyi Yang https://orcid.org/0000-0001-8219-9460
Sudip Gurung https://orcid.org/0000-0003-4522-2072
Subhajit Bej https://orcid.org/0000-0002-3561-1341
Ho Wai Howard Lee https://orcid.org/0000-0003-3962-3726

References

[1] Kadic M, Milton G W, van Hecke M and Wegener M 2019 3D metamaterials *Nat. Rev. Phys.* **1** 198–210

[2] Smith D R, Pendry J B and Wiltshire M C 2004 Metamaterials and negative refractive index *Science* **305** 788–92

[3] Liu Y and Zhang X 2011 Metamaterials: a new frontier of science and technology *Chem. Soc. Rev.* **40** 2494–507

[4] Cai W and Shalaev V M 2010 *Optical Metamaterials: Fundamentals and Applications* (New York, NY: Springer) https://doi.org/10.1007/978-1-4419-1151-3

[5] Urbas A M *et al* 2016 Roadmap on optical metamaterials *J. Opt.* **18** 093005

[6] Yu N and Capasso F 2014 Flat optics with designer metasurfaces *Nat. Mater.* **13** 139–50

[7] Kildishev A V, Boltasseva A and Shalaev V M 2013 Planar photonics with metasurfaces *Science* **339** 1232009

[8] Meinzer N, Barnes W L and Hooper I R 2014 Plasmonic meta-atoms and metasurfaces *Nat. Photon.* **8** 889–98

[9] Yu N, Genevet P, Kats M A, Aieta F, Tetienne J-P, Capasso F and Gaburro Z 2011 Light propagation with phase discontinuities: generalized laws of reflection and refraction *Science* **334** 333–7

[10] Aieta F, Genevet P, Kats M A, Yu N, Blanchard R, Gaburro Z and Capasso F 2012 Aberration-free ultrathin flat lenses and axions at telecom wavelengths based on plasmonic metasurfaces *Nano Lett.* **12** 4932–6

[11] Kang M, Feng T, Wang H-T and Li J 2012 Wave front engineering from an array of thin aperture antennas *Opt. Express* **20** 15882–90

[12] Genevet P, Yu N, Aieta F, Lin J, Kats M A, Blanchard R, Scully M O, Gaburro Z and Capasso F 2012 Ultra-thin plasmonic optical vortex plate based on phase discontinuities *Appl. Phys. Lett.* **100** 013101

[13] Yang K-Y *et al* 2014 High-efficiency broadband meta-hologram with polarization-controlled dual images *Nano Lett.* **14** 225–30

[14] Ni X, Kildishev A V and Shalaev V M 2013 Metasurface holograms for visible light *Nat. Commun.* **4** 2807

[15] Zheng G *et al* 2015 Metasurface holograms reaching 80% efficiency *Nat. Nanotechnol.* **10** 308–12

[16] Genevet P and Capasso F 2015 Holographic optical metasurfaces: a review of current progress *Rep. Prog. Phys.* **78** 024401

[17] Huang Y-W, Chen W T, Tsai W-Y, Wu P C, Wang C-M, Sun G and Tsai D P 2015 Aluminum plasmonic multicolor meta-hologram *Nano Lett.* **15** 3122–7

[18] Lin J, Mueller J P B, Wang Q, Yuan G, Antoniou N, Yuan X-C and Capasso F 2013 Polarization-controlled tunable directional coupling of surface plasmon polaritons *Science* **340** 331–4

[19] Jin J, Luo J, Zhang X, Gao H, Li X, Pu M, Gao P, Zhao Z and Luo X 2016 Generation and detection of orbital angular momentum via metasurface *Sci. Rep.* **6** 24286

[20] Li G, Kang M, Chen S, Zhang S, Pun E Y-B, Cheah K W and Li J 2013 Spin-enabled plasmonic metasurfaces for manipulating orbital angular momentum of light *Nano Lett.* **13** 4148–51

[21] Karimi E, Schulz S A, De Leon I, Qassim H, Upham J and Boyd R W 2014 Generating optical orbital angular momentum at visible wavelengths using a plasmonic metasurface *Light Sci. Appl.* **3** e167

[22] Lin D, Fan P, Hasman E and Brongersma M L 2014 Dielectric gradient metasurface optical elements *Science* **345** 298–302

[23] West P R, Stewart J L, Kildishev A V, Shalaev V M, Shkunov V V, Strohkendl F, Zakharenkov Y A, Dodds R K and Byren R 2014 All-dielectric subwavelength metasurface focusing lens *Opt. Express* **22** 26212–21

[24] Arbabi A, Horie Y, Bagheri M and Faraon A 2015 Dielectric metasurfaces for complete control of phase and polarization with subwavelength spatial resolution and high transmission *Nat. Nanotechnol.* **10** 937–43

[25] Yu Y F, Zhu A Y, Paniagua-Domínguez R, Fu Y H, Luk'yanchuk B and Kuznetsov A I 2015 High-transmission dielectric metasurface with 2π phase control at visible wavelengths *Laser Photon. Rev.* **9** 412–8

[26] Khorasaninejad M and Capasso F 2015 Broadband multifunctional efficient meta-gratings based on dielectric waveguide phase shifters *Nano Lett.* **15** 6709–15

[27] Khorasaninejad M, Aieta F, Kanhaiya P, Kats M A, Genevet P, Rousso D and Capasso F 2015 Achromatic metasurface lens at telecommunication wavelengths *Nano Lett.* **15** 5358–62

[28] Aieta F, Kats M A, Genevet P and Capasso F 2015 Multiwavelength achromatic metasurfaces by dispersive phase compensation *Science* **347** 1342–5

[29] Kamali S M, Arbabi A, Arbabi E, Horie Y and Faraon A 2016 Decoupling optical function and geometrical form using conformal flexible dielectric metasurfaces *Nat. Commun.* **7** 11618

[30] Arbabi E, Arbabi A, Kamali S M, Horie Y and Faraon A 2016 Multiwavelength polarization-insensitive lenses based on dielectric metasurfaces with meta-molecules *Optica* **3** 628–33

[31] Arbabi E, Arbabi A, Kamali S M, Horie Y and Faraon A 2017 Controlling the sign of chromatic dispersion in diffractive optics with dielectric metasurfaces *Optica* **4** 625–32

[32] Arbabi A, Horie Y, Ball A J, Bagheri M and Faraon A 2015 Subwavelength-thick lenses with high numerical apertures and large efficiency based on high-contrast transmitarrays *Nat. Commun.* **6** 7069

[33] Arbabi A, Arbabi E, Kamali S M, Horie Y, Han S and Faraon A 2016 Miniature optical planar camera based on a wide-angle metasurface doublet corrected for monochromatic aberrations *Nat. Commun.* **7** 13682

[34] Yang Y, Kravchenko I I, Briggs D P and Valentine J 2014 All-dielectric metasurface analogue of electromagnetically induced transparency *Nat. Commun.* **5** 5753

[35] Yang Y, Wang W, Moitra P, Kravchenko I I, Briggs D P and Valentine J 2014 Dielectric meta-reflectarray for broadband linear polarization conversion and optical vortex generation *Nano Lett.* **14** 1394–9

[36] Guo R, Rusak E, Staude I, Dominguez J, Decker M, Rockstuhl C, Brener I, Neshev D N and Kivshar Y S 2016 Multipolar coupling in hybrid metal-dielectric metasurfaces *ACS Photonics* **3** 349–53

[37] Chong K E *et al* 2015 Polarization-independent silicon metadevices for efficient optical wavefront control *Nano Lett.* **15** 5369–74

[38] Sautter J, Staude I, Decker M, Rusak E, Neshev D N, Brener I and Kivshar Y S 2015 Active tuning of all-dielectric metasurfaces *ACS Nano* **9** 4308–15

[39] Kim J, Choudhury S, DeVault C, Zhao Y, Kildishev A V, Shalaev V M, Alù A and Boltasseva A 2016 Controlling the polarization state of light with plasmonic metal oxide metasurface *ACS Nano* **10** 9326–33

[40] Gregory S A, Wang Y, de Groot C H and Muskens O L 2015 Extreme subwavelength metal oxide direct and complementary metamaterials *ACS Photonics* **2** 606–14

[41] Sun K, Xiao W, Ye S, Kalfagiannis N, Kiang K S, Groot C H and Muskens O L 2020 Embedded metal oxide plasmonics using local plasma oxidation of AZO for planar metasurfaces *Adv. Mater.* **32** 2001534

[42] Sun K *et al* 2018 Metasurface optical solar reflectors using AZO transparent conducting oxides for radiative cooling of spacecraft *ACS Photonics* **5** 495–501

[43] Devlin R C, Khorasaninejad M, Chen W T, Oh J and Capasso F 2016 Broadband high-efficiency dielectric metasurfaces for the visible spectrum *Proc. Natl Acad. Sci. USA* **113** 10473–8

[44] Khorasaninejad M, Chen W T, Devlin R C, Oh J, Zhu A Y and Capasso F 2016 Metalenses at visible wavelengths: diffraction-limited focusing and subwavelength resolution imaging *Science* **352** 1190–4

[45] Zhu A Y, Chen W-T, Khorasaninejad M, Oh J, Zaidi A, Mishra I, Devlin R C and Capasso F 2017 Ultra-compact visible chiral spectrometer with meta-lenses *APL Photonics* **2** 036103

[46] Khorasaninejad M, Chen W T, Zhu A Y, Oh J, Devlin R C, Roques-Carmes C, Mishra I and Capasso F 2017 Visible wavelength planar metalenses based on titanium dioxide *IEEE J. Sel. Top. Quantum Electron.* **23** 43–58

[47] Chen W T, Zhu A Y, Sisler J, Bharwani Z and Capasso F 2019 A broadband achromatic polarization-insensitive metalens consisting of anisotropic nanostructures *Nat. Commun.* **10** 355

[48] Colburn S, Zhan A, Bayati E, Whitehead J, Ryou A, Huang L and Majumdar A 2018 Broadband transparent and CMOS-compatible flat optics with silicon nitride metasurfaces *Opt. Mater. Express* **8** 2330–44

[49] Zhan A, Colburn S, Trivedi R, Fryett T K, Dodson C M and Majumdar A 2016 Low-contrast dielectric metasurface optics *ACS Photonics* **3** 209–14

[50] Boltasseva A and Atwater H A 2011 Low-loss plasmonic metamaterials *Science* **331** 290–1

[51] Fan Z-B, Qiu H-Y, Zhang H-L, Pang X-N, Zhou L-D, Liu L, Ren H, Wang Q-H and Dong J-W 2019 A broadband achromatic metalens array for integral imaging in the visible *Light Sci. Appl.* **8** 67

[52] Wang S *et al* 2018 A broadband achromatic metalens in the visible *Nat. Nanotechnol.* **13** 227–32

[53] Chen W T, Zhu A Y, Sisler J, Huang Y-W, Yousef K M A, Lee E, Qiu C-W and Capasso F 2018 Broadband achromatic metasurface-refractive optics *Nano Lett.* **18** 7801–8

[54] Faraji-Dana M, Arbabi E, Arbabi A, Kamali S M, Kwon H and Faraon A 2018 Compact folded metasurface spectrometer *Nat. Commun.* **9** 4196

[55] Zhou J, Qian H, Chen C-F, Zhao J, Li G, Wu Q, Luo H, Wen S and Liu Z 2019 Optical edge detection based on high-efficiency dielectric metasurface *Proc. Natl Acad. Sci. USA* **116** 11137–40

[56] Kwon H, Arbabi E, Kamali S M, Faraji-Dana M and Faraon A 2019 Single-shot quantitative phase gradient microscopy using a system of multifunctional metasurfaces *Nat. Photon.* **14** 109–14

[57] Xie Y-Y *et al* 2020 Metasurface-integrated vertical cavity surface-emitting lasers for programmable directional lasing emissions *Nat. Nanotechnol.* **15** 125–30

[58] Hu Y, Luo X, Chen Y, Liu Q, Li X, Wang Y, Liu N and Duan H 2019 3D-integrated metasurfaces for full-colour holography *Light Sci. Appl.* **8** 86

[59] Wen D *et al* 2015 Helicity multiplexed broadband metasurface holograms *Nat. Commun.* **6** 8241

[60] Yesilkoy F, Arvelo E R, Jahani Y, Liu M, Tittl A, Cevher V, Kivshar Y and Altug H 2019 Ultrasensitive hyperspectral imaging and biodetection enabled by dielectric metasurfaces *Nat. Photon.* **13** 390–6

[61] Rubin N A, D'Aversa G, Chevalier P, Shi Z, Chen W T and Capasso F 2019 Matrix Fourier optics enables a compact full-Stokes polarization camera *Science* **365** eaax1839

[62] Divitt S, Zhu W, Zhang C, Lezec H J and Agrawal A 2019 Ultrafast optical pulse shaping using dielectric metasurfaces *Science* **364** 890–4

[63] Jiang Q, Jin G and Cao L 2019 When metasurface meets hologram: principle and advances *Adv. Opt. Photonics* **11** 518–76

[64] Luo X 2018 Subwavelength optical engineering with metasurface waves *Adv. Opt. Mater.* **6** 1701201

[65] Chen H-T, Taylor A J and Yu N 2016 A review of metasurfaces: physics and applications *Rep. Prog. Phys.* **79** 076401

[66] Kamali S M, Arbabi E, Arbabi A and Faraon A 2018 A review of dielectric optical metasurfaces for wavefront control *Nanophotonics* **7** 1041–68

[67] Lee G Y, Sung J and Lee B 2019 Recent advances in metasurface hologram technologies *ETRI J.* **41** 10–22

[68] Chen S, Li Z, Zhang Y, Cheng H and Tian J 2018 Phase manipulation of electromagnetic waves with metasurfaces and its applications in nanophotonics *Adv. Opt. Mater.* **6** 1800104

[69] Bozhevolnyi S I, Genevet P and Ding F 2018 *Metasurfaces: Physics and Applications* (Switzerland: MDPI Appl. Sci.) https://doi.org/10.3390/books978-3-03897-345-4

[70] Lee D, Gwak J, Badloe T, Palomba S and Rho J 2020 Metasurfaces-based imaging and applications: from miniaturized optical components to functional imaging platforms *Nanoscale Adv.* **2** 605–25

[71] Huang L, Zhang S and Zentgraf T 2018 Metasurface holography: from fundamentals to applications *Nanophotonics* **7** 1169–90

[72] Wan W, Gao J and Yang X 2017 Metasurface holograms for holographic imaging *Adv. Opt. Mater.* **5** 1700541

[73] Choudhury S M, Wang D, Chaudhuri K, DeVault C, Kildishev A V, Boltasseva A and Shalaev V M 2018 Material platforms for optical metasurfaces *Nanophotonics* **7** 959–87

[74] Chen M, Kim M, Wong A M H and Eleftheriades G V 2018 Huygens' metasurfaces from microwaves to optics: a review *Nanophotonics* **7** 1207–31

[75] He Q, Sun S, Xiao S and Zhou L 2018 High-efficiency metasurfaces: principles, realizations, and applications *Adv. Opt. Mater.* **6** 1800415

[76] Ding F, Pors A and Bozhevolnyi S I 2018 Gradient metasurfaces: a review of fundamentals and applications *Rep. Prog. Phys.* **81** 026401

[77] Chang S, Guo X and Ni X 2018 Optical metasurfaces: progress and applications *Annu. Rev. Mater. Res.* **48** 279–302

[78] Wei Q, Huang L, Zentgraf T and Wang Y 2020 Optical wavefront shaping based on functional metasurfaces *Nanophotonics* **9** 987–1002

[79] Xiong B, Deng L, Peng R and Liu Y 2019 Controlling the degrees of freedom in metasurface designs for multi-functional optical devices *Nanoscale Adv.* **1** 3786–806

[80] Chen S, Liu W, Li Z, Cheng H and Tian J 2020 Metasurface-empowered optical multiplexing and multifunction *Adv. Mater.* **32** e1805912

[81] Scheuer J 2020 Optical metasurfaces are coming of age: short- and long-term opportunities for commercial applications *ACS Photonics* **7** 1323–54

[82] Quevedo-Teruel O *et al* 2019 Roadmap on metasurfaces *J. Opt.* **21** 073002

[83] He J, Dong T, Chi B and Zhang Y 2020 Metasurfaces for terahertz wavefront modulation: a review *J. Infrared Millim. Terahertz Waves* **41** 607–31

[84] Krasnok A, Tymchenko M and Alù A 2018 Nonlinear metasurfaces: a paradigm shift in nonlinear optics *Mater. Today* **21** 8–21

[85] Li L *et al* 2017 Electromagnetic reprogrammable coding-metasurface holograms *Nat. Commun.* **8** 197

[86] He S, Yang H, Jiang Y, Deng W and Zhu W 2019 Recent advances in MEMS metasurfaces and their applications on tunable lens *Micromachines* **10** 505

[87] Shaltout A M, Shalaev V M and Brongersma M L 2019 Spatiotemporal light control with active metasurfaces *Science* **364** eaat3100

[88] Nemati A, Wang Q, Hong M and Teng J 2018 Tunable and reconfigurable metasurfaces and metadevices *Opto-Electron. Adv.* **1** 180009

[89] Cui T, Bai B and Sun H B 2019 Tunable metasurfaces based on active materials *Adv. Funct. Mater.* **29** 1806692

[90] Lee C-W, Choi H J and Jeong H 2020 Tunable metasurfaces for visible and SWIR applications *Nano Convergence* **7** 3

[91] He Q, Sun S and Zhou L 2019 Tunable/reconfigurable metasurfaces: physics and applications *Research* **2019** 1849272

[92] Li A, Singh S and Sievenpiper D 2018 Metasurfaces and their applications *Nanophotonics* **7** 989–1011

[93] Cheng J, Fan F and Chang S 2019 Recent progress on graphene-functionalized metasurfaces for tunable phase and polarization control *Nanomaterials* **9** 398

[94] Shah D, Kudyshev Z A, Saha S, Shalaev V M and Boltasseva A 2020 Transdimensional material platforms for tunable metasurface design *MRS Bull.* **45** 188–95

[95] Keren-Zur S, Michaeli L, Suchowski H and Ellenbogen T 2018 Shaping light with nonlinear metasurfaces *Adv. Opt. Photonics* **10** 309–53

[96] Huang Y-W *et al* 2019 Structured semiconductor interfaces: active functionality on light manipulation *Proc. IEEE* **108** 772–94

[97] Naik G V, Shalaev V M and Boltasseva A 2013 Alternative plasmonic materials: beyond gold and silver *Adv. Mater.* **25** 3264–94

[98] Naik G V, Kim J and Boltasseva A 2011 Oxides and nitrides as alternative plasmonic materials in the optical range *Opt. Mater. Express* **1** 1090–9

[99] Li S Q, Guo P, Zhang L, Zhou W, Odom T W, Seideman T, Ketterson J B and Chang R P H 2011 Infrared plasmonics with indium-tin-oxide nanorod arrays *ACS Nano* **5** 9161–70

[100] Guler U, Naik G V, Boltasseva A, Shalaev V M and Kildishev A V 2012 Performance analysis of nitride alternative plasmonic materials for localized surface plasmon applications *Appl. Phys.* B **107** 285–91

[101] Dominici L, Michelotti F, Brown T M, Reale A and Carlo A D 2009 Plasmon polaritons in the near infrared on fluorine doped tin oxide films *Opt. Express* **17** 10155–67

[102] Franzen S, Rhodes C, Cerruti M, Gerber R W, Losego M, Maria J-P and Aspnes D E 2009 Plasmonic phenomena in indium tin oxide and ITO–Au hybrid films *Opt. Lett.* **34** 2867–9

[103] Kim J, Naik G V, Emani N K, Guler U and Boltasseva A 2013 Plasmonic resonances in nanostructured transparent conducting oxide films *IEEE J. Sel. Top. Quantum Electron.* **19** 4601907

[104] Liu X, Park J, Kang J-H, Yuan H, Cui Y, Hwang H Y and Brongersma M L 2014 Quantification and impact of nonparabolicity of the conduction band of indium tin oxide on its plasmonic properties *Appl. Phys. Lett.* **105** 181117

[105] West P R, Ishii S, Naik G V, Emani N K, Shalaev V M and Boltasseva A 2010 Searching for better plasmonic materials *Laser Photon. Rev.* **4** 795–808

[106] Verma R K and Gupta B D 2010 Surface plasmon resonance based fiber optic sensor for the IR region using a conducting metal oxide film *J. Opt. Soc. Am.* A **27** 846–51

[107] Rhodes C, Franzen S, Maria J-P, Losego M, Leonard D N, Laughlin B, Duscher G and Weibel S 2006 Surface plasmon resonance in conducting metal oxides *J. Appl. Phys.* **100** 054905

[108] Michelotti F, Dominici L, Descrovi E, Danz N and Menchini F 2009 Thickness dependence of surface plasmon polariton dispersion in transparent conducting oxide films at 155 μm *Opt. Lett.* **34** 839–41

[109] Abb M, Sepúlveda B, Chong H M H and Muskens O L 2012 Transparent conducting oxides for active hybrid metamaterial devices *J. Opt.* **14** 114007

[110] Noginov M A, Gu L, Livenere J, Zhu G, Pradhan A K, Mundle R, Bahoura M, Barnakov Y A and Podolskiy V A 2011 Transparent conductive oxides: plasmonic materials for telecom wavelengths *Appl. Phys. Lett.* **99** 021101

[111] Buonsanti R, Llordes A, Aloni S, Helms B A and Milliron D J 2011 Tunable infrared absorption and visible transparency of colloidal aluminum-doped zinc oxide nanocrystals *Nano Lett.* **11** 4706–10

[112] Traviss D, Bruck R, Mills B, Abb M and Muskens O L 2013 Ultrafast plasmonics using transparent conductive oxide hybrids in the epsilon-near-zero regime *Appl. Phys. Lett.* **102** 121112

[113] Calzolari A, Ruini A and Catellani A 2014 Transparent conductive oxides as near-IR plasmonic materials: the case of Al-doped ZnO derivatives *ACS Photonics* **1** 703–9

[114] Lee H W, Papadakis G, Burgos S P, Chander K, Kriesch A, Pala R, Peschel U and Atwater H A 2014 Nanoscale conducting oxide PlasMOStor *Nano Lett.* **14** 6463–8

[115] Anopchenko A, Gurung S, Tao L, Arndt C and Lee H W H 2018 Atomic layer deposition of ultra-thin and smooth Al-doped ZnO for zero-index photonics *Mater. Res. Express* **5** 014012

[116] Huang Y-W, Lee H W H, Sokhoyan R, Pala R A, Thyagarajan K, Han S, Tsai D P and Atwater H A 2016 Gate-tunable conducting oxide metasurfaces *Nano Lett.* **16** 5319–25

[117] Alam M Z, De Leon I and Boyd R W 2016 Large optical nonlinearity of indium tin oxide in its epsilon-near-zero region *Science* **352** 795–7

[118] Kim J *et al* 2016 Role of epsilon-near-zero substrates in the optical response of plasmonic antennas *Optica* **3** 339–46

[119] Alù A, Silveirinha M G, Salandrino A and Engheta N 2007 Epsilon-near-zero metamaterials and electromagnetic sources: tailoring the radiation phase pattern *Phys. Rev.* B **75** 155410

[120] Vasudev A P, Kang J-H, Park J, Liu X and Brongersma M L 2013 Electro-optical modulation of a silicon waveguide with an ‘epsilon-near-zero’ material *Opt. Express* **21** 26387–97

[121] Lu Z, Zhao W and Shi K 2012 Ultracompact electroabsorption modulators based on tunable epsilon-near-zero-slot waveguides *IEEE Photon. J.* **4** 735–40

[122] Wood M G, Campione S, Parameswaran S, Luk T S, Wendt J R, Serkland D K and Keeler G A 2018 Gigahertz speed operation of epsilon-near-zero silicon photonic modulators *Optica* **5** 233–6

[123] Kafaie Shirmanesh G, Sokhoyan R, Pala R A and Atwater H A 2018 Dual-gated active metasurface at 1550 nm with wide ($>300^\circ$) phase tunability *Nano Lett.* **18** 2957–63

[124] Shirmanesh G K, Sokhoyan R, Wu P C and Atwater H A 2020 Electro-optically tunable multifunctional metasurfaces *ACS Nano* **14** 6912–20

[125] Park J, Kang J-H, Kim S J, Liu X and Brongersma M L 2017 Dynamic reflection phase and polarization control in metasurfaces *Nano Lett.* **17** 407–13

[126] Park J, Kang J-H, Liu X and Brongersma M L 2015 Electrically tunable epsilon-near-zero (ENZ) metafilm absorbers *Sci. Rep.* **5** 15754

[127] Zhao H, Zhang R, Chorsi H T, Britton W A, Chen Y, Iyer P P, Schuller J A, Negro L D and Klamkin J 2019 Gate-tunable metafilm absorber based on indium silicon oxide *Nanophotonics* **8** 1803–10

[128] Thyagarajan K, Sokhoyan R, Zornberg L and Atwater H A 2017 Millivolt modulation of plasmonic metasurface optical response via ionic conductance *Adv. Mater.* **29** 1701044

[129] Yi F, Shim E, Zhu A Y, Zhu H, Reed J C and Cubukcu E 2013 Voltage tuning of plasmonic absorbers by indium tin oxide *Appl. Phys. Lett.* **102** 221102

[130] George D, Li L, Lowell D, Ding J, Cui J, Zhang H, Philipose U and Lin Y 2017 Electrically tunable diffraction efficiency from gratings in Al-doped ZnO *Appl. Phys. Lett.* **110** 071110

[131] Howes A, Wang W, Kravchenko I and Valentine J 2018 Dynamic transmission control based on all-dielectric Huygens metasurfaces *Optica* **5** 787–92

[132] Kim S J and Brongersma M L 2017 Active flat optics using a guided mode resonance *Opt. Lett.* **42** 5–8

[133] Yoon G, So S, Kim M, Mun J, Ma R and Rho J 2017 Electrically tunable metasurface perfect absorber for infrared frequencies *Nano Convergence* **4** 36

[134] Hwang J and Roh J W 2017 Electrically tunable two-dimensional metasurfaces at near-infrared wavelengths *Opt. Express* **25** 25071–8

[135] Zhang J, Yang J, Schell M, Anopchenko A, Tao L, Yu Z and Lee H W H 2019 Gate-tunable optical filter based on conducting oxide metasurface heterostructure *Opt. Lett.* **44** 3653–6

[136] Sabri R, Forouzmand A and Mosallaei H 2020 Multi-wavelength voltage-coded metasurface based on indium tin oxide: independently and dynamically controllable near-infrared multi-channels *Opt. Express* **28** 3464–81

[137] Riedel C A, Sun K, Muskens O L and de Groot C 2017 Nanoscale modeling of electro-plasmonic tunable devices for modulators and metasurfaces *Opt. Express* **25** 10031–43

[138] Forouzmand A and Mosallaei H 2017 Real-time controllable and multifunctional metasurfaces utilizing indium tin oxide materials: a phased array perspective *IEEE Trans. Nanotechnol.* **16** 296–306

[139] Forouzmand A, Salary M M, Kafaie Shirmanesh G, Sokhoyan R, Atwater H A and Mosallaei H 2019 Tunable all-dielectric metasurface for phase modulation of the reflected and transmitted light via permittivity tuning of indium tin oxide *Nanophotonics* **8** 415–27

[140] Forouzmand A, Salary M M, Inampudi S and Mosallaei H 2018 A tunable multigate indium-tin-oxide-assisted all-dielectric metasurface *Adv. Opt. Mater.* **6** 1701275

[141] Forouzmand A and Mosallaei H 2016 Tunable two dimensional optical beam steering with reconfigurable indium tin oxide plasmonic reflectarray metasurface *J. Opt.* **18** 125003

[142] Zeng B, Huang Z, Singh A, Yao Y, Azad A K, Mohite A D, Taylor A J, Smith D R and Chen H-T 2018 Hybrid graphene metasurfaces for high-speed mid-infrared light modulation and single-pixel imaging *Light Sci. Appl.* **7** 51

[143] Chen J-H, Jang C, Xiao S, Ishigami M and Fuhrer M S 2008 Intrinsic and extrinsic performance limits of graphene devices on SiO_2 *Nat. Nanotechnol.* **3** 206–9

[144] Hwang E H and Das Sarma S 2008 Acoustic phonon scattering limited carrier mobility in two-dimensional extrinsic graphene *Phys. Rev.* B **77** 115449

[145] Liu M, Yin X, Ulin-Avila E, Geng B, Zentgraf T, Ju L, Wang F and Zhang X 2011 A graphene-based broadband optical modulator *Nature* **474** 64–7

[146] Falkovsky L A and Pershoguba S S 2007 Optical far-infrared properties of a graphene monolayer and multilayer *Phys. Rev.* B **76** 153410

[147] Liu C, Bai Y, Zhou J, Zhao Q and Qiao L 2017 A review of graphene plasmons and its combination with metasurface *J. Korean Ceram. Soc.* **54** 349–65

[148] Novoselov K S *et al* 2004 Electric field effect in atomically thin carbon films *Science* **306** 666–9

[149] Ju L *et al* 2011 Graphene plasmonics for tunable terahertz metamaterials *Nat. Nanotechnol.* **6** 630–4

[150] Liu P Q, Valmorra F, Maissen C and Faist J 2015 Electrically tunable graphene anti-dot array terahertz plasmonic crystals exhibiting multi-band resonances *Optica* **2** 135–40

[151] Lee S H *et al* 2012 Switching terahertz waves with gate-controlled active graphene metamaterials *Nat. Mater.* **11** 936–41

[152] Yao Y, Kats M A, Genevet P, Yu N, Song Y, Kong J and Capasso F 2013 Broad electrical tuning of graphene-loaded plasmonic antennas *Nano Lett.* **13** 1257–64

[153] Emani N K, Chung T-F, Kildishev A V, Shalaev V M, Chen Y P and Boltasseva A 2014 Electrical modulation of fano resonance in plasmonic nanostructures using graphene *Nano Lett.* **14** 78–82

[154] Gao W *et al* 2014 High-contrast terahertz wave modulation by gated graphene enhanced by extraordinary transmission through ring apertures *Nano Lett.* **14** 1242–8

[155] Kim S, Jang M S, Brar V W, Mauser K W, Kim L and Atwater H A 2018 Electronically tunable perfect absorption in graphene *Nano Lett.* **18** 971–9

[156] Yao Y, Shankar R, Kats M A, Song Y, Kong J, Loncar M and Capasso F 2014 Electrically tunable metasurface perfect absorbers for ultrathin mid-infrared optical modulators *Nano Lett.* **14** 6526–32

[157] Sherrott M C, Hon P W C, Fountaine K T, Garcia J C, Ponti S M, Brar V W, Sweatlock L A and Atwater H A 2017 Experimental demonstration of >230° phase modulation in gate-tunable graphene–gold reconfigurable mid-infrared metasurfaces *Nano Lett.* **17** 3027–34

[158] Han S, Kim S, Kim S, Low T, Brar V W and Jang M S 2020 Complete complex amplitude modulation with electronically tunable graphene plasmonic metamolecules *ACS Nano* **14** 1166–75

[159] Zhang X *et al* 2018 Dynamic photochemical and optoelectronic control of photonic fano resonances via monolayer MoS_2 trions *Nano Lett.* **18** 957–63

[160] Lee B, Liu W, Naylor C H, Park J, Malek S C, Berger J S, Johnson A T C and Agarwal R 2017 Electrical tuning of exciton–plasmon polariton coupling in monolayer MoS_2 integrated with plasmonic nanoantenna lattice *Nano Lett.* **17** 4541–7

[161] Liu W *et al* 2019 Observation and active control of a collective polariton mode and polaritonic band gap in few-layer WS_2 strongly coupled with plasmonic lattices *Nano Lett.* **20** 790–8

[162] Ni P, De Luna Bugallo A, Arellano Arreola V M, Salazar M F, Strupiechonski E, Brändli V, Sawant R, Alloing B and Genevet P 2019 Gate-tunable emission of exciton–plasmon polaritons in hybrid MoS_2-gap-mode metasurfaces *ACS Photonics* **6** 1594–601

[163] van de Groep J, Song J-H, Celano U, Li Q, Kik P G and Brongersma M L 2020 Exciton resonance tuning of an atomically thin lens *Nat. Photon.* **14** 426–30

[164] Brongersma M L 2021 The road to atomically thin metasurface optics *Nanophotonics* **10** 643–54

[165] Andrienko D 2018 Introduction to liquid crystals *J. Mol. Liq.* **267** 520–41

[166] Khoo I C, Diaz A, Liou J, Stinger M V, Huang J and Ma Y 2010 Liquid crystals tunable optical metamaterials *IEEE J. Sel. Top. Quantum Electron.* **16** 410–7

[167] Kossyrev P A, Yin A, Cloutier S G, Cardimona D A, Huang D, Alsing P M and Xu J M 2005 Electric field tuning of plasmonic response of nanodot array in liquid crystal matrix *Nano Lett.* **5** 1978–81

[168] Decker M, Kremers C, Minovich A, Staude I, Miroshnichenko A E, Chigrin D, Neshev D N, Jagadish C and Kivshar Y S 2013 Electro-optical switching by liquid-crystal controlled metasurfaces *Opt. Express* **21** 8879–85

[169] Buchnev O, Podoliak N, Kaczmarek M, Zheludev N I and Fedotov V A 2015 Electrically controlled nanostructured metasurface loaded with liquid crystal: toward multifunctional photonic switch *Adv. Opt. Mater.* **3** 674–9

[170] Xie Z-W, Yang J-H, Vashistha V, Lee W and Chen K-P 2017 Liquid-crystal tunable color filters based on aluminum metasurfaces *Opt. Express* **25** 30764–70

[171] Buchnev O, Ou J Y, Kaczmarek M, Zheludev N I and Fedotov V A 2013 Electro-optical control in a plasmonic metamaterial hybridised with a liquid-crystal cell *Opt. Express* **21** 1633–8

[172] Chen K-P, Ye S-C, Yang C-Y, Yang Z-H, Lee W and Sun M-G 2016 Electrically tunable transmission of gold binary-grating metasurfaces integrated with liquid crystals *Opt. Express* **24** 16815–21

[173] Komar A *et al* 2017 Electrically tunable all-dielectric optical metasurfaces based on liquid crystals *Appl. Phys. Lett.* **110** 071109

[174] Sun M *et al* 2019 Efficient visible light modulation based on electrically tunable all dielectric metasurfaces embedded in thin-layer nematic liquid crystals *Sci. Rep.* **9** 8673

[175] Wang R, He S, Chen S, Zhang J, Shu W, Luo H and Wen S 2018 Electrically driven generation of arbitrary vector vortex beams on the hybrid-order Poincaré sphere *Opt. Lett.* **43** 3570–3

[176] Li S-Q, Xu X, Maruthiyodan Veetil R, Valuckas V, Paniagua-Domínguez R and Kuznetsov A I 2019 Phase-only transmissive spatial light modulator based on tunable dielectric metasurface *Science* **364** 1087–90

[177] Komar A, Paniagua-Domínguez R, Miroshnichenko A, Yu Y F, Kivshar Y S, Kuznetsov A I and Neshev D 2018 Dynamic beam switching by liquid crystal tunable dielectric metasurfaces *ACS Photonics* **5** 1742–8

[178] Bohn J, Bucher T, Chong K E, Komar A, Choi D-Y, Neshev D N, Kivshar Y S, Pertsch T and Staude I 2018 Active tuning of spontaneous emission by Mie-resonant dielectric metasurfaces *Nano Lett.* **18** 3461–5

[179] Liu Y J, Si G Y, Leong E S P, Xiang N, Danner A J and Teng J H 2012 Light-driven plasmonic color filters by overlaying photoresponsive liquid crystals on gold annular aperture arrays *Adv. Mater.* **24** OP131–5

[180] Chen H-T, Padilla W J, Zide J M O, Gossard A C, Taylor A J and Averitt R D 2006 Active terahertz metamaterial devices *Nature* **444** 597–600

[181] Jun Y C, Gonzales E, Reno J L, Shaner E A, Gabbay A and Brener I 2012 Active tuning of mid-infrared metamaterials by electrical control of carrier densities *Opt. Express* **20** 1903–11

[182] Chan W L, Chen H-T, Taylor A J, Brener I, Cich M J and Mittleman D M 2009 A spatial light modulator for terahertz beams *Appl. Phys. Lett.* **94** 213511

[183] Park J, Kang J-H, Liu X, Maddox S J, Tang K, McIntyre P C, Bank S R and Brongersma M L 2018 Dynamic thermal emission control with InAs-based plasmonic metasurfaces *Sci. Adv.* **4** eaat3163

[184] Lee J, Jung S, Chen P-Y, Lu F, Demmerle F, Boehm G, Amann M-C, Alù A and Belkin M A 2014 Ultrafast electrically tunable polaritonic metasurfaces *Adv. Opt. Mater.* **2** 1057–63

[185] Benz A, Montaño I, Klem J F and Brener I 2013 Tunable metamaterials based on voltage controlled strong coupling *Appl. Phys. Lett.* **103** 263116

[186] Wu P C, Pala R A, Kafaie Shirmanesh G, Cheng W-H, Sokhoyan R, Grajower M, Alam M Z, Lee D and Atwater H A 2019 Dynamic beam steering with all-dielectric electro-optic III–V multiple-quantum-well metasurfaces *Nat. Commun.* **10** 3654

[187] Wuttig M, Bhaskaran H and Taubner T 2017 Phase-change materials for non-volatile photonic applications *Nat. Photon.* **11** 465–76

[188] Sámson Z L, MacDonald K F, De Angelis F, Gholipour B, Knight K, Huang C C, Di Fabrizio E, Hewak D W and Zheludev N I 2010 Metamaterial electro-optic switch of nanoscale thickness *Appl. Phys. Lett.* **96** 143105

[189] Gholipour B, Zhang J, MacDonald K F, Hewak D W and Zheludev N I 2013 An all-optical, non-volatile, bidirectional, phase-change meta-switch *Adv. Mater.* **25** 3050–4

[190] Michel A-K U, Chigrin D N, Maß T W W, Schönauer K, Salinga M, Wuttig M and Taubner T 2013 Using low-loss phase-change materials for mid-infrared antenna resonance tuning *Nano Lett.* **13** 3470–5

[191] Michel A-K U, Zalden P, Chigrin D N, Wuttig M, Lindenberg A M and Taubner T 2014 Reversible optical switching of infrared antenna resonances with ultrathin phase-change layers using femtosecond laser pulses *ACS Photonics* **1** 833–9

[192] Yin X, Schäferling M, Michel A-K U, Tittl A, Wuttig M, Taubner T and Giessen H 2015 Active chiral plasmonics *Nano Lett.* **15** 4255–60

[193] Tittl A *et al* 2015 A switchable mid-infrared plasmonic perfect absorber with multispectral thermal imaging capability *Adv. Mater.* **27** 4597–603

[194] Qu Y, Li Q, Du K, Cai L, Lu J and Qiu M 2017 Dynamic thermal emission control based on ultrathin plasmonic metamaterials including phase-changing material GST *Laser Photon. Rev.* **11** 1700091

[195] Chen Y G, Kao T S, Ng B, Li X, Luo X G, Luk'yanchuk B, Maier S A and Hong M H 2013 Hybrid phase-change plasmonic crystals for active tuning of lattice resonances *Opt. Express* **21** 13691–8

[196] Cao T, Wei C, Simpson R E, Zhang L and Cryan M J 2014 Fast tuning of double Fano resonance using a phase-change metamaterial under low power intensity *Sci. Rep.* **4** 4463

[197] Petronijevic E and Sibilia C 2016 All-optical tuning of EIT-like dielectric metasurfaces by means of chalcogenide phase change materials *Opt. Express* **24** 30411–20

[198] Carrillo S G-C, Nash G R, Hayat H, Cryan M J, Klemm M, Bhaskaran H and Wright C D 2016 Design of practicable phase-change metadevices for near-infrared absorber and modulator applications *Opt. Express* **24** 13563–73

[199] Hwang C-Y *et al* 2017 Switchable subwavelength plasmonic structures with phase-change materials for reflection-type active metasurfaces in the visible region *Appl. Phys. Express* **10** 122201

[200] Michel A-K U, Wuttig M and Taubner T 2017 Design parameters for phase-change materials for nanostructure resonance tuning *Adv. Opt. Mater.* **5** 1700261

[201] Karvounis A, Gholipour B, MacDonald K F and Zheludev N I 2016 All-dielectric phase-change reconfigurable metasurface *Appl. Phys. Lett.* **109** 051103

[202] Shrekenhamer D *et al* 2017 *2017 11th Int. Congress on Engineered Materials Platforms for Novel Wave Phenomena (Metamaterials)* (IEEE) pp 313–5

[203] Dong W, Qiu Y, Zhou X, Banas A, Banas K, Breese M B H, Cao T and Simpson R E 2018 Tunable mid-infrared phase-change metasurface *Adv. Opt. Mater.* **6** 1701346

[204] Hosseini P, Wright C D and Bhaskaran H 2014 An optoelectronic framework enabled by low-dimensional phase-change films *Nature* **511** 206–11

[205] Wang Q, Rogers E T F, Gholipour B, Wang C-M, Yuan G, Teng J and Zheludev N I 2016 Optically reconfigurable metasurfaces and photonic devices based on phase change materials *Nat. Photon.* **10** 60–5

[206] Li P, Yang X, Maß T W W, Hanss J, Lewin M, Michel A-K U, Wuttig M and Taubner T 2016 Reversible optical switching of highly confined phonon-polaritons with an ultrathin phase-change material *Nat. Mater.* **15** 870–5

[207] Chen Y, Li X, Sonnefraud Y, Fernández-Domínguez A I, Luo X, Hong M and Maier S A 2015 Engineering the phase front of light with phase-change material based planar lenses *Sci. Rep.* **5** 8660

[208] Chu C H *et al* 2016 Active dielectric metasurface based on phase-change medium *Laser Photon. Rev.* **10** 986–94

[209] Alaee R, Albooyeh M, Tretyakov S and Rockstuhl C 2016 Phase-change material-based nanoantennas with tunable radiation patterns *Opt. Lett.* **41** 4099–102

[210] Yin X, Steinle T, Huang L, Taubner T, Wuttig M, Zentgraf T and Giessen H 2017 Beam switching and bifocal zoom lensing using active plasmonic metasurfaces *Light Sci. Appl.* **6** e17016

[211] Li T, Huang L, Liu J, Wang Y and Zentgraf T 2017 Tunable wave plate based on active plasmonic metasurfaces *Opt. Express* **25** 4216–26

[212] Guo Z, Yang X, Shen F, Zhou Q, Gao J and Guo K 2018 Active-tuning and polarization-independent absorber and sensor in the infrared region based on the phase change material of $Ge_2Sb_2Te_5$ (GST) *Sci. Rep.* **8** 12433

[213] Forouzmand A and Mosallaei H 2018 Dynamic beam control via Mie-resonance based phase-change metasurface: a theoretical investigation *Opt. Express* **26** 17948–63

[214] de Galarreta C R, Alexeev A M, Au Y Y, Lopez-Garcia M, Klemm M, Cryan M, Bertolotti J and Wright C D 2018 Nonvolatile reconfigurable phase-change metadevices for beam steering in the near infrared *Adv. Funct. Mater.* **28** 1704993

[215] Wright C *et al* 2018 Phase-change metadevices for the dynamic and reconfigurable control of light 2–5 July 2018) Zurich Switzerland *Novel Optical Materials and Applications*

[216] Zhang M *et al* 2018 Plasmonic metasurfaces for switchable photonic spin–orbit interactions based on phase change materials *Adv. Sci.* **5** 1800835

[217] Cao T *et al* 2018 Tuneable thermal emission using chalcogenide metasurface *Adv. Opt. Mater.* **6** 1800169

[218] Gholipour B, Piccinotti D, Karvounis A, MacDonald K F and Zheludev N I 2019 Reconfigurable ultraviolet and high-energy visible dielectric metamaterials *Nano Lett.* **19** 1643–8

[219] Choi C *et al* 2019 Metasurface with nanostructured $Ge_2Sb_2Te_5$ as a platform for broadband-operating wavefront switch *Adv. Opt. Mater.* **7** 1900171

[220] de Galarreta C R *et al* 2020 Reconfigurable multilevel control of hybrid all-dielectric phase-change metasurfaces *Optica* **7** 476–84

[221] Yang D-S, Baum P and Zewail A H 2016 Ultrafast electron crystallography of the cooperative reaction path in vanadium dioxide *Struct. Dyn.* **3** 034304

[222] Wan C *et al* 2019 On the optical properties of thin-film vanadium dioxide from the visible to the far infrared *Ann. Phys., Lpz.* **531** 1900188

[223] Driscoll T *et al* 2008 Dynamic tuning of an infrared hybrid-metamaterial resonance using vanadium dioxide *Appl. Phys. Lett.* **93** 024101

[224] Goldflam M D *et al* 2014 Voltage switching of a VO_2 memory metasurface using ionic gel *Appl. Phys. Lett.* **105** 041117

[225] Kats M A, Blanchard R, Genevet P, Yang Z, Qazilbash M M, Basov D N, Ramanathan S and Capasso F 2013 Thermal tuning of mid-infrared plasmonic antenna arrays using a phase change material *Opt. Lett.* **38** 368–70

[226] Rensberg J *et al* 2016 Active optical metasurfaces based on defect-engineered phase-transition materials *Nano Lett.* **16** 1050–5

[227] Kocer H, Butun S, Banar B, Wang K, Tongay S, Wu J and Aydin K 2015 Thermal tuning of infrared resonant absorbers based on hybrid gold–VO_2 nanostructures *Appl. Phys. Lett.* **106** 161104

[228] Earl S K, James T D, Gómez D E, Marvel R E, Haglund R F and Roberts A 2017 Switchable polarization rotation of visible light using a plasmonic metasurface *APL Photonics* **2** 016103

[229] Ma J, Luo Y, Wu X, Xu H, Jing H, Wu Z, Jiang Y and Liu Z 2017 Infrared metasurface with tunable composite right/left-handed dispersion *Mater. Res. Express* **4** 115802

[230] Sun M, Taha M, Walia S, Bhaskaran M, Sriram S, Shieh W and Unnithan R R 2018 A photonic switch based on a hybrid combination of metallic nanoholes and phase-change vanadium dioxide *Sci. Rep.* **8** 11106

[231] Guo P, Weimer M S, Emery J D, Diroll B T, Chen X, Hock A S, Chang R P H, Martinson A B F and Schaller R D 2016 Conformal coating of a phase change material on ordered plasmonic nanorod arrays for broadband all-optical switching *ACS Nano* **11** 693–701

[232] Ligmajer F *et al* 2018 Epitaxial VO_2 nanostructures: a route to large-scale, switchable dielectric metasurfaces *ACS Photonics* **5** 2561–7

[233] Hashemi M R M, Yang S-H, Wang T, Sepúlveda N and Jarrahi M 2016 Electronically-controlled beam-steering through vanadium dioxide metasurfaces *Sci. Rep.* **6** 35439

[234] Zhu Z, Evans P G, Haglund R F Jr and Valentine J G 2017 Dynamically reconfigurable metadevice employing nanostructured phase-change materials *Nano Lett.* **17** 4881–5

[235] Takeya H, Frame J, Tanaka T, Urade Y, Fang X and Kubo W 2018 Bolometric photodetection using plasmon-assisted resistivity change in vanadium dioxide *Sci. Rep.* **8** 12764

[236] Kim Y, Wu P C, Sokhoyan R, Mauser K, Glaudell R, Kafaie Shirmanesh G and Atwater H A 2019 Phase modulation with electrically tunable vanadium dioxide phase-change metasurfaces *Nano Lett.* **19** 3961–8

[237] Howes A, Zhu Z, Curie D, Avila J R, Wheeler V D, Haglund R F and Valentine J G 2020 Optical limiting based on Huygens' metasurfaces *Nano Lett.* **20** 4638–44

[238] Kim M, Jeong J, Poon J K S and Eleftheriades G V 2016 Vanadium-dioxide-assisted digital optical metasurfaces for dynamic wavefront engineering *J. Opt. Soc. Am.* B **33** 980–8

[239] Savaliya P B, Thomas A, Dua R and Dhawan A 2017 Tunable optical switching in the near-infrared spectral regime by employing plasmonic nanoantennas containing phase change materials *Opt. Express* **25** 23755–72

[240] Zheng X, Xiao Z and Ling X 2018 A tunable hybrid metamaterial reflective polarization converter based on vanadium oxide film *Plasmonics* **13** 287–91

[241] Ji R, Hua Y, Chen K, Long K, Fu Y, Zhang X and Zhuang S 2019 A switchable metalens based on active tri-layer metasurface *Plasmonics* **14** 165–71

[242] Zheludev N I and Plum E 2016 Reconfigurable nanomechanical photonic metamaterials *Nat. Nanotechnol.* **11** 16

[243] Ou J Y, Plum E, Jiang L and Zheludev N I 2011 Reconfigurable photonic metamaterials *Nano Lett.* **11** 2142–4

[244] Rigden J S 1996 *Macmillan Encyclopedia of Physics* (New York: Simon and Schuster) p 353

[245] Lapine M, Shadrivov I V, Powell D A and Kivshar Y S 2012 Magnetoelastic metamaterials *Nat. Mater.* **11** 30–3

[246] Valente J, Ou J-Y, Plum E, Youngs I J and Zheludev N I 2015 A magneto-electro-optical effect in a plasmonic nanowire material *Nat. Commun.* **6** 7021

[247] Chang C, Chiang C-F, Liu C-H and Liu C-H 2005 A lobster-sniffing-inspired method for micro-objects manipulation using electrostatic micro-actuators *J. Micromech. Microeng.* **15** 812–21

[248] Tao H, Strikwerda A C, Fan K, Padilla W J, Zhang X and Averitt R D 2009 Reconfigurable terahertz metamaterials *Phys. Rev. Lett.* **103** 147401

[249] Zhu W M *et al* 2011 Switchable magnetic metamaterials using micromachining processes *Adv. Mater.* **23** 1792–6

[250] Zhu W M, Liu A Q, Bourouina T, Tsai D P, Teng J H, Zhang X H, Lo G Q, Kwong D L and Zheludev N I 2012 Microelectromechanical Maltese-cross metamaterial with tunable terahertz anisotropy *Nat. Commun.* **3** 1274

[251] Zhao X, Schalch J, Zhang J, Seren H R, Duan G, Averitt R D and Zhang X 2018 Electromechanically tunable metasurface transmission waveplate at terahertz frequencies *Optica* **5** 303–10

[252] Lin Y-S and Lee C 2014 Tuning characteristics of mirrorlike T-shape terahertz metamaterial using out-of-plane actuated cantilevers *Appl. Phys. Lett.* **104** 251914

[253] Zhang W *et al* 2012 Micromachined switchable metamaterial with dual resonance *Appl. Phys. Lett.* **101** 151902

[254] Zhu W M *et al* 2011 Polarization dependent state to polarization independent state change in THz metamaterials *Appl. Phys. Lett.* **99** 221102

[255] Manjappa M *et al* 2018 Reconfigurable MEMS Fano metasurfaces with multiple-input–output states for logic operations at terahertz frequencies *Nat. Commun.* **9** 4056

[256] Liu X and Padilla W J 2017 Reconfigurable room temperature metamaterial infrared emitter *Optica* **4** 430–3

[257] Roy T, Zhang S, Jung I W, Troccoli M, Capasso F and Lopez D 2018 Dynamic metasurface lens based on MEMS technology *APL Photonics* **3** 021302

[258] Mao Y, Pan Y, Zhang W, Zhu R, Xu J and Wu W 2016 Multi-direction-tunable three-dimensional meta-atoms for reversible switching between midwave and long-wave infrared regimes *Nano Lett.* **16** 7025–9

[259] Liu X and Padilla W J 2016 Thermochromic infrared metamaterials *Adv. Mater.* **28** 871–5

[260] Ou J-Y, Plum E, Zhang J and Zheludev N I 2013 An electromechanically reconfigurable plasmonic metamaterial operating in the near-infrared *Nat. Nanotechnol.* **8** 252–5

[261] Pitchappa P, Pei Ho C, Kropelnicki P, Singh N, Kwong D-L and Lee C 2014 Micro-electro-mechanically switchable near infrared complementary metamaterial absorber *Appl. Phys. Lett.* **104** 201114

[262] Valente J, Ou J-Y, Plum E, Youngs I J and Zheludev N I 2015 Reconfiguring photonic metamaterials with currents and magnetic fields *Appl. Phys. Lett.* **106** 111905

[263] Zhang J, MacDonald K F and Zheludev N I 2013 Nonlinear dielectric optomechanical metamaterials *Light Sci. Appl.* **2** e96

[264] Ou J-Y, Plum E, Zhang J and Zheludev N I 2016 Giant nonlinearity of an optically reconfigurable plasmonic metamaterial *Adv. Mater.* **28** 729–33

[265] Arbabi E, Arbabi A, Kamali S M, Horie Y, Faraji-Dana M and Faraon A 2018 MEMS-tunable dielectric metasurface lens *Nat. Commun.* **9** 812

[266] She A, Zhang S, Shian S, Clarke D R and Capasso F 2018 Adaptive metalenses with simultaneous electrical control of focal length, astigmatism, and shift *Sci. Adv.* **4** eaap9957

[267] Holsteen A L, Cihan A F and Brongersma M L 2019 Temporal color mixing and dynamic beam shaping with silicon metasurfaces *Science* **365** 257–60

[268] Karvounis A, Aspiotis N, Zeimpekis I, Ou J Y, Huang C C, Hewak D and Zheludev N I 2019 Mechanochromic reconfigurable metasurfaces *Adv. Sci.* **6** 1900974

[269] Xu X, Peng B, Li D, Zhang J, Wong L M, Zhang Q, Wang S and Xiong Q 2011 Flexible visible-infrared metamaterials and their applications in highly sensitive chemical and biological sensing *Nano Lett.* **11** 3232–8

[270] Pryce I M, Aydin K, Kelaita Y A, Briggs R M and Atwater H A 2010 Highly strained compliant optical metamaterials with large frequency tunability *Nano Lett.* **10** 4222–7

[271] Walia S, Shah C M, Gutruf P, Nili H, Chowdhury D R, Withayachumnankul W, Bhaskaran M and Sriram S 2015 Flexible metasurfaces and metamaterials: a review of materials and fabrication processes at micro- and nano-scales *Appl. Phys. Rev.* **2** 011303

[272] Kamali S M, Arbabi E, Arbabi A, Horie Y and Faraon A 2016 Highly tunable elastic dielectric metasurface lenses *Laser Photon. Rev.* **10** 1002–8

[273] Donner J S, Morales-Dalmau J, Alda I, Marty R and Quidant R 2015 Fast and transparent adaptive lens based on plasmonic heating *ACS Photonics* **2** 355–60

[274] Liu L, Chen W-c, Powell D A, Padilla W J, Karouta F, Hattori H T, Neshev D N and Shadrivov I V 2014 Post-processing approach for tuning multi-layered metamaterials *Appl. Phys. Lett.* **105** 151102

[275] Schneider F, Draheim J, Kamberger R and Wallrabe U 2009 Process and material properties of polydimethylsiloxane (PDMS) for optical MEMS *Sensors Actuators* A **151** 95–9

[276] Iwaszczuk K, Strikwerda A C, Fan K, Zhang X, Averitt R D and Jepsen P U 2012 Flexible metamaterial absorbers for stealth applications at terahertz frequencies *Opt. Express* **20** 635–43

[277] Zhu L, Kapraun J, Ferrara J and Chang-Hasnain C J 2015 Flexible photonic metastructures for tunable coloration *Optica* **2** 255–8

[278] Liu X *et al* 2010 Metamaterials on parylene thin film substrates: design, fabrication, and characterization at terahertz frequency *Appl. Phys. Lett.* **96** 011906

[279] Rogers J A, Someya T and Huang Y 2010 Materials and mechanics for stretchable electronics *Science* **327** 1603–7

[280] Pryce I M, Aydin K, Kelaita Y A, Briggs R M and Atwater H A 2011 Characterization of the tunable response of highly strained compliant optical metamaterials *Phil. Trans. R. Soc.* A **369** 3447–55

[281] Aksu S, Huang M, Artar A, Yanik A A, Selvarasah S, Dokmeci M R and Altug H 2011 Flexible plasmonics on unconventional and nonplanar substrates *Adv. Mater.* **23** 4422–30

[282] Gutruf P, Zou C, Withayachumnankul W, Bhaskaran M, Sriram S and Fumeaux C 2015 Mechanically tunable dielectric resonator metasurfaces at visible frequencies *ACS Nano* **10** 133–41

[283] Mateus C F R, Huang M C Y, Deng Y, Neureuther A R and Chang-Hasnain C J 2004 Ultrabroadband mirror using low-index cladded subwavelength grating *IEEE Photon. Technol. Lett.* **16** 518–20

[284] Huang M C Y, Zhou Y and Chang-Hasnain C J 2007 A surface-emitting laser incorporating a high-index-contrast subwavelength grating *Nat. Photon.* **1** 119

[285] Huang L, Chen X, Mühlenbernd H, Li G, Bai B, Tan Q, Jin G, Zentgraf T and Zhang S 2012 Dispersionless phase discontinuities for controlling light propagation *Nano Lett.* **12** 5750–5

[286] Ee H-S and Agarwal R 2016 Tunable metasurface and flat optical zoom lens on a stretchable substrate *Nano Lett.* **16** 2818–23

[287] Horie Y, Arbabi A, Arbabi E, Kamali S M and Faraon A 2017 High-speed, phase-dominant spatial light modulation with silicon-based active resonant antennas *ACS Photonics* **5** 1711–7

[288] Boyd R W 2020 *Nonlinear Optics* 4th edn (Cambridge, MA: Academic)

[289] Bloembergen N, Armstrong J, Ducuing J and Pershan P 1962 Interactions between light waves in a nonlinear dielectric *Phys. Rev.* **127** 1918–39

[290] Hanke T, Krauss G, Träutlein D, Wild B, Bratschitsch R and Leitenstorfer A 2009 Efficient nonlinear light emission of single gold optical antennas driven by few-cycle near-infrared pulses *Phys. Rev. Lett.* **103** 257404

[291] Metzger B, Hentschel M, Lippitz M and Giessen H 2012 Third-harmonic spectroscopy and modeling of the nonlinear response of plasmonic nanoantennas *Opt. Lett.* **37** 4741–3

[292] Scalora M *et al* 2010 Second-and third-harmonic generation in metal-based structures *Phys. Rev.* A **82** 043828

[293] Klein M W, Enkrich C, Wegener M and Linden S 2006 Second-harmonic generation from magnetic metamaterials *Science* **313** 502–4

[294] Kruk S, Weismann M, Bykov A Y, Mamonov E A, Kolmychek I A, Murzina T, Panoiu N C, Neshev D N and Kivshar Y S 2015 Enhanced magnetic second-harmonic generation from resonant metasurfaces *ACS Photonics* **2** 1007–12

[295] Linden S *et al* 2012 Collective effects in second-harmonic generation from split-ring-resonator arrays *Phys. Rev. Lett.* **109** 015502

[296] Celebrano M *et al* 2015 Mode matching in multiresonant plasmonic nanoantennas for enhanced second harmonic generation *Nat. Nanotechnol.* **10** 412–7

[297] Klein M W, Wegener M, Feth N and Linden S 2007 Experiments on second- and third-harmonic generation from magnetic metamaterials *Opt. Express* **15** 5238–47

[298] Ciracì C, Poutrina E, Scalora M and Smith D R 2012 Origin of second-harmonic generation enhancement in optical split-ring resonators *Phys. Rev.* B **85** 201403

[299] O'Brien K *et al* 2015 Predicting nonlinear properties of metamaterials from the linear response *Nat. Mater.* **14** 379–83

[300] Czaplicki R *et al* 2018 Less is more: enhancement of second-harmonic generation from metasurfaces by reduced nanoparticle density *Nano Lett.* **18** 7709–14

[301] Segal N, Keren-Zur S, Hendler N and Ellenbogen T 2015 Controlling light with metamaterial-based nonlinear photonic crystals *Nat. Photon.* **9** 180–4

[302] Rose A, Huang D and Smith D R 2011 Controlling the second harmonic in a phase-matched negative-index metamaterial *Phys. Rev. Lett.* **107** 063902

[303] Zheludev N I and Emel yanov V I 2003 Phase matched second harmonic generation from nanostructured metallic surfaces *J. Opt. A: Pure Appl. Opt.* **6** 26

[304] Keren-Zur S, Avayu O, Michaeli L and Ellenbogen T 2016 Nonlinear beam shaping with plasmonic metasurfaces *ACS Photonics* **3** 117–23

[305] Li J, Chen S, Yang H, Li J, Yu P, Cheng H, Gu C, Chen H-T and Tian J 2015 Simultaneous control of light polarization and phase distributions using plasmonic metasurfaces *Adv. Funct. Mater.* **25** 704–10

[306] Huang L *et al* 2013 Three-dimensional optical holography using a plasmonic metasurface *Nat. Commun.* **4** 2808

[307] Li G, Chen S, Pholchai N, Reineke B, Wong P W H, Pun E Y B, Cheah K W, Zentgraf T and Zhang S 2015 Continuous control of the nonlinearity phase for harmonic generations *Nat. Mater.* **14** 607–12

[308] Almeida E, Shalem G and Prior Y 2016 Subwavelength nonlinear phase control and anomalous phase matching in plasmonic metasurfaces *Nat. Commun.* **7** 10367

[309] Li G, Zhang S and Zentgraf T 2017 Nonlinear photonic metasurfaces *Nat. Rev. Mater.* **2** 17010

[310] Tymchenko M, Gomez-Diaz J S, Lee J, Nookala N, Belkin M A and Alù A 2015 Gradient nonlinear Pancharatnam–Berry metasurfaces *Phys. Rev. Lett.* **115** 207403

[311] Chen S *et al* 2014 Symmetry-selective third-harmonic generation from plasmonic metacrystals *Phys. Rev. Lett.* **113** 033901

[312] Gennaro S D, Li Y, Maier S A and Oulton R F 2019 Nonlinear Pancharatnam–Berry phase metasurfaces beyond the dipole approximation *ACS Photonics* **6** 2335–41

[313] Walter F, Li G, Meier C, Zhang S and Zentgraf T 2017 Ultrathin nonlinear metasurface for optical image encoding *Nano Lett.* **17** 3171–5

[314] Schlickriede C, Waterman N, Reineke B, Georgi P, Li G, Zhang S and Zentgraf T 2018 Imaging through nonlinear metalens using second harmonic generation *Adv. Mater.* **30** 1703843

[315] Li G, Sartorello G, Chen S, Nicholls L H, Li K F, Zentgraf T, Zhang S and Zayats A V 2018 Spin and geometric phase control four-wave mixing from metasurfaces *Laser Photon. Rev.* **12** 1800034

[316] Shcherbakov M R *et al* 2014 Enhanced third-harmonic generation in silicon nanoparticles driven by magnetic response *Nano Lett.* **14** 6488–92

[317] Yang Y, Wang W, Boulesbaa A, Kravchenko I I, Briggs D P, Puretzky A, Geohegan D and Valentine J 2015 Nonlinear Fano-resonant dielectric metasurfaces *Nano Lett.* **15** 7388–93

[318] Liu S *et al* 2016 Resonantly enhanced second-harmonic generation using III–V semiconductor all-dielectric metasurfaces *Nano Lett.* **16** 5426–32

[319] Smirnova D A, Khanikaev A B, Smirnov L A and Kivshar Y S 2016 Multipolar third-harmonic generation driven by optically induced magnetic resonances *ACS Photonics* **3** 1468–76

[320] Miroshnichenko A E, Evlyukhin A B, Yu Y F, Bakker R M, Chipouline A, Kuznetsov A I, Luk'yanchuk B, Chichkov B N and Kivshar Y S 2015 Nonradiating anapole modes in dielectric nanoparticles *Nat. Commun.* **6** 8069

[321] Semmlinger M, Zhang M, Tseng M L, Huang T-T, Yang J, Tsai D P, Nordlander P and Halas N J 2019 Generating third harmonic vacuum ultraviolet light with a $\mathrm{TiO_2}$ metasurface *Nano Lett.* **19** 8972–8

[322] Semmlinger M, Tseng M L, Yang J, Zhang M, Zhang C, Tsai W-Y, Tsai D P, Nordlander P and Halas N J 2018 Vacuum ultraviolet light-generating metasurface *Nano Lett.* **18** 5738–43

[323] Azzam S I, Shalaev V M, Boltasseva A and Kildishev A V 2018 Formation of bound states in the continuum in hybrid plasmonic-photonic systems *Phys. Rev. Lett.* **121** 253901

[324] Bogdanov A A *et al* 2019 Bound states in the continuum and Fano resonances in the strong mode coupling regime *Adv. Photon.* **1** 016001

[325] Hsu C W, Zhen B, Stone A D, Joannopoulos J D and Soljačić M 2016 Bound states in the continuum *Nat. Rev. Mater.* **1** 16048

[326] Koshelev K, Lepeshov S, Liu M, Bogdanov A and Kivshar Y 2018 Asymmetric metasurfaces with high-Q resonances governed by bound states in the continuum *Phys. Rev. Lett.* **121** 193903

[327] Liu Z, Xu Y, Lin Y, Xiang J, Feng T, Cao Q, Li J, Lan S and Liu J 2019 High-Q quasibound states in the continuum for nonlinear metasurfaces *Phys. Rev. Lett.* **123** 253901

[328] Koshelev K, Tang Y, Li K, Choi D-Y, Li G and Kivshar Y 2019 Nonlinear metasurfaces governed by bound states in the continuum *ACS Photonics* **6** 1639–44

[329] Xu L *et al* 2019 Dynamic nonlinear image tuning through magnetic dipole quasi-BIC ultrathin resonators *Adv. Sci.* **6** 1802119

[330] Liu S, Vabishchevich P P, Vaskin A, Reno J L, Keeler G A, Sinclair M B, Staude I and Brener I 2018 An all-dielectric metasurface as a broadband optical frequency mixer *Nat. Commun.* **9** 2507

[331] Liu H *et al* 2018 Enhanced high-harmonic generation from an all-dielectric metasurface *Nat. Phys.* **14** 1006–10

[332] Vampa G *et al* 2017 Plasmon-enhanced high-harmonic generation from silicon *Nat. Phys.* **13** 659–62

[333] Wang L, Kruk S, Koshelev K, Kravchenko I, Luther-Davies B and Kivshar Y 2018 Nonlinear wavefront control with all-dielectric metasurfaces *Nano Lett.* **18** 3978–84

[334] Gao Y, Fan Y, Wang Y, Yang W, Song Q and Xiao S 2018 Nonlinear holographic all-dielectric metasurfaces *Nano Lett.* **18** 8054–61

[335] Löchner F J *et al* 2018 Polarization-dependent second harmonic diffraction from resonant GaAs metasurfaces *ACS Photonics* **5** 1786–93

[336] Reineke B, Sain B, Zhao R, Carletti L, Liu B, Huang L, De Angelis C and Zentgraf T 2019 Silicon metasurfaces for third harmonic geometric phase manipulation and multiplexed holography *Nano Lett.* **19** 6585–91

[337] Xu Y *et al* 2018 Reconfiguring structured light beams using nonlinear metasurfaces *Opt. Express* **26** 30930–43

[338] Wang X F, Wang Z W, Yu J G, Liu C L, Zhao X J and Gong Q H 2004 Large and ultrafast third-order optical nonlinearity of $\mathrm{GeS_2}$–$\mathrm{Ga_2S_3}$–CdS chalcogenide glass *Chem. Phys. Lett.* **399** 230–3

[339] Shcherbakov M R *et al* 2015 Ultrafast all-optical switching with magnetic resonances in nonlinear dielectric nanostructures *Nano Lett.* **15** 6985–90

[340] Kang L, Cui Y, Lan S, Rodrigues S P, Brongersma M L and Cai W 2014 Electrifying photonic metamaterials for tunable nonlinear optics *Nat. Commun.* **5** 4680

[341] Lee K-T, Taghinejad M, Yan J, Kim A S, Raju L, Brown D K and Cai W 2019 Electrically biased silicon metasurfaces with magnetic Mie resonance for tunable harmonic generation of light *ACS Photonics* **6** 2663–70

[342] Shcherbakov M R, Werner K, Fan Z, Talisa N, Chowdhury E and Shvets G 2019 Photon acceleration and tunable broadband harmonics generation in nonlinear time-dependent metasurfaces *Nat. Commun.* **10** 1345

[343] Yablonovitch E 1974 Self-phase modulation of light in a laser-breakdown plasma *Phys. Rev. Lett.* **32** 1101

[344] Wilks S C, Dawson J M, Mori W B, Katsouleas T and Jones M E 1989 Photon accelerator *Phys. Rev. Lett.* **62** 2600

[345] Wang F and Harutyunyan H 2018 Tailoring the quality factors and nonlinear response in hybrid plasmonic-dielectric metasurfaces *Opt. Express* **26** 120–9

[346] Lee J *et al* 2014 Giant nonlinear response from plasmonic metasurfaces coupled to intersubband transitions *Nature* **511** 65–9

[347] Lee J, Nookala N, Gomez-Diaz J S, Tymchenko M, Demmerle F, Boehm G, Amann M C, Alù A and Belkin M A 2016 Ultrathin second-harmonic metasurfaces with record-high nonlinear optical response *Adv. Opt. Mater.* **4** 664–70

[348] Liu H, Li G X, Li K F, Chen S M, Zhu S N, Chan C T and Cheah K W 2011 Linear and nonlinear Fano resonance on two-dimensional magnetic metamaterials *Phys. Rev.* B **84** 235437

[349] Shen Q, Hoang T B, Yang G, Wheeler V D and Mikkelsen M H 2018 Probing the origin of highly-efficient third-harmonic generation in plasmonic nanogaps *Opt. Express* **26** 20718–25

[350] Alam M Z, Schulz S A, Upham J, De Leon I and Boyd R W 2018 Large optical nonlinearity of nanoantennas coupled to an epsilon-near-zero material *Nat. Photon.* **12** 79

[351] Deng J, Tang Y, Chen S, Li K, Zayats A V and Li G 2020 Giant enhancement of second-order nonlinearity of epsilon-near-zero medium by a plasmonic metasurface *Nano Lett.* **20** 5421–7

[352] Capretti A, Wang Y, Engheta N and Dal Negro L 2015 Comparative study of second-harmonic generation from epsilon-near-zero indium tin oxide and titanium nitride nanolayers excited in the near-infrared spectral range *ACS Photonics* **2** 1584–91

[353] Yuan Q, Fang L, Fang H, Li J, Wang T, Jie W, Zhao J and Gan X 2019 Second harmonic and sum-frequency generations from a silicon metasurface integrated with a two-dimensional material *ACS Photonics* **6** 2252–9

[354] Chemla D, Miller D, Smith P, Gossard A and Wiegmann W 1984 Room temperature excitonic nonlinear absorption and refraction in GaAs/AlGaAs multiple quantum well structures *IEEE J. Quantum Electron.* **20** 265–75

[355] Dingle R, Wiegmann W and Henry C H 1974 Quantum states of confined carriers in very thin $\mathrm{Al}_x\mathrm{Ga}_{1-x}\mathrm{As}$–GaAs–$\mathrm{Al}_x\mathrm{Ga}_{1-x}\mathrm{As}$ heterostructures *Phys. Rev. Lett.* **33** 827

[356] Vodopyanov K L, O'Neill K, Serapiglia G B, Phillips C C, Hopkinson M, Vurgaftman I and Meyer J R 1998 Phase-matched second harmonic generation in asymmetric double quantum wells *Appl. Phys. Lett.* **72** 2654–6

[357] Gomez-Diaz J, Lee J, Tymchenko M, Belkin M A and Alù A 2015 *2015 IEEE Int. Symp. on Antennas and Propagation USNC/URSI National Radio Science Meeting* (IEEE) pp 1084–5

[358] Liu Y, Lee J, March S, Nookala N, Palaferri D, Klem J F, Bank S R, Brener I and Belkin M A 2018 Difference-frequency generation in polaritonic intersubband nonlinear metasurfaces *Adv. Opt. Mater.* **6** 1800681

[359] Campione S, Benz A, Sinclair M B, Capolino F and Brener I 2014 Second harmonic generation from metamaterials strongly coupled to intersubband transitions in quantum wells *Appl. Phys. Lett.* **104** 131104

[360] Benz A, Campione S, Moseley M W, Wierer J J, Allerman A A, Wendt J R and Brener I 2014 Optical strong coupling between near-infrared metamaterials and intersubband transitions in III-nitride heterostructures *ACS Photonics* **1** 906–11

[361] Yu J, Park S, Hwang I, Kim D, Jung J Y and Lee J 2019 Third-harmonic generation from plasmonic metasurfaces coupled to intersubband transitions *Adv. Opt. Mater.* **7** 1801510

[362] Nookala N *et al* 2016 Ultrathin gradient nonlinear metasurface with a giant nonlinear response *Optica* **3** 283–8

[363] Duan X and Liu N 2019 Magnesium for dynamic nanoplasmonics *Acc. Chem. Res.* **52** 1979–89

[364] Tittl A, Mai P, Taubert R, Dregely D, Liu N and Giessen H 2011 Palladium-based plasmonic perfect absorber in the visible wavelength range and its application to hydrogen sensing *Nano Lett.* **11** 4366–9

[365] Strohfeldt N, Tittl A, Schäferling M, Neubrech F, Kreibig U, Griessen R and Giessen H 2014 Yttrium hydride nanoantennas for active plasmonics *Nano Lett.* **14** 1140–7

[366] Sterl F, Strohfeldt N, Walter R, Griessen R, Tittl A and Giessen H 2015 Magnesium as novel material for active plasmonics in the visible wavelength range *Nano Lett.* **15** 7949–55

[367] Duan X, Kamin S, Sterl F, Giessen H and Liu N 2016 Hydrogen-regulated chiral nanoplasmonics *Nano Lett.* **16** 1462–6

[368] Duan X, Kamin S and Liu N 2017 Dynamic plasmonic colour display *Nat. Commun.* **8** 14606

[369] Chen Y, Duan X, Matuschek M, Zhou Y, Neubrech F, Duan H and Liu N 2017 Dynamic color displays using stepwise cavity resonators *Nano Lett.* **17** 5555–60

[370] Duan X and Liu N 2018 Scanning plasmonic color display *ACS Nano* **12** 8817–23

[371] Li J, Kamin S, Zheng G, Neubrech F, Zhang S and Liu N 2018 Addressable metasurfaces for dynamic holography and optical information encryption *Sci. Adv.* **4** eaar6768

[372] Yu P, Li J, Zhang S, Jin Z, Schütz G, Qiu C-W, Hirscher M and Liu N 2018 Dynamic Janus metasurfaces in the visible spectral region *Nano Lett.* **18** 4584–9

[373] Li J, Chen Y, Hu Y, Duan H and Liu N 2020 Magnesium-based metasurfaces for dual-function switching between dynamic holography and dynamic color display *ACS Nano* **14** 7892–8

[374] Sun S, Yang W, Zhang C, Jing J, Gao Y, Yu X, Song Q and Xiao S 2018 Real-time tunable colors from microfluidic reconfigurable all-dielectric metasurfaces *ACS Nano* **12** 2151–9

[375] Hecht J 2018 Lidar for self-driving cars *Opt. Photonics News* **29** 26]–33

[376] Akselrod G M 2019 Optics for automotive lidar: metasurface beam steering enables solid-state, high-performance lidar *Laser Focus World* 14036818

[377] He Z, Sui X, Jin G and Cao L 2019 Progress in virtual reality and augmented reality based on holographic display *Appl. Opt.* **58** A74–81

[378] Kress B C 2019 Optical waveguide combiners for AR headsets: features and limitation *Digit. Opt. Technol.* **2019** 11062

[379] Hong C, Colburn S and Majumdar A 2017 Flat metaform near-eye visor *Appl. Opt.* **56** 8822–7

[380] Shi Z J, Chen W T and Capasso F 2018 Wide field-of-view waveguide displays enabled by polarization-dependent metagratings *Digit. Opt. Immersive Disp.* **10676** 1067615

[381] Kamali S M, Arbabi E and Faraon A 2019 Metasurface-based compact light engine for AR headsets *Opt. Des. Challenge* **11040** 1104002

[382] Lee G-Y, Hong J-Y, Hwang S, Moon S, Kang H, Jeon S, Kim H, Jeong J-H and Lee B 2018 Metasurface eyepiece for augmented reality *Nat. Commun.* **9** 4562

[383] Li Q-T, Dong F, Wang B, Chu W, Gong Q, Brongersma M L and Li Y 2017 Free-space optical beam tapping with an all-silica metasurface *ACS Photonics* **4** 2544–9

[384] Stern J 2018 *Wall Str. J.*

[385] Brongersma M L 2019 Metasurfaces for augmented and virtual reality *SPIE NanoScience + Engineering Metamaterials, Metadevices, and Metasystems 2019* (San Diego, California, United States) vol 11080 (International Society for Optics and Photonics) p 110800R

[386] Kim J *et al* 2019 Foveated AR *ACM Trans. Graph.* **38** 99

[387] Koulieris G A, Akşit K, Stengel M, Mantiuk R K, Mania K and Richardt C 2019 Near-eye display and tracking technologies for virtual and augmented reality *Comput. Graph. Forum* **38** 493–519

[388] Malek S C, Ee H-S and Agarwal R 2017 Strain multiplexed metasurface holograms on a stretchable substrate *Nano Lett.* **17** 3641–5

[389] Ren H, Fang X, Jang J, Bürger J, Rho J and Maier S A 2020 Complex-amplitude metasurface-based orbital angular momentum holography in momentum space *Nat. Nanotechnol.* **15** 948–55

[390] Gregg P, Kristensen P, Rubano A, Golowich S, Marrucci L and Ramachandran S 2019 Enhanced spin orbit interaction of light in highly confining optical fibers for mode division multiplexing *Nat. Commun.* **10** 4707

[391] Xie G *et al* 2015 Performance metrics and design considerations for a free-space optical orbital-angular-momentum-multiplexed communication link *Optica* **2** 357–65

[392] Bozinovic N, Yue Y, Ren Y, Tur M, Kristensen P, Huang H, Willner A E and Ramachandran S 2013 Terabit-scale orbital angular momentum mode division multiplexing in fibers *Science* **340** 1545–8

[393] Kruk S, Ferreira F, Mac Suibhne N, Tsekrekos C, Kravchenko I, Ellis A, Neshev D, Turitsyn S and Kivshar Y 2018 Transparent dielectric metasurfaces for spatial mode multiplexing *Laser Photon. Rev.* **12** 1800031

[394] Xu H X *et al* 2019 Wavevector and frequency multiplexing performed by a spin-decoupled multichannel metasurface *Adv. Mater. Technol.* **5** 1900710

[395] Li Y, Li X, Chen L, Pu M, Jin J, Hong M and Luo X 2017 Orbital angular momentum multiplexing and demultiplexing by a single metasurface *Adv. Opt. Mater.* **5** 1600502

[396] Jin J, Pu M, Wang Y, Li X, Ma X, Luo J, Zhao Z, Gao P and Luo X 2017 Multi-channel vortex beam generation by simultaneous amplitude and phase modulation with two-dimensional metamaterial *Adv. Mater. Technol.* **2** 1600201

[397] Overvig A C, Shrestha S, Malek S C, Lu M, Stein A, Zheng C and Yu N 2019 Dielectric metasurfaces for complete and independent control of the optical amplitude and phase *Light Sci. Appl.* **8** 92

[398] Zhang X *et al* 2019 Direct polarization measurement using a multiplexed Pancharatnam–Berry metahologram *Optica* **6** 1190–8

[399] Arbabi E, Kamali S M, Arbabi A and Faraon A 2018 Full-Stokes imaging polarimetry using dielectric metasurfaces *ACS Photonics* **5** 3132–40

[400] Balthasar Mueller J P, Rubin N A, Devlin R C, Groever B and Capasso F 2017 Metasurface polarization optics: independent phase control of arbitrary orthogonal states of polarization *Phys. Rev. Lett.* **118** 113901

[401] Dutta-Gupta S, Dabidian N, Kholmanov I, Belkin M A and Shvets G 2017 Electrical tuning of the polarization state of light using graphene-integrated anisotropic metasurfaces *Phil. Trans. R. Soc.* A **375** 20160061

[402] Dabidian N *et al* 2016 Experimental demonstration of phase modulation and motion sensing using graphene-integrated metasurfaces *Nano Lett.* **16** 3607–15

[403] Keren-Zur S and Ellenbogen T 2019 Direct space to time terahertz pulse shaping with nonlinear metasurfaces *Opt. Express* **27** 20837–47

[404] Rahimi E and Şendur K 2015 Femtosecond pulse shaping by ultrathin plasmonic metasurfaces *J. Opt. Soc. Am.* B **33** A1–7

[405] Decker M, Staude I, Falkner M, Dominguez J, Neshev D N, Brener I, Pertsch T and Kivshar Y S 2015 High-efficiency dielectric Huygens' surfaces *Adv. Opt. Mater.* **3** 813–20

[406] Shcherbakov M R, Eilenberger F and Staude I 2019 Interaction of semiconductor metasurfaces with short laser pulses: from nonlinear-optical response toward spatiotemporal shaping *J. Appl. Phys.* **126** 085705

[407] Chamanara N, Vahabzadeh Y and Caloz C 2019 Simultaneous control of the spatial and temporal spectra of light with space–time varying metasurfaces *IEEE Trans. Antennas Propag.* **67** 2430–41

[408] Rahimi E and Şendur K 2018 Thermally controlled femtosecond pulse shaping using metasurface based optical filters *Nanophotonics* **7** 659–68

[409] Frumker E and Silberberg Y 2007 Femtosecond pulse shaping using a two-dimensional liquid-crystal spatial light modulator *Opt. Lett.* **32** 1384–6

[410] Weiner A M 2000 Femtosecond pulse shaping using spatial light modulators *Rev. Sci. Instrum.* **71** 1929–60

[411] Monmayrant A, Weber S and Chatel B 2010 A newcomer's guide to ultrashort pulse shaping and characterization *J. Phys. B: At. Mol. Opt. Phys.* **43** 103001

[412] Frumker E and Silberberg Y 2007 Phase and amplitude pulse shaping with two-dimensional phase-only spatial light modulators *J. Opt. Soc. Am.* B **24** 2940–7

[413] Weiner A M, Leaird D E, Patel J S and Wullert J R 1990 Programmable femtosecond pulse shaping by use of a multielement liquid-crystal phase modulator *Opt. Lett.* **15** 326

[414] Weiner A M 2011 Ultrafast optical pulse shaping: a tutorial review *Opt. Commun.* **284** 3669–92

[415] Li W and Fan S 2018 Nanophotonic control of thermal radiation for energy applications *Opt. Express* **26** 15995–6021

[416] Inoue T, Zoysa M D, Asano T and Noda S 2014 Realization of dynamic thermal emission control *Nat. Mater.* **13** 928–31

[417] Brar V W, Sherrott M C, Jang M S, Kim S, Kim L, Choi M, Sweatlock L A and Atwater H A 2015 Electronic modulation of infrared radiation in graphene plasmonic resonators *Nat. Commun.* **6** 7032

[418] Wu C, Khanikaev A B, Adato R, Arju N, Yanik A A, Altug H and Shvets G 2012 Fano-resonant asymmetric metamaterials for ultrasensitive spectroscopy and identification of molecular monolayers *Nat. Mater.* **11** 69–75

[419] Rodrigo D *et al* 2018 Resolving molecule-specific information in dynamic lipid membrane processes with multi-resonant infrared metasurfaces *Nat. Commun.* **9** 2160

[420] Rodrigo D, Limaj O, Janner D, Etezadi D, Garcia de Abajo F J, Pruneri V and Altug H 2015 Mid-infrared plasmonic biosensing with graphene *Science* **349** 165–8

[421] Solomon M L, Hu J, Lawrence M, García-Etxarri A and Dionne J A 2019 Enantiospecific optical enhancement of chiral sensing and separation with dielectric metasurfaces *ACS Photonics* **6** 43–9

[422] Tittl A, Leitis A, Liu M, Yesilkoy F, Choi D-Y, Neshev D N, Kivshar Y S and Altug H 2018 Imaging-based molecular barcoding with pixelated dielectric metasurfaces *Science* **360** 1105–9

[423] Guo X, Ding Y, Duan Y and Ni X 2019 Nonreciprocal metasurface with space–time phase modulation *Light Sci. Appl.* **8** 123

[424] Shaltout A, Kildishev A and Shalaev V 2015 Time-varying metasurfaces and Lorentz non-reciprocity *Opt. Mater. Express* **5** 2459–67

[425] Hadad Y, Sounas D L and Alu A 2015 Space–time gradient metasurfaces *Phys. Rev.* B **92** 100304

[426] Shi Y and Fan S 2016 Dynamic non-reciprocal meta-surfaces with arbitrary phase reconfigurability based on photonic transition in meta-atoms *Appl. Phys. Lett.* **108** 021110

[427] Lawrence M, Barton D R III and Dionne J A 2018 Nonreciprocal flat optics with silicon metasurfaces *Nano Lett.* **18** 1104–9

[428] Shaltout A M, Lagoudakis K G, van de Groep J, Kim S J, Vučković J, Shalaev V M and Brongersma M L 2019 Spatiotemporal light control with frequency-gradient metasurfaces *Science* **365** 374–7

[429] Xu L, Curwen C A, Hon P W C, Chen Q-S, Itoh T and Williams B S 2015 Metasurface external cavity laser *Appl. Phys. Lett.* **107** 221105

[430] Hashizume J and Koyama F 2004 Plasmon-enhancement of optical near-field of metal nanoaperture surface-emitting laser *Appl. Phys. Lett.* **84** 3226–8

[431] Arbabi A, Arbabi E, Horie Y, Kamali S M and Faraon A 2017 Planar metasurface retroreflector *Nat. Photon.* **11** 415–20

[432] Ha S T, Fu Y H, Emani N K, Pan Z, Bakker R M, Paniagua-Domínguez R and Kuznetsov A I 2018 Directional lasing in resonant semiconductor nanoantenna arrays *Nat. Nanotechnol.* **13** 1042–7

[433] Curwen C A, Reno J L and Williams B S 2019 Broadband continuous single-mode tuning of a short-cavity quantum-cascade VECSEL *Nat. Photon.* **13** 855–9

[434] Kim H *et al* 2017 Corrugation-assisted metal-coated angled fiber facet for wavelength-dependent off-axis directional beaming *Opt. Express* **25** 8366–85

[435] Jia P and Yang J 2014 A plasmonic optical fiber patterned by template transfer as a high-performance flexible nanoprobe for real-time biosensing *Nanoscale* **6** 8836–43

[436] Jia P and Yang J 2013 Integration of large-area metallic nanohole arrays with multimode optical fibers for surface plasmon resonance sensing *Appl. Phys. Lett.* **102** 243107

[437] Zhang Z, Chen Y, Liu H, Bae H, Olson D A, Gupta A K and Yu M 2015 On-fiber plasmonic interferometer for multi-parameter sensing *Opt. Express* **23** 10732–40

[438] Reader-Harris P and Di Falco A 2014 Nanoplasmonic filters for hollow core photonic crystal fibers *ACS Photonics* **1** 985–9

[439] Arabi H E, Joe H-E, Nazari T, Min B-K and Oh K 2013 A high throughput supra-wavelength plasmonic bull's eye photon sorter spatially and spectrally multiplexed on silica optical fiber facet *Opt. Express* **21** 28083–94

[440] Du J *et al* 2016 *CLEO: Applications and Technology* (Optical Society of America) p JTu5A.104

[441] Liu Y, Xu H, Stief F, Zhitenev N and Yu M 2011 Far-field superfocusing with an optical fiber based surface plasmonic lens made of nanoscale concentric annular slits *Opt. Express* **19** 20233–43

[442] Saleh A A E, Sheikhoelislami S, Gastelum S and Dionne J A 2016 Grating-flanked plasmonic coaxial apertures for efficient fiber optical tweezers *Opt. Express* **24** 20593–603

[443] Xomalis A *et al* 2018 Fibre-optic metadevice for all-optical signal modulation based on coherent absorption *Nat. Commun.* **9** 182

[444] Yang J, Ghimire I, Wu P C, Gurung S, Arndt C, Tsai D P and Lee H W H 2019 Photonic crystal fiber metalens *Nanophotonics* **8** 443–9

[445] Principe M *et al* 2017 Optical fiber meta-tips *Light Sci. Appl.* **6** e16226

[446] Yu N and Capasso F 2015 Optical metasurfaces and prospect of their applications including fiber optics *J. Lightwave Technol.* **33** 2344–58

[447] Pahlevaninezhad H *et al* 2018 Nano-optic endoscope for high-resolution optical coherence tomography *in vivo Nat. Photon.* **12** 540–7

[448] Swartzlander G, Johnson L and Betts B 2020 Light sailing into the great beyond *Opt. Photonics News* **31** 30–7

[449] Liewer P C, Mewaldt R A, Ayon J A, Garner C, Gavit S and Wallace R A 2001 Interstellar probe using a solar sail: conceptual design and technological challenges *Outer Heliosphere: The Next Frontiers, Proc.* vol 11 pp 411–20

[450] Chu Y-J L, Tabiryan N V and Swartzlander G A 2019 Experimental verification of a bigrating beam rider *Phys. Rev. Lett.* **123** 244302

[451] Chu Y-J L, Jansson E M and Swartzlander G A 2018 Measurements of radiation pressure owing to the grating momentum *Phys. Rev. Lett.* **121** 063903

[452] Atwater H A, Davoyan A R, Ilic O, Jariwala D, Sherrott M C, Went C M, Whitney W S and Wong J 2018 Materials challenges for the Starshot lightsail *Nat. Mater.* **17** 861–7

[453] Ilic O, Went C M and Atwater H A 2018 Nanophotonic heterostructures for efficient propulsion and radiative cooling of relativistic light sails *Nano Lett.* **18** 5583–9

[454] Myilswamy K V, Krishnan A and Povinelli M L 2020 Photonic crystal lightsail with nonlinear reflectivity for increased stability *Opt. Express* **28** 8223–32

[455] Siegel J, Wang A Y, Menabde S G, Kats M A, Jang M S and Brar V W 2019 Self-stabilizing laser sails based on optical metasurfaces *ACS Photonics* **6** 2032–40

[456] Ilic O and Atwater H A 2019 Self-stabilizing photonic levitation and propulsion of nanostructured macroscopic objects *Nat. Photon.* **13** 289–95

[457] Ullery D C, Soleymani S, Heaton A, Orphee J, Johnson L, Sood R, Kung P and Kim S M 2018 Strong solar radiation forces from anomalously reflecting metasurfaces for solar sail attitude control *Sci. Rep.* **8** 10026

[458] Spencer D A, Johnson L and Long A C 2019 Solar sailing technology challenges *Aerosp. Sci. Technol.* **93** 105276

[459] Yildirim D U, Ghobadi A, Soydan M C, Atesal O, Toprak A, Caliskan M D and Ozbay E 2019 Disordered and densely packed ITO nanorods as an excellent lithography-free optical solar reflector metasurface *ACS Photonics* **6** 1812–22

[460] Sun K, Riedel C A, Urbani A, Simeoni M, Mengali S, Zalkovskij M, Bilenberg B, de Groot C H and Muskens O L 2018 VO$_2$ thermochromic metamaterial-based smart optical solar reflector *ACS Photonics* **5** 2280–6

[461] Khorasaninejad M, Zhu A Y, Roques-Carmes C, Chen W T, Oh J, Mishra I, Devlin R C and Capasso F 2016 Polarization-insensitive metalenses at visible wavelengths *Nano Lett.* **16** 7229–34

[462] Papaioannou M, Plum E, Valente J, Rogers E T and Zheludev N I 2016 Two-dimensional control of light with light on metasurfaces *Light Sci. Appl.* **5** e16070

[463] Leach J, Gibson G M, Padgett M J, Esposito E, McConnell G, Wright A J and Girkin J M 2006 Generation of achromatic Bessel beams using a compensated spatial light modulator *Opt. Express* **14** 5581–7

[464] Ostrovsky A S, Rickenstorff-Parrao C and Arrizón V 2013 Generation of the 'perfect' optical vortex using a liquid-crystal spatial light modulator *Opt. Lett.* **38** 534–6

[465] Mitchell K J, Turtaev S, Padgett M J, Čižmár T and Phillips D B 2016 High-speed spatial control of the intensity, phase and polarisation of vector beams using a digital micro-mirror device *Opt. Express* **24** 29269–82

[466] Ma Q *et al* 2019 Smart metasurface with self-adaptively reprogrammable functions *Light Sci. Appl.* **8** 98

[467] Zhang X G, Tang W X, Jiang W X, Bai G D, Tang J, Bai L, Qiu C-W and Cui T J 2018 Light-controllable digital coding metasurfaces *Adv. Sci.* **5** 1801028

[468] Liu F *et al* 2019 Intelligent metasurfaces with continuously tunable local surface impedance for multiple reconfigurable functions *Phys. Rev. Appl.* **11** 044024

[469] Li L *et al* 2019 Intelligent metasurface imager and recognizer *Light Sci. Appl.* **8** 97

[470] Ma Q, Hong Q R, Gao X X, Jing H B, Liu C, Bai G D, Cheng Q and Cui T J 2020 Smart sensing metasurface with self-defined functions in dual polarizations *Nanophotonics* **9** 3271–8

[471] Gioti M *et al* 2020 Plasmonic and phononic properties of epitaxial conductive transition metal nitrides *J. Opt.* **22** 084001

[472] Shah D, Catellani A, Reddy H, Kinsey N, Shalaev V, Boltasseva A and Calzolari A 2018 Controlling the plasmonic properties of ultrathin TiN films at the atomic level *ACS Photonics* **5** 2816–24

[473] Sherrott M C, Whitney W S, Jariwala D, Biswas S, Went C M, Wong J, Rossman G R and Atwater H A 2019 Anisotropic quantum well electro-optics in few-layer black phosphorus *Nano Lett.* **19** 269–76

[474] Whitney W S, Sherrott M C, Jariwala D, Lin W-H, Bechtel H A, Rossman G R and Atwater H A 2017 Field effect optoelectronic modulation of quantum-confined carriers in black phosphorus *Nano Lett.* **17** 78–84

[475] Zhou R, Ullah K, Yang S, Lin Q, Tang L, Liu D, Li S, Zhao Y and Wang F 2020 Recent advances in graphene and black phosphorus nonlinear plasmonics *Nanophotonics* **9** 1695–715

[476] Zhao H, Guo Q, Xia F and Wang H 2015 Two-dimensional materials for nanophotonics application *Nanophotonics* **4** 128–42

[477] Boltasseva A and Shalaev V M 2019 Transdimensional photonics *ACS Photonics* **6** 1–3

[478] Chen S *et al* 2020 Conductive polymer nanoantennas for dynamic organic plasmonics *Nat. Nanotechnol.* **15** 35–40

[479] Chen W T, Zhu A Y, Sanjeev V, Khorasaninejad M, Shi Z, Lee E and Capasso F 2018 A broadband achromatic metalens for focusing and imaging in the visible *Nat. Nanotechnol.* **13** 220–6

[480] Li N, Xu Z, Dong Y, Hu T, Zhong Q, Fu Y H, Zhu S and Singh N 2020 Large-area metasurface on CMOS-compatible fabrication platform: driving flat optics from lab to fab *Nanophotonics* **9** 3071–87

[481] Checcucci S, Bottein T, Gurioli M, Favre L, Grosso D and Abbarchi M 2019 Multifunctional metasurfaces based on direct nanoimprint of titania sol–gel coatings *Adv. Opt. Mater.* **7** 1801406

[482] She A, Zhang S, Shian S, Clarke D R and Capasso F 2018 Large area metalenses: design, characterization, and mass manufacturing *Opt. Express* **26** 1573–85

[483] Colburn S, Zhan A and Majumdar A 2018 Varifocal zoom imaging with large area focal length adjustable metalenses *Optica* **5** 825–31

[484] Faraji-Dana M, Arbabi E, Kwon H, Kamali S M, Arbabi A, Bartholomew J G and Faraon A 2019 Hyperspectral imager with folded metasurface optics *ACS Photonics* **6** 2161–7

[485] Park J-S, Zhang S, She A, Chen W T, Lin P, Yousef K M A, Cheng J-X and Capasso F 2019 All-glass, large metalens at visible wavelength using deep-ultraviolet projection lithography *Nano Lett.* **19** 8673–82

[486] Fan J A 2020 Freeform metasurface design based on topology optimization *MRS Bull.* **45** 196–201

[487] Jafar-Zanjani S, Inampudi S and Mosallaei H 2018 Adaptive genetic algorithm for optical metasurfaces design *Sci. Rep.* **8** 11040

[488] An S *et al* 2019 A deep learning approach for objective-driven all-dielectric metasurface design *ACS Photonics* **6** 3196–207

[489] Nadell C C, Huang B, Malof J M and Padilla W J 2019 Deep learning for accelerated all-dielectric metasurface design *Opt. Express* **27** 27523–35

[490] Liu Z, Zhu D, Rodrigues S P, Lee K-T and Cai W 2018 Generative model for the inverse design of metasurfaces *Nano Lett.* **18** 6570–6

[491] Jiang J and Fan J A 2019 Global optimization of dielectric metasurfaces using a physics-driven neural network *Nano Lett.* **19** 5366–72

[492] Phan T, Sell D, Wang E W, Doshay S, Edee K, Yang J and Fan J A 2019 High-efficiency, large-area, topology-optimized metasurfaces *Light Sci. Appl.* **8** 48

[493] Chung H and Miller O D 2020 High-NA achromatic metalenses by inverse design *Opt. Express* **28** 6945–65

[494] Kudyshev Z A, Kildishev A V, Shalaev V M and Boltasseva A 2020 Machine-learning-assisted metasurface design for high-efficiency thermal emitter optimization *Appl. Phys. Rev.* **7** 021407

[495] Sajedian I, Badloe T and Rho J 2019 Optimisation of colour generation from dielectric nanostructures using reinforcement learning *Opt. Express* **27** 5874–83

[496] Campbell S D, Sell D, Jenkins R P, Whiting E B, Fan J A and Werner D H 2019 Review of numerical optimization techniques for meta-device design *Opt. Mater. Express* **9** 1842–63

[497] Yang J and Fan J A 2017 Topology-optimized metasurfaces: impact of initial geometric layout *Opt. Lett.* **42** 3161–4

[498] Liu D, Tan Y, Khoram E and Yu Z 2018 Training deep neural networks for the inverse design of nanophotonic structures *ACS Photonics* **5** 1365–9

[499] Chung H and Miller O D 2020 Tunable metasurface inverse design for 80% switching efficiencies and 144° angular deflection *ACS Photonics* **7** 2236–43

[500] Hougne P, Imani M F, Diebold A V, Horstmeyer R and Smith D R 2020 Learned integrated sensing pipeline: reconfigurable metasurface transceivers as trainable physical layer in an artificial neural network *Adv. Sci.* **7** 1901913

[501] Grinblat G, Li Y, Nielsen M P, Oulton R F and Maier S A 2016 Enhanced third harmonic generation in single germanium nanodisks excited at the anapole mode *Nano Lett.* **16** 4635–40

[502] Li L, Ruan H, Liu C, Li Y, Shuang Y, Alù A, Qiu C-W and Cui T J 2019 Machine-learning reprogrammable metasurface imager *Nat. Commun.* **10** 1082

Jingyi Yang is currently a PhD candidate from Professor Howard Lee's Lab at University of California, Irvine. She received her Bachelor and Master degrees in China Jiliang University in 2013 and 2016, respectively. Her research interests include active metasurfaces and zero-index photonics on optical fibers and planar platforms, as well as electrically tunable photonic devices. She is a recipient of 2021 IEEE Photonics Society Graduate Student Scholarship, 2021 OSA Corning Women in Optical Communications Scholarship, 2019 SPIE Laser Technology, Engineering and Applications Scholarship, and the 2018 OSA Emil Wolf Outstanding Student Paper Award.

Sudip Gurung received his B.Sc. and M.Sc. degrees from Tribhuvan University, Nepal. He was a graduate research assistant at Baylor University and has transferred to the University of California, Irvine. His research interest includes plasmonics, nonlinear epsilon-near-zero metamaterials, active metasurfaces, and their nanophotonic applications.

Subhajit Bej received the Bachelor of Science (Physics Honors) degree in 2007 and the post-B. Sc. Bachelor of Technology (Optics and Optoelectronics) in 2010, both from the University of Calcutta, India. He received his M.Sc. degree in Photonics in 2012 and a PhD degree in Physics in 2017 from the University of Eastern Finland (UEF). During his doctoral studies, he got specialized in computational nanophotonics, fabrication of optical metamaterials, and experimental ultrafast spectroscopy. From October 2017 to January 2020, he worked in Dr Howard Lee's research group at Baylor University in Waco, Texas, as a post-doctoral research associate. There he performed experimental research on extreme nonlinear light-matter interactions in epsilon-near-zero metamaterials. At present, he is a post-doctoral fellow at Tampere University, Finland, funded by the Photonics Flagship (PREIN) project of the Academy of Finland. His current research focuses on experimental nonlinear nanophotonics, quantum metasurfaces, and novel nanofabrication techniques.

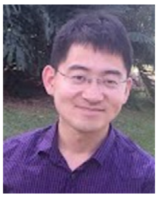

Peinan Ni is currently a Senior Research Fellow at Optoelectronic Research Center, Tampere University, Finland. He received his BS degree from Harbin Institute of Technology in 2009 and his PhD degree in Physics from University of Chinese Academy of Sciences in 2014, respectively. His research span across the interdisciplinary fields of semiconductor optoelectronic, nanophotonic, metasurface and plasmonic, with particular focus on the development of active metasurface for on-chip applications. He has published more than 40 scientific articles in peer-reviewed journal and conference proceedings. He is currently serving as a guest-editor of a special issue on metasurface for the journal of Frontiers in Photonics.

Howard Lee is currently an Associate Professor in the Department of Physics and Astronomy at UC Irvine. Before joining UCI, he was an Associated Professor in the Department of Physics at Baylor University and IQSE Fellow and visiting professor in the Institute for Quantum Science and Engineering (IQSE) at Texas A & M. He was a Postdoctoral Fellow at the Caltech, working with Professor Harry Atwater in active plasmonics/metasurfaces. He received his PhD in Physics from the Max Planck Institute for the Science of Light in Germany in 2012 under the supervision of Professor Philip Russell. His work on nano-optics, plasmonics/metasurfaces, and photonic crystal fibers has led to more than 45 journal publications in various journals, such as *Science*, *Nano Letters*, *Advanced Materials*, *ACS Photonics*, and *Laser & Photonics Reviews* as well as 50 invited talks and 130 conference papers. Dr Lee is a recipient of a 2021 Finalist of Rising Stars of Light, 2020 SPIE Rising Researcher, a 2020 Baylor Outstanding Professor Award, a 2019 DARPA Director's Fellowship, a 2019 IEEE OGC Young Scientist Award, a 2018 NSF CAREER Award, a 2017 DARPA Young Faculty Award, a 2018 OSA Ambassador, a 2017 APS Robert S Hyer Award, a 2018 Baylor Young Investigator Award, a 2016 Baylor Proposal Development Award, and a 2012 Croucher Postdoctoral Fellowship. He organized more than 10 technical sessions in nanophotonics/metasurfaces in international conferences (CLEO, META, PQE, MRS) and serves as Lead Symposium Organizer for plasmonic/metasurface symposiums at 2019–2022 MRS Fall Meeting and 2020–2022 MRS Spring Meeting. He is a Founding Associate Editor for *OSA Continuum* and Associate Editor for *Nature Scientific Reports* and *Photonics* journals.